Cranfield University
School of Applied Sciences

Bekim Gashi

Thermal and Deformation Analysis of Joint Interfaces in Machine Tools

PhD Thesis

Cranfield University
School of Applied Sciences
Precision Engineering Centre

PhD Thesis
Academic Year 2007 - 2008

Bekim Gashi

Thermal and Deformation Analysis of Joint Interfaces in Machine Tools

Supervisors: Prof. P. Shore, Prof. D.J. Stephenson

May 2008

This thesis is submitted in partial fulfilment of the requirements
for a degree of Doctor of Philosophy

Abstract

Machine tools are made up of many different parts connected together. In order to understand and create more accurate thermal and deformation numerical models the heat transfer characteristics of machine tool interfaces need to be understood. Previously heat transfer across interfaces has not been incorporated in finite element models in thermal and deformation analysis of machine tools. To a varying degree the issue of interfaces will have an effect on the overall performance of machine tools, and clearly if not considered and resolved at the strategic design stage they may be difficult and expensive to correct, once machine tools are operational. An inability to adequately understand and model the interfaces in machine tools is therefore a major limitation to current knowledge.

In this research programme heat transfer and corresponding thermal deformation of metal blocks in contact having pre-defined interface geometries, were experimentally and numerically investigated. Factors such as the contact pressure, the contact conformance, and the interface material were investigated. It was found that the most influential factors were contact pressure and contact conformance. Interface material was also found to have a bigger influence if the contact area was non-conforming. When interface material was thicker than the surface roughness, the heat flow across the interface was reduced as fewer contact asperities came into contact.

In order to optimise modelling it was necessary to optimise the convection coefficient - this was found to have an effect on overall heat transfer across the interface. It was also found that the overall contact area is important and not the spread of contact regions for the same overall contact. This was investigated using two different contact geometry arrangements.

The numerical prediction of heat transfer across an interface is accurate if the contact is conforming. However, if the contact is non-conforming an accurate prediction is not possible. This is due to the fact that direct modelling of non-conformance is not achievable. It was found that the most influential factor on thermal deformation is contact pressure, on the other hand factors such as interface material and interface geometry showed very little effect.

Acknowledgement

Firstly my gratitude goes to my supervisors Prof. P. Shore and Prof. D. J. Stephenson for their great support. They have given me a lot of encouragement and professional guidance in many practical and theoretical aspects. Without their knowledge and expertise the completion of this research would have been very difficult indeed.

Three other people that deserve plenty of thanks are Mr A. Baldwin, Mr. J. Hedge and Mr A. Hughes who with their truly amazing technical skills have helped me and shared their vast knowledge in many aspects including manufacturing, measurements and preparation of the experimental samples.

Personal thanks go to my parents and the rest of my family. They have always supported me in many ways throughout this research. Many thanks go to my best friend Teresa for her help and encouragement. She is truly a great friend with an optimistic and positive approach and someone that I look up to. Another friend Melissa deserves a lot of thanks for her support and encouragement during my writing up stage. Thanks must also be given to Mr. B. Broxup for proof reading the thesis.

Finally thank you to all of my colleagues that I have met here in this multinational and multicultural "village". Some of the colleagues have become very close friends to me and with whom I have spent a great amount of valuable time. I hope the friendship will continue for many years.

Content

List of Figures

List of Tables

Glossary

Symbol	Physical Quantity	Units
A	Area	m^2
a	Radius of Contact Spot	m
a_e	Grinding Depth of Cut	m
C_g	Specific Constant of Gas	N/m°C
C_p	Specific Heat Capacity	kJ/kg
D	Diameter	m
d_f	Deviation in Flatness	μm
d_p	Bolt Pitch Diameter	m
E	Modulus of Elasticity	GPa
e_{ch}	Limiting Chip Energy	J
F	Force	N
F_{pl}	Bolt Preload	N
g	Acceleration due to Gravity	m/s^2
H	Micro-Hardness	Pa
H_f	Heat Generated Power (bearings)	J
h	Convection Coefficient	W/ m^2°C
h_c	Thermal Contact Conductance	W/m^2°C
I	Current	Ampere
k	Thermal Conductivity	W/m°C
L, x	Length, Distance	m
L_c	Characteristic Length	m
l_c	Contact Length	m
M	Frictional Torque (bearings)	N
m	Mass	kg
m	Mean Absolute Slope of Asperities	rad
n_c	Number of Contact Spots	Scalar
n	Spot Density of Asperities	$1/m^2$
n	Rotating Speed (bearings)	rpm
P	Contact Pressure	MPa

P_g	Pressure	Torr
P_t	Surface Form Error	μm
p	Thread Pitch	mm
q	Heat Flow	W
Q	Heat Flux	W/m^2
Q′	Heat Generation	J/m^3
R	Electrical Resistance	Ω
R	Radius of Curvature of Waviness	m
R_a	Average Surface Roughness	μm
R_j	Thermal Joint Resistance	$m^2°C/W$
S_f	Yield Stress	MPa
T	Temperature	°C
t	Time	s
t	Thickness	m
T	Temperature	°C
T_{ch}	Chip Temperature	°C
T_w	Surface Temperature	°C
TCR	Thermal Contact Resistance	$m^2°C/W$
V	Voltage	volts
V	Volume	m^3
v_w	Feed Rate	m/s
W	Surface Waviness	μm
W_a	Average Waviness	μm
W_t	Total Waviness Height	μm
x	Asperity Height	μm
α	Diffusivity	m^2/s
β	Coefficient of Thermal Expansion	μm/°C
β'	Thread Profile Half angle	degrees
ΔT	Temperature Difference	°C
δ	Distance	m
ε	Contact Spot Size	μm

η	Efficiency	%
ν	Kinematic Viscosity	m^2/s
ρ	Density	kg/m^3
σ_t	Tensile Stress	MPa
$\sigma=5.669x10^{-8}$	Stefan-Boltzmann Constant	W/m^2K
τ	Time Constant	s
τ	Torque	Nm
υ_i	Cutting Speed	m/s

Subscripts

A	Surface
a	Apparent, average, ambient
B	Surface B
c	Contact, collar
e	Elastic
f	Flatness
g	Gap, gas
i	Initial
j	Joint
l	Layer
m	Mean
mac	Macroscopic
max	Maximum
mic	Microscopic
p	Plastic
r	Radiative, real
s	Harmonic mean, surface
t, tot	Total
w	Surface, waviness
0	Reference quantities
1, 2	Solid 1 and 2
∞	Fluid

Dimensionless Numbers

b	Elastic-plastic correlation coefficient
C_c	Dimensionless contact conductance
c	Micro-hardness correlation coefficients
$e = 2.718....$	Euler's number
e^x	Exponential function
f_{ep}	Elastic-plastic parameter
Gr	Grashof Number
H	Dimensionless similarity variable
J	The Jacobian determinant at integration points
K	Surface parameters, Torque coefficient
K_n	Knudsen Number
N_u	Nusselt Number
P_r	Prandtl Number
R	Rayleigh Number
R^2	Correlation coefficient between data points and line
s	Element stretch
α_g	Gas parameter
β	Accommodation parameter
γ	Specific heat ratio for interfacial material
ε	Emissivity, mechanical strain
θ	Dimensionless temperature
λ	Mean plane separation
μ_c	Friction coefficient (collar)
μ_t	Friction coefficient (thread)
υ	Poisson's ratio
φ	Plasticity index
ψ	Spreading/constriction parameter

1 Introduction

1.1 Machine Tools

Machine tools are made up of many members connected together. Some members are stationary, such as the machine structure, the other members move relative to each other in a specific direction. This relative motion of say tool to the workpiece allows the material to be machined to a desired shape or form. There are a number of different techniques available in shaping and forming the material, including: a) cutting excess material, b) shearing the material, c) squeezing metallic parts through extrusion to the desired shape, d) applying electricity or ultrasound etc.

A typical five-axis machine tool consists of a base, column, worktable, head, tool and tool holder, spindle bearing system and various linear and/or rotary axes. A schematic representation is shown in Figure 1-1.

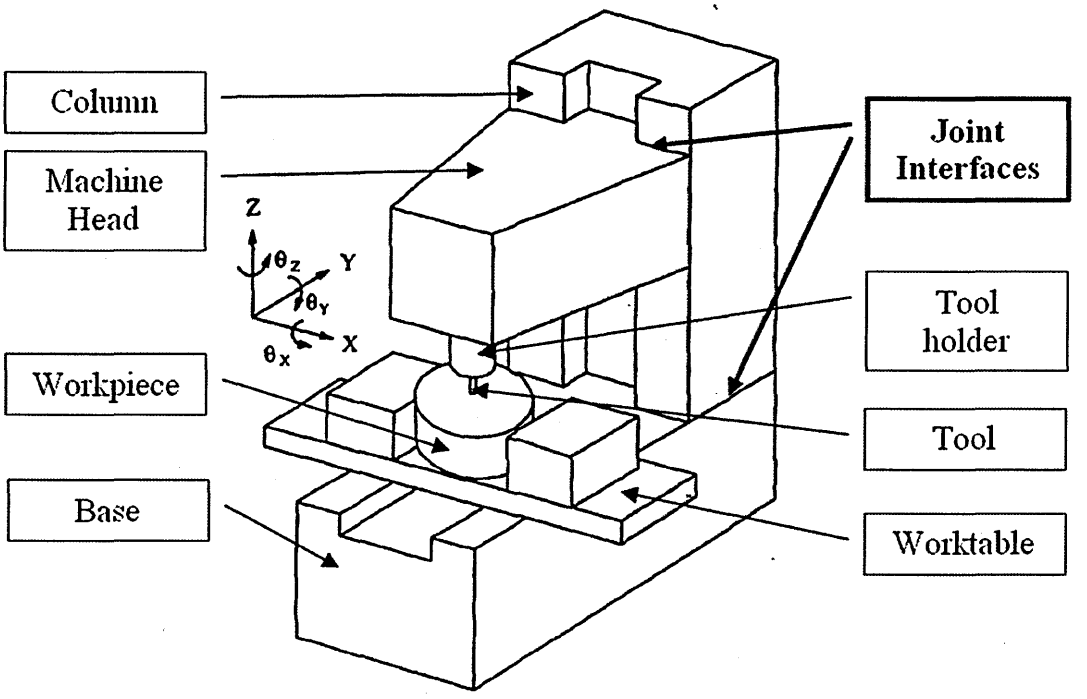

Figure 1-1. A typical five-axis machine tool [1]

In general, a machine tool structure can be subdivided as follows:

1. Members are classified as the building blocks of the machine tool. This includes: carriage bodies, beds that support the workpiece, the columns that connect the base of the machine tool to the headstock, spindle shafts etc.

2. Joints in machine tools provide two separate functions:

a. Large or complex machine components are joined together where installation of the components would be very difficult to manufacture in one piece.

b. For connecting two or more machine components that must be able to move relative to each-other such as the tool and the workpiece.

Moreover, machine joints can be classified as sliding or fixed joints. Sliding joints are provided in the form of bearings (rolling, hydrostatic etc), lubricated sliding faces, etc. A sliding joint is often restrained in specific directions and is free to move in a desired direction. Fixed joints on the other hand are static and are held together under specific pressure by means of bolts, studs, rivets etc. The pressure exerted at the contact can be of any required intensity, and it will depend on the number and size of bolts used and the amount of torque applied to them.

1.2 Sources of Error in Machine Tools

Errors are defined as the difference in the position of the tool from the programmed value to produce a part of a desired size or shape. Errors are undesirable in machine tools since they affect their performance. In general errors can be grouped into three major classes; geometric and kinematic errors, errors induced due to the cutting force and thermal errors, see Figure 1-2 [2].

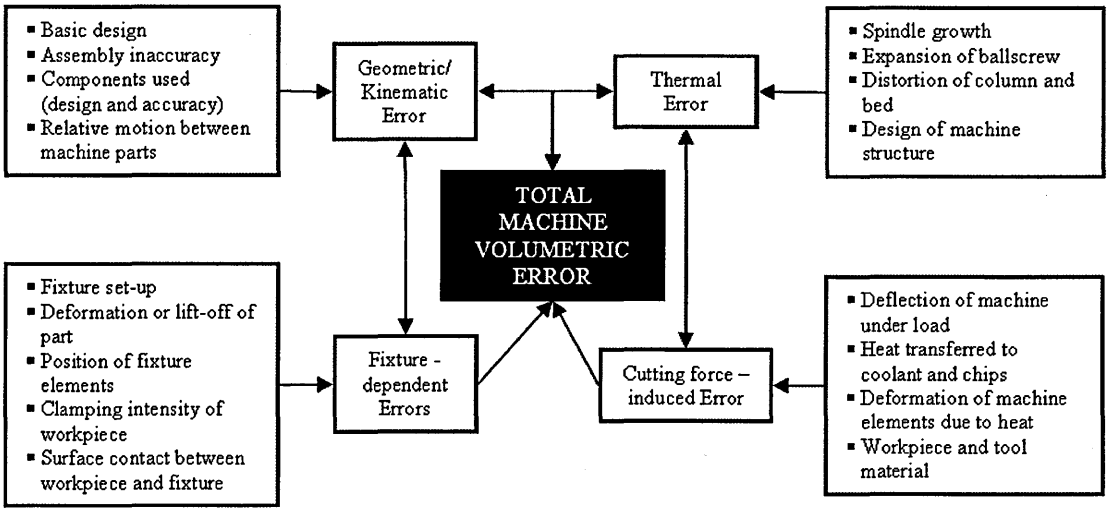

Figure 1-2. Overview of the error budget in a machine tool [2]

Geometric and kinematic errors of a machine are mostly stable over time. The changes can arise due to wear of the elements, squareness error, etc. Geometric errors can be accurately measured at any time. Force-induced errors can be predicted by numerical techniques and can be measured by well-designed experimental techniques. Thermal errors are more complex then the other errors due to the interaction of many heat sources and the fluctuation of ambient temperature [134]. Therefore, thermal errors are likely to cause the greatest apparent non-repeatability. It has been stated that the contribution of thermally-induced displacements of machine tool structures may exceed 50% of the total machining error [3,4].

1.3 Heat Transfer Across Joint Interfaces

Research and experience shows that thermal errors can be reduced at the design stage. This can be achieved by carefully selecting appropriate materials, e.g., with a low thermal expansion coefficient. However, selection of materials alone does not eliminate the error problem. In order to improve the thermal behaviour of machine tools, manufacturers have incorporated direct or indirect thermal compensation techniques. In the past, companies have invested in experimental analysis and prototyping in order to investigate the behaviour of complex machine tool structures. Nowadays besides experimental investigation, companies and/or research institutions can make extensive use of finite element methods in order to carry out complex thermal and deformation analysis.

One approach to modelling machine tool thermal and deformation behaviour is to use mathematical models. Mathematical models although accurate are very difficult and in many situations impossible to use on geometrically complicated systems. Over the last few decades, the power of computers has made it possible to solve very complicated engineering problems using finite element modelling. With advancements in finite element modelling, design and various analyses of different types of machine tool structures can be carried out at the design stage. However, designers normally do not incorporate joint interfaces in FEA modelling; a consequence is increased uncertainties in results and correlation to actual machine tool behaviour. An inability to adequately understand and model heat transfer across joint interfaces in machine tools is therefore a major limitation to current knowledge and capability. There is an important need to

augment the capability of finite element modelling to include the relationship between joint interfaces and machine tool thermal performance. Heat transfer across joint interfaces will have an effect on the overall performance of the machine tool.

Hence this research intends to investigate this problem. It aims to provide a better understanding of the heat transfer across joint interfaces having different surface characteristics with special attention paid in assessing the capability of FEA modelling in predicting the thermal and deformation behaviour of bolted joints.

1.4 Aims and Objectives of this Research

The aim of this research is to investigate and understand heat transfer and dimensional distortion across joint interfaces, formed by metal bodies having pre-defined surface geometry. The investigation was performed using experimental techniques and finite element analysis (hereafter referred to as FEA). Three objectives have been laid out to meet the overall aim:

1. Using experimental techniques investigate heat transfer across metal bodies in contact by measuring transient temperature distribution at selected locations using thermocouples.
2. Using experimental techniques investigate associated dimensional distortion of test structure using appropriate non-contact displacement transducers (hereafter referred to as NCDT).
3. Using FEA develop, and validate accurate three dimensional heat transfer and associated dimensional distortion models, of specific machine tool interfaces based on the experimental data collected.

1.5 Research Methodology

After the design of the experiments was established the appropriate material was selected to be used as specimens for analysis. Before the experimental tests were conducted the specimens were measured and checked for compliance with design specifications. Two different experimental rigs were developed and evaluated namely two block analysis and three block analysis.

1.5.1 Two Block Analysis

Two steel blocks were held together by a high tensile bolt inserted through their centre. Transient temperature data was collected experimentally using T-type thermocouples via a data acquisition board controlled by a computer. Data collected experimentally such as temperature input, initial conditions, and values calculated such as convection coefficient and thermal couplings were later used as boundary conditions in FEA.

1.5.2 Three Block Analysis

Three steel blocks were held together by two high tensile bolts inserted at specific locations. Transient temperature and thermal deformation data was collected experimentally using T-type thermocouples and non-contact displacement transducers respectively via two data acquisition boards controlled by a computer. Data collected experimentally such as temperature input, initial conditions, and values calculated such as convection coefficient and thermal couplings and bolt preload were later used as boundary conditions in FEA. The approach of the research within this thesis is shown diagrammatically in Figure 1.3.

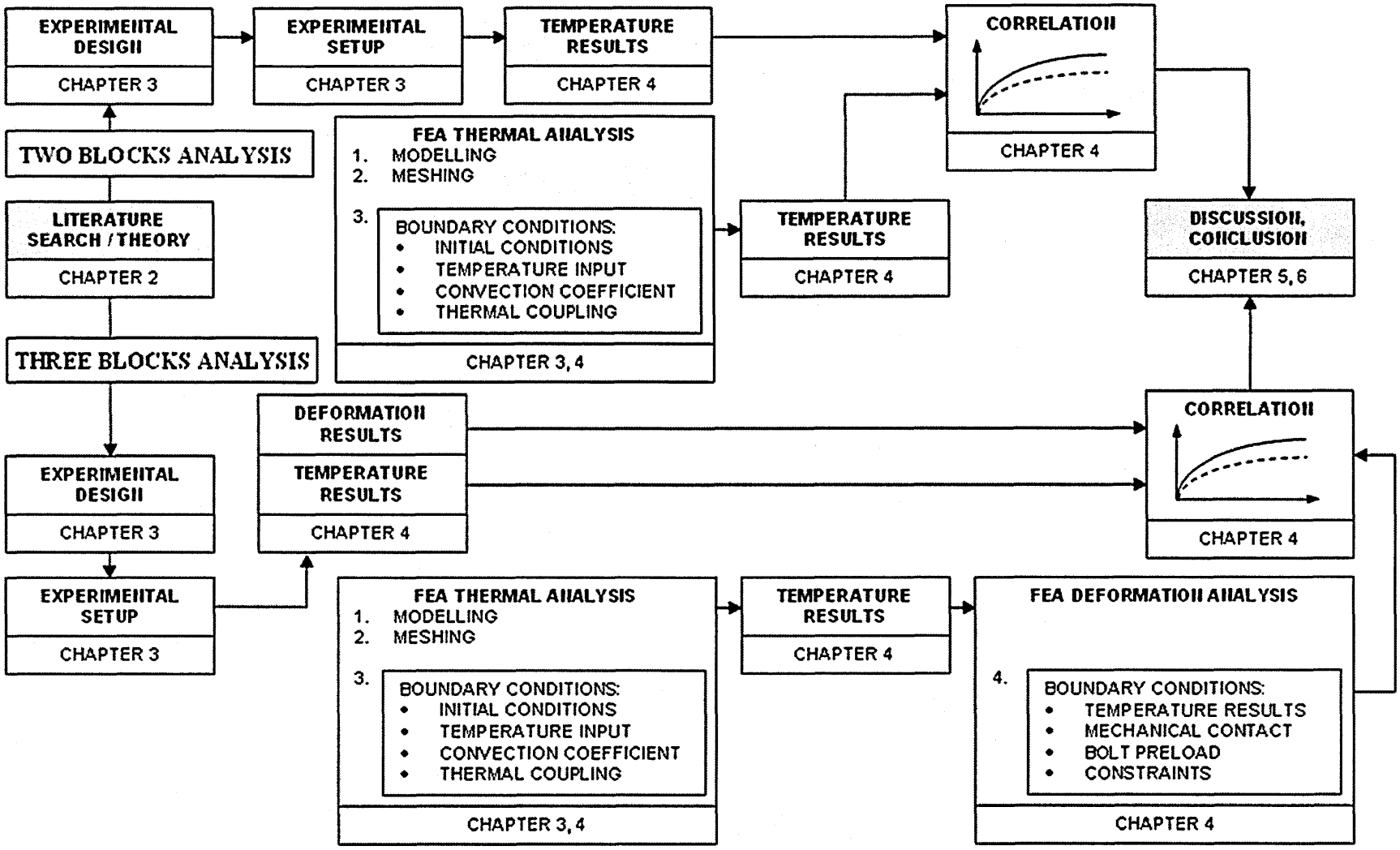

Figure 1-3. Research Methodology

2 Literature Review

2.1 Machine Tools

The demand for more intricate products has led to designing precision machine tools that can achieve nanometre-level accuracy. To achieve this level of accuracy with precision machine tools, an interactive consideration of structural design factors and thermal stability is necessary [5]. The most widely used classifications in manufacture with higher precision are:

- Precision engineering – is the manufacturing of parts to tolerances smaller than 1 part in 10^4 or perhaps 10^5.
- Micro-engineering – is where the dimensions of the features of the component being manufactured are small, that is in the order of 1 part in 10^6.
- Nanotechnology – was first coined by Taniguchi in 1974, and is defined as the manipulation and manufacture of materials and devices at a very small scale, namely in the order of 1 part in 10^9 [6].

Performance of machine tools is defined as the accuracy of the cutting tool relative to the workpiece. Due to thermal deformation of machine structures, the relative position changes which lowers the accuracy of machining.

Past research has shown that thermal deformation of machine tool structure account for as much as 50% of workpiece inaccuracy. Moreover, thermal deformations often reveal complex mechanical behaviours. The deformation is mainly due to the following:

- Continuously changing machine operating conditions.
- Various kinds of internal and external heat sources in and around machines.
- Complicated machine structures and machine parts that are made of different materials.

ANSI standard B-89.6.2 [7] was published to express measures of the effects of deviation from the standard temperature 20°C. Generally, thermal errors due to uniform temperatures other than 20°C can be analysed and compensated by accurate measurements of temperature gradients. Alternatively the errors could be reduced by

temperature-controlled fluid showers or temperature-controlled enclosures. Nowadays, many modern CMM's and precision machine tools are equipped with software error correction between tool and workpiece [5]. As an alternative, materials with low expansion coefficients are increasingly used in machine tool structures [6].

Machine tool manufacturers reduce thermal errors by incorporating sophisticated temperature control into machine tools. Although temperature control of machine structures is beneficial because it reduced thermal deformation, the high cost often prohibits the manufacturers from applying this approach [7].

The most common cause of apparent non-repeatability is heat related. More specifically, if the temperature is changing with time, then thermal distortion of the structural loop becomes complicated. Interestingly, temperature problems also seem to be the least widely appreciated error source in machine tools [2].

The international standard temperature, where a solid object has its true size, is 20°C. This implies that the temperature distribution must be constant and uniform throughout the object. By international agreement, an object at any other temperature other than 20°C contains thermally induced errors [8].

2.2 Thermal Errors in Machine Tools

Some machine tools incorporate sophisticated controls in order to reduce dynamic, kinematic, force-induced and thermal errors. Moreover, the influence of heat, especially non-uniform temperature, overshadows other errors. Additionally, thermal effects typically have a long time constant so they can not easily be identified nor quickly corrected once they begin [3].

In order to handle the problem of non-uniform temperatures, some experts have proposed generalised approaches as follows:

1. Control and minimise heat generation within the machine tool process and its environment.
2. Redesign the machine tool elements so they are less sensitive to heat.
3. Compensate for thermal errors using various software compensation methods [2].

It is advocated that machine design should be optimised before compensation techniques are applied. "It is quite misleading to believe that real-time correction for thermal deformations could fully overcome design defects connected with thermal phenomena" [4]. Due to inaccurate knowledge of the heat sources and the mechanism of heat transfer, exact prediction of the behaviour of a machine tool at the design stage is extremely difficult. Thermal deformation of machine tools can be reduced by; firstly incorporating materials with a low thermal coefficient of expansion, and, secondly by incorporating well designed temperature control systems [3].

One of the pioneers in understanding thermal effects was Professor John Loxham [9]. He recognised the relationship between the predictability of celestial bodies and automatic machines, as cited in [10]. The following statement was written in 1970, and it's known as Loxham's Principle:

> *"An automatic manufacturing process is always operating perfectly. It may not be doing what is required, but if that is so it is because it has not been suitably arranged".*
>
> Loxham (1970)

Bryan (1990) [4] published a report on thermal error research. In his report Bryan classified the problem of thermal errors as the effects of uniform temperatures other than 20°C. The 20°C temperature was agreed during the meeting of the International Committee of Weights and Measures held in Paris in 1931.

He also provided a comprehensive diagram showing thermal effects on machine tools and CMM's as shown in Figure 2-1. According to Bryan's survey identification of the effects of uniform temperatures other than 20°C dated back to 1920's [4].

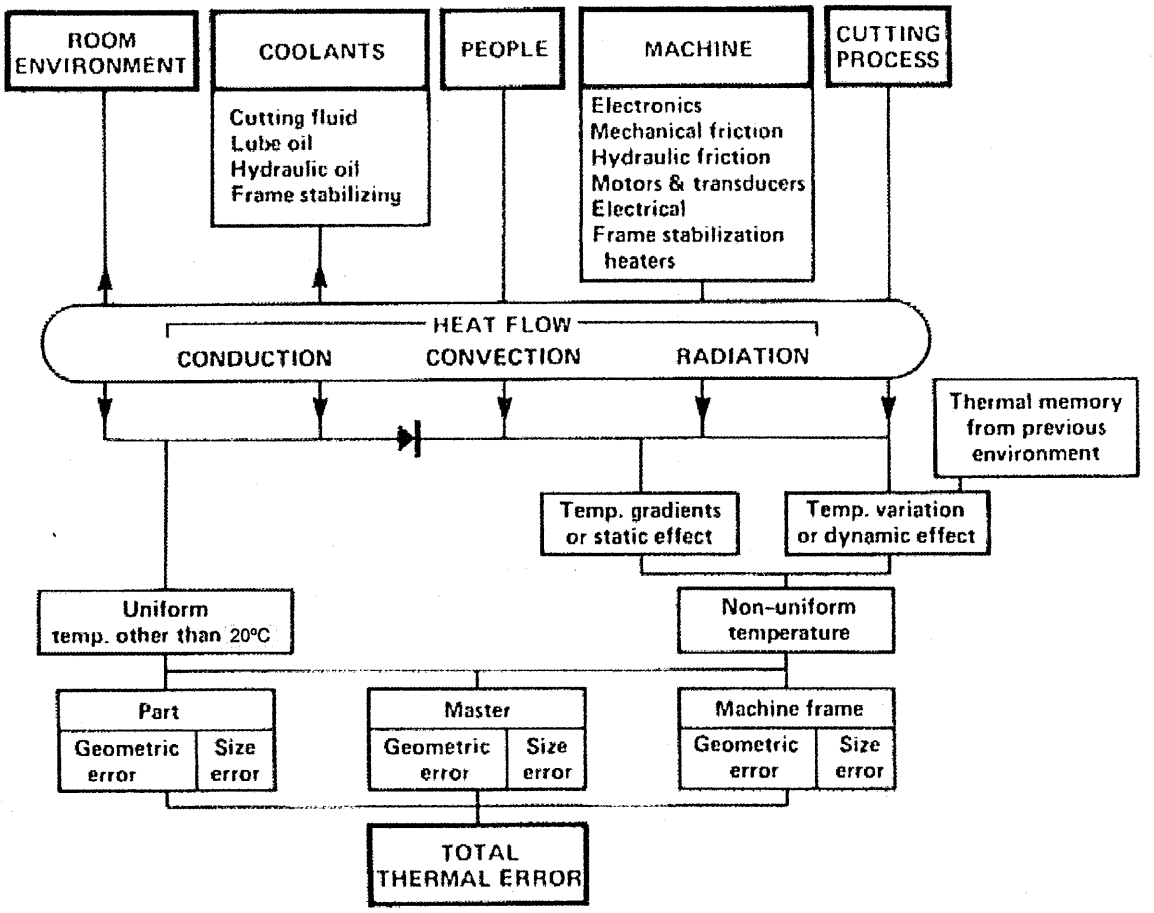

Figure 2-1. Thermal effects diagram [4]

This comprehensive diagram shows six sources of thermal influence:

1. Heat generated from the machining process e.g. grinding, turning, milling etc.
2. Heat generated by the machine itself. e.g. heat generated by the spindle bearings, motors, etc.
3. Heat generated by people in the machine tool shop floor.
4. Heating or cooling provided by cooling systems.
5. Heating or cooling changes in the machine floor, and
6. Thermal memory from previous environment.

In the early stages of thermal error research most of the work was devoted to problems in dimensional metrology and used a defined temperature point of 20°C as an international standard for measurements. ANSI standard B-89.6.2 was published to

express measures of the effects of deviation from the standard temperature and nominal expansion coefficients as a consequence of the research efforts [7].

Normally, machine tools are composed of members made of different materials jointed together (e.g., bolted, interference fit, adhesives etc). This means that the members have different thermal and mechanical properties. In this case the members expand and/or contract at different rates and magnitudes. This type of error is known as differential expansion [4].

The complication arises when dealing with non-uniform temperatures, which can be classified to static effects due to temperature gradients and dynamic effects due to temperature variations. The temperature variations due to dynamic effects are time and spatial dependent therefore are more complicated than the static effects. This means that reducing the dynamic temperature effects is often difficult [4,12].

2.3 Heat Sources in Machine Tools

During the machining process kinematic energy due to material removal is converted into thermal energy. Heat is generated due to the friction forces between the tool and the workpiece, heat sources from bearings, heat sources from motors, etc. All of the energy supplied to the machine tool is converted into heat. This heat will circulate through conduction, convection and radiation and it will affect the machine including the workpiece. In order to understand the thermal behaviour of machine tools it's essential to know the sources and the magnitude of heat. Heat sources in machine tools are many and can be classified as *external* and *internal*. The effect of external and internal heat sources to the deformation of a typical machine tool is shown in Figure 2-2 [2].

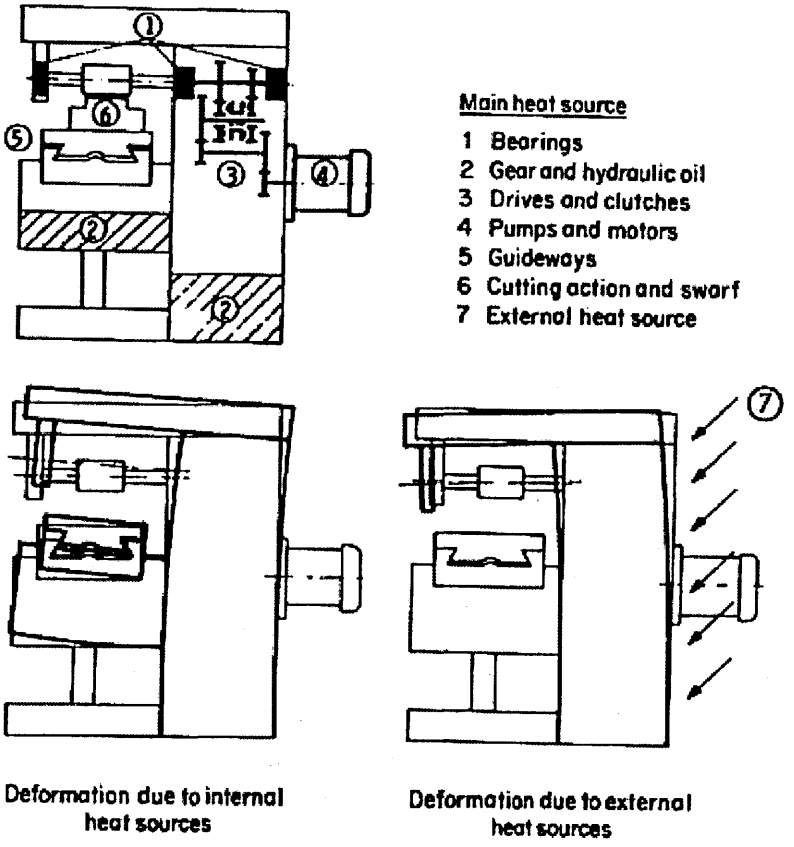

Figure 2-2. Examples of thermally induced displacements on a milling machine [2]

2.3.1 External Heat Sources

External heat sources are many including the daily variation of the surrounding ambient temperature in machine tools environment, or exposure to direct sunlight. In a typical machine shop floor, a difference in ambient temperature as high as 5°C may be seen at any one time, as reported in [3]. Heat generated by people is another external heat source. An average person generates about 105 watts of heat. This heat could interact with the machine tool members and cause thermal deformation [14]. Thermal memory from previous environment is another external heat source. Normally, machined parts are transported from a shop-floor to the inspection or packaging room that might be under different environment conditions [4,12].

2.3.2 Internal Heat Sources

The main internal heat sources are normally generated by driving motors, friction in bearings, friction of guide-ways, heat generated due to the machining process and coolant pumps [15,16]. Often internal heat sources are more influential than external

heat sources because the heat is directly conducted into the machine structure. It has been reported that one of the main heat sources is the machine spindle and bearings [3].

2.3.3 Heat Generated due to the Cutting Process

Heat generated from the machining process is often one of major sources of thermal error. In many machining processes it takes precedence over all other sources of heat generated [2,17]. The rate of heat generated due to the cutting process can be expressed using the following equation:

$$q = \frac{\sum \eta_i F_i v_i t_i}{t_{tot}} \qquad \text{Eq. 1}$$

Where η_i is the process efficiency, F_i and v_i are the force and the cutting speed respectively, t_i is the time of operation and $t_{tot}=\Sigma t_i$ is the total time of operation. The efficiency η_i is normally taken as a unity, i.e. all of the process energy is converted to heat. The amount of heat generated varies from process to process and is a function of several parameters. A rough comparison of removal energies by different processes is shown in Table 2-1 [18].

Manufacturing process	Specific energy [J/mm^3]
Convectional fine grinding/honing	50 – 100 or more
Convectional grinding	24 – 60 or more
CBN grinding	20 – 40 or more
Hard turning	8 – 15
Soft turning	2 – 7
Diamond turning	0.1 - 1

Table 2-1. Rough guide of specific removal energy levels of various processes [18]

2.3.4 Heat Generated by Driving Motors

Motors are used in order to move machine members relative to each-other. Electric motors convert electrical energy to mechanical energy [19]. Due to friction amongst motor elements, the work output from a motor is always less than the work input. This means that the motor efficiency is always less than 100 percent. The efficiency is defined as the relation of the output power to the input power, that is:

Efficiency η = Output / Input Eq. 2

In machine tools, linear motors can be used as actuator devices if accurate movements are required. A high speed drive system generates heat, and temperatures higher than

100°C have been reported [20]. A combination of each part of the machine tool will affect the positional accuracy of a machine tool [21,22]. It was found that if no precision cooler is used the heat generated in the linear motor was directly conducted to the machine tool members, causing thermal deformation [19].

2.3.5 Heat Generated by Machine Tool Bearings

Machine tool bearings are complex and made up of many parts held together. It has been reported that the major heat generation of the bearing system is caused by forces from the cutting process increasing the friction between the races and the balls of the bearings [23]. The heat generated by bearings is thought to be the dominant cause of temperature change, with the major heat source being generated by the cutting process and the chips [24]. The spindle including spindle housing growth can amount to 100 μm or more, considering the thermal load, design and cooling conditions. The heat generated by the bearing can be calculated using the following equations:

$$H_f = 1.047 \times 10^{-4} nM \qquad \text{Eq. 3}$$

$$M = M_1 + M_2 \qquad \text{Eq. 4}$$

Where H_f is the heat generated power, n is the rotating speed of the bearing, M is the total frictional torque which is the sum of the torque due to the applied load M_1 and torque due to the viscosity of lubricant M_2 [24].

Internal heat sources and contact heat conductance can vary with the thermal deformation of the bearing surroundings as well as with operating conditions [24]. The most important factor in the spindle-bearing system is found to be the bearing pressure [25].

The power loss is generated due to the preload of the spindle system and the friction torques. The power loss can be up to 100 W for a 100 mm diameter ball bearing running at 10,000 rpm. For a hydrostatic bearing of the same size, running at the same rotational speed the power loss can reach 1 kW [3].

The bearing material plays an important part in its performance. It has been found that the most appropriate combination of bearing material is the ceramic ball, steel inner and

outer race [25]. Koch [26] has shown that the hybrid bearings made of ceramic balls generates less friction therefore reduced thermo-elastic deformation, as cited in [3].

Understanding the thermal behaviour of spindles is of great importance to machine tool designers. Many researchers have investigated the thermal behaviour of machine tool spindles. Some of the researchers have developed finite difference models to characterise the thermal behaviour of spindles [27,28]. Other researchers such as Lin et al., [29] studied the thermo-mechanical-dynamic behaviour of a spindle and developed a new model and validated the model with experimental and sensitivity analysis.

Choi et al., [30] investigated experimentally and numerically a spindle bearing system for a five axis machining centre. The spindle system was purposely manufactured to investigate the thermal characteristics of the spindle bearing. Temperatures as high as 58°C were reported, see Figure 2-3.

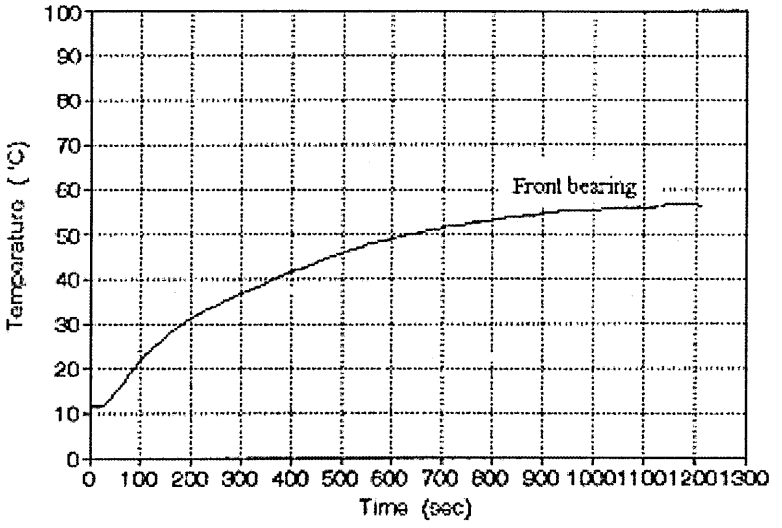

Figure 2-3. Temperature rise of the front bearing with respect to time when the spindle rotational speed was 3500 rpm [30]

2.4 Modelling of Thermal Errors

In the past decade researchers have employed various techniques to model thermal errors such as: finite element analysis, neural networks, coordinates transformation methods and hybrid methods to name a few. The complex interaction between the heat sources and machine elements creates complex thermal behaviour of the machine structure [2,12,31]. The factors affecting the thermal state of a machine tool are shown in Figure 2-4.

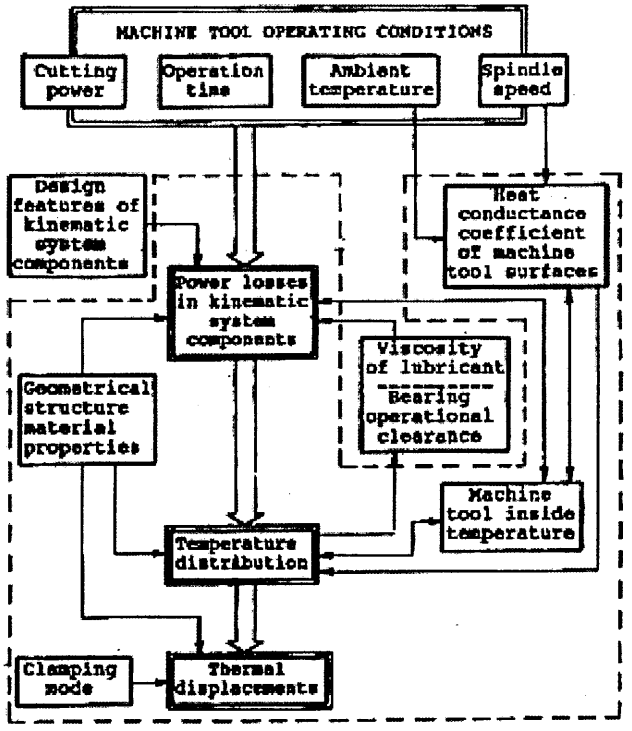

Figure 2-4. Factors effecting the thermal state of a machine tool [32]

Finite element techniques are used extensively nowadays as means of modelling and predicting temperature distribution and associated thermal deformation of machine tools. Analytical methods although accurate methods for predicting thermal behaviour of machine tools have their limitations when dealing with complicated structures found in machine tools. An accurate mathematical modelling of complicated three-diemnsional machine tool elements is cumbersome and in many situations not possible.

Jedrezejwski et al [33] used finite element analysis to model the temperature distribution and thermal deformation of a machine structure. He applied optimisation methods to the elements that contributed the most to the heat generation. The optimisation was used in order to minimise and reduce thermal errors in the machine tool. Following his previous study, Jedrezejwski et al [32] presented a new method of modelling thermal behaviour of a machine tool. The method works by assuming that the amount of energy dissipated in the components of the kinematic system is a function of the operational conditions. In this study they modelled the whole machine structure, in order to account for the actual conditions of heat flow, see Figure 2-5. However, the finite element models were created in a milling machine thereore are limited in their application because can not be applied to more sophisticated machine tools. Moreover

the models do not take into consideration heat transfer across joint interfaces therefore introducing inaccuracies.

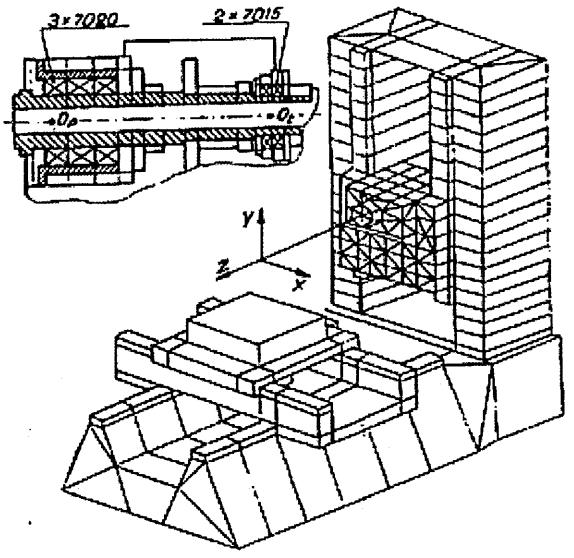

Figure 2-5. Finite element modelling of a machine tool [32]

Venugopal et al. [34] calculated the thermal profile in a particular domain, and then determined the corresponding deformation by solving the thermo-elastic equations using finite difference methods.

The temperature distribution along a ball-screw system was analysed using finite element methods by Kim et al. [35]. They found that heat generated due to friction was the main source of thermal deformation.

2.5 Compensation For Thermal Errors

One approach in reducing thermal errors in machine tools is to apply compensation methods. The compensation methods work by calculating or measuring the motion of machine tool axes due to deformation, and return the tool tip as close as possible to the original un-deformed shape [1].

Extensive research has been carried out under a variety of thermal conditions in order to compensate for the thermally induced errors in machine tools [3,36,37]. There are two types of compensation techniques namely, direct or indirect [3]. Direct compensation techniques work by directly measuring the displacement between the tool and the workpiece and compensating for any errors. This technique is simple and effective but

the measurement of thermal drifts is not always possible, due to the difficulties encountered with locating the sensors e.g., on moving parts [38].

The indirect compensation techniques are based in the use of mathematical models. These models utilize a deformation model based on the temperature measurement and deformation [39]. These models can generally be classified into the following categories:

1. Empirical compensation function [40-42]
2. Numerical simulation [43,44] and
3. Generalised modelling methods [45].

Empirical compensation function can only be used if the machine tool has reached thermal steady-state conditions. In the case of transient thermal behaviour, this approach can only be used if machine tool's control cycle is between 5-10 min [45]. Numerical simulation and generalised modelling methods on the other hand are appropriate for applications, in which the transient effects of machine operating cycle can not be neglected [46].

These methods although powerful, have limitations in terms of real-time estimation of the heat input to the machine tool system [46]. However, a real-time error compensation control has been developed by Chen et. al [47]. The controller can compensate for thermal errors at a period of 48 ms/cycle. The external PC measures the thermal errors and the values are then fed into the CNC controller in real time. This method has its advantages since it can be applied to many modern CNC controllers without difficulty, see Figure 2-6. Experimental results conducted on a vertical machining centre show that 70-90% reduction of thermal errors was achieved after compensation, with an improvement in the accuracy from 40 μm to within 5 μm [47]. Nevertheless, this method has its disadvantages because the coefficients in the thermal model need long time to tune in across a machine duty cycle. Moreover the thermal model is tuned to a specific machine and can not be used as a universal model to other machine tools. This is due to the limitations associated with the algorithm which is applicable only to a specific machine tool.

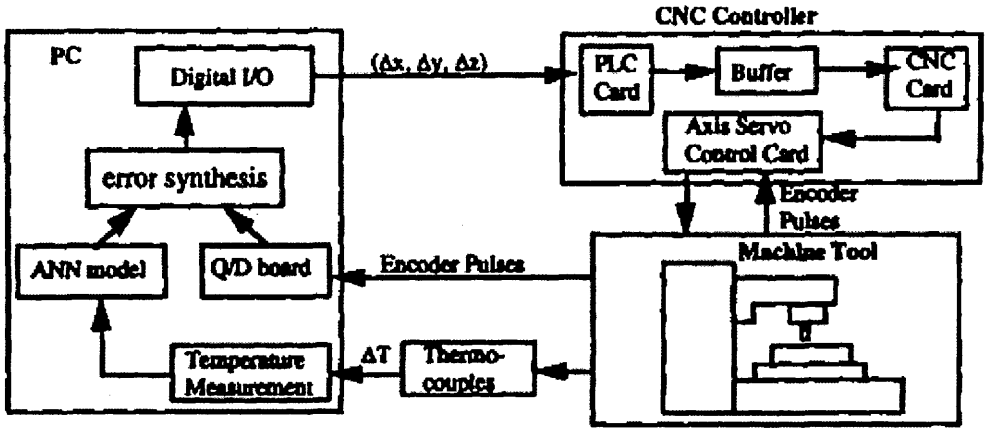

Figure 2-6. Block diagram of a real-time thermal error compensation scheme [47]

Positioning errors for a turning machine was obtained using the homogeneous transformation matrix by Donmez [39]. This method works by storing the error vector components at different locations in the machine workspace.

Chen et al. [48] proposed a multiple regression analysis and an artificial neural network for the real-time prediction of thermal errors. Both approaches automatically search for interaction terms between different temperature variables using a systematic and computerised algorithm. Based on their results a substantial improvement in the accuracy of a finished workpiece was obtained using these strategies. Other researchers used a neural network strategy for the estimation of errors due to thermal loading, Srinivasa et al [49].

A model composed of hybrid filters and static feed-forward neural network (FNN) was proposed by Kang et al. [50]. This model was used to improve the accuracy and reduce computation times from 48 h to 8 h for the prediction of thermal deformation in a machine tool. The hybrid filters used consisted of linear regression, moving average, and auto-regression. It reports that this method can yield better prediction results in comparison to using finite element model.

A simple analytical method to obtain the total volumetric error at the tool throughout the workspace of individual components on a five-axis CNC machine tool was developed by Srivastava et al [1]. An error compensation scheme has also been presented to improve the total position and orientation accuracy at the tool. Simulation results indicate that substantial error reductions at the tool tip are possible [1].

Thermally induced machine tool errors can be classified as quasi-static errors that vary slowly in time and are related to the structure of the machine tool. These errors are not only time-variant but also spatial variant. The process where the interaction of a system to its surroundings is very slow and remains arbitrarily close to equilibrium at all times its said to be a quasi-static process for that system [51].

The problem with thermal error compensation models is the accuracy and the robustness [52]. Some of the models e.g. neural network [53] and polynomial regression [39] have a very good interpolation ability, but very poor extrapolation capability. Thus, model estimation is unreliable outside the range of tested working conditions [34]

Modelling techniques are extensively used at the design stages of machine tools, as means of understanding and predicting their behaviour under specific working conditions. It was previously thought that there is no easy means to determine the temperature sensitivity of a machine tool before it has been built and tested [12]. However, with advancement in numerical methods, such as finite element modelling, the accurate prediction is possible if the boundary conditions are accurately known and defined. However, in complex systems an accurate determination of boundary conditions is often difficult.

Many researchers have applied numerical techniques in modelling thermal behaviour of specific machine tool members, and found that the predicted results correlate well with experimental results. However, the numerical models could be further improved if joint interfaces were incorporated into the models [26,34,54,55].

Since machine tools are made up of many members joined together using various methods, e.g., bolted, stud, riveted etc, understanding the thermal behaviour of joint interfaces is extremely important. Excluding joint interfaces in numerical modelling will mean ignoring thermal errors at the joint that contribute towards the total thermal errors. Every engineering surface has a specific topography that is defined by its roughness, waviness and flatness. These topography parameters will influence heat transfer across joints that in turn will affect machine tool accuracy. Other factors that influence heat transfer across a joint are contact pressure, interface material, contact geometry etc. The next section in this Chapter attempts to provide the past research in this important field.

2.6 Heat Transfer Across Bodies in Contact

When two solid blocks are brought into contact, and if heat is applied at the open end of left block, this heat will be conducted into the first block, across the interface, and into the second block. If the blocks are insulated the heat flow would be one-dimensional in the axial direction. As the consequence of the contact at the interface, the temperature profile through the two blocks is discontinuous at the interface, as shown in Figure 2-7 [56-60].

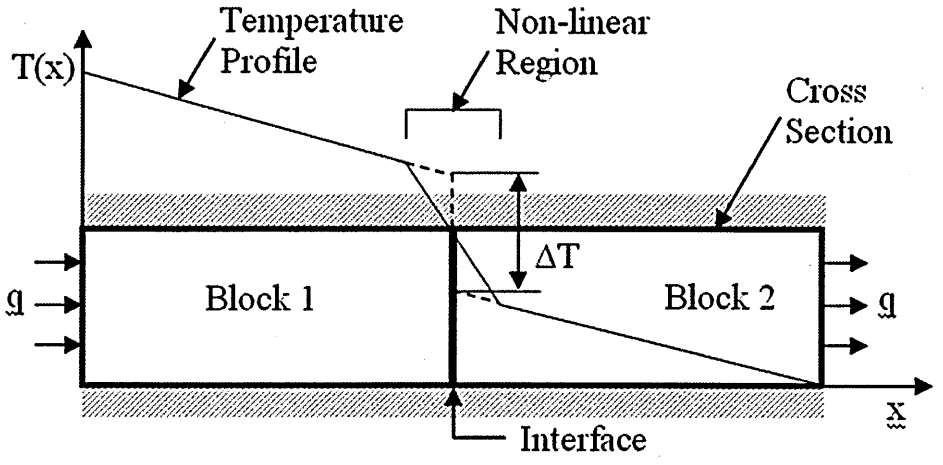

Figure 2-7. Schematic representation of temperature profile across bodies in contact with interface resistance (after [69])

A number of different models have been presented in the literature review for prediction of thermal contact resistance [57,58,61-68] (hereafter referred to as TCR). TCR is the resistance of heat flow across interface due to imperfect contact. TCR depends on many parameters including macro and micro geometry, interface material, surface topography, contact pressure [65-68].

The topographies of machined metallic surfaces are built up of irregularities of varying wavelengths. These irregularities play an important role in heat transfer across joints, see Figure 2-8.

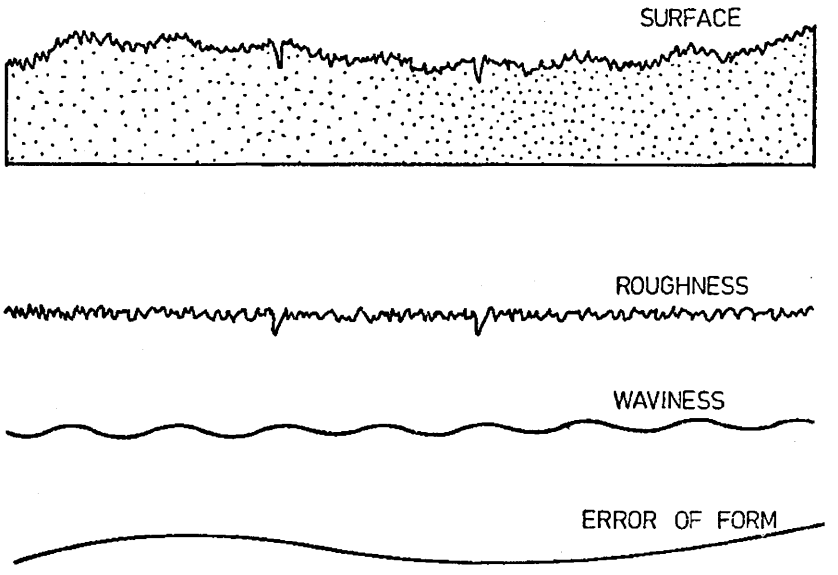

Figure 2-8. Relationship between surface roughness, waviness and error of form of a typical engineering surface [70]

The long wavelengths are considered to be errors of form, the medium wavelengths represent the waviness of the surface and the small wavelengths which are superimposed upon the waviness are classified as surface roughness. The waviness and the roughness are as result of surface finish processes. Surfaces processes using shaping, milling and grinding have directional 'lays'. Those that have been processed using spark erosion, sandblasting and lapping have an isotropic distribution in all direction along surface [70], see Figure 2-9.

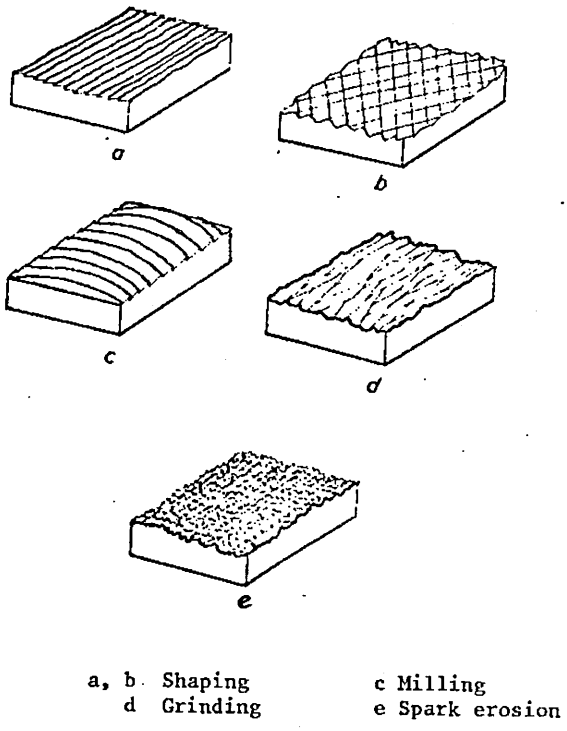

Figure 2-9. Direction pattern of engineering surfaces generated using various machining processes [70]

Figure 2-10 illustrates six types of joints that are characterised by whether the contacting surfaces are smooth and non-conforming (Figure 2-10a), rough and non-conforming (Figure 2-10b) or rough and conforming (Figure 2-10c). Each joint can comprise of interface material (Figure 2-10 d to f) [71].

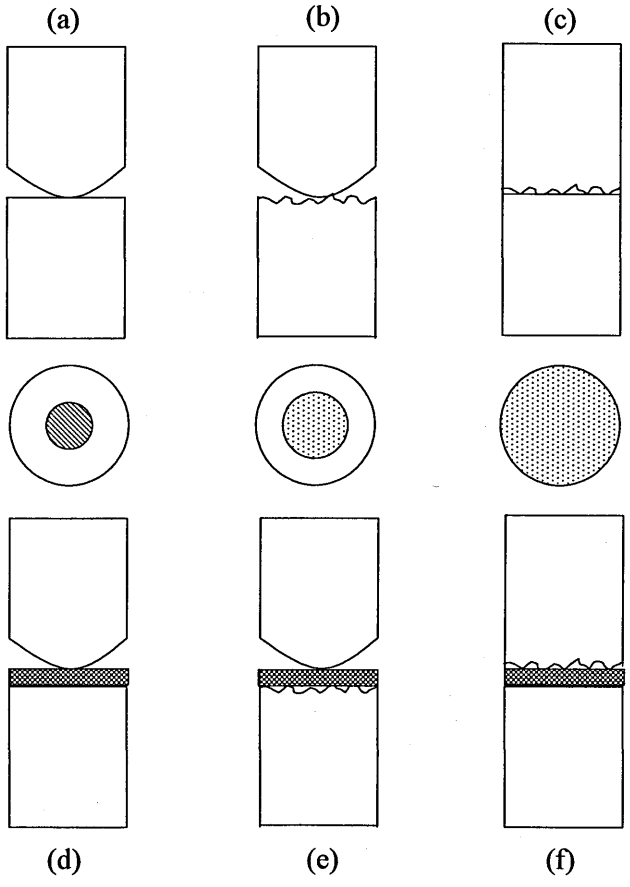

Figure 2-10. Six types of joints [129]

Thermal energy can be transferred between contacting bodies by three modes:

1. Conduction through contacting asperities
2. Conduction through interface material and,
3. Thermal radiation across the gap if the interface material is transparent to radiation.

Radiation heat transfer across the interface can be assumed negligible if the interface temperature is not higher than 600°C [72].

2.6.1 Thermal Contact Resistance

TCR consist of three separate problems: geometrical characteristics, mechanical configuration and properties and thermal boundary conditions. Each sub-problem also includes a micro and macro scale component, see Figure 2-11 [67].

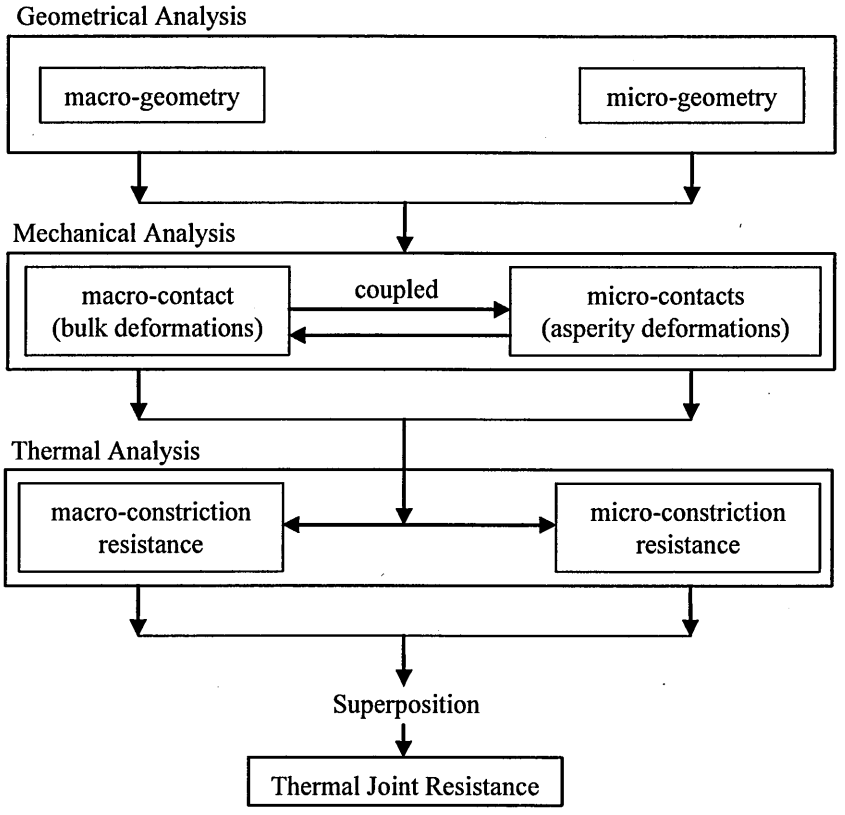

Figure 2-11. Thermal contact problem [67]

The rate of heat transfer across the joint depends on a number of parameters, as explained in section 2.6 [66]. These parameters have an effect on the thermal contact resistance and consequently on the heat transfer across a joints. The magnitude of effect varies from parameter to parameter, which will be discussed below.

a. Effect of Interfacial Temperature

When the temperature at the interface is raised, the TCR will decrease. This phenomenon has been observed and reported by many investigators [73-75]. If the interface is under high vacuum, the TCR decreases slightly if the interface temperature is in the range of 0°C to 100°C. However, the effect is more evident if the interface temperature is higher than 100°C. This is thought to be due to the following:

a) If the interface temperature is >100°C, the radiation increases and becomes the dominant of heat transfer modes. This is predominantly true for surfaces with high emissivity.

b) As the interface temperature increases the material hardness decreases.

If the materials are put into contact with each other after they have been heated, rather than put into contact while they cold, e.g. room temperature, then the surface oxide layer will have thickened and the contact resistance would be expected to increase.

If an interface material with a higher thermal conductivity is present at the interface, the contact conductance will rise slightly with temperature, due to an increase in the thermal conductivity.

b. Effect of Period of Heating and Heat Flux

Contact resistance should decrease with time of heating; this is due to the decrease in the hardness of the metals in contact. Figure 2-12 shows the increase in material hardness as the temperature decreases and consequently decrease in thermal contact conductance [76].

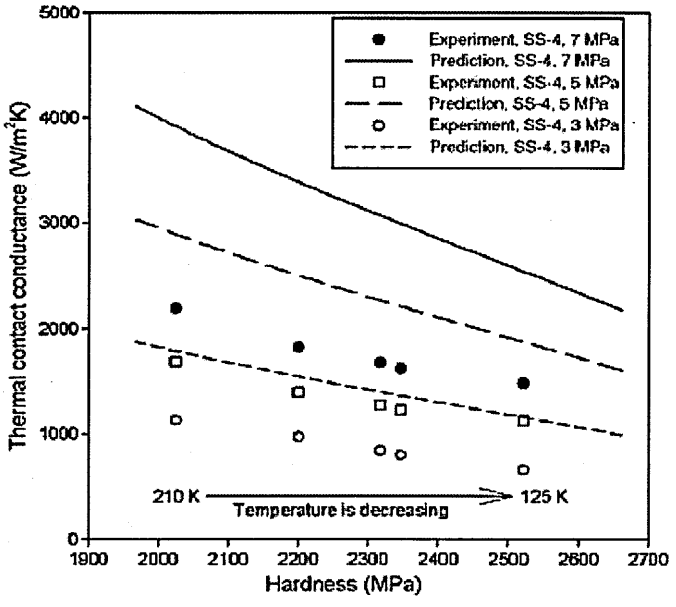

Figure 2-12. Relationship between thermal contact conductance, material hardness, and temperature for stainless steel 304 [76]

Mann [77] measured experimentally the micro-hardness of stainless steel 304 using a diamond pyramid indenter as cited by Ruiping and Lie [76]. Figure 2-13 shows the comparison of hardness, yield strength S_y and the ultimate strength S_u for stainless steel 304 as a function of temperature. The hardness of material drops linearly from 2700 MPa at 80°C to 1500 MPa at 300°C.

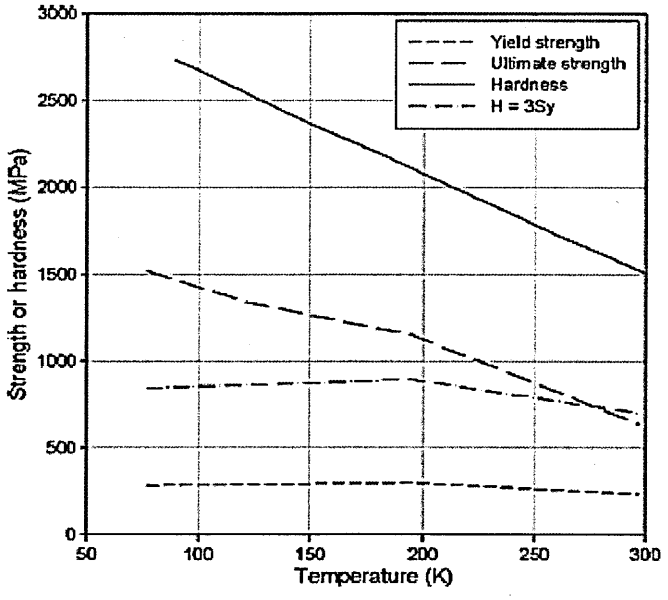

Figure 2-13. Mechanical strength and hardness of stainless steel 304 at low temperatures [76]

An increase in the contact resistance is found to be temporary, i.e. when the specimens under investigation were returned to room temperature there was no indication that the higher conductance had been reserved as reported by Barzelay [74].

Contact resistance is reported as being independent of heat flux by many investigators, although Barzelay [74] have reported a slight dependency. The effects are more evident if the contact is formed by two dissimilar materials.

c. Effect of Contaminant Films at the Interface

A surface of a metal specimen is usually covered by a contaminant film [78]. Since the kinetics of oxide growth involve the diffusion of metal ions through oxide film, the topography of metal oxide depends largely upon environmental conditions during the growth period. Oxides are much less ductile than most light metals. The presence of surface oxides reduces the metal to metal contact. The presence of the contaminant films at the interface formed by metal bodies is more evident at low contact pressure and can contribute to hysteretic effect during load cycling [79].

The presence of contact asperities on rough surfaces is likely to penetrate the contaminant films. If the contacting surfaces are smooth (without asperities) no penetration takes place. Therefore, smooth surfaces are more prone to increased resistance due to contaminant films than rough surfaces [79].

d. Effect of Interface Material

Another method to control the TCR is to use interfacial materials. The interfacial material can be in form of grease or metallic foil. If the interface material is not too thick, it may not be enough to increase the real contacting areas or if the interface material is too thick in comparison to surface roughness this would provide additional resistance. If the interface material is hard or harder than parent material with low thermal conductivity this would always increase contact resistance. If the interface material is soft with a high thermal conductivity, this would decrease the contact resistance.

Brunot et al [80] investigated the effect of aluminium shims on TCR across joint made of steel. They noted the reduction in TCR given that the interface material was softer than the specimen material. Other researchers such as Brazelay et al [75] used both aluminium and brass shims at the interface and same conclusions was drawn.

The most significant finding was the recognition of the thickness of the interface material, which is a function of both contact pressure and properties of the interfacial material. Some of the most recent research carried out by Antonetti et al [81] showed that the presence of interfacial material has a significant influence in TCR. It was also found that the agreement between the measured and analytical values of joint conductance (the reciprocal of joint resistance) for the interface layer thicknesses of: 0.81 μm, 1.2 μm, 1.4 μm, and 5.1 μm are very good, as shown in Figure 2-14.

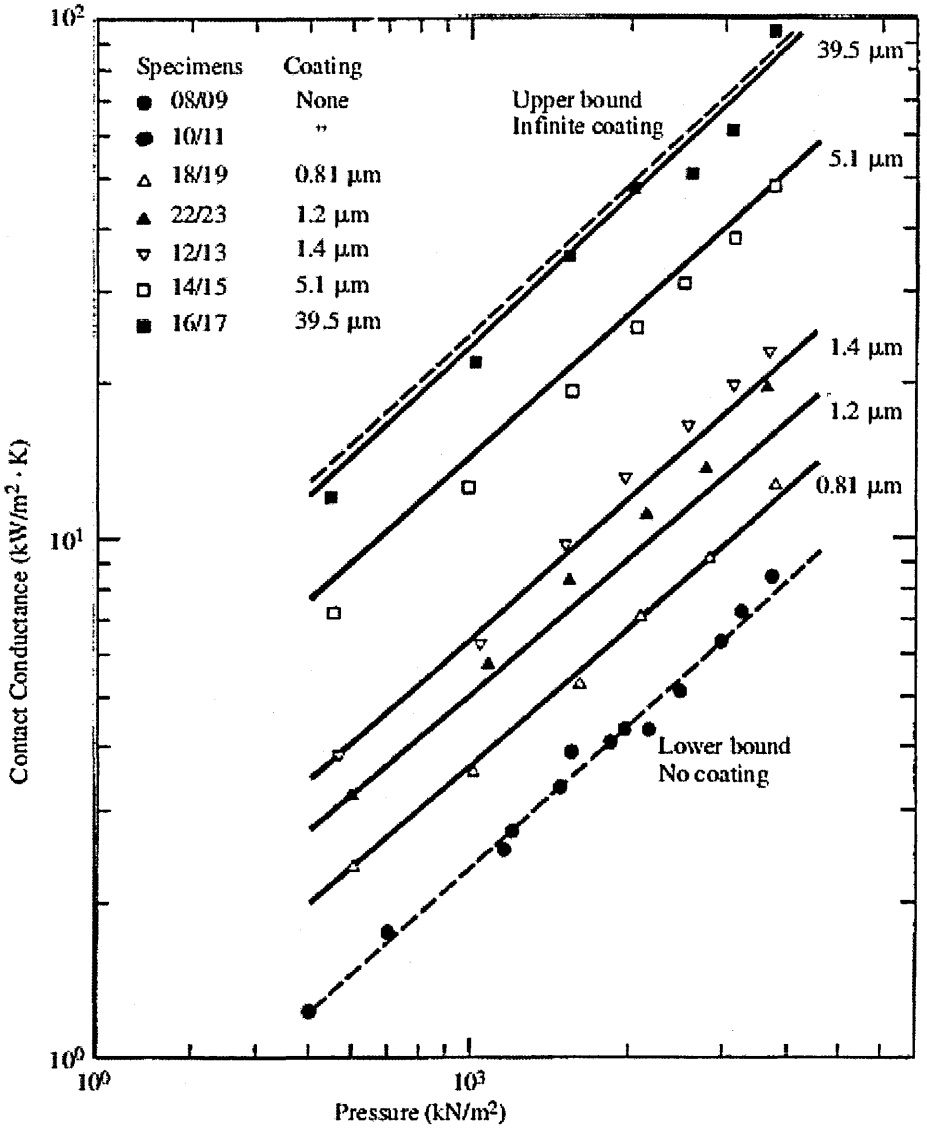

Figure 2-14. Effect of layer thickness and contact pressure on joint conductance in vacuum [81]

e. Effect of Load and Load History on TCR

It has been investigated and found that the effect of loading history and the number of load cycles and overloading pressure has an effect on the TCR [82]. Moreover, the value of TCR in the unloading process is less than in loading process for the same load.

The value of TCR can be decreased by as much as 51% by overloading the joint beyond the normal operating contact pressure. The effect of overloading on TCR might be due to the change of shape of asperities during the unloading process [82]. For the same contact pressure the TCR at the stage of decreasing pressure is found to be lower than

during the stage of increasing pressure [83]. The variation of TCR with applied load can be described by:

$$TCR = \frac{K}{P^m} \qquad \text{Eq. 5}$$

Where P is the contact pressure, K is a constant and m is power index which depend upon the load, surface topography, material properties, loading and temperature histories. The power index m has been shown to vary from zero to greater than unity. The value of m is determined by the range of applied loading and is higher during loading (approx. 1.0), when the deformation is mostly plastic than during unloading (approx. 0.3 to 0.5) when the recovery is mainly elastic [83].

In practical engineering applications, contact pressure may exceed its operating condition. If surfaces in contact are flat and smooth, the influence of the low pressure is less obvious. This is due mainly to the dominant effect of contaminant films but also because less surface deformation occurs. Contact surfaces that are smooth and wavy tend to deform elastically. Flat but rough contact surfaces tend to deform plastically. Whereas, surfaces that are wavy and rough undergo elasto-plastic deformation [70]. The joint conductance data for highly rough stainless steel 304 surfaces are shown in Figure 2-15.

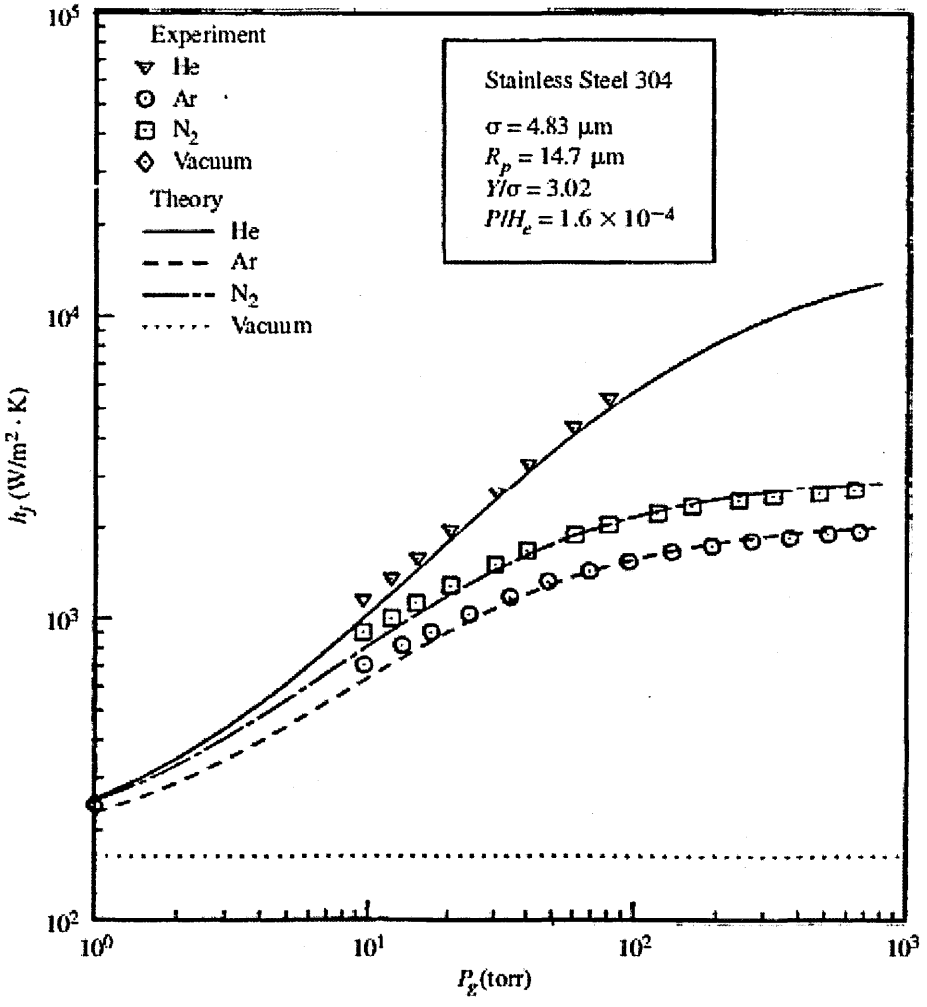

Figure 2-15. Joint conductance data for conforming rough contact made of stainless steel 304 [84]

f. Effect of Surface Flatness and Waviness

Machined surfaces are characterised by the roughness, waviness and flatness. The surface topography depends on the machining process, the speed of machining, the depth of cut and the material [85]. Modern machine tools are capable of producing sub-microns surface finish. The costs of producing high quality surface finish are higher than poorer quality finish. If the contribution to improve the heat transfer across machine joints is not required, then high quality machining can not be justified.

A number of studies have been carried out to investigate the heat transfer across a non-conforming contact. When the waviness and flatness deviations are high in comparison to average roughness, the contact is thought to be non-conforming, see Figure 2-16.

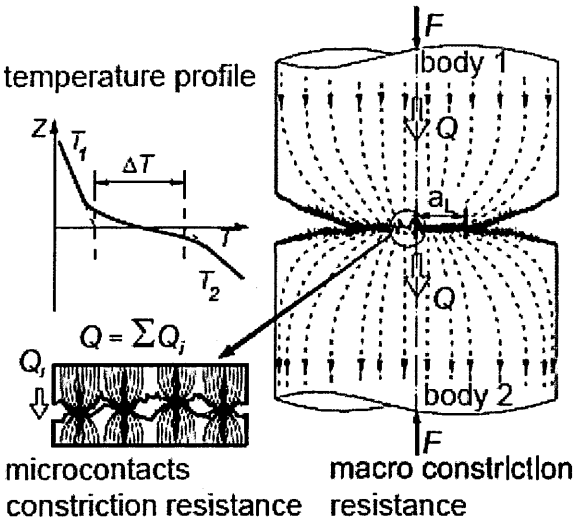

Figure 2-16. Non-conforming rough contact [64]

Kumar et al [85] observed that surface waviness had a stronger influence than the surface flatness deviation. It was found experimentally that "flatness deviation less than ten times the average roughness and waviness less than about four times the average roughness, do not significantly affect the contact conductance". The influence of material properties and contact pressure on heat transfer across a joint interface was also incorporated in the model. The correlation between mathematical models and experimental results was found to be within 17%. The discrepancy between mathematical prediction and experimental measurements it's thought to be due to the assumption of perfect peak to peak contact between asperities in the model, see Figure 2-17 and Figure 2-18 [85].

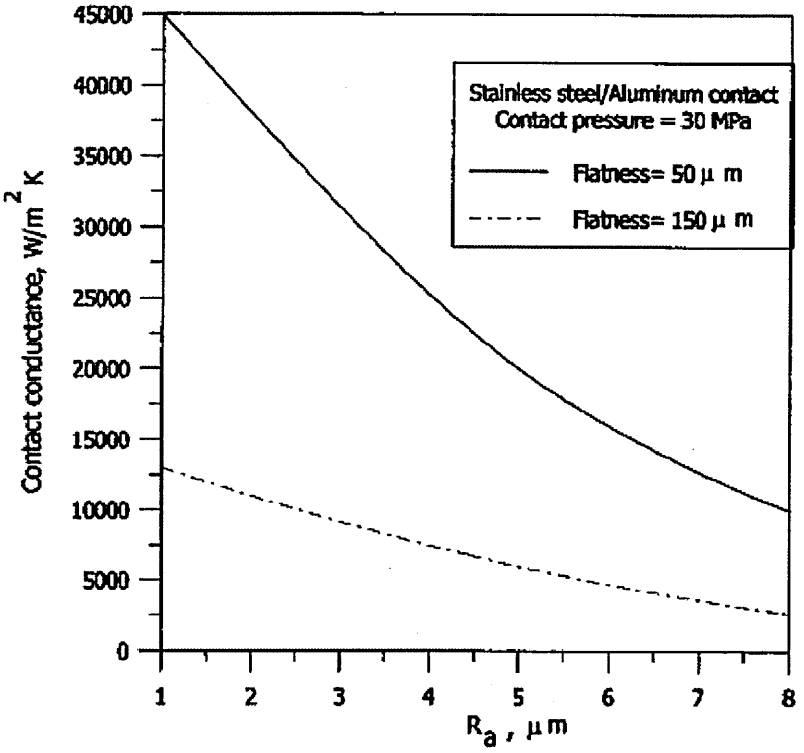

Figure 2-17. Contact conductance versus mean roughness having different flatness deviations [85]

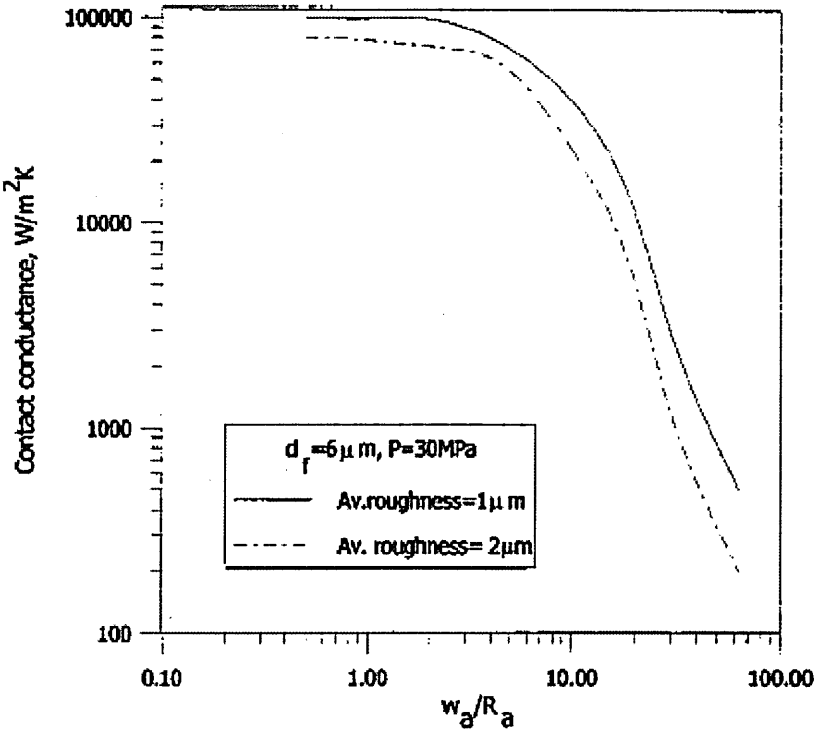

Figure 2-18. Influence of waviness in thermal contact conductance [85]

g. Effect of Heat Losses to the Surroundings

It has been reported that a major source of uncertainty in heat transfer across an interface is the heat loss to the surroundings by convection, conduction and radiation surrounding the test piece [86].

The uncertainties mainly occur when contact pressures are low (0.05 MPa to 1 MPa), when materials are poor conductors and when the contact flatness deviation is high.

2.7 Application in Machine Tools

Machine tools are generally built by combination of fixed structural members, moving slides and rotating joints. The components comprise a closed chain between the tool contact point and the workpiece. The thermal state of the machine tool joints influences the geometrical errors of the individual parts of the machine [2].

The importance of thermal contact resistance at the joints in machine tool applications is considerable [87]. The transfer of heat across structural members is an important factor in the performance of the machine tools. In certain applications maximising the heat transfer across the joints would be beneficial. In other applications the effort is to minimise the heat flow across the joints. For example if a high TCR across machine joint can be achieved the heat flow across individual members and consequently across the joint will be reduced. The end result is increased machine performance [88].

2.8 Thermal Contact Resistance at Bolted Joints

Bolted joints are frequently found in machine tools. Bolted joints are complex because of their geometric configurations, the material they made of and the number of bolts used. The pressure distributions near and around the location of the bolts are not uniform and the region influenced by the bolts is difficult to predict.

An approximate analytical solution for predicting the thermal contact resistance of bolted joints was developed by Lee et al [89]. The model was developed based on a contact formed by two square plates of the same material but different thicknesses. They assumed perfectly flat and smooth contacting surfaces and insulated surface areas of the plates. The comparison between analytical and numerical data showed good agreement.

2.9 Modelling TCR

A number of experimental investigations have been carried out in the last five decades in order to develop mathematical models to predict heat transfer across interfaces formed by metal bodies in contact [57,59,60,69,81,84,90,91].

One of the first mathematical models was developed in 1960's. Cooper et al [57] developed the pioneering TCR model (CMY model) with a surface contact of elastic deformation. This pioneering work laid the foundation for many later research studies.

Most of FEA modelling ignores the TCR at the joints. This causes inaccuracies in the thermal modelling. Min et al [24] carried out an experimental and numerical thermal analysis of a machine tool spindle, taking into account the thermal resistance at the joint and found that the model is much more accurate than the traditional model which ignores the joint interfaces, see Figure 2-19.

They found that the maximum temperature, taking into account contact resistance, occurs at the inner ring of bearing 2, around 31°C. The maximum temperature at the same location, without taking into account contact resistance was found to be around 33°C.

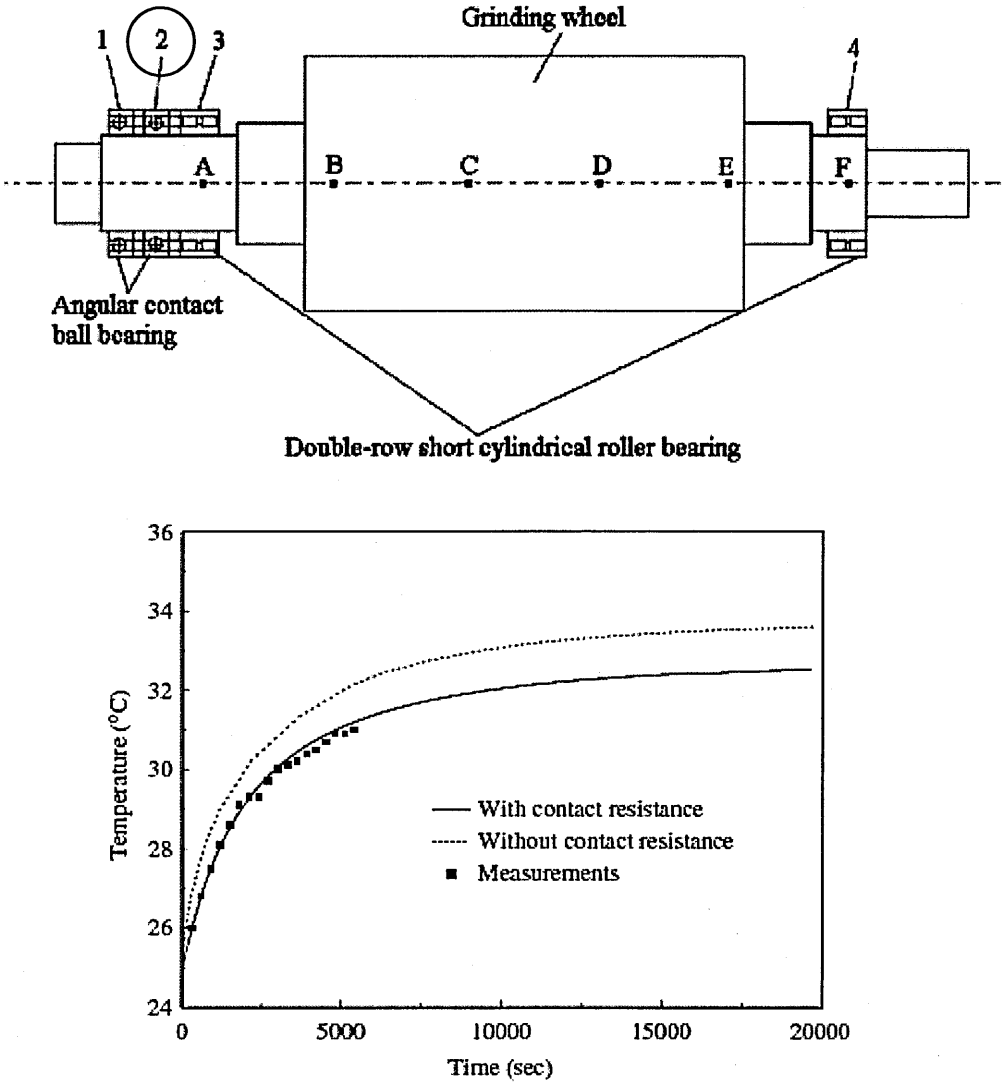

Figure 2-19. Comparison of temperature histories among the three results of location 2 [24]

It has been shown that it's not easy to predict theoretically the thermal behaviour of the machine tool, specifically the thermal behaviour of machine joint [32]. The error characteristics of the joints are considered linear with axis position. This linear feature is preserved as the machine heats up. However, the linear functions shift with time in an exponentially decaying fashion [1].

A joint in a machine tool represents the contact between members with their contacting surfaces having a certain surface roughness, surface waviness and surface flatness. The surface texture varies from surface to surface and it depends on the machining process used, as explained in previous section. Contact between surfaces is thus discontinuous and the real area of contact A_r is a small fraction of the nominal contact area A_n, usually

less then 5% [58,67]. The convergence of the heat flow lines towards these contact spots results in the thermal constriction resistance [2], see Figure 2-20.

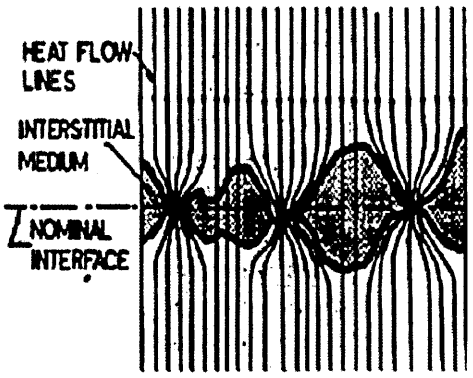

Figure 2-20. Heat transfer across a joint interface [88]

According to Ramesh et al [2] the mechanism of heat transfer across the machine joints shows that conduction is the only significant mode of heat transfer. The first recognition of the conditions of heat transfer across machine joint was reported by Attia et al [87,92]. It was shown that "thermal deformation of structural elements in contact is affected significantly by the non-uniformity of the distribution of the thermal contact resistance".

Attia et al, analysed the behaviour of the machine tool structure under various thermal conditions [54,87,88,92-95]. The theory presented is based on the recognition that the distribution of contact pressure along the joint controls the transfer of heat transfer from one structural member to another [87,88,93].

Analysis of a computer simulated case study of the nonlinear thermo-elastic behaviour of the joint between the column and the knee in a milling machine is presented by Attia et al [92]. The significance of this behaviour on the thermal deformation of contacting structural elements is investigated. The results indicate the significance of heat transfer across the joint in predicting the overall thermal deformation of a machine tool.

Following the theory of nonlinear thermo-elastic behaviour of structural joints [54], the conditions of heat transfer between contacting elements are analysed [93]. It is revealed that due to the interactions at the joint, the structure behaves thermally as a second order system.

The factors such as: surface topography, contact pressure, interface material etc, and their significance on heat transfer across joint interface were discussed in the previous sections. The following sections aim to explain the theory in detail.

2.10 Surface Topography

The topography of the contacting surfaces is one of the most significant factors that influence the TCR. The surface of every engineering component has some form of texture. The true or total profile surfaces exhibit both roughness, waviness and in some cases form error, as shown in Figure 2-21 [96].

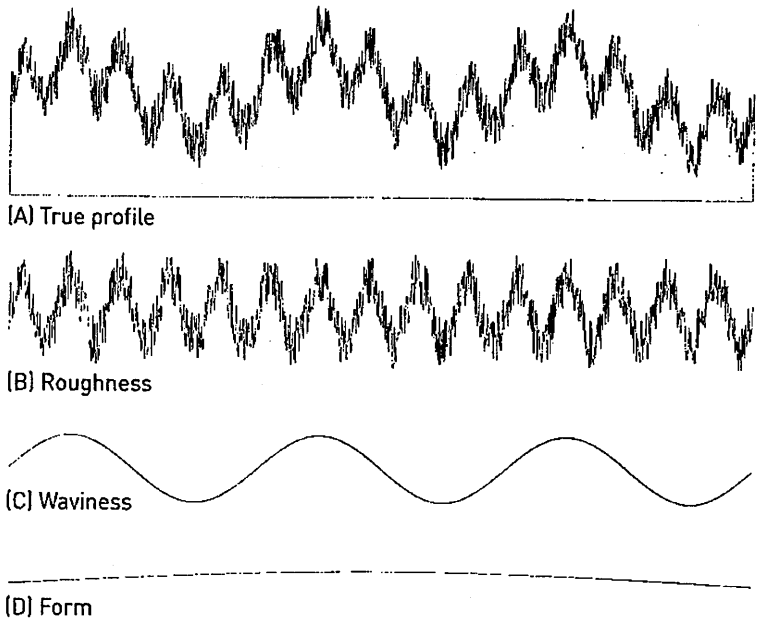

Figure 2-21. The profile of a machined surface showing the surface roughness, waviness and surface form [97]

In order to predict heat transfer across metal bodies in contact using analytical or FEA methods, the factors influencing heat flow across the joint must be known. These factors are explained in the following sections.

a. Surface Roughness

Surface roughness is the standard deviation of distribution of surface asperity peaks about a regular carrier profile in the surface. If the surfaces are flat then the carrier profile is linear. For a wavy and rough surface as in this research the periodic component would influence the roughness value that depends on where the test was made, and the sampling length chosen [96].

Average Surface Roughness (Ra)

The average roughness is "the integral of the absolute value of the roughness profile height over the evaluation length L", and is defined as follows [96]:

$$R_a = \frac{1}{L}\int_0^L |Z(x)|dx \qquad \text{Eq. 6}$$

The average roughness is the most commonly used parameter in surface finish measurement. Graphically, "the average roughness is the area between the roughness profile and its centre line divided by the evaluation length". The evaluation length is normally five sample lengths l, with each sample length equal to one cut-off, see Figure 2-22.

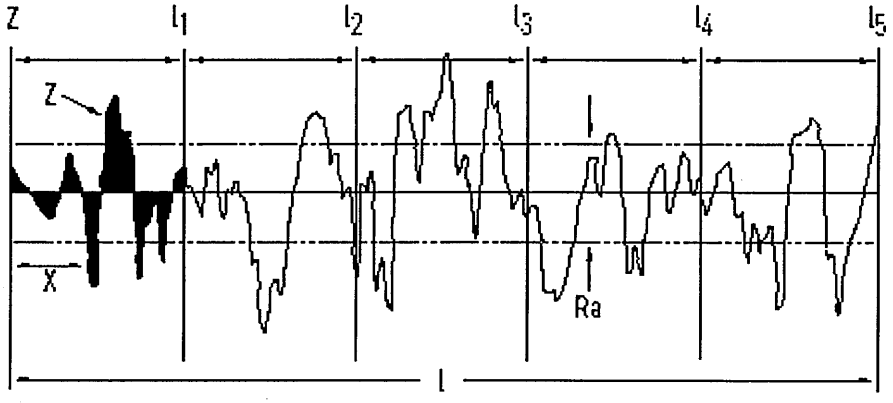

Figure 2-22. Graphical representation of average surface roughness Ra [97].

Maximum Peak to Valley Height of the Profile (Rt)

The peak roughness R_p is the height of the highest peak in the roughness profile over the evaluation length. Similarly, R_v is the depth of the deepest valley in the roughness profile over the evaluation length. The maximum peak to valley height of the profile, R_t, is the sum of the highest peak R_p and the deepest valley R_v as shown in Figure 2-23.

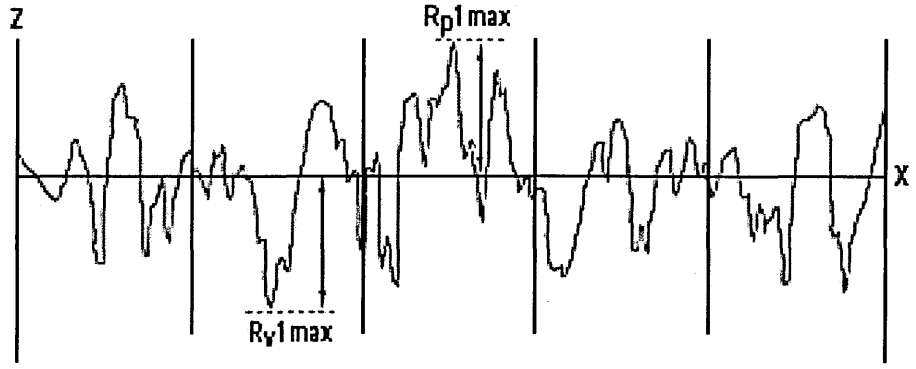

Figure 2-23. Maximum peak to valley height R_t is the sum of R_p and R_v [97]

b. Surface Waviness (W)

The surface texture deviation has a major influence in applications such as heat transfer across joints. Statistical parameters of the waviness can be evaluated just as they are for the roughness. Waviness is calculated from the total profile and represents the longer spatial wavelength features of the surface [96], see Figure 2-24.

Average Waviness (Wa)

This is the arithmetic absolute average waviness, analogous to average surface roughness R_a. The average waviness is given by the following integral [96]:

$$W_a = \frac{1}{L}\int_0^L |Z(x)|dx \qquad \text{Eq. 7}$$

Total Waviness Height (Wt)

Like maximum peak to valley height of the profile Rt, Wt is the height from the lowest valley to the highest peak of the waviness profile.

$$W_t = W_p + W_v \qquad \text{Eq. 8}$$

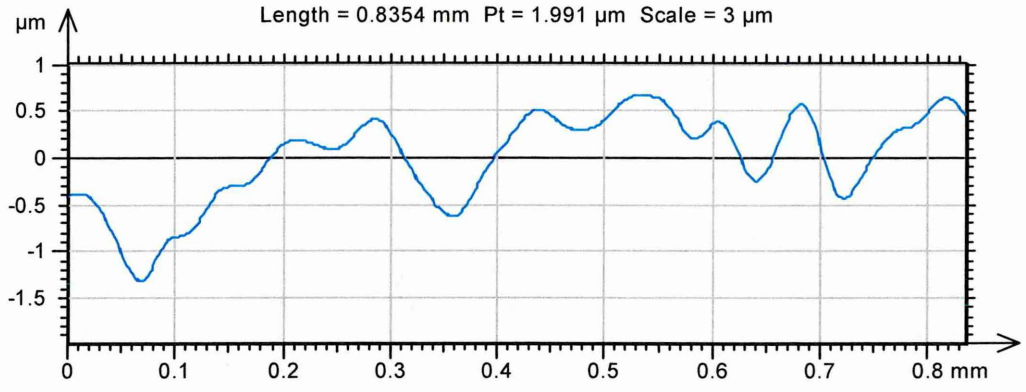

Figure 2-24. Graphical representation of surface waviness [97]

c. Mean Absolute Slope (m)

The mean absolute slopes, m_1 and m_2, of surface asperities may be determined by sampling and averaging slopes at consecutive positions in the roughness profile see Figure 2-26. The asperity slopes can be calculated using the following formula:

$$m_{1,2} = \tan\theta_{1,2} \qquad \text{Eq. 9}$$

The absolute mean asperity slope m, and the asperity slopes of a surface across the sampling length can be determined using the following:

$$m = \frac{1}{L}\int_0^L \left|\frac{dZ(x)}{dx}\right| dx, \quad m' = \sqrt{\frac{1}{L}\int_0^L \left(\frac{dZ(x)}{dx}\right)^2 dx} \qquad \text{Eq. 10}$$

It has been shown by Cooper et al [57] that for Gaussian surfaces the relationship between the mean and the RMS values of the asperity slopes takes the form:

$$m' \approx 1.25m \qquad \text{Eq. 11}$$

Empirical correlations relating mean roughness to RMS asperity slope were suggested by Lambert and Fletcher [98] and Antonetti et al [91], see Figure 2-25.

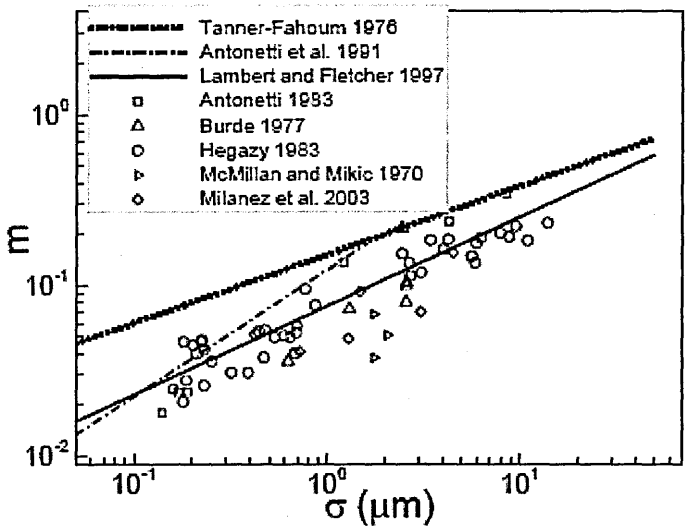

Figure 2-25. Relationship between m and σ showing the correlation of experimental data and theory [65]

It has been found that the contact asperities of the softer of the two surfaces in contact deform plastically. Under contact pressure the mean planes through each surface are separated by a distance known as the mean plane separation, Y. "If two solids with surface roughness σ_1 and σ_2, and with mean surface slopes m_1 and m_2 respectively, are brought into contact as shown in Figure 2-26(a), the actual micro-contact configuration is equivalent to the contact between a perfectly flat smooth surface and a surface with roughness and slope" as shown in Figure 2-26(b) and are defined a [90].

$$\sigma = \sqrt{(\sigma^2{}_1 + \sigma^2{}_2)} \quad \text{and} \quad m = \sqrt{(m^2{}_1 + m^2{}_2)} \qquad \text{Eq. 12}$$

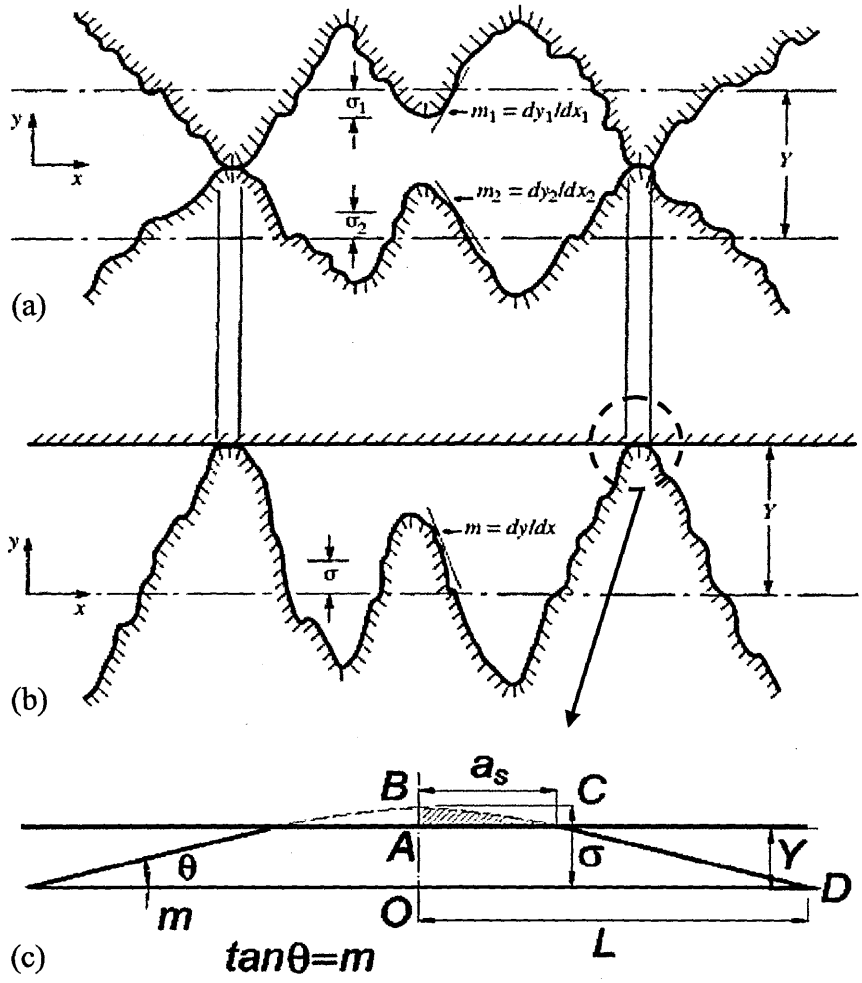

Figure 2-26. Typical joint between conforming rough surfaces; (a) contact between two rough surfaces, (b) contact between rough and flat surface, (c) schematic geometry of micro-contact [90]

Both contact configurations (a) and (b) shown in Figure 2-26, have same mean plane separation value Y. When Y tends to infinity, no contact bridges are formed and when Y becomes zero the mean planes coincide and half of the nominal plane area is in contact. Full contact would only be achieved when Y=-∞. Alternatively for contacts formed between solids with surfaces having Gaussian height distributions when Y=3σ then 0.27% of potential contact would be made, when Y=0 then 50% contact would be made and when Y=-3σ then 99.73% contact would be made [90]. Knowledge of both the mean slope of the surface asperities and the roughness gives an indication of the relative number of micro-contact areas expected.

d. Mean Radius of Curvature

The mean radius of curvature of the asperity peaks, $\bar{\sigma}$, is obtained by sampling the curvature of each peak detected in the roughness profile. The value of radius of curvature indicates the deformation behaviour under normal loading. The longer the radius of curvature the more elastic deformation will occur during the contact [70].

2.11 Modes of Heat Transfer

2.11.1 Conduction

When temperature gradient exists in a body, there is an energy transfer from the high temperature region to the low temperature region. In such a case the energy is transferred by conduction [99]. Joseph Fourier published his book Théorie Analytique de la Chaleur in 1822. According to Fourier's law of conduction the one-dimensional energy transfer can be expressed by the following expression, see Figure 2-27:

$$q = -kA\frac{\partial T}{\partial x} \qquad \text{Eq. 13}$$

Where q is the heat transfer rate, k is the thermal conductivity of the material, A is the area and $\partial T/\partial x$ is the temperature gradient in the direction of heat flow.

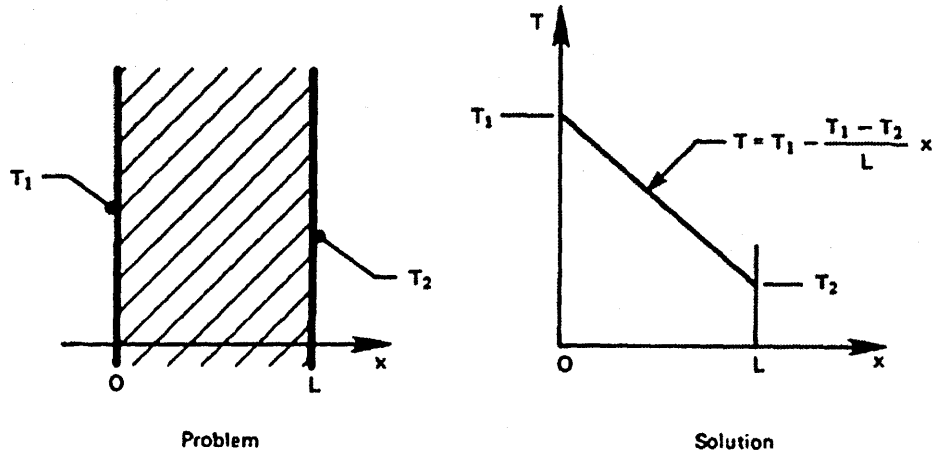

Figure 2-27. One-dimensional heat conduction [100]

For a general case where the temperature is changing with time and heat sources may be present within a body, the following applies:

Energy conducted in left face + Heat generated within element =

Change in internal energy + Energy conducted out right face

For the statement above, one-dimensional heat conduction equation can be obtained by combining the energy equations:

$$-kA\frac{\partial T}{\partial x}+\dot{q}Adx=\rho C_pA\frac{\partial T}{\partial \tau}dx-A[k\frac{\partial T}{\partial x}+\frac{\partial}{\partial x}(k\frac{\partial T}{\partial x})dx] \quad \text{Eq. 14}$$

Where $\dot{q}$ is the energy generated per unit volume, C_p is the specific heat capacity of material, ρ is the material density. For a three dimensional heat flow problems we need to consider only heat conducted in and out of a unit volume in all three coordinate directions. So the general three-dimensional heat conduction equation is:

$$\frac{\partial}{\partial x}(k\frac{\partial T}{\partial x})+\frac{\partial}{\partial y}(k\frac{\partial T}{\partial y})+\frac{\partial}{\partial z}(k\frac{\partial T}{\partial z})+\dot{q}=\rho C_p\frac{\partial T}{\partial \tau} \quad \text{Eq. 15}$$

If thermal conductivity is constant Eq.15 can be written as:

$$\frac{\partial^2 T}{\partial x^2}+\frac{\partial^2 T}{\partial y^2}+\frac{\partial^2 T}{\partial z^2}+\frac{\dot{q}}{k}=\frac{1}{\alpha}\frac{\partial T}{\partial \tau} \quad \text{Eq. 16}$$

For cylindrical coordinate system Eq.15 becomes:

$$\frac{1}{r}\frac{\partial}{\partial r}(kr\frac{\partial T}{\partial r})+\frac{1}{r^2}\frac{\partial}{\partial \phi}(k\frac{\partial T}{\partial \phi})+\frac{\partial}{\partial z}(k\frac{\partial T}{\partial z})+\dot{q}=\rho c\frac{\partial T}{\partial \tau} \quad \text{Eq. 17}$$

For spherical coordinate system Eq.15 becomes:

$$\frac{1}{r^2}\frac{\partial}{\partial r}(kr^2\frac{\partial T}{\partial r})+\frac{1}{r^2\sin^2\theta}\frac{\partial}{\partial \phi}(k\frac{\partial T}{\partial \phi})+\frac{1}{r^2\sin\theta}\frac{\partial}{\partial \theta}(k\sin\theta\frac{\partial T}{\partial \theta})+\dot{q}=\rho C_p\frac{\partial T}{\partial \tau} \quad \text{Eq. 18}$$

An important quantity of material is called thermal diffusivity, defined as:

$$\alpha=\frac{k}{\rho C_p} \quad \text{Eq. 19}$$

Where k is thermal conductivity of material, ρ is material density and C_p is specific heat capacity. Thermal diffusivity is as important to transient conduction as thermal conductivity is to steady-state conduction. The larger the value of α the faster heat will diffuse through the material [99].

The specific heat of the material is defined as the amount of energy required to raise a unit mass of material by one unit of temperature at constant pressure:

$$c = \frac{Q}{m \times \Delta T} \qquad \text{Eq. 20}$$

Where Q is thermal energy, m is the mass and ΔT is change in temperature. Each of the general three-dimensional heat conduction equations Eq.15, Eq.17 and Eq.18 are second order in the spatial coordinates and first order in time. In order to obtain the solution of the above equations, a total of six boundary conditions and one initial condition are required.

2.11.2 Convection

Steady-State Convection

When a hot body is exposed to a cooler environment, heat is transferred from the body to the surrounding ambient by convection. According to Newton's law of cooling, heat transfer by convection is [99]:

$$q' = \frac{Q}{A} = h_a(T_{body} - T_\infty) \qquad \text{Eq. 21}$$

Where h_a is the average convection coefficient or heat transfer coefficient, T_{body} is the body surface temperature, T_∞ is the fluid temperature. Heat convection is complicated and depends on temperature difference, surface roughness and surface geometry. In situations when fluid is forced past the hot body (forced convection) and ΔT is not too large, then h is independent of ΔT.

Transient Convection

If the heat input at a surface is suddenly changed from e.g., 20°C to 70°C, the steady-state natural convection flow is eventually obtained following a transient process. At the instant the heat is applied the surface starts heating up. In response to this sudden change in temperature the fluid immediately adjacent to the surface gets hotter than the surrounding fluid and due to temperature change the fluid rises. Employing the Laplace's transformation for a step change in the heat flux the solution for transient convection coefficient is given as [71]:

$$\frac{T-T_a}{T_w-T_a}=\theta=\frac{2q\sqrt{\alpha t}}{k}=\left[\frac{\exp(-\eta^2)}{\sqrt{\pi}}-\eta\times erfc(\eta)\right] \qquad \text{Eq. 22}$$

Where T is local temperature, T_a is ambient temperature, T_w is surface temperature and θ is dimensionless because is the ratio of temperatures. The dimensionless similarity variable η is defined as:

$$\eta=\frac{y}{\sqrt{\alpha t}}=\frac{y}{x}\left(\frac{Gr_x}{5}\right)^{1/5} \qquad \text{Eq. 23}$$

Where y is the upwards vertical direction, see Figure 2-28. Grashof number Gr approximates the ratio of the buoyancy force to the viscous force acting on the fluid, and is defined as:

$$Gr_x=\frac{g\beta x^3(T_w-T_\infty)}{\nu^2} \qquad \text{Eq. 24}$$

Where g is the acceleration due to gravity, β is the coefficient of thermal expansion and ν is the kinematic viscosity.

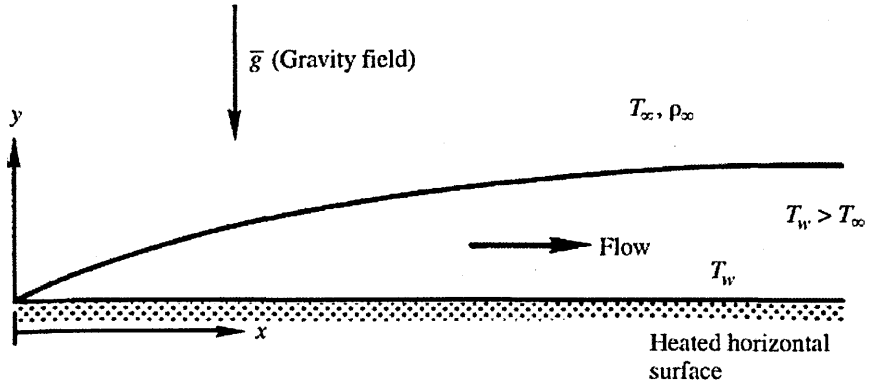

Figure 2-28. Natural convection boundary layer over a semi-infinite horizontal surface [71]

An important method used in solving convective heat transfer problems is lumped capacity method. This method was used in predicting the transient cooling of blocks used in this research, see appendix A for details.

An important parameter is the time constant defined as the time required for a physical quantity to change its initial magnitude at time zero, by the factor (1-1/e) when the

physical quantity is varying as a function of time f (t). This function can either be in a form of decreasing or increasing exponentials Eq.25 and Eq.26 respectively [7]:

$$f(t) = e^{-(\tau)t} \quad \text{Eq. 25}$$

$$f(t) = 1 - e^{-(\tau)t} \quad \text{Eq. 26}$$

Where τ = 1/t is the time constant of the physical quantity. The factor (1-1/e) = 0.63212..., since the value of e = 2.71828..., hence the time constant measures the time required for the body to achieve approximately 63.2% of its total change [7]. The temperature drop of a body from an initial temperature to a final temperature can be related to the following exponential function:

$$T = T_a + (T_i - T_a)e^{-\left(\frac{\bar{h}A}{mc}\right)t} \quad \text{Eq. 27}$$

$$k = \tau = \frac{\rho V c}{\bar{h}A} \quad \text{Eq. 28}$$

Where t is the time, ρ density of the material, V is the volume, C_p is specific heat capacity, T_i is initial body temperature, T_a is the ambient temperature.

2.11.3 Radiation

All bodies emit energy by electromagnetic radiation. The intensity of radiation depends upon the temperature of the body and the nature of its surface. Radiation heat transfer is only significant at high temperatures >600°C. Heat loss by radiation is [99]:

$$Q = \varepsilon \sigma A_o (T^4 - T_a{}^4) \quad \text{Eq. 29}$$

Where ε is the emissivity which is a measure of the material ability to absorb or radiate heat, σ is Stefan-Boltzmann constant (approx. 5.67×10^{-8} W/m^{2}K^4).

2.12 Composite Systems with Resistance

In a situation when two lumped thermal capacity bodies are in contact, with different boundary conditions on outer surfaces as shown in Figure 2-29.

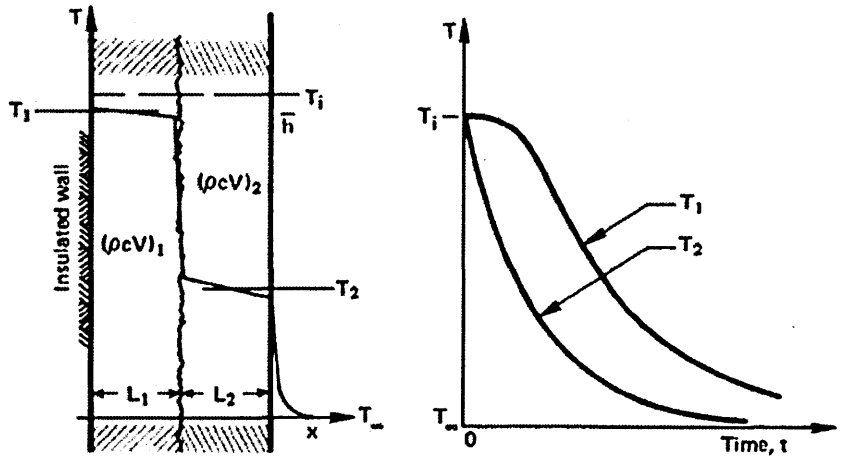

Figure 2-29. Two bodies in contact with interface contact resistance [100]

The differential equations representing the above situation are:

$$left\_body: -(\rho CV)_1 \frac{dT_1}{dt} = h_c A(T_1 - T_2) \qquad \text{Eq. 30}$$

$$right\_body: -(\rho CV)_2 \frac{dT_2}{dt} = \bar{h} A(T_2 - T_\infty) - h_c A(T_1 - T_2) \qquad \text{Eq. 31}$$

The initial conditions on the temperature T_1 and T_2 are:

$$T_1(t=0) = T_2(t=0) = T_i \qquad \text{Eq. 32}$$

The two time constants following Eq. 30 and Eq. 31 are:

$$T_1 \equiv \frac{(\rho CV)_1}{h_c A} \qquad \text{Eq. 33}$$

$$T_2 \equiv \frac{(\rho CV)_2}{\bar{h} A} \qquad \text{Eq. 34}$$

Then Eq. 30 takes the form:

$$T_2 = T_1 \frac{dT_1}{dt} + T_1 \qquad \text{Eq. 35}$$

After substituting Eq. 30 into Eq. 31 yields the following expression:

$$\frac{d^2 T_1}{dt^2} + \left(\frac{1}{T_1} + \frac{1}{T_2} + \frac{h_c}{\bar{h} T_2} \right) \frac{dT_1}{dt} + \frac{T_1 - T_\infty}{T_1 T_2} = 0 \qquad \text{Eq. 36}$$

Substituting $T_1 - T_\infty \equiv \theta$ into Eq. 36 we get second order ordinary differential equation:

$$\frac{d^2\theta}{dt^2} + b\frac{d\theta}{dt} + c\theta = 0 \qquad \text{Eq. 37}$$

So by integrating Eq. 37 twice and substituting the relevant terms the particular solution is obtained:

$$\frac{T_1 - T_\infty}{T_i - T_\infty} \equiv \frac{\theta}{\theta_i} = \frac{b/2 + \sqrt{(b/2)^2 - c}}{2\sqrt{(b/2)^2 - c}} \exp\left[-\frac{b}{2} + \sqrt{\left(\frac{b}{2}\right)^2 - c}\right] t + \frac{-b/2 + \sqrt{(b/2)^2 - c}}{2\sqrt{(b/2)^2 - c}} \exp\left[-\frac{b}{2} - \sqrt{\left(\frac{b}{2}\right)^2 - c}\right] t \qquad \text{Eq. 38}$$

2.13 Heat Transfer Across Joint Interfaces

The heat transfer across the joint interface is related to thermal contact resistance and temperature drop across the interface [98]. The boundary between two metal bodies in contact acts as a resistance to the flow of heat. Due to roughness of the contacting surfaces and the surface form error real contacts in the form of micro-contacts occur only at the top of surface asperities. Most of the heat at the interface is conducted through the contact asperities [101]. If the interface is bare filled with air the heat flow across the interface is constrained to pass through contact asperities having higher thermal conductivity. The bulk gaps filled with air act as resistance to heat flow giving rise to thermal contact resistance. TCR is complex and is a function of many parameters; surface roughness, interfacial material, contact pressure, etc. as explained in the following section.

Thermal Contact Resistance

TCR is the resistance to heat flow across interface of two parts. As an example, imagine heat flowing through an insulated homogenous body then a linear temperature change occurs as shown in Figure 2-30(a). If two solids are brought into contact as indicated in Figure 2-30(b), with the sides of the bars insulated so that heat flows only in the axial direction. The actual temperature profile through the two solids in contact varies approximately as shown in Figure 2-30. The temperature drop at interface is said to be the result of the TCR [99].

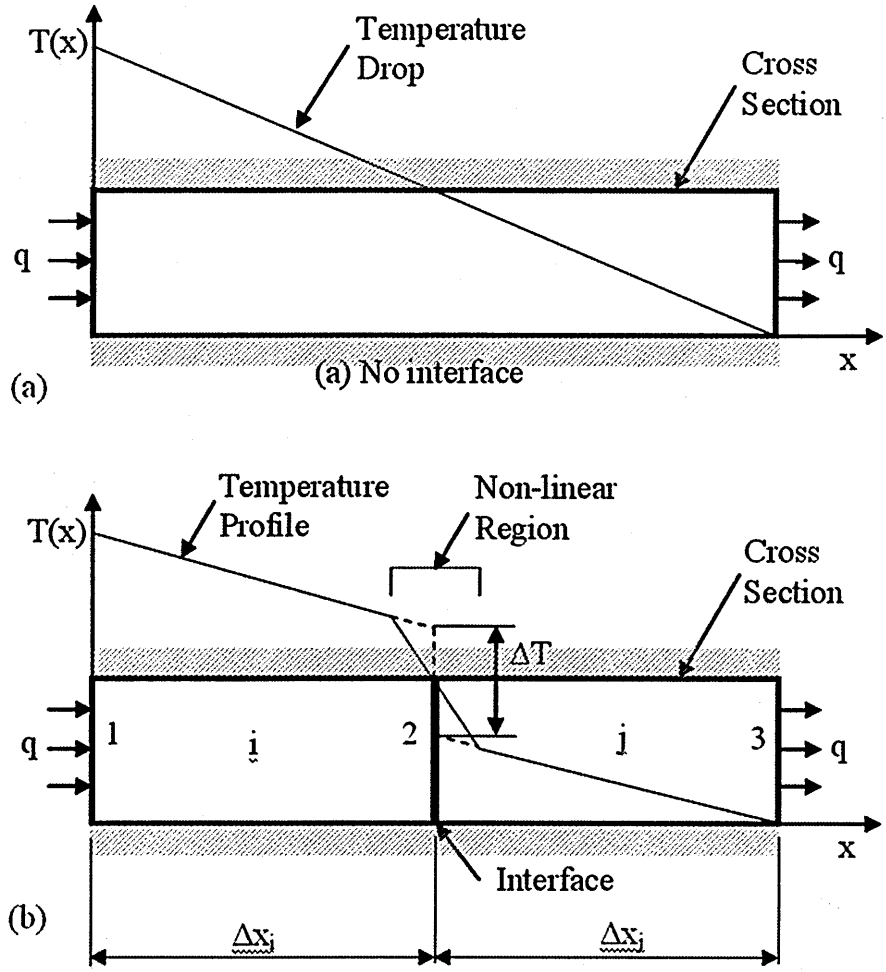

Figure 2-30. Graphical representation of heat flow and temperature gradient within (a) continuous body (b) bodies in contact [after 70]

Performing an energy balance on the two materials in Figure 2-30(b), we obtain:

$$q = k_i A \frac{T_1 - T_{2i}}{\Delta x_i} = \frac{T_{2i} - T_{2j}}{\frac{1}{h_c A}} = k_j A \frac{T_{2j} - T_3}{\Delta x_j} \qquad \text{Eq. 39}$$

Rearranging Eq.39 gives the following:

$$q = \frac{T_1 - T_3}{\frac{\Delta x_i}{k_i A} + \frac{1}{h_c A} + \frac{\Delta x_j}{k_j A}} \qquad \text{Eq. 40}$$

The quantity 1/ (h_cA) in Eq. 40 is called thermal contact resistance and h_c is called the thermal contact conductance [99].

TCR problems basically consist of three separate problems: 1) geometrical, 2) mechanical and 3) thermal, see section 2.6.1, Figure 2-11 [67].

The rate of heat transfer across the joint depends on a number of parameters: thermal properties of solids and interfacial material, surface roughness characteristics, surface waviness and flatness, applied load, contact micro-hardness etc [66]. These parameters have an influence on the thermal contact resistance and consequently on the heat transfer across the joint.

In order to understand and predict the TCR, each of the three components affecting TCR must be taken into account and studied thoroughly, as explained in the following sections. Due to the number of factors influencing TCR, such as macro and micro thermal resistances, the size the shape and the distribution of asperities on the surface, the surface form error etc. the mathematical models developed are based on the following general assumptions:

- Thermal conductivity and physical parameters of contacting materials are constant (isotropic solids).
- The thickness of contacting solids is high in comparison to the roughness and waviness.
- Contacting surfaces are free of oxides, static and no hysteretic effect.
- Radiation is negligible.
- Steady and limited heat flux at micro-contacts ($< 10^7$ W/m^2).
- Interfacial material perfectly wets contacting surfaces.

If contacting solids are rough and conforming as shown in Figure 2-31, heat transfer across the joint occurs by conduction through the micro contacts, through the interfacial material and by radiation across the micro gap.

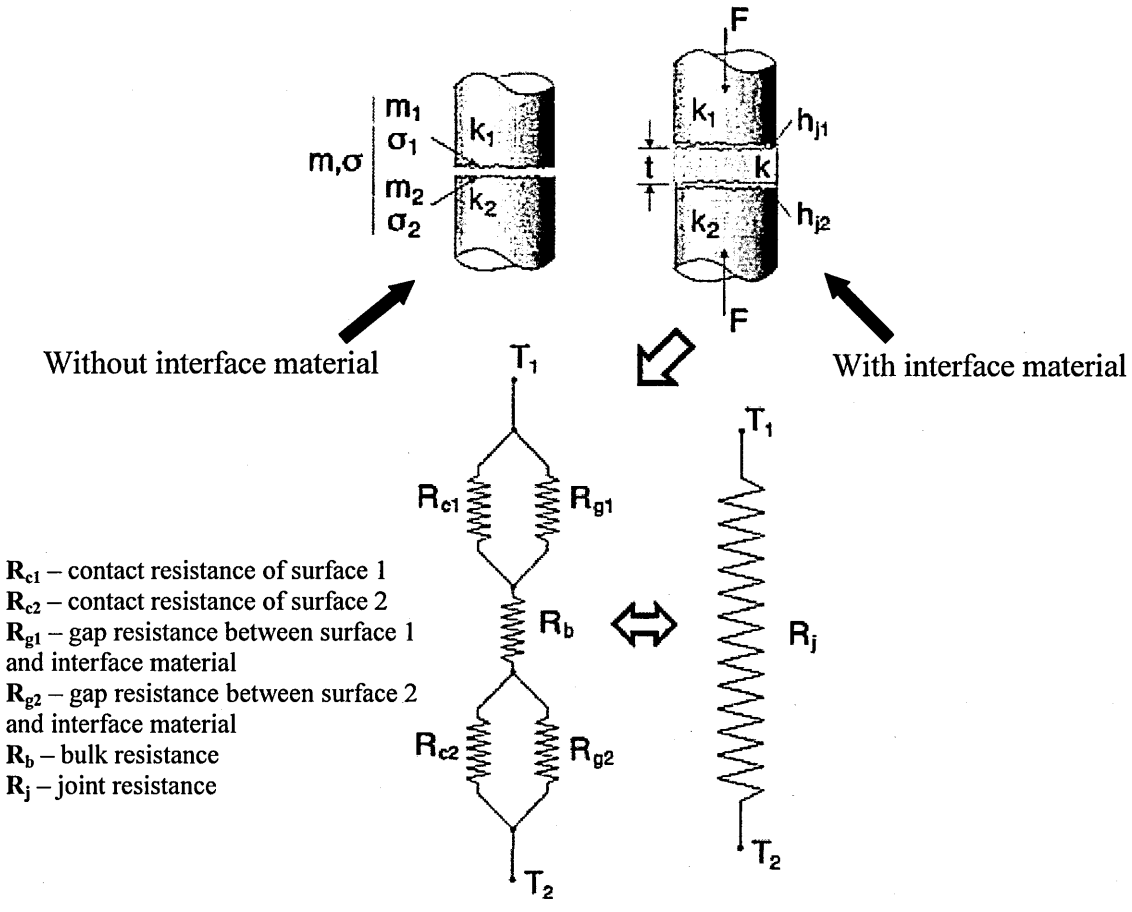

Figure 2-31. Typical contact between conforming rough solids [72]

The total steady-state heat transfer rate across joint R_j is the sum of three separate steady-state heat transfer rates [71]:

$$Q_j = Q_c + Q_g + Q_r \qquad \text{Eq. 41}$$

Where Q_j is the joint heat transfer, Q_c is the contact heat transfer, Q_g is the gap heat transfer and Q_r represents the radiative heat transfer. The joint heat transfer rate is related to the effective temperature drop across the joint ΔT, nominal contact area A_a, joint resistance R_j, and joint conductance h_j and is defined as [71]:

$$Q_j = h_j A_a \Delta T_j \qquad \text{Eq. 42}$$

Contact and gap components of heat transfer are similarly defined as:

$$Q_g = h_g A_g \Delta T_j \qquad \text{Eq. 43}$$

$$Q_r = h_r A_g \Delta T_j \qquad \text{Eq. 44}$$

Where A_g is the gap area at interface

The thermal joint conductance h_j is defined in the manner of the film coefficient in convective heat transfer. It is related to the heat transfer at the joint, temperature drop at the interface and the apparent contact area, i.e,

$$h_j = \frac{Q_j}{(\Delta T_j A_a)} = \frac{1}{R_j A_a} \qquad \text{Eq. 45}$$

Rearranging Eq. 45 gives an expression for joint resistance R_j:

$$R_j = \frac{\Delta T_j}{Q_j} = \frac{1}{h_j A_a} \qquad \text{Eq. 46}$$

For most contact problems the real area of contact is much smaller then the apparent contact area, i.e., $A_c/A_a = 0.02$. It is the convention to use the apparent contact area in the definition of the contact conductance. This is because $A_g = A_a - A_c$ and $A_c/A_a << 1$, then the effective gap area is approximately equal to the apparent area $A_g \approx A_a$ (see Figure 2-33). From the above relationships the interaction between the resistances and the conductances can be drawn as follows:

$$h_j = h_c + h_g + h_r \qquad \text{Eq. 47}$$

Joint resistance is the reciprocal of joint conductance, i.e:

$$\frac{1}{R_j} = \frac{1}{R_c} + \frac{1}{R_g} + \frac{1}{R_r} \qquad \text{Eq. 48}$$

The radiation terms in Eq. 47 and Eq. 48 can be ignored [72]. This leads to $R_r \rightarrow \infty$ and $h_r \rightarrow 0$ and Eq. 47 and Eq. 48 take the form:

$$h_j = h_c + h_g \qquad \text{Eq. 49}$$

$$\frac{1}{R_j} = \frac{1}{R_c} + \frac{1}{R_g} \qquad \text{Eq. 50}$$

If a joint formed by two conforming rough solids contains interface material as shown in Figure 2-31, and if the interface material is thicker than the surface roughness σ_1 and σ_2, i.e. $t >> \sigma = \sqrt{(\sigma_1 + \sigma_2)}$, then a more complicated thermo-mechanical joint is created. The complication arises because the materials in contact might have different thermal

and mechanical properties and also different surface finishes. If the interface material is filling the gaps in both surfaces the joint resistance generally is a function of five resistances [72]:

$$R_j = f(R_{c1}, R_{g1}, R_{c2}, R_{g2}, R_l) \qquad \text{Eq. 51}$$

Where, R_l is layer thermal resistance and is given as:

$$R_l = \frac{t}{k_l A_a} \qquad \text{Eq. 52}$$

Where t, is the interfacial layer thickness, k_l is the thermal conductivity of the interfacial material. The layer thickness will decrease with the increase in contact pressure P; otherwise the thickness will remain unchanged under the increased load if layer material is incompressible. Two factors affecting layer thickness are contact pressure P and its modulus of elasticity E. Thermal joint resistance is given by the following expression:

$$R_l = \left(\frac{1}{R_{c1}} + \frac{1}{R_{g1}}\right)^{-1} + R_l + \left(\frac{1}{R_{c2}} + \frac{1}{R_{g2}}\right)^{-1} \qquad \text{Eq. 53}$$

Area of Contact

"Contact between metallic bodies can be explained by using two independent considerations. The first approach would be to consider the local behaviour of geometric features and the second is the global or average behaviour. It is useful to consider a single asperity in contact with a perfectly flat smooth surface, at different pressure range and shapes, and then to consider the number and distribution of asperities both in position and height across the surface. Knowledge of the shape and distribution of contact asperities should allow estimating the real area of contact A_r which is a small portion of the nominal area of contact A_a "[96].

As the contact asperities undergo both elastic and plastic deformations, the pattern of contact will depend upon the magnitude and direction of contact pressure, the topography of contacting surfaces, material hardness and interface material. Figure 2-32 shows three modes of contact between solid bodies which are defined as follows:

- Apparent contact area which is the plane passing through the interface between two contacting bodies.

- The micro-contact area enclosed by contours surrounding locations where contact results from deformation of the surface variation.

- The real contact area which is the sum of all the micro-contact areas where actual touching of the solids occur.

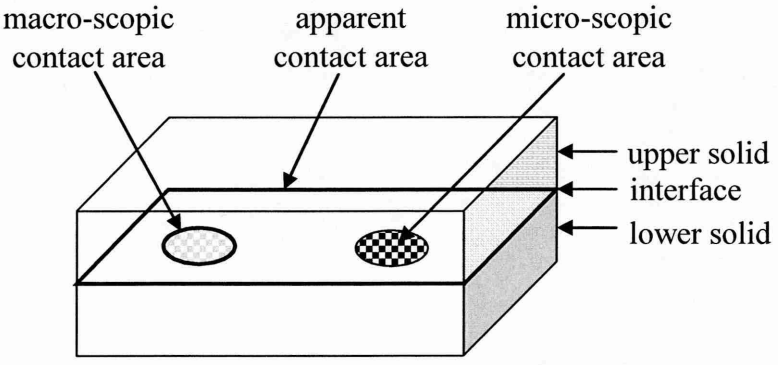

Figure 2-32. Schematic diagram of two solids in contact showing three modes of contact [70]

With increase in contact pressure, the deformation of the contacting asperities increases as a result other smaller asperities may come into contact. This leads to an increase in the real area of contact A_r and hence an increase in contact conductance [101]. The parameters affecting the area must be found by measuring the surface topography and/or calculating using analytical methods. A typical approach in calculating real area of contact is to consider one of the surfaces to be perfectly smooth flat and the other surface rough as shown in Figure 2-33 [66]. Whitehouse [96] argues that the validity of such approach is questionable and likely to produce problems in the analysis, especially if the surface slopes are above 5.7°.

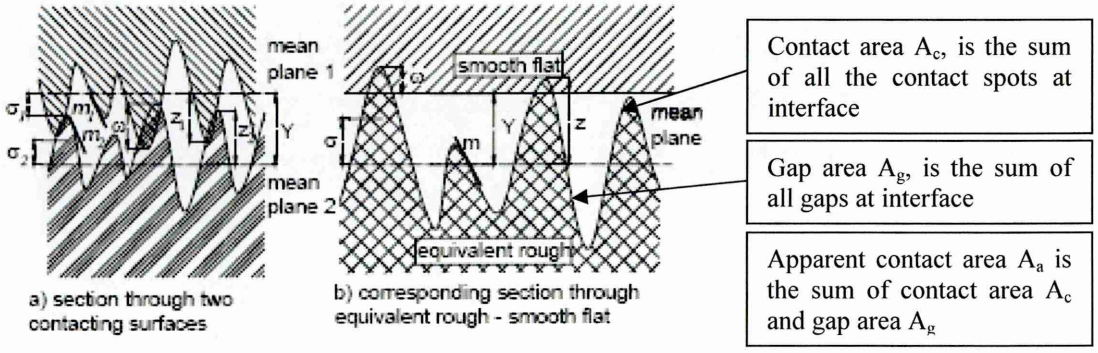

Figure 2-33. Contact between two rough and the equivalent contact between a smooth flat and a rough surface [66]

2.13.1 Conforming Contacts

When the flatness deviation is low in comparison to average roughness, the contact is thought to be conforming. Moreover if the effect of surface curvature on contact pressure distribution is negligible the surface is ideally flat [82].

If the contact is in a gaseous environment e.g., air and the contact is conforming rough, then heat transfer across interface occurs by three modes [64]. A number of mathematical models and correlations of the thermal contact resistance have been developed over the last few decades [57,61,90,102,103]. The models and correlations have been review by many authors and are available in the literature [62,86,90,98,103].

Modes of Deformation

The three modes of deformation of contacting asperities are;

- *Plastic deformation* of asperities or the softer contacting asperities,
- *Elastic deformation* of all contacting asperities and
- Combination of both *plastic-elastic* deformation of asperities [57] as cited in [71].

Each of the deformation modes will be dealt with separately in the following sections.

a. Plastic Contact Model

One of the first plastic models was developed by Cooper et al [57]. This model has been modified significantly in the last three decades. More accurate models have been created by Yovanovich et al [104] based in Cooper's et al model as explained below.

If h_i is the thermal conductance associated with a single contact asperity in vacuum, the overall thermal contact conductance of the joint is the sum of all the asperities on the contact surface, i.e. [105]

$$h_j = \sum_n h_i = 2k_s \sum_n \frac{a_i}{\psi_i} \qquad \text{Eq. 54}$$

Where a_i is the radius of the contact spot and k_s is the harmonic mean of the thermal conductivity k_1 and k_2 of the solids 1 and 2 in contact respectively, and is defined as:

$$k_s = \frac{2k_1k_2}{k_1 + k_2} \qquad \text{Eq. 55}$$

The spreading/constriction parameter Ψ_i based on isothermal contact spots is approximated by [57]:

$$\psi(\varepsilon) = (1-\varepsilon)^{1.5}, for 0 < \varepsilon < 0.3 \qquad \text{Eq. 56}$$

The relative contact spot size ε is related to the real contact area A_r and apparent contact area A_a as follows:

$$\varepsilon = \sqrt{\frac{A_r}{A_a}} \qquad \text{Eq. 57}$$

Assuming that all contact spots n, have the same mean radius a_m and neglecting the variation in Ψ_i the total conductance is:

$$h_j = \frac{2k_s n a_m}{\psi} \qquad \text{Eq. 58}$$

The mean spot radius a_m and the contact spot density n depend on the contact surface topography and its deformation under contact pressure. If the deformation of asperities is plastic the following equations can be used to calculate thermal contact conductance or resistance [57,106]:

The ratio between the real contact areas A_r to the apparent contact area A_a is given by:

$$\frac{A_r}{A_a} = \frac{1}{2} erfc\left(\frac{\lambda}{\sqrt{2}}\right) \qquad \text{Eq. 59}$$

The complementary error function 'erfc' is defined in terms of mean square of error function 'erf'. This function gives the probability that the error of a single measurement lies between –x and +x values if the measured data are described by a normal distribution with standard deviation, and is defined by [107]:

$$erfc(x) = 1 - erf(x) = \frac{2}{\sqrt{\pi}} \int_x^{\infty} e^{-t^2} dt \qquad \text{Eq. 60}$$

In order to find out whether the deformation of asperities is plastic or elastic a parameter called plasticity index φ can be used as proposed by Mikic [61]:

$$\varphi = \frac{H}{E \times m} \qquad \text{Eq. 61}$$

Where H is the hardness of the softer material, m is the mean surface slope and E is the equivalent modulus of elasticity or stiffness of contact materials, defined as:

$$\frac{1}{E}=\frac{1-\upsilon_1^{\,2}}{E_1}+\frac{1-\upsilon_2^{\,2}}{E_2} \qquad \text{Eq. 62}$$

According to Mikic if plasticity index is $\varphi<0.33$ the deformation would be fully plastic and the ratio of real to apparent contact area for smaller contact pressures is:

$$\frac{A_r}{A_a}=\frac{P}{H_p} \qquad \text{Eq. 63}$$

Where P is the contact pressure, H_p is the plastic micro-hardness of the softer material in contact. If the contact pressure is large Eq.63 takes the form:

$$\frac{A_r}{A_a}=\frac{P}{P+H_p} \qquad \text{Eq. 64}$$

The relative mean plane separation λ for plastic asperity deformation is:

$$\lambda=\sqrt{2}erfc^{-1}\left(\frac{2P}{H_p}\right) \qquad \text{Eq. 65}$$

The $erfc^{-1}(2P/H_p)$ term in Eq.65 is approximated by the following expression and it is accurate to the maximum relative error of 2% for the range $10^{-6} \le P/H_c \le 2x10^{-2}$ as shown in Table 2-2 [108]:

$$erfc^{-1}\left(\frac{2P}{H_p}\right)\approx 0.9638\left[-\ln\left(5.589\frac{P}{H_p}\right)\right]^{1/2} \qquad \text{Eq. 66}$$

P/H_p	$erfc^{-1}(2P/H_p)$	Eq.66	% difference
$1x10^{-6}$	3.362	3.352	0.3
$5x10^{-6}$	3.123	3.121	0.1
$1x10^{-5}$	3.016	3.017	0.0
$5x10^{-5}$	2.751	2.757	-0.2
$1x10^{-4}$	2.630	2.638	-0.3
$5x10^{-4}$	2.327	2.337	-0.5
$1x10^{-3}$	2.185	2.195	-0.5
$5x10^{-3}$	1.822	1.823	-0.1
$1x10^{-2}$	1.645	1.637	0.5
$2x10^{-2}$	1.452	1.427	1.8

Table 2-2. The accuracy of the inverse complementary function erfc-1(2P/Hp) approximation [108]

The micro-hardness may be defined by means of Vickers micro-hardness measurements, and its given by the following expression [109,110]:

$$H_v = c_1\left(\frac{dv}{d_0}\right)^{c_2} \qquad \text{Eq. 67}$$

Where d_0 represents some convenient reference value for the average diagonal and c_1 and c_2 are the correlation coefficients. The spot density is given by:

$$n = \frac{1}{16}\left(\frac{m}{\sigma}\right)^2 \frac{\exp(-\lambda)^2}{erfc\left(\frac{\lambda}{\sqrt{2}}\right)} \qquad \text{Eq. 68}$$

The equivalent surface roughness σ and the effective mean absolute surface slope are defined by Eq. 12:

$$\sigma = \sqrt{(\sigma^2{}_1 + \sigma^2{}_2)} \quad \text{and} \quad m = \sqrt{(m^2{}_1 + m^2{}_2)}$$

Where σ_1 and σ_2 are the root mean square roughness of surfaces 1 and 2 respectively, and m_1 and m_2 are the mean asperity slopes of surfaces 1 and 2 respectively. If asperity slopes are not known, they can be approximately calculated using the correlation proposed by Antonetti et al [91]:

$$m_{1,2} = 0.125(\sigma_{1,2} \times 10^6)^{0.402}, \text{ for } 0.216\ \mu m < \sigma_{1,2} < 9.6\ \mu m \qquad \text{Eq. 69}$$

The mean radius of the contact spot a_m is defined as follows:

$$a_m = \sqrt{\frac{8}{\pi}}\frac{\sigma}{m}\exp\left(\frac{\lambda}{2}\right)^2 erfc\left(\frac{\lambda}{\sqrt{2}}\right) \qquad \text{Eq. 70}$$

Substituting Eq.55, Eq.68 and Eq.71 into Eq.58, the expression for thermal contact conductance for plastic deformation is obtained:

$$h = \frac{k_s}{2\pi\psi}\frac{m}{\sigma}\exp\left[-\left\{erfc^{-1}\left(\frac{2A_r}{A_a}\right)\right\}^2\right] \qquad \text{Eq. 71}$$

The ratio of roughness to asperity slope σ/m, in Eq.71 its thought to being proportional to radius of contact spot a_s and it should be recognised as a parameter characterising the geometrical property of the surface, as proposed by Kimura [111], i.e.,

$$a_s \propto \frac{\sigma}{m} \qquad \text{Eq. 72}$$

Another important parameter is the dimensionless contact conductance, and for plastic deformation is defined as follows:

$$C_c \equiv \frac{h_c \sigma}{k_s m} = \frac{1}{2\sqrt{2\pi}} \frac{\exp\left(-\frac{\lambda^2}{2}\right)}{\left[1 - \sqrt{\frac{1}{2}} erfc\left(\frac{\lambda}{\sqrt{2}}\right)\right]^{1.5}} \qquad \text{Eq. 73}$$

A simplified version of Eq.73 is given by Yovanovich [106] as:

$$C_c \equiv \frac{h_c \sigma}{k_s m} = 1.25\left(\frac{P}{H_p}\right)^{0.95} \qquad \text{Eq. 74}$$

Where the ratio of P/H_p is the relative contact pressure and H_p is called the effective plastic micro-hardness of the joint. Good agreement, within ±1.5% between Eq.74 and experimental data is reported in the literature, for a range of surface roughness σ/m in the range $2 \leq \lambda \leq 4.75$ for various metals [109,110], see Figure 2-34.

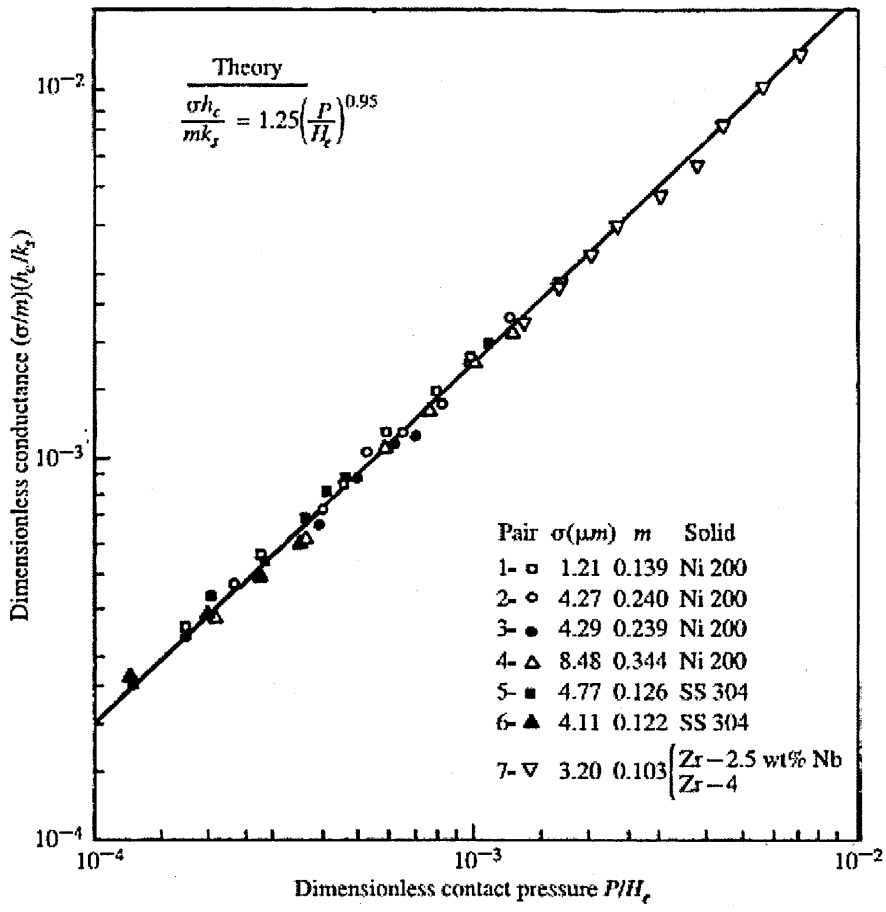

Figure 2-34. Comparison of contact conductance model and experimental data in vacuum for plastic deformation [71]

The micro-hardness depends on many parameters including: method of surface preparation, contact pressure P, mean surface roughness of contacting surfaces σ, mean absolute surface slope m, and the type of material [66]. The surface micro-hardness correlations in the form of Vickers micro-hardness was proposed by Hegazy [110]. Later on, Song et al [108] developed an explicit correlation in which the micro-hardness relates to applied contact pressure, as follows:

$$\frac{P}{H_{mic}} = \left(\frac{P}{H'}\right)^{\frac{1}{1+0.071c_2}} \qquad \text{Eq. 75}$$

b. Elastic Contact Model

The elastic deformation of asperities occurs when the change in shape is temporary; this means that deformation is reversible after the force is removed. In other words elastic deformation is a change in shape of a material at low stress. If the deformation of asperities is elastic (temporary) the following correlations can be used to calculate thermal contact conductance or resistance [57,106]. For the sake of simplicity, only equations that differ from the plastic deformation section will be given here.

$$\frac{A_r}{A_a} = \frac{1}{4} erfc\left(\frac{\lambda}{\sqrt{2}}\right) \qquad \text{Eq. 76}$$

$$a_m = \frac{2}{\sqrt{\pi}} \frac{\sigma}{m} \exp\left(\frac{\lambda}{2}\right)^2 erfc\left(\frac{\lambda}{\sqrt{2}}\right) \qquad \text{Eq. 77}$$

$$\lambda = \sqrt{2} erfc^{-1}\left(\frac{4P}{H_e}\right) \qquad \text{Eq. 78}$$

According to Mikic [61] if plasticity index is φ>3 the deformation would be fully elastic and the ratio of real to apparent contact area is:

$$\frac{A_r}{A_a} = \frac{P\sqrt{2}}{E \times m} \qquad \text{Eq. 79}$$

Substituting Eq.76, Eq.77 and Eq.78 into Eq.58 the expression for thermal contact conductance for elastic deformation is obtained:

$$h = \frac{k_s}{2\pi\psi} \frac{m}{\sigma} \exp\left[-\left\{erfc^{-1}\left(\frac{2A_r}{A_a}\right)\right\}^2\right] \qquad \text{Eq. 80}$$

The dimensionless contact conductance for elastic deformation is defined as follows:

$$C_c \equiv \frac{h_c \sigma}{k_s m} = \frac{1}{4\sqrt{\pi}} \frac{\exp\left(-\frac{\lambda^2}{2}\right)}{\left[1 - \sqrt{\frac{1}{4} erfc\left(\frac{\lambda}{\sqrt{2}}\right)}\right]^{1.5}} \qquad \text{Eq. 81}$$

A simplified version of Eq.81 is given by Yovanovich [106] as:

$$C_c \equiv \frac{h_c \sigma}{k_s m} = 1.54\left(\frac{P}{H_e}\right)^{0.94} \qquad \text{Eq. 82}$$

Eq. 82 is accurate within ±2% for the relative contact pressure range $10^{-5} \leq P/H_e \leq 0.2$ [109,110]. Thus if the contacting surfaces formed by two metal bodies are nominally flat and rough Gaussian surfaces Eq.75 and Eq.82 can be used to predict thermal contact conductance for plastic and elastic deformation respectively. A surface is Gaussian when the asperities of a surface are isotropic and randomly distributed over the entire surface as shown by Williamson et al [112].

The plasticity index φ sets the criteria and calculates the mode of deformation. The above equations can not predict thermal contact conductance if the deformation is elastic-plastic, i.e., $0.33<\varphi<3$. Next section explains the situation when the mode of deformation is a combination of both.

c. Elastic-Plastic Contact Model

When the asperities undergo a combination of elastic and plastic deformation the prediction models become more complex. The elastic-plastic contact conductance models presented here were created by Sridhar et al [90] and are based on the elastic models created by Mikic [61] and the plastic model created by Cooper et al [57] as cited in [71].

$$\frac{A_r}{A_a} = \frac{f_{ep}}{2} erfc\left(\frac{\lambda}{\sqrt{2}}\right) \qquad \text{Eq. 83}$$

$$n = \frac{1}{16}\left(\frac{\sigma}{m}\right)^2 \frac{\exp\left(-\lambda^2\right)}{erfc\left(\frac{\lambda}{\sqrt{2}}\right)} \qquad \text{Eq. 84}$$

$$a_m = \sqrt{\frac{8}{\pi}}\sqrt{f_{ep}}\frac{\sigma}{m}\exp\left(\frac{\lambda^2}{\sqrt{2}}\right)erfc\left(\frac{\lambda}{\sqrt{2}}\right) \qquad \text{Eq. 85}$$

$$\lambda = \sqrt{2}erfc^{-1}\left(\frac{1}{f_{ep}}\frac{2P}{H_{pe}}\right) \qquad \text{Eq. 86}$$

Where f_{ep} is an elastic-plastic parameter defined as:

$$f_{ep} = \frac{\sqrt{\left[1+\left(\frac{6.5}{\varepsilon_c}\right)^2\right]}}{\left[1+\left(\frac{13}{\varepsilon_c}\right)^{1.2}\right]^{1/1.2}} \text{ for } 0<\varepsilon_c<\infty \qquad \text{Eq. 87}$$

The parameter f_{ep} is a function of a dimensionless contact strain ε_c and depends on the work hardening of the material.

$$\varepsilon_c = 1.67\left(\frac{mE}{S_f}\right) \qquad \text{Eq. 88}$$

Where the parameter S_f is the material yield stress and generally must be determined experimentally for each material. The thermal contact conductance for this complex case depends on the value of dimensionless contact strain ε_c. For the three limiting cases the correlations are approximately given by the following [62,63,113,114]:

$$C_c = 1.54\left(\frac{P}{H_{ep}}\right)^{0.94}, \quad 0<\varepsilon_c<5 \qquad \text{Eq. 89}$$

$$C_c = 1.245 b_1\left(\frac{P}{H_{ep}}\right)^{b_2}, \quad 5<\varepsilon_c<400 \qquad \text{Eq. 90}$$

$$C_c = 1.25\left(\frac{P}{H_{ep}}\right)^{0.95}, \quad 400<\varepsilon_c<\infty \qquad \text{Eq. 91}$$

The elastic-plastic correlation coefficients b_1 and b_2 depend on the dimensional contact strain ε_c and are defined as:

$$b_1 = \left[1+\frac{46{,}690.2}{\varepsilon_c^{2.49}}\right]^{1/30} \qquad \text{Eq. 92}$$

$$b_2 = \left[\frac{1}{1+2086.9/\varepsilon^{1.842}}\right]^{1/600} \qquad \text{Eq. 93}$$

The conductance of gap material depends on many parameters: surface roughness, mean asperity slope, gas pressure and gas temperature, contact pressure, micro-hardness of

contacting asperities and the ratio of gap thermal conductivity to material thermal conductivity of contacting material [72]. Gap conductance contributes little in the overall joint conductance if the interface fluid is gas e.g., air. This is due to the low value of thermal conductivity of gas compared to that of metals e.g., steel. The contribution is more significant at low contact pressures. Thermal conduction in a gas layer assuming two parallel plates is categorised into four heat flow regimes: (a) continuum gas conduction, (b) temperature jump or slip, (c) transition and (d) free molecule as shown in Figure 2-35.

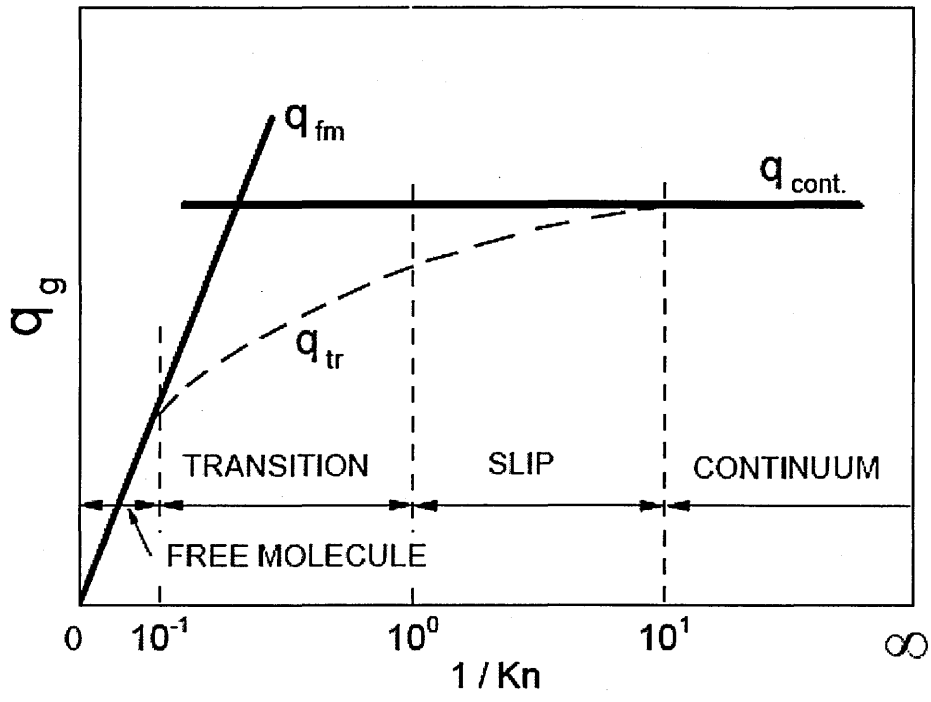

Figure 2-35. Heat flow regimes as function of Knudsen number [66]

A parameter which decides the regimes is called the Knudsen number defined as follows [115]:

$$K_n = \frac{\Lambda}{\delta} \qquad \text{Eq. 94}$$

Where Λ is the molecular mean free path and δ is the distance between the parallel plates. The molecular mean free path is proportional to the gas temperature and inversely proportional to gas pressure. i.e.

$$\Lambda = C_{\Lambda} \frac{T_g}{P_g}$$ Eq. 95

Where Cg is a specific constant of gas, Tg is the gas temperature, Pg is the gas pressure.

Heat flow regime	Knudsen number K_n	Explanation
Continuum gas conduction	$K_n < 0.01$	Heat transfer is as a result of energy exchange between gas molecules via collision
Temperature jump/slip	$0.01 < K_n < 0.1$	Due to the discontinuity of temperature at interface, the energy exchange is incomplete resulting in temperature jump/slip
Transition regime	$0.1 < K_n \geq 10$	This is the intermediate transition regime so both intermolecular and molecule collisions make a contribution to heat transfer
Free molecule	$K_n \geq 10$	The pressure is near vacuum conditions, there is no intermolecular collision and the regime is referred to as free molecular

Table 2-3. Four regimes categorising the thermal conduction in a gas layer [115]

Kennard [116] proposed the following expression for gap conductance between parallel plates as cited in [72]:

$$h_g = \frac{k_g}{\delta + M}$$ Eq. 96

Since h_g is the reciprocal of thermal resistance, $h_g = 1/(R_g A_a)$, an expression for the gap thermal resistance R_g is:

$$R_g = \frac{\delta + M}{k_g A_a}$$ Eq. 97

Where k_g is the thermal conductivity of gas substance, δ is the effective gap thickness and M is the gas parameter. The gas parameter M is the thermal resistance resulting from the 'rarefied gas' phenomena in microscopically small gaps and depends on the gas type, gas pressure, gas temperature and the thermal accommodation coefficient, α. The gas parameter M is defined as follows [69]:

$$M = \alpha \times \beta \times \Lambda$$ Eq. 98

Where gas and accommodation parameters are defined as follows:

$$\alpha = \frac{2-\alpha_1}{\alpha_1} + \frac{2-\alpha_2}{\alpha_2} \qquad \text{Eq. 99}$$

$$\beta = \frac{2\gamma}{(\gamma+1)P_r} \qquad \text{Eq. 100}$$

$$\gamma = \frac{C_p}{C_v} \qquad \text{Eq. 101}$$

Where α_1 and α_2 are a measure of the energy exchanged between the gas molecules and the solid surfaces, γ is the specific heat ratio for the interfacial material, P_r is the gas Prandtl number. The molecular mean free path is defined as [69]:

$$\Lambda = \left(\Lambda_0 \frac{T_g}{T_0} \frac{P_0}{P_g} \right) \qquad \text{Eq. 102}$$

Where, Λ_0 is the molecular mean free path at the reference pressure P_0 and reference temperature T_0.

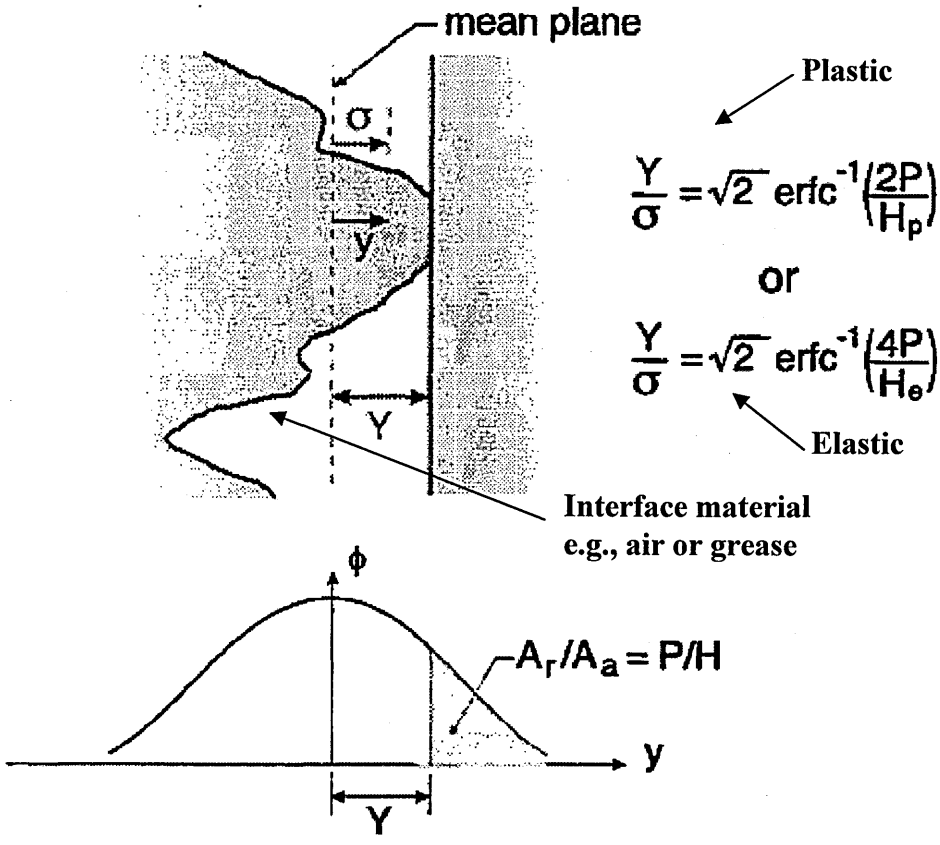

Figure 2-36. Illustration of gap thickness between a smooth flat and a rough surface in contact [72]

The effective gap thickness, δ or Y is a function of three parameters: surface roughness, contact pressure and the elastic properties of the asperities as shown in Figure 2-36. The following expression based on the Maxwell's theory for the heat flux Q_g through a gas layer between two parallel plates for all gas-phase regimes was proposed by Yovanovich et al [117]:

$$Q_g = \left(\frac{k_g}{Y+M}\right)(T_1 - T_2) \qquad \text{Eq. 103}$$

T_1 and T_2 are the uniform temperatures of the two parallel plates.

Thermal Grease at Interface

One way to control the TCR is the use of interfacial materials at interface. Greases exhibit a better thermal performance compared to say air because of higher thermal conductivity, and compared to metallic foils due to their ability to completely wet the contacting surfaces. The general contact conductance model for interfaces filled with grease is the sum of contact conductance h_c and gap conductance h_g and can be expressed as follows:

$$h_j = h_c + h_g = \frac{1}{R_j A_a} \qquad \text{Eq. 104}$$

If the grease perfectly wets the contact surfaces, then the gap conductance controls the heat flow across interface ($h_g >> h_c$) and the joint resistance can be written as [72]:

$$h_j = h_g = \frac{k}{Y}, \text{ for } 2 < Y/\sigma < 5 \qquad \text{Eq.105}$$

The contact conductance for conforming rough contact assuming plastic deformation of asperities is given by [104]:

$$h_c = 1.25 k_s \frac{m}{\sigma}\left(\frac{P}{H_c}\right)^{0.95} \qquad \text{Eq. 106}$$

Where k_s, m, σ, P, H_c are harmonic mean thermal conductivity, effective mean absolute asperity slope, effective surface roughness, contact pressure and contact micro-hardness respectively as previously defined. The gap conductance h_g is modelled as an equivalent

layer of thickness Y, filled with thermal grease having thermal conductivity k_g as shown in Figure 2-36, and it is given by the following expression [118]:

$$h_g = \frac{k_g}{Y} \qquad \text{Eq. 107}$$

Where Y is the gap parameter defined as the distance between the mean planes passing through the roughness of the contacting surfaces. This parameter is a function of root mean square roughness of contacting surfaces σ, the contact pressure P and the effective micro-hardness of the softer material in contact H_c. Yovanovich [104] developed the following expression:

$$Y = \sqrt{2} erfc^{-1}\left(\frac{P}{H_c}\right)\sigma \qquad \text{Eq. 108}$$

The Eq. 108 is applicable to most practical situations and it is valid for the following ranges of P/H_c:

$$2 \le \frac{Y}{\sigma} \le 4.75 \quad \text{and} \quad 10^{-6} \le \frac{P}{H_c} \le 2\times10^{-2} \qquad \text{Eq. 109}$$

2.13.2 Non-Conforming Contacts

If the contact surfaces of a joint formed by two metal bodies in contact has roughness as well as out-of-flatness and out-of-waviness deviation, the contact is thought of being non-conforming, in other words, when the effect of surface curvature on contact pressure distribution is significant the surface is non-flat. The overall contact is a combination of micro-contacts made between the asperities due to the surface roughness and the contact made between the higher areas on the surfaces due to the surface curvature, referred to as macro-contacts and it is the area where micro-contacts are distributed as shown in Figure 2-37 [65].

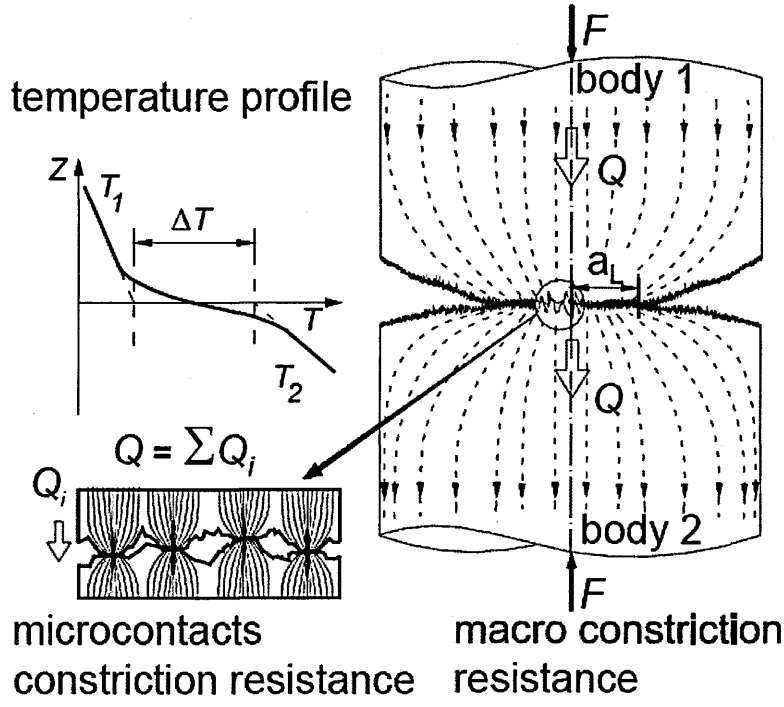

Figure 2-37. A typical non-conforming contact comprising of micro and macro constriction resistance and the temperature profile across the joint interface [64]

A number of mathematical models and correlations of the thermal contact resistance for non-conforming contacts have been developed over the last few decades [63,64,68,85,119-122]. In general the joint resistance in vacuum conditions is a function of microscopic and macroscopic resistance and is defined as:

$$R_j = R_{mic} + R_{mac} \qquad \text{Eq. 110}$$

Where, R_{mic} and R_{mac} are microscopic and macroscopic thermal resistances and are defined as:

$$R_{mic} = \frac{\Psi_{mic}}{2k_a N a_s} \quad \text{Eq. 111}$$

$$R_{mac} = \frac{\Psi_{mac}}{2k_a a_L} \quad \text{Eq. 112}$$

Where Ψ_{mic} is the average spreading/constriction resistance, N is the number of micro-contacts distributed over the contour area of radius a_L, as is the average micro-contact spot radius, Ψ_{mac} is the spreading/constriction resistance for the contour area of radius a_L, k_s is the harmonic mean thermal conductivity of the joint defined as:

$$k_s = \frac{2k_1 k_2}{k_1 + k_2} \quad \text{Eq. 113}$$

Heat transfer across non-conforming contacts is more mathematically involved than for conforming contacts. This is because other than surface roughness, surface waviness and surface out-of-flatness deviations are considered.

Surface Flatness

Flatness is represented as a maximum deviation of the machined plane from the intended plane represented by d_f, see Figure 2-38(c) [85]. Consider the case when surface A with high degree of flatness comes into contact with a surface B with flatness deviation. In this case only part of the overall contact area is in real contact as shown by shaded area in Figure 2-39(b).

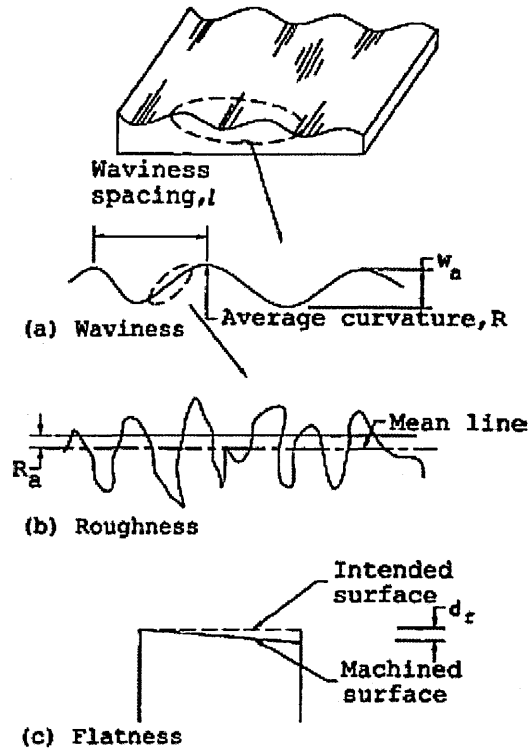

Figure 2-38. A schematic representation of surface [85]

In order to determine the extent y_c over which the surfaces are in contact, the following relationship is proposed by Kumar et al [85]:

$$\frac{y_c}{D} = \frac{x_{\max A} + x_{\max B} - \varepsilon_{\min}}{d_f} \qquad \text{Eq. 114}$$

Where x_{maxA} is the maximum asperity height of surface A, x_{maxB} is the maximum asperity height of surface B and D is the diameter of the surface, see Figure 2-39.

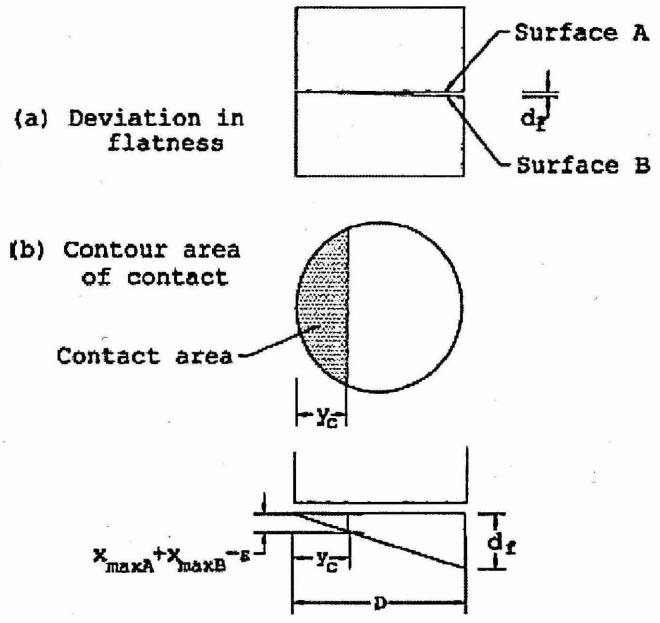

Figure 2-39. A schematic representation of non-flat contact formed by two surfaces [85]

The contact area depends on the contact pressure. The contact area can be determined if the apparent contact area is divided into small strips of width d_y as shown in Figure 2-40.

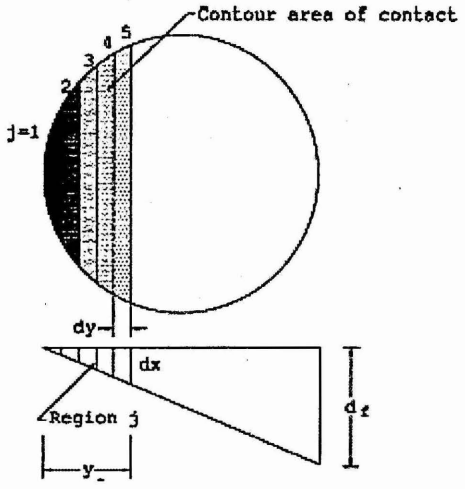

Figure 2-40. Discretisation of contact area [85]

The minimum clearance ε_{min} and therefore the maximum pressure would occur at strip j=1 for a given contact pressure. The pressure in each strip will vary along y_c and could be approximated as the ratio of the pressure to the elemental area, assuming constant

pressure in each strip. The pressure in each strip can be found using the following expression:

$$P_j = P_1\sqrt{\left[1-\left(\frac{j\times dy}{y_c}\right)^2\right]} \qquad \text{Eq. 115}$$

Where P_j is the pressure at strip j=1. At low contact pressures only strip j is in contact. As contact pressure increases so does the area of contact, consequently bringing more strips into contact. The additional clearance dx_j at the boundary of each discretised strip is given by the following [85]:

$$dx_j = \frac{1}{2}\left[\frac{j\times dy\times dx}{D}+\frac{(j+1)\times dy\times d_f}{D}\right] \qquad \text{Eq. 116}$$

The net clearance for a rough non-flat surface is given by:

$$\varepsilon_j = \varepsilon_{\min} + dx_j \qquad \text{Eq. 117}$$

Surface Waviness

The average waviness w_a is represented by the peak to valley height of the measured profile from which roughness is removed by suitable filtering as explained in Chapter 2. The contact strips with waviness is modelled as the sum of the contour area of each contacting waviness peak based on the two-dimensional representation of average waviness height, spacing and curvature see Figure 2-38. According to Hertzian theory of contact, when two peaks of radii R_1 and R_2 are brought into contact, the width w of contact zone is given by [85]:

$$w = \left[\frac{3\pi(K_1+K_2)}{2\left(\frac{1}{R_1}+\frac{1}{R_2}\right)}P\right]^{1/3} \qquad \text{Eq. 118}$$

Where R_1 and R_2 are the radius of curvature of waviness peak for surface 1 and 2 respectively, P is the contact pressure and K_1 and K_2 are dimensionless surface parameters defined as:

$$K_1 = \frac{1-\nu^2{}_1}{\pi \times E_1} \quad \text{Eq. 119}$$

$$K_2 = \frac{1-\nu^2{}_2}{\pi \times E_2} \quad \text{Eq. 120}$$

Where E_1 and E_2 are the modulus of elasticity for material 1 and 2 respectively, υ_1 and υ_2 are Poisson's ration for material 1 and 2 respectively. The total constriction resistance can now be formulated and is the sum of the resistance due to roughness, resistance due to flatness deviation and resistance due to waviness:

$$R_t = R_s + R_f + R_w \quad \text{Eq. 121}$$

So, the total contact conductance following Eq. 121 is given by:

$$h_t = \frac{1}{R_t \times A_a} \quad \text{Eq. 122}$$

The thermal contact resistance due to surface roughness is given by:

$$R_s = \frac{\Psi_s}{2k_s \sum_{n_c} a_i} \quad \text{Eq. 123}$$

Where n_c is the number of contact asperities, a_i is the radius of each contact formed by two contacting asperities and k_s is the harmonic mean thermal conductivity of materials in contact. The constriction parameter Ψ is given by Eq. 56. Thermal contact resistance due to flatness deviation is as follows [85]:

$$R_f = \frac{\Psi_f}{2k_s a_f} \quad \text{Eq. 124}$$

Thermal contact resistance due to waviness is:

$$R_w = \frac{\Psi_w}{2k_s a_w} \quad \text{Eq. 125}$$

Following Eq.125 the total contact conductance can be written as:

$$h_t = \frac{1}{\left[\frac{\psi_s}{2k_s \sum_{n_c} a_i} + \frac{\psi_f}{2k_s a_f} + \frac{\psi_w}{2k_s a_w}\right] \times A_a}$$ Eq. 126

2.14 Summary Review

It is recognised that thermal errors represent the biggest apparent non-repeatability in machine tools [3,4]. The influence of temperature, especially the non-uniform temperature within the machine tool members, overshadows other errors, such as kinematic, dynamic and force-induced errors [134].

From the literature review presented here, it can be said that there has been tremendous amount of research related to thermal issues in machine tools. Some researchers have concentrated in finding the sources of heat and the magnitude produced by each source [2,3,14-20,24-30]. Other researchers have developed and implemented thermal compensation methods [38-55].

A traditional approach in thermal analysis is to conduct experimental tests and gather temperature data while machine tool is operational. In order to get a fuller understanding of the heat sources, researchers monitor the temperature data at various locations on the machine tool using appropriate temperature sensors. Special attention is paid in monitoring the temperatures generated by the machining process; bearings [2,15-16], driving motors [19-22] and in many cases the coolant [2, 15-16]. Usually there is an experimental design involved whereby researchers vary appropriate design factors such as depth of cut, feed rate, workpiece material.

From experimental temperature data, researchers have developed direct and indirect compensation methods in order to compensate for thermal errors [3,5-7,36-37,47]. Direct compensation techniques work by directly measuring the displacement between the tool and the workpiece and compensating for any induced errors [38]. Whereas the indirect compensation technique employs a deformation model based on the temperature measurement, and on models correlating temperature to deformation [39]. Compensation techniques are attractive because they reduce the overall thermal errors. However, thermal errors can not be eliminated completely by compensation, but can be minimised to a significant degree.

Since the inception of the Fourier's law of conduction in 1822, mathematical modelling of heat transfer has become possible. The models can be applied to any dimensional geometry and solutions can be obtained by specifying boundary and initial conditions [99]. However, for complex two-dimensional and three-dimensional geometries, the

analytical models can be cumbersome and are therefore often replaced by numerical technique known as finite element modelling [126]. Finite element modelling works by approximating the solution of partial differential equations [126]. With advancements in the FEM, designers and researchers can model complicated machine tool structures under complex boundary conditions in order to predict the thermal behaviour of machine tools before they are built and tested [12,26,30,33-34,40,54].

However, an important and usually ignored boundary condition in mathematical models for machine tool applications is the effect of heat transfer across joint interfaces. Machine tools are made of many members of the same or in most cases different material that are in static or dynamic contact. Machine structural joints are in static contact, held together under specific pressure. However bearings, lubricated sliding faces etc, are in dynamic contact which are often free to move in a desired direction. When heat is generated at a specific location in a machine tool, this heat is conducted through a member, across joint interfaces to other machine tool members. A consequence of heat flow into machine tool structural members is increased uncertainties in machine tool performance. An inability to adequately understand and model heat transfer across joint interfaces in machine tools is therefore a major limitation to current knowledge and capability.

Heat transfer across joint interfaces in certain cases can be predicted using appropriate mathematical models. The early models were not as advanced, in other words the models did not include factors such as waviness and flatness deviations. Aerospace was one of the first industries to apply the models of heat transfer across interfaces. As research went on, the models became more comprehensive. With increasing demand for better and more complex products, researchers have developed more comprehensive mathematical models that can be applied even in the case of non-conforming contacts [57,58,61-68].

Most mathematical models have been validated experimentally under various influencing factors. However, almost all of the experimental research was done under vacuum conditions, which makes the accuracy of models uncertain if the surrounding gas is air. Furthermore, most of the models are developed for specific applications e.g., low contact pressures, small out of flatness and waviness deviations, vacuum

conditions, which mean that they can not be applied in other situations. The difficulties with modelling thermal contact arises due to the number of factors that influence heat transfer across bodies in contact. An accurate determination of the magnitude of all factors is usually difficult, and in many situations impossible.

This research investigates both experimentally and numerically the influence of most influential factors as detailed in Chapter 3. The experimental investigation is carried out using specially built measuring rigs. The first rig is designed to measure temperature distribution across two steel blocks in contact held by a high tensile bolt, detailed in section 3.3. The second rig is designed to measure temperature distribution and dimensional distortion of three steel blocks in contact held by two high tensile bolts, detailed in section 3.4. Both experimental rigs were simulated using numerical modelling. Experimental situation were modelled numerically by applying appropiate boundary conditions including the design factors investigated experimentally. Flowchart showing the research methodology is shown in Figure 1-3.

One of the most influential factors is the contact non-conformance due to poor surface finish. Contact non-conformance will be investigated experimentally. Furthermore special attention will be paid in assessing the capability of modelling in predicting the heat transfer across joint interfaces having some deviation from perfect contact. Another important factor in thermal problems is the prediction and definition of the convection coefficient. Convection coefficient is transient in transient heat transfer. As heat flows into a system ,the temperature of the system rises until the sytem reaches the steady state condition. The effect of convection coefficient on the heat transfer across bodies in cotact has not been rigorously studied before. Hence this research will investigate this numerically by varying the coefficient from as low as 1 $W/m^2°C$ to an order of magnitude higher to 10 $W/m^2°C$.

Another important factor on heat transfer across interfaces is the real contact area, A_r. The real contact area depends on the topography of surfaces in contact. The topography of machined surfaces has some magnitude of roughness, waviness and flatness. The degree of magnitude varies, and is dependent on the machining process used. The quality of a surface can be described using appropriate parameters, as explained in section 2.10. The effect of contact area on heat transfer across interface will be

investigated by introducing slots on one of the contacting surfaces. The introduction of slots reduces the cotact area by half. Moreover the effect of spread of contact regions on heat transfer across interfaces will be investigated by having two interface geometries with smaller and bigger contact ridges.

3 Experimental Procedures and Equipment

3.1 Introduction

The experimental study of heat transfer across metal bodies in contact can be traced back to 1949 [80], when researchers used various experimental methods to investigate heat transfer across interfaces of two materials. Almost all of these previous studies were conducted under vacuum conditions and low contact pressures. Clearly studies performed under such conditions are attractive, as they are more accurate since the factors such as environmental varying conditions do not influence the results. However, machine tools are normally exposed to varying ambient conditions and the lack of data under such conditions is a significant disadvantage. While significant insight can be gained from environmentally controlled experiments, studies carried out under ambient conditions are more relevant to machine tools.

The aim of this research has been to produce measurements that can be applied directly to machine tool joint interfaces and that can be compared with the existing analytical models, and finite element models.

3.2 Experimental Investigation

The underlying principle in design and analysis of experiments is to vary some input parameters which are considered to have an effect on the output of the process under study, and observe the response of the system, as shown in Figure 3-1. The input parameters chosen for such purposes are called design factors [123].

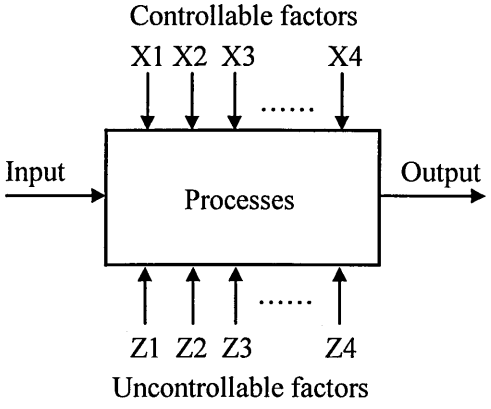

Figure 3-1. General model of a process or system [123]

In this research two different and separate experiments were conducted. Each experiment including its purpose, equipment and sensory devices used is explained in detail in the following sections.

This Chapter is therefore divided into two sections as follows:

- Section 3.3 introduces experimental setup and design for the first set of tests two block analysis, including the levels and ranges of design factors.
- Section 3.4 introduces experimental design for the second set of tests for three blocks analysis including the levels and ranges of design factors.

3.3 Two Block Analysis

This set of tests comprises of two cubical (60x60x60 mm) steel blocks in static contact, held together using a single 8 mm diameter high tensile steel bolt placed through their centre. The purpose of this experimental investigation is to measure the temperature gradients along the individual blocks, and consequently find out the temperature drop across the joint interface. Heat transfer across a joint interface is a function of many factors, as explained in Chapter 2. A diagram showing the model of experimental process is shown in Figure 3-2 (after Montgomery [123]).

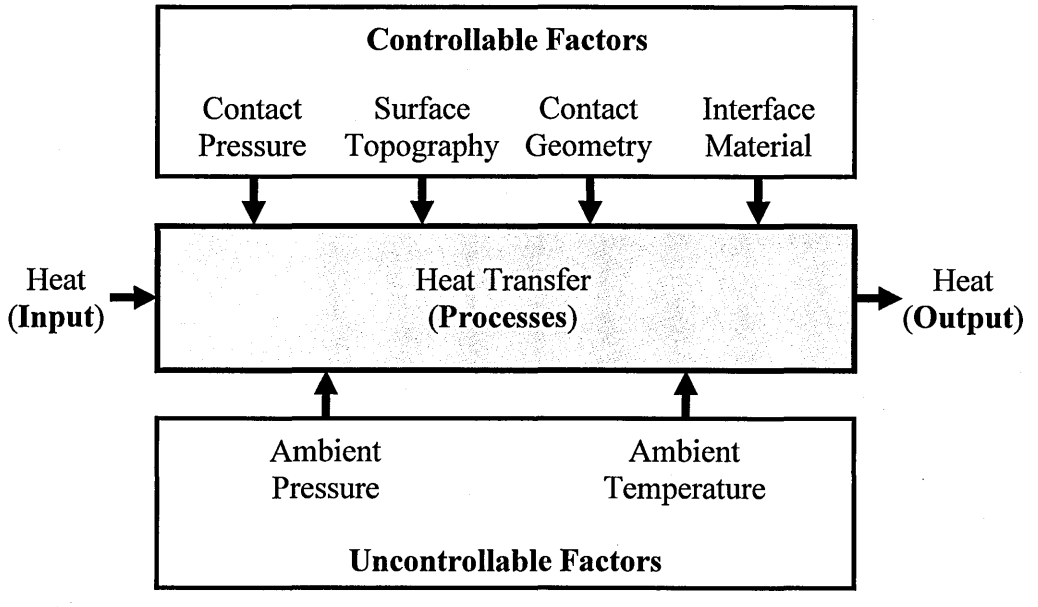

Figure 3-2. Model of experimental process for two block analysis (after Montgomery [123])

3.3.1 Experimental Design

A series of experiments were performed to test the validity of the analytical and numerical models and also to enhance understanding of the mechanisms controlling the heat transfer of bolted joint interfaces. There are a number of factors that influence heat transfer across interface. The most influential and applicable factors are considered here.

Most machine tools are exposed to varying ambient conditions, therefore all thermal experiments were performed on steel (AISI 1213) under varying ambient conditions. For these series of tests, the following four design factors and their levels were considered:

1. *Contact pressure* is one of most significant factor in heat transfer across joint interface. With increased pressure the surface contact asperities deform. Due to deformation of contact asperities the real contact area increases. As the contact area increases the heat flow channels increase and consequently the contact conductance increases. In these sets of tests three levels of contact pressure were used for analysis: 5.64 MPa, 10 MPa and 14.2 MPa corresponding to 25 Nm, 50 Nm and 75 Nm applied torques respectively.
2. *Interface geometry* was another factor used in experimental design. Two different arrangements were considered.

a. First arrangement comprising of a steel block (60x60x60 mm) with 2 mm wide and 2 mm deep slots (referred to as block 'X') at contact interface was placed in contact with a nominally flat block (60x60x60 mm) (referred to as block 'Z').

b. Second arrangement comprising of a steel block (60x60x60 mm) with 3.75 mm wide and 2 mm deep slots (referred to as block 'Y') at contact interface was placed in contact with the same nominally flat block 'Z'.

By placing slotted blocks 'X' and 'Y' in contact with block 'Z', the apparent contact area is reduced by half. The width of slots at contact interfaces were chosen in such a way so the apparent contact area in both arrangements above remains the same, as shown in Table 3-1.

Blocks in contact	Surface area of single ridge [m]	Number of ridges	Total apparent contact area [m^2]
Block 'X' in contact with block 'Z'	0.002x0.06=0.00012	15 Figure 3-4(a)	0.0012x15=0.0018
Block 'Y' in contact with block 'Z'	0.00375x0.06=0.000225	8 Figure 3-4(b)	0.000225x8=0.0018

Table 3-1. Apparent contact areas for two different arrangements

3. *Surface topography* is another significant factor influencing heat transfer across a joint interface. The topography of engineering surfaces is a function of surface roughness, waviness and flatness deviation in heat transfer applications. If waviness and flatness deviations are very small in comparison to roughness, then the surface can be thought of as being flat and waviness and flatness can be assumed as being insignificant (this contact is referred to as 'conforming'). Whereas, if the surface waviness and flatness deviation is bigger than the surface roughness then the waviness and flatness can not be ignored, and must be taken into consideration (this contact is referred to as 'non-conforming').

Two different contact surface qualities are considered: *poorly conforming contact* having higher waviness and flatness deviation, and *good conformance contact* having lower waviness and flatness deviation. The surface topography parameters are given in Table 3-4.

4. *Interfacial material* is the fourth factor considered. Theoretically speaking, interfacial material should influence heat transfer across the joint interfaces. Having a material with higher thermal conductivity at the interface, should increase thermal contact conductance and subsequently enhance heat transfer across the joint interface. Two different interfacial materials were considered: air and thermal grease, see Table 3-3.

In total twenty four tests were executed by varying the design factors. Tests A1 to B6 represent the case when the contacting surfaces were cut and tests C1 to D6 when the contacting surfaces were ground. Each test was repeated twice to ensure consistency. Table 3-2 shows details of experimental design. A typical test e.g., A1 comprises of:

- Block 'Y' in contact with block 'Z'
- Contact pressure of 5.64 MPa
- Interfacial material air, and

- Ground contact surfaces, as highlighted in Table 3-2

All other tests A2-D6 are organised in the same way.

Test	Blocks in contact	Contact pressure [MPa]	Interface material	Surface finish
A1	Y (3.75 mm slots) and Z	5.64	Air	Poorer conformance
A3		14.2		
A4		5.64	Grease	
A5		10		
A6		14.2		
B1	X (2 mm slots) and Z	5.64	Air	
B2		10		
B3		14.2		
B4		5.64	Grease	
B5		10		
B6		14.2		
C1	Y (3.75 mm slots) and Z	5.64	Air	Good conformance
C2		10		
C3		14.2		
C4		5.64	Grease	
C5		10		
C6		14.2		
D1	X (2 mm slots) and Z	5.64	Air	
D2		10		
D3		14.2		
D4		5.64	Grease	
D5		10		
D6		14.2		

Table 3-2. Experimental design for two block analysis

3.3.2 Experimental Setup

The experimental system consists of a 400 W hotplate placed on top of the assembly, an insulating board placed on top of the hotplate, upper and lower blocks, and a steel block placed in a plastic container filled with flowing water. The axial temperature gradient measurements are made using six calibrated T-type thermocouples, a connector block with amplifier, a data acquisition board and a personal computer. The setup is shown schematically in Figure 3-3.

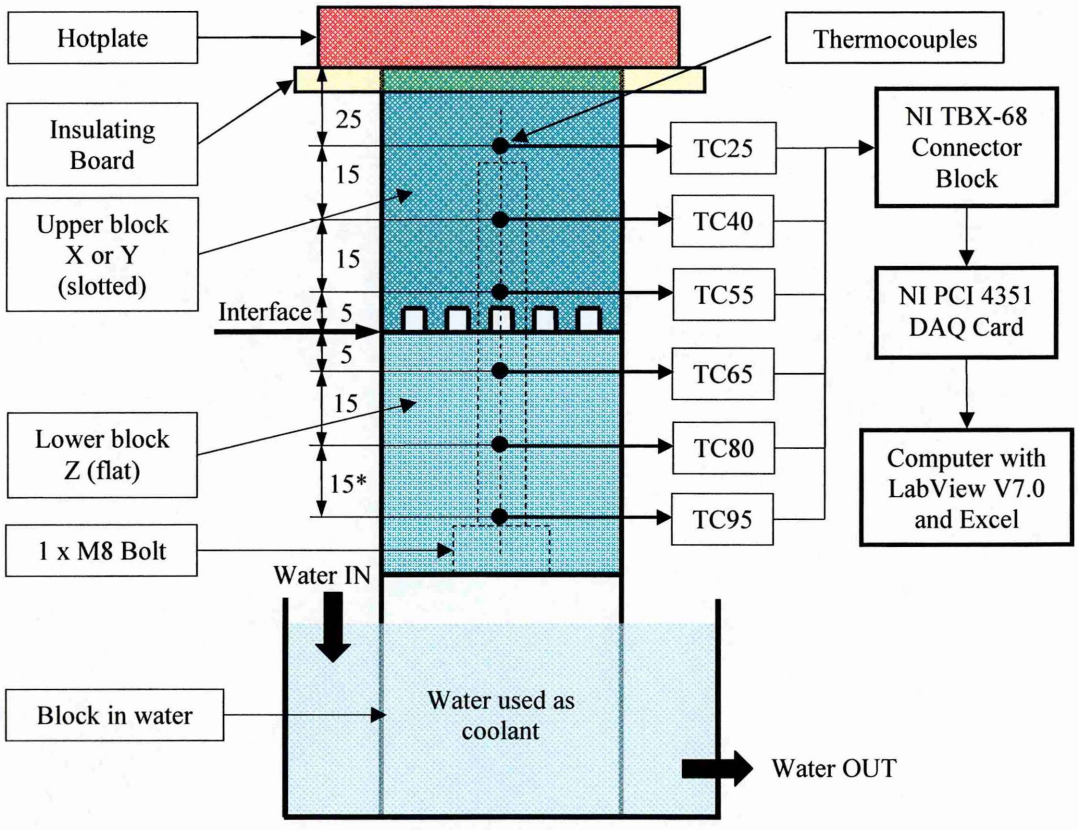

Figure 3-3. Experimental setup for two block analysis (*note: all dimensions in mm)

Thermocouples are named with letters 'TC' followed by a two digit number. The 'TC' stands for 'thermocouple', whereas the two digit number following the letters 'TC' represents the distance of the sensor from the hotplate in mm.

3.3.3 Test Blocks

The test blocks (see Figure 3-4) are made from steel (AISI 1213). The blocks are cut from the same piece and machined to their specified dimensions 60x60x60 mm. Each block had three small holes of 1 mm in diameter, 10 mm deep, drilled in one of the faces to accommodate the thermocouples. The holes were placed at 15 mm intervals to each other with the closest hole 5 mm away from interface, see Table 3-3 for material properties.

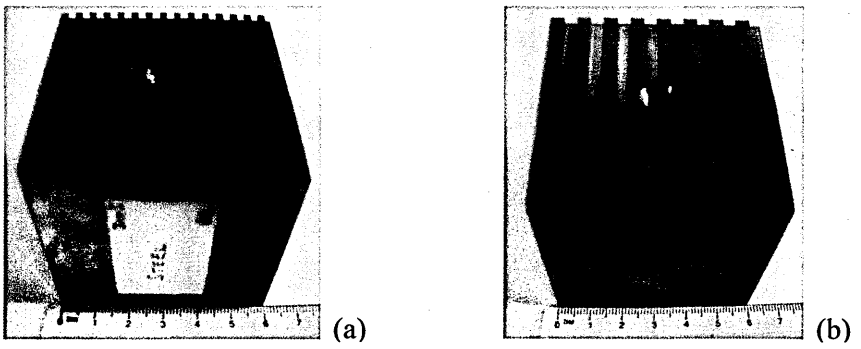

Figure 3-4. (a) Block X with 2 mm wide by 2 mm deep slots, (b) block Y with 3.75 mm wide by 2 mm deep slots

Property \ Material	Blocks (AISI 1213)	Bolts (ASTM A574M)	Air	Grease
Density, ρ	7870	7850	1.17	-
Modulus of elasticity, E	205	205	-	-
Vickers hardness, H_v[(1)]	2.334	3.766	-	-
Poisson's ratio, υ	0.29	0.29	-	-
Tensile stress, σ_t	385	1300		
Yield stress, S_f	240	1170		
Thermal conductivity, k	51.9	44.5	0.026	0.9
Specific heat capacity, Cp	486	475	1.0057	34.8
Coefficient of thermal expansion	12.3	10.4	-	-

(1) Vickers hardness values 238 and 384 were multiplied by 0.009807 to convert to GPa

Table 3-3. Properties of materials used in experiments

A small contact region at the interface between blocks X and Z, Y and Z is shown in Figure 3-5.

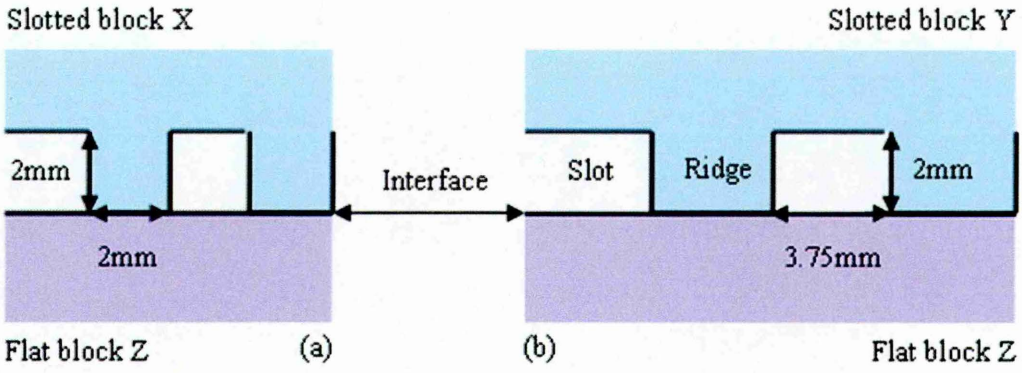

Figure 3-5. (a) Block 'X' in contact with block 'Z', (b) block 'Y' in contact with block 'Z'

For the first set of tests (tests A1 to B6) contacting surfaces were cut, deliberately made to have high value of roughness and out of flatness deviation. For the second set of tests (tests C1 to D6) contacting surfaces were ground in order to achieve a better surface finish with small out of flatness and waviness deviation.

The profiles of contacting surfaces were measured using a Form Talysurf 120-L stylus profilometer; see Table 4-2 for specifications. The output of profile measurement as a function of sample is recorded to evaluate the surface characteristics. A later section explains the measurement of surface topography in detail. Surface topography parameters are shown in Table 3-4.

Block	Contact surface quality	Surface roughness R_a [μm]	Max. peak to valley height Rt [μm]	Surface form error Pt [μm]
X	Poor conformance	0.12	9.22	26.68
	Good conformance	0.14	3.19	5.8
Y	Poor conformance	0.12	6.81	13
	Good conformance	0.03	3.82	7.52
Z	Poor conformance	0.11	6.47	13.97
	Good conformance	0.13	4.02	6.52

Table 3-4. Topography parameters of contacting surfaces for two block analysis

3.3.4 Profilometric Measuring Equipment

A Form Talysurf 120L profilometer was used to obtain profile traces for the specimen contacting surfaces. A picture of the instrument used is shown in Figure 3-6 and instrument characteristics are shown in Table 3-5.

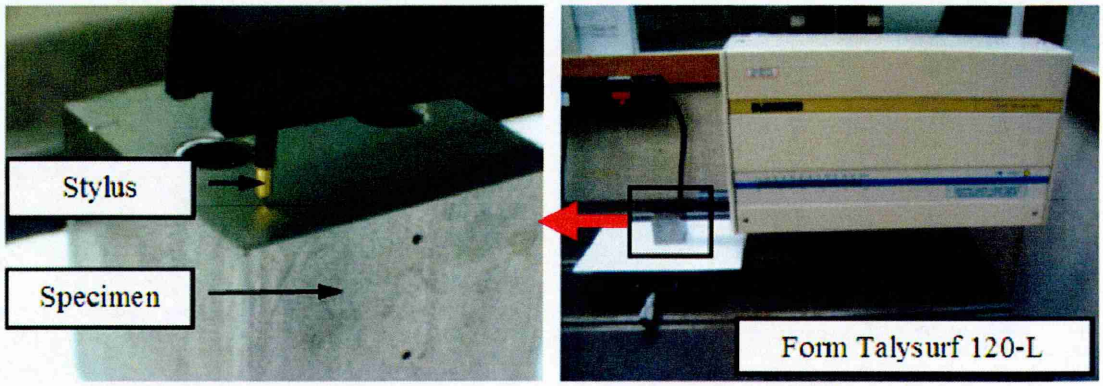

Figure 3-6. A typical measurement of a surface topography using Form Talysurf 120-L profilometer

Each specimen was held stationary and the stylus of the instrument was programmed to run horizontally across the surface at a constant speed of 0.5 mm/s. For slotted blocks 'X' and 'Y' the top surface of each ridge was measured individually. For flat block 'Z' each of the corresponding contact surface with the ridges was measured. The measurement data for the contact surfaces are averaged out and the relevant parameter values are shown in Table 3-4.

Traverse Length	120 mm
Traverse Speed	1 mm/sec maximum
Measuring Speeds	1 mm and 0.5 mm/sec ±5%
Return Speed	up to 5 mm/sec
Gauge Type	Phase Grating Interferometer
Resolution (vertical)	10 nm
Stylus diameter	2 μm
Range to Resolution Ratio	12.8 nm @ 10 mm range
Straightness Accuracy	780,000:1
Data Resolution (vertical)	0.5 μm over 120 mm traverse

Table 3-5. Characteristics of Form Talysurf 120-L profilometer [97]

3.3.5 Thermocouples

There are a number of different types of temperature sensors available in today's market. All of them deduce temperature by sensing some change in a physical characteristic. The following six types of temperature sensors with which one's likely to

come across are: thermocouples, resistive temperature devices (RTD's and thermistors), infrared radiators, bimetallic devices, liquid expansion devices, and change-of-state devices.

Thermocouples are rugged, relatively accurate, economical, and easy to use. Therefore thermocouples appear to be the best choice. Other researchers involved in a similar type of research have in the past, used thermocouples as means of measuring the temperature gradient across bodies in contact [57,60,124]. The thermocouple working principle is based upon the findings of Seebeck (1821) who showed that a small electric current will flow in a circuit composed of two dissimilar conductors when their junctions are kept at different temperatures. The electromotive force (emf) produced under these conditions is known as the "Seebeck emf". The pair of conductors that constitute the thermoelectric circuit is called thermocouple.

In principle, a thermocouple can be made from almost any two metals. In practice, several thermocouple types have become standard because of desirable qualities such as linearity of the voltage drop as a function of temperature and large voltage to temperature ratio. Some common thermocouple types are designated as J, K, R, S and T. The thermocouple leads, one made of copper and one of constantan (T-type) are joined by welding or soldering. Constantan is an alloy consisting of 55% copper and 45% nickel. A T-type thermocouple is shown in Figure 3-7.

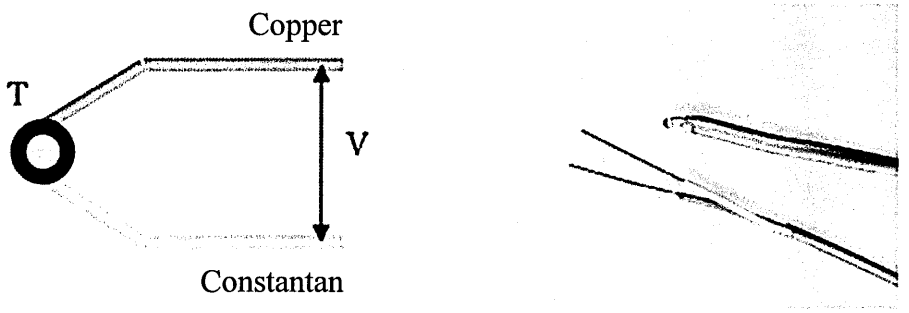

Figure 3-7. The voltage V across the copper and constantan wires is a function of the temperature T at the junction.

The electromotive force may be constant over a small temperature range but over larger ranges it varies linearly with temperature, such as T-type thermocouple. Some typical voltage temperature curves for commonly used thermocouples are shown in Figure 3-8.

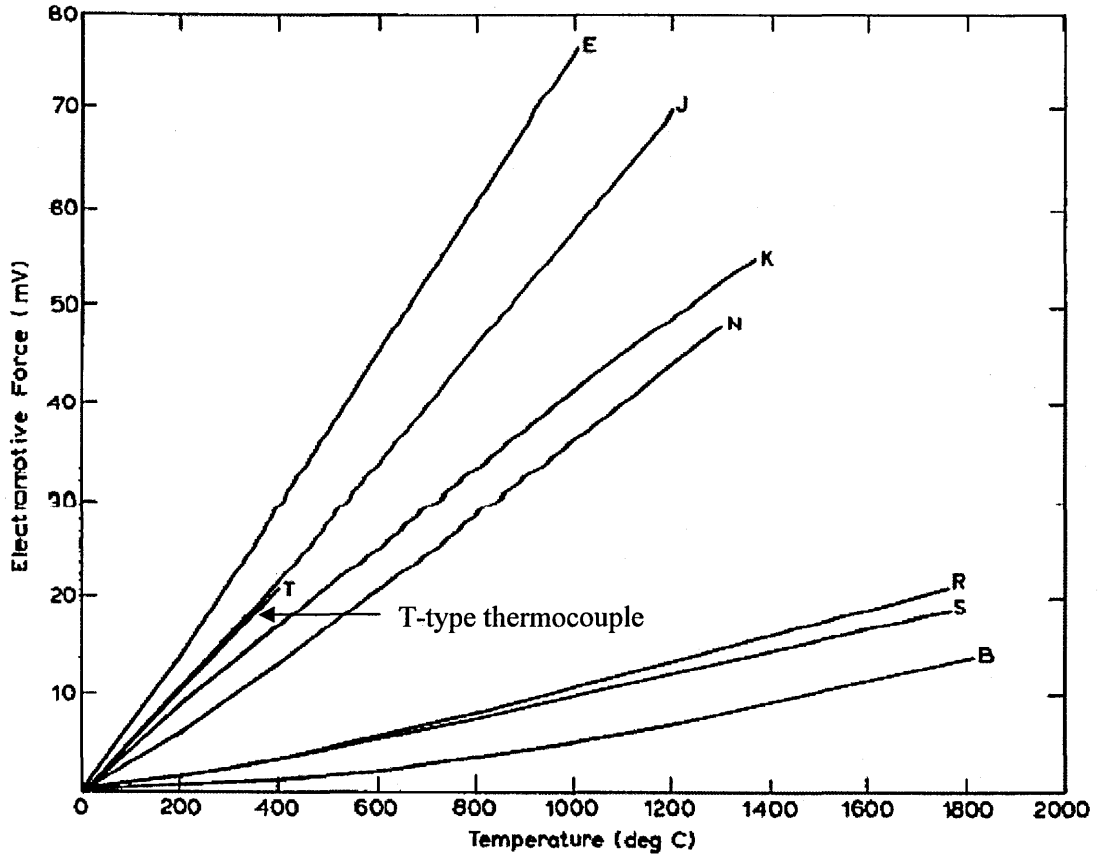

Figure 3-8. Voltage versus temperature for common thermocouples [71]

Calibrating Thermocouples

All thermocouples used for measurement were calibrated using a purposely made system. The system consisted of a glass jar with a plastic lid. The thermocouples were placed in 1 mm diameter holes drilled in the plastic lid of the glass jar filled with water. With thermocouples in the jar the transient temperature data were measured and recorded, Figure 3-9 shows the results.

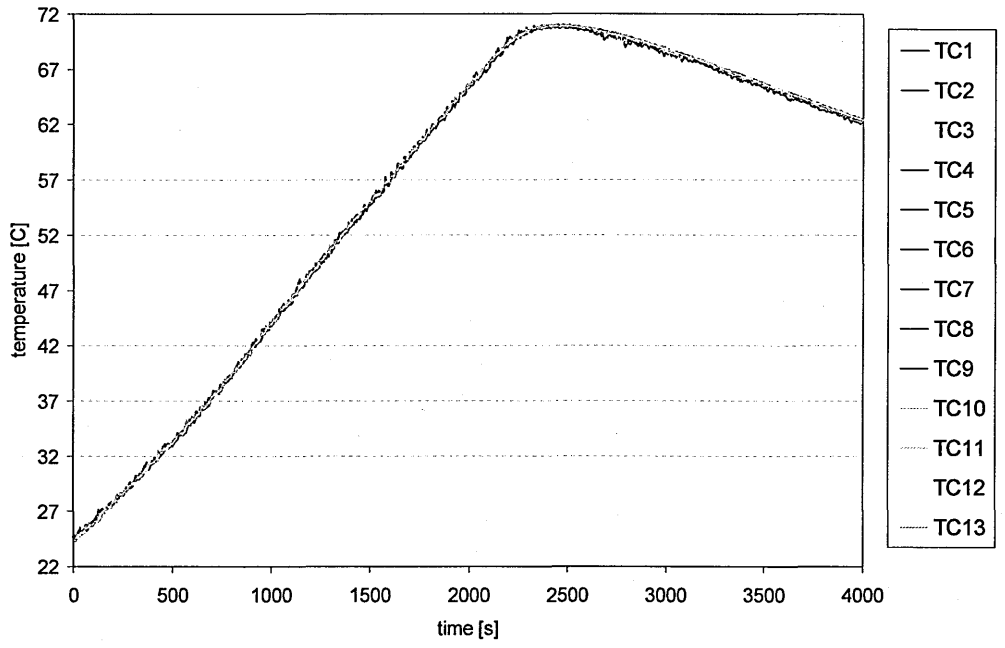

Figure 3-9. Thermocouples calibration data

The maximum difference between adjacent thermocouples is shown in Table 3-6. The maximum error is 0.38°C between thermocouples TC3 and TC4.

Thermocouples	TC1-TC2	TC2-TC3	TC3-TC4	TC4-TC5	TC5-TC6	TC6-TC7
Temperature Difference [°C]	0.29	0.09	0.22	0.06	0.28	0.15
Thermocouples	TC7-TC8	TC8-TC9	TC9-TC10	TC10-C11	TC11-C12	TC12-C13
Temperature Difference [°C]	0.35	0.10	0.38 (max)	0.03	0.34	0.21

Table 3-6. The maximum error in thermocouples

3.3.6 Test Procedure

The two steel blocks were bolted together with an 8 mm high tensile steel bolt (AISI 4000) placed through their centre. The hole in the lower block 'Z' was 1 mm bigger in diameter than the bolt's diameter to allow for thermal expansion. The 'blind' tapped hole in the upper blocks 'X' and 'Y' was 40 mm deep.

A measured torque was applied to the bolt using a torque wrench and the corresponding contact pressure was found experimentally using a pressure transducer (see Appendix B). It was found that torques of 25 Nm, 50 Nm and 75 Nm correspond to 5.64 MPa, 10 MPa and 14.12 MPa contact pressures respectively, see Appendix B for detail.

The assembly was placed on top of another steel block that was surrounded by constant flowing water in a plastic container. The water was allowed to flow continuously at a slow flow-rate throughout the tests using an inlet pipe securely attached to the plastic container and an outlet hole to prevent overflow, see Figure 3-3.

Heat was applied on the top surface of the upper specimens 'X' and 'Y' by means of a hotplate with the rest of the assembly exposed to surrounding ambient temperature conditions. Heat was conducted through the upper block across the interface and through the lower block.

At the end of the top specimen an insulating board was attached securely to prevent the heat from escaping sideways onto the specimen. A 60x60 mm cut-away hole was created on the insulating board so the upper specimen would fit tightly. This insulating board ensured minimal convection around the edges at the end of the upper specimen. The hot-plate was cleaned with high performance lubricant, and a layer of thermal grease was applied in between the hot-plate and the solid to ensure good surface contact with no air pockets between the hot-plate and the assembly.

All experiments were prepared and setup the day before and left all night that is for at least twelve hours to thermally settle down. This period ensured that the assembly was at steady-state under ambient conditions before the tests were conducted. Experiments were conducted in an environment free of human presence or other activities. During the heating, the temperature profile followed an increasing exponential (Eq. 26 in Chapter 2) until it reached steady-state condition, see Figure 3-11.

$$T(t) = 1 - e^{-xt}$$

After steady-state condition was reached, the hotplate was switched off. During the cooling period the temperature profile followed decreasing exponential response (Eq. 25 in Chapter 2), see Figure 3-11:

$$T(t) = e^{-xt}$$

T-type thermocouples (manufacturer omega, temperature range -270°C to 400°C, tolerance value ±0.2°C, ϕ 1 mm Teflon insulation) were placed in each specimen in holes 10 mm deep and 15 mm apart from each other along the longitudinal axis of the specimen. TC55 in the upper specimen and TC65 in the lower specimen were each

placed 5 mm away from the interface. Aluminium foil was wrapped around thermocouples near the tip in order to prevent them from moving, see Figure 3-10.

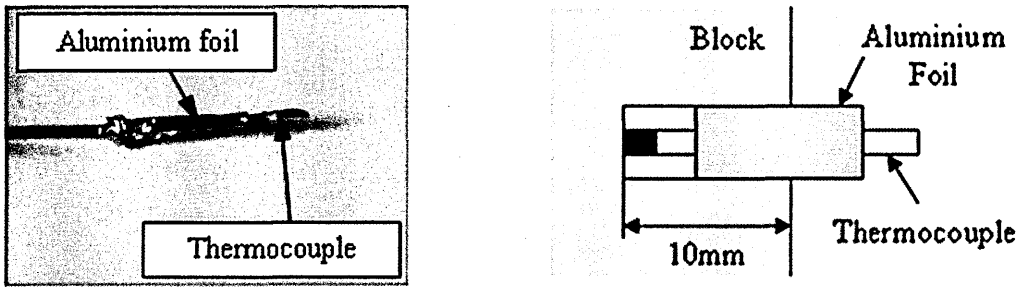

Figure 3-10. Preparation and insertion of thermocouples

One thermocouple was used to monitor the ambient temperature placed not far from the setup, and two thermocouples were used to monitor the inlet and outlet water temperature.

A software user interface was created using LabView V-7.0. Transient temperatures were monitored and written to a data file every five seconds for each thermocouple using a NI PCI-4351 data acquisition board controlled by a computer. After a specific time thermal equilibrium was reached, in other words temperature readings changed no further. Although steady-state was reached at about 6000s, the tests were left to run longer to ensure perfect thermal equilibrium before data processing. Thirty data points were recorded prior to applying heat. The hotplate was switched on and left running for about four hours. One thousand data points were averaged out at steady-state and the values used to plot the temperature profile, calculate the temperature drop and corresponding TCR, see Figure 3-11.

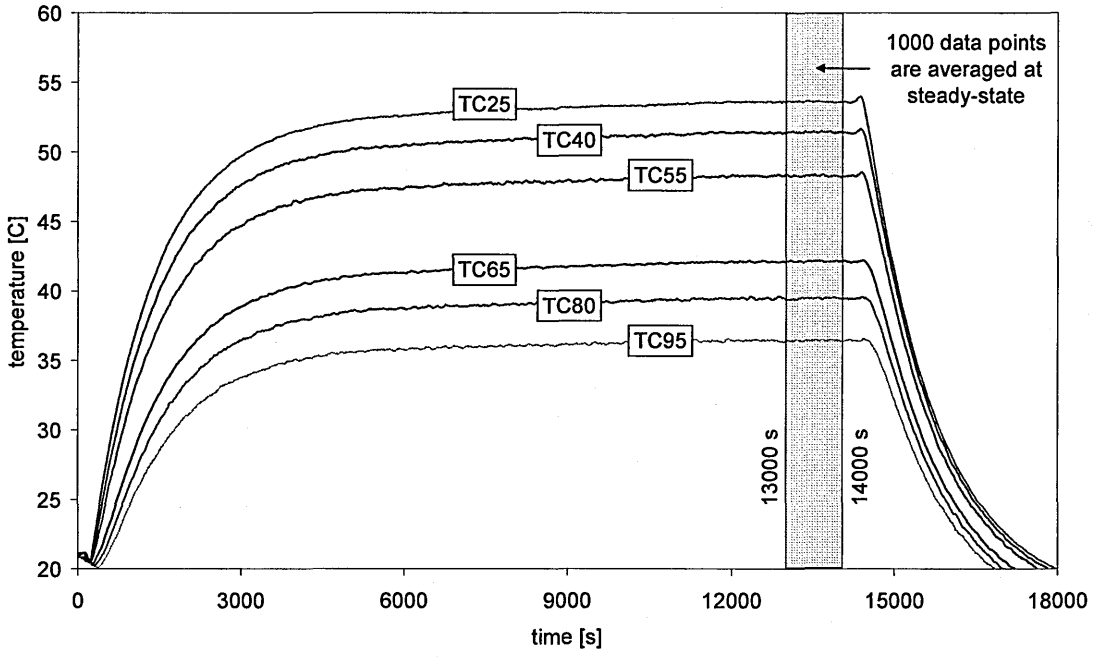

Figure 3-11. Temperature histories for a typical test

3.3.7 Data Processing

A software user interface using LabView® V-7.0 was designed and built in order to control the time and the amount of data captured. Raw data for each thermocouple was collected and written to a Microsoft® Office Excel spreadsheet for manipulation and analysis.

The original temperature signal comprises of the signal and the noise with a peak-to-valley of around 0.3°C. In order to discard the noise in the measuring signal, the least-square fit was applied to the original temperature signal. One thousand data points were averaged out at the steady-state and the mean temperature value used to calculate the temperature drop and the corresponding TCR at the interface see Figure 3-12.

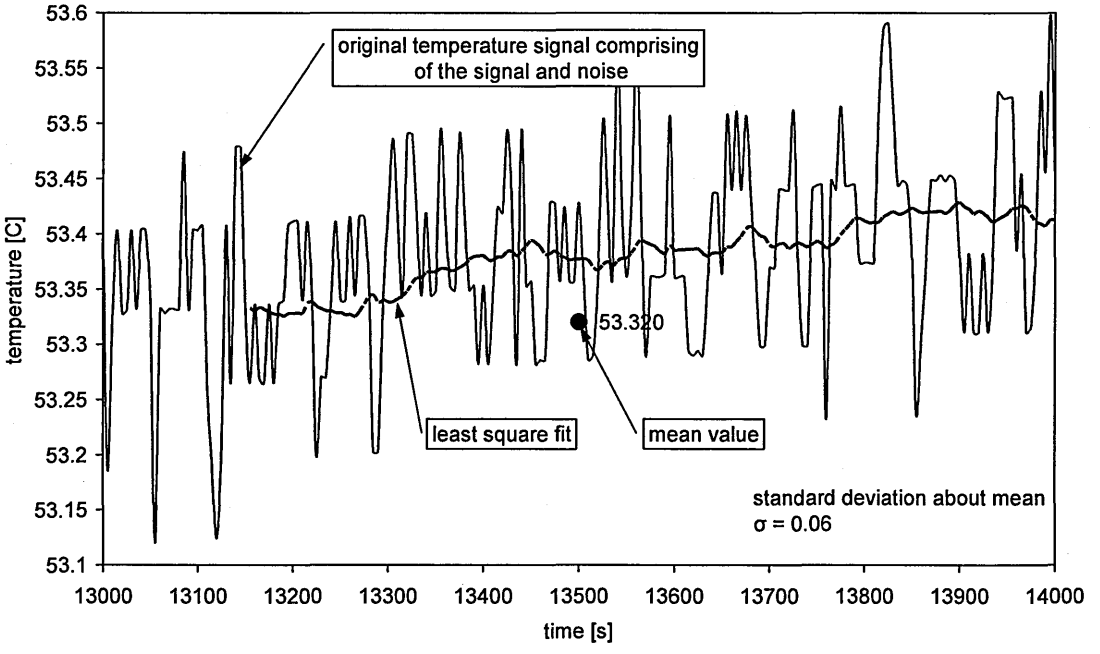

Figure 3-12. Original temperature signal at steady-state, corresponding least-square fit, mean value and standard deviation

From theory of heat transfer explained in Chapter 2, the thermal contact conductance is defined as:

$$h = \frac{q}{\Delta T} \qquad \text{Eq. 127}$$

Where q is the axial heat flux through the interface, ΔT is the temperature drop across the interface. The heat flux across the interface is found by averaging the heat flux q_1 and q_2 through the upper and lower specimen respectively:

$$q = \frac{q_1 + q_2}{2} \qquad \text{Eq. 128}$$

Since the material properties of the specimen are known the heat flux q_1 and q_2 are obtained directly from the measured least square fits of the temperature along each specimen:

$$q_1 = \frac{Q_1}{A_1} = -k_1 (\frac{dT}{dx})_1 = -k_1 \lambda_1 \qquad \text{Eq. 129}$$

$$q_2 = \frac{Q_2}{A_2} = -k_2(\frac{dT}{dx})_2 = -k_2\lambda_2$$ Eq. 130

Where Q1 and Q2 are heat flow through upper and lower specimen respectively, A_1 and A_2 are the cross sectional areas through which heat flows of the upper and lower specimen respectively, λ_1 and λ_2 are least-square fitted temperature gradients found from the measured thermocouple temperatures.

Least square is a mathematical technique for estimating the true value of some quantity based on a consideration of errors in observations or measurements, in this case temperature. The method works by attempting to find a function which closely approximates the deviation of data from the best-fit line, R^2.

The temperatures of the upper and lower contact surfaces T_u and T_l respectively are obtained by extrapolating the temperature profiles of each contacting specimen to the interface with the temperature gradient, λ. The temperature drop across the interface ΔT is the difference between T_u and T_l representing the temperatures at the interface in the upper and the lower specimen respectively see Figure 3-13.

$$\Delta T = T_u - T_l$$ Eq. 131

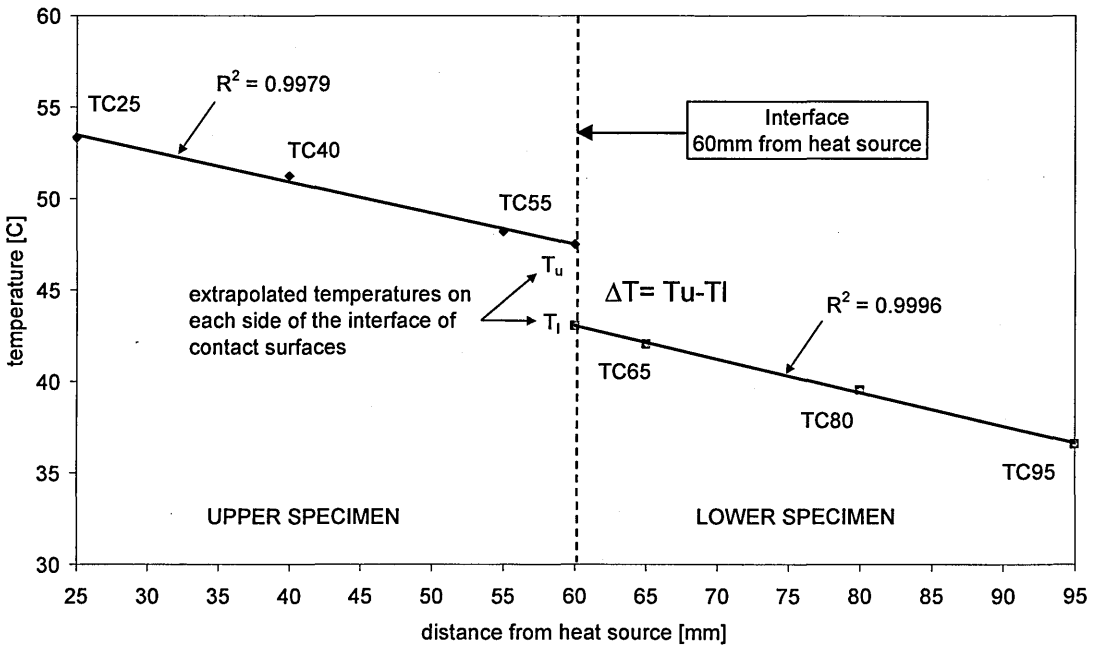

Figure 3-13. Experimental method for measuring temperature drop across interface

3.4 Three Block Analysis

This set of tests comprises of a nominally flat cubical steel block (40x40x40 mm) and two steel blocks (90x15x40 mm) in static contact, held together using two 8 mm diameter high tensile steel bolt placed at specific locations. The purpose of this experimental investigation is to measure the temperature gradients along the individual blocks, temperature drop at two interfaces and the thermal deformation of the assembly. The deformation measurement is achieved by having three blocks in contact forming two joint interfaces. A diagram showing the model of experimental process is shown in Figure 3-2 (after Montgomery [123]).

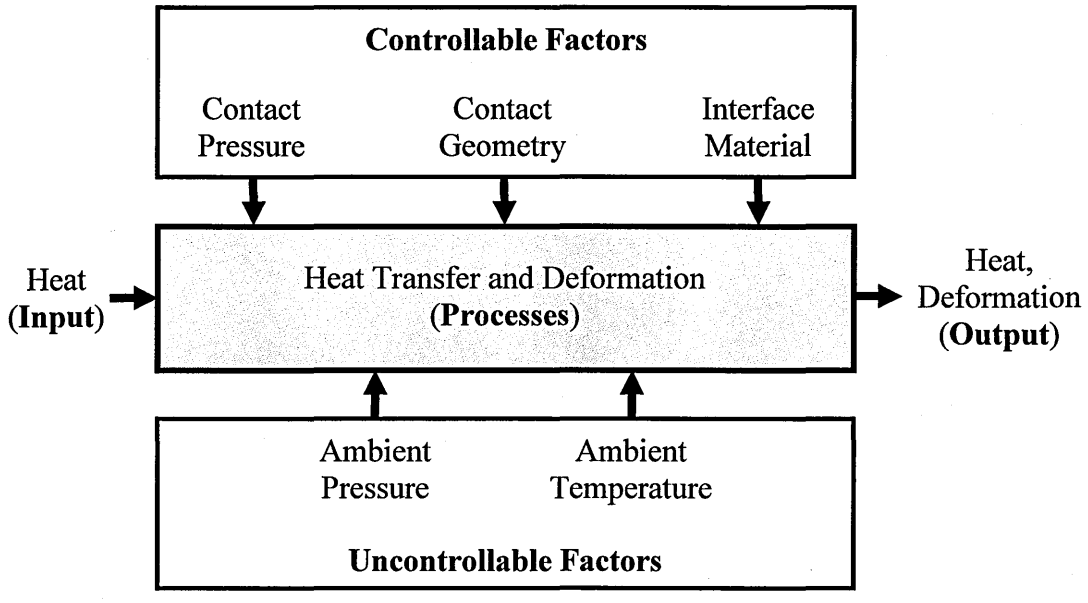

Figure 3-14. Model of experimental process for three blocks analysis (after Montgomery [123])

3.4.1 Experimental Design

A number of experiments were conducted to assess the validity of the finite element methods for predicting thermal deformation of a bolted test structure. All experiments were performed on steel under surrounding ambient air at room temperature. Interface geometry reduced the contact area at interface as explained in Section 4.3. Reduction in contact area influences heat transfer across the interface. The influence of contact area and it's location from the heat source on thermal deformation is not known. The following tests tend to investigate this phenomenon. The factors considered as being

most influential and applicable are considered here. Three design factors and their levels were considered as follows:

1. *Contact pressure* as for two block analysis, the contact pressure was varied. Two levels of contact pressure were considered for analysis: 5.64 MPa and 10 MPa.
2. *Interface geometry* was another factor used in experimental design. Three different arrangements were considered:

a. A nominally flat slotted steel block was placed between two nominally flat steel plates. The slotted surface was placed in contact with the top plate, see Figure 3-15.

b. A same nominally flat slotted steel block was placed between two nominally flat steel plates. The slotted surface was placed in contact with the bottom plate, see Figure 3-16.

c. A nominally flat steel block was placed between two nominally flat steel plates, see Figure 3-17.

3. *Interfacial material* - two different interfacial materials were considered: air and thermal grease, properties of which are given in Table 3-3.

The experiment system consists of:

- Three steel blocks bolted together using two 8 mm diameter high tensile steel bolts placed at specific locations
- A hotplate to supply heat from the bottom
- A support steel plate (90x20x40 mm) placed on top of the hotplate
- An insulating board placed on top of the hotplate to prevent heat escaping sideways. A cutaway hole (90x20x40 mm) was created in the centre to accommodate the support plate.
- Thirteen T-type thermocouples for temperature measurement, and
- Three non-contact displacement transducers for deformation measurement

A picture showing the setup slotted block in contact with upper block is shown in Figure 3-18.

3.4.2 Experimental Setup

a. Slotted Block in Contact with Upper Block

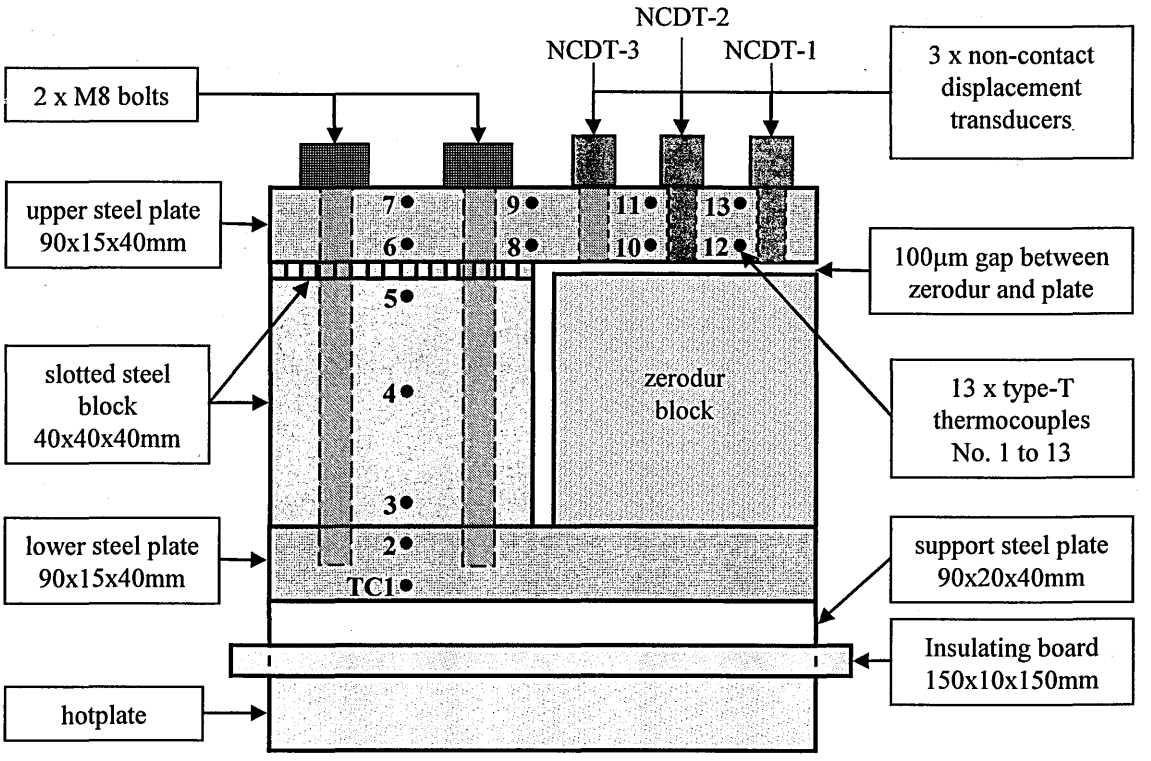

Figure 3-15. Experimental setup (slotted block in contact with upper block)

Test	Blocks in contact	Contact pressure [MPa]	Interface material
E1	Slotted block in contact with upper block	5.64	Air
E2		10	
E3		5.64	Grease
E4		10	

Table 3-7. Experimental design (slotted block in contact with upper block)

b. Slotted Block in Contact with Lower Block

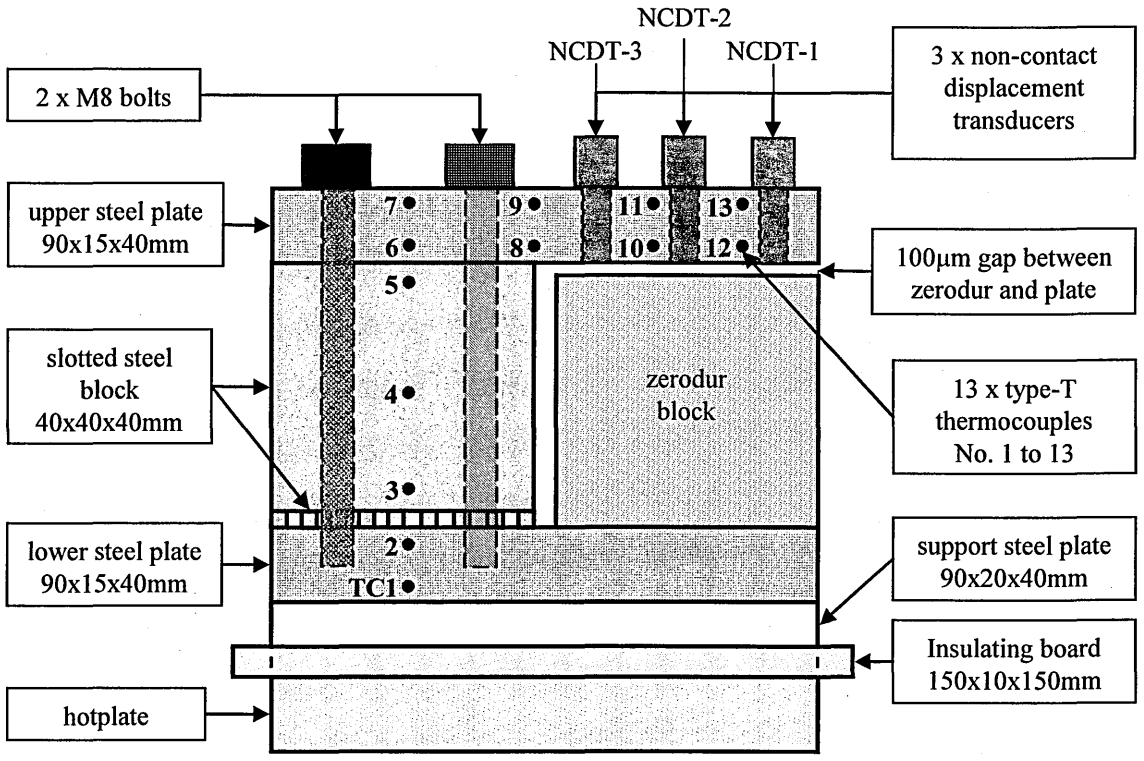

Figure 3-16. Experimental setup (slotted block in contact with lower block)

Test	Blocks in contact	Contact pressure [MPa]	Interface material
F1	Slotted block in contact with lower block	5.64	Air
F2		10	
F3		5.64	Grease
F4		10	

Table 3-8. Experimental design (slotted block in contact with lower block)

c. Flat Block

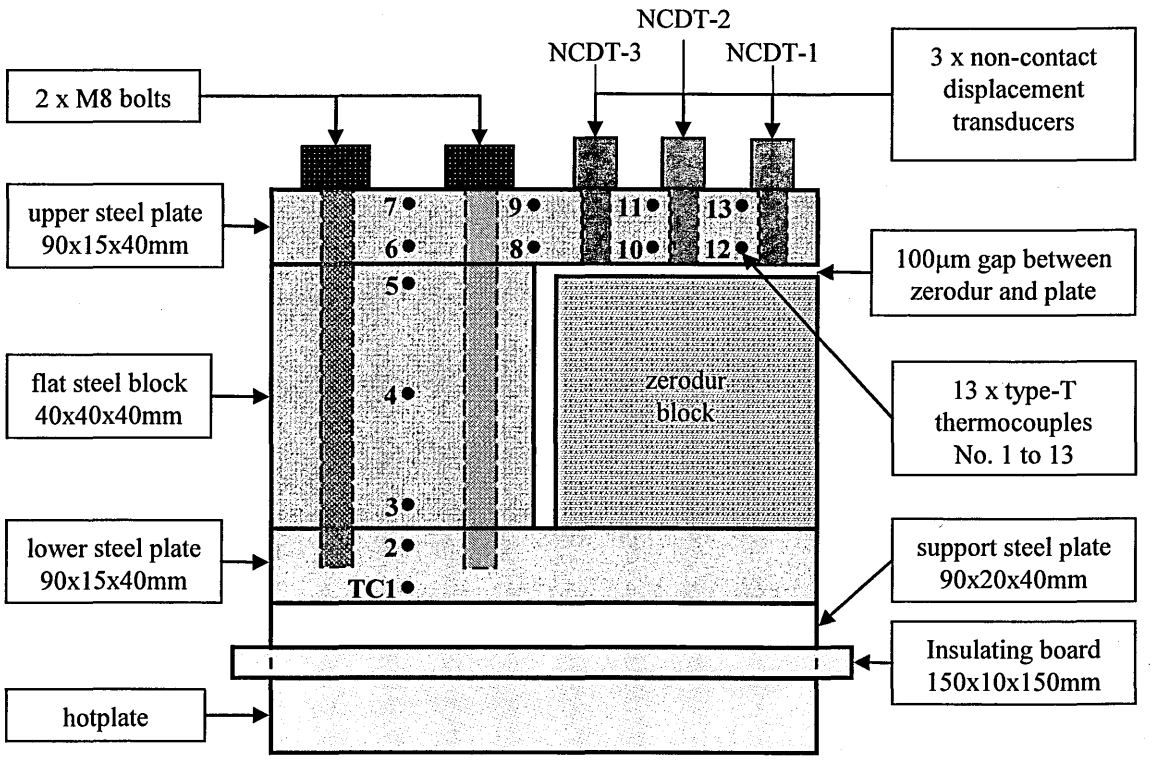

Figure 3-17. Experimental setup (flat block in contact with lower and upper blocks)

Test	Blocks in contact	Contact pressure [MPa]	Interface material
G1	Flat block	5.64	Air
G2		10	
G3		5.64	Grease
G4		10	

Table 3-9. Experimental design (flat block)

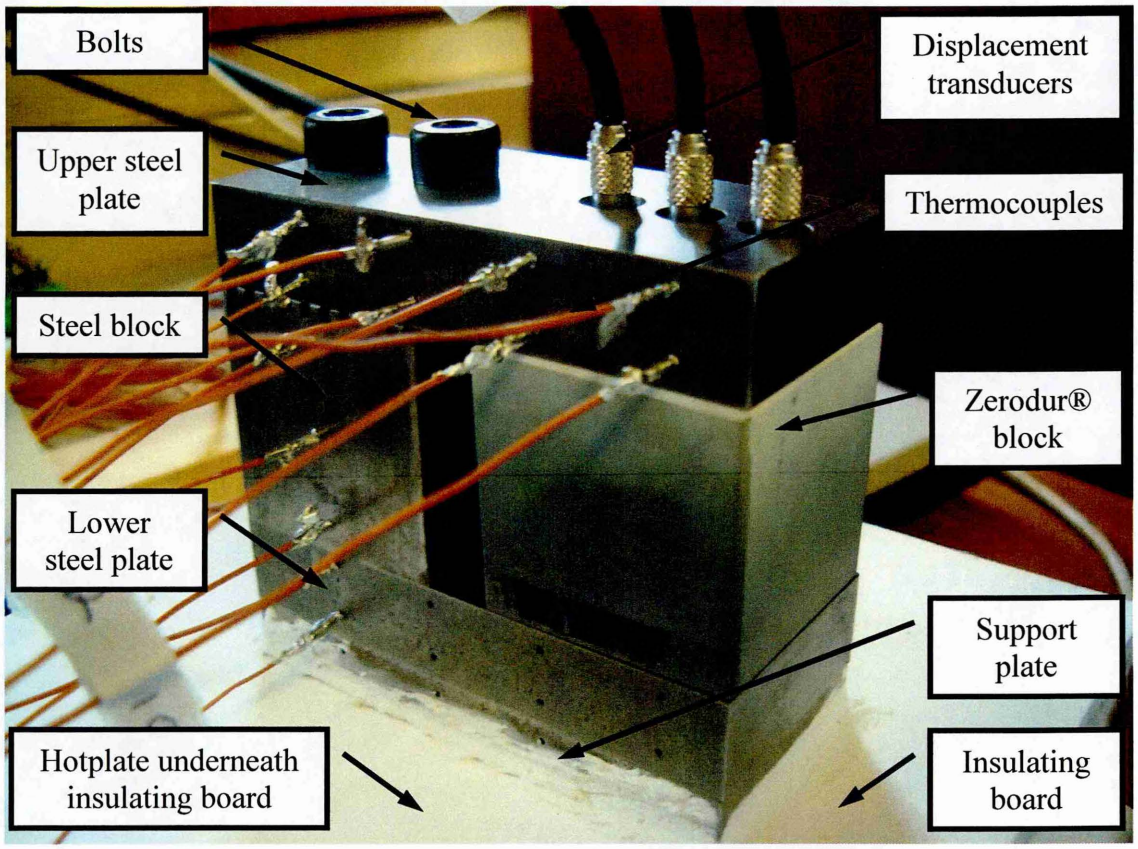

Figure 3-18. Picture showing slotted block in contact with upper block

3.4.3 Test Blocks

The test blocks are made from steel (AISI 1213). These blocks were cut from the same square piece and machined to their specified dimensions. Each block had holes of 1 mm in diameter and 10 mm deep, drilled in one of the faces to accommodate the thermocouples. The upper block had three identical 'housings' precisely machined to accommodate non-contact displacement transducers (hereafter referred to as NCDT's). Upper, lower and the flat blocks had nominally flat contact surfaces. Slotted block had nominally flat contact surfaces including 2 mm deep by 2 mm wide slots on one surface see Figure 3-19.

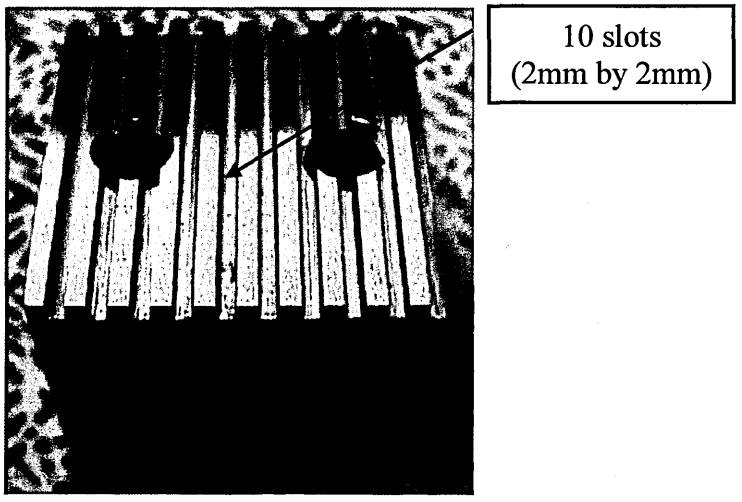

Figure 3-19. Slotted steel block used in three blocks analysis

The profiles of contacting surfaces were measured using a Form Talysurf 120-L stylus profilometer, see Table 4-2 for specifications. The output of profile measurement as a function of sample is recorded to evaluate the surface characteristics. Surface topography parameters are shown in Table 3-10.

Part	Surface	Surface roughness R_a [μm]	Max. peak to valley height Rt [μm]	Surface form error Pt [μm]
flat block	upper surface	0.1452	1.7420	0.9362
	lower surface	0.2124	1.6606	0.9830
slotted block	upper surface	0.1452	1.7420	0.9362
	lower surface	0.2124	1.6606	0.9830
upper block	contact surface	0.1956	1.8231	0.8584
lower block	contact surface	0.1369	1.2476	0.8582

Table 3-10. Topography parameters of contacting surfaces for three blocks analysis

3.4.4 Test Procedure

The assembly comprises of a steel block (with slots or without) 40x40x40 mm and two steel blocks 90x40x15 mm. All three blocks were made from same steel (AISI 1213). The block were bolted together using two M8 high tensile steel bolts (AISI 4000). On the right hand side, a block made of glass ceramic Zerodur® (40x40x39.9 mm) was placed on top of the lower plate. Zerodur® it's known for having an extremely low thermal expansion coefficient and good dimensional stability, therefore the top surface of the Zerodur® block acts as a reference plane relative to NCDT's sensing surfaces, see Figure 3-20.

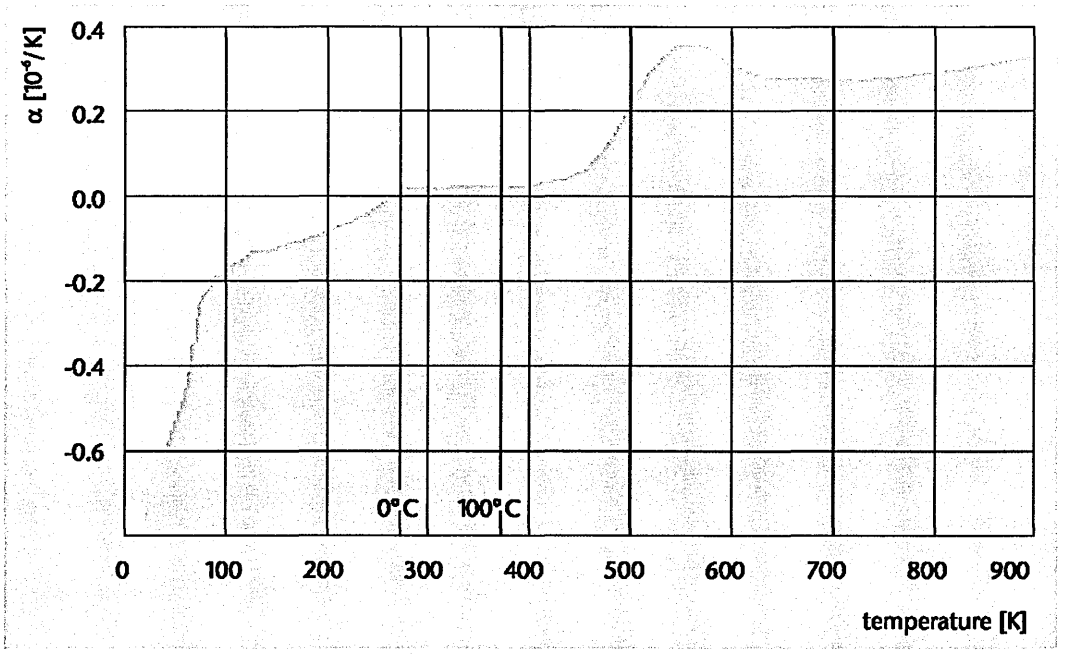

Figure 3-20. Linear thermal expansion coefficient of Zerodur® as a function of temperature [125]

At the end of the lower plate an insulating board was attached securely to prevent heat from escaping sideways onto the solid. A 90x40 mm cut-away hole was created on the board so the assembly would fit tightly. Thermal grease was placed around the edges of the insulating board to prevent heat escaping sideways. This insulating board ensured minimal convection around the edges.

In total thirteen T-type thermocouples were placed in holes 1.1 mm in diameter and 10 mm deep of which two were inserted in the bottom block, three in the middle block and eight in the top block. Dimensional distortion was measured using three NCDT's (manufacturer micro-epsilon S600-0.2, 6 mm in diameter, measuring range 200μm, resolution 8 nm) placed in holes accurately drilled in the upper block, see Figure 3-18 and Figure 3-22. NCDT's were arranged in such a way as to measure the vertical deformation and the bending of the assembly.

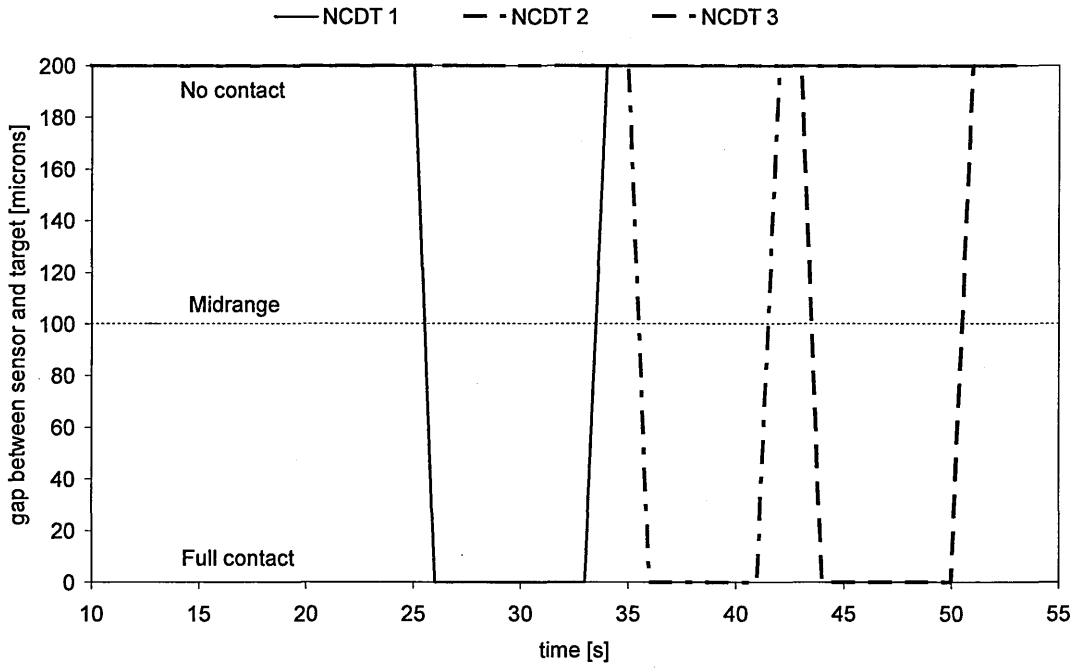

Figure 3-21. Full working range of NCDT's 200 microns

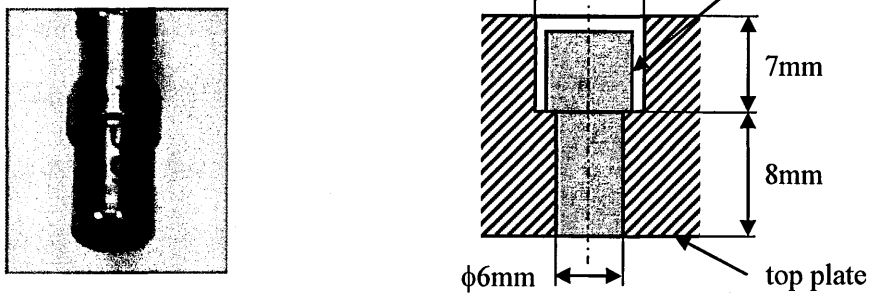

Figure 3-22. Non-contact displacement transducer and the housing

Top surface of Zerodur® block was coated with approximately 10μm thick aluminium film to ensure better response from transducers, see Figure. 3-23. This is because the NCDT's work best when the target surface is conductive.

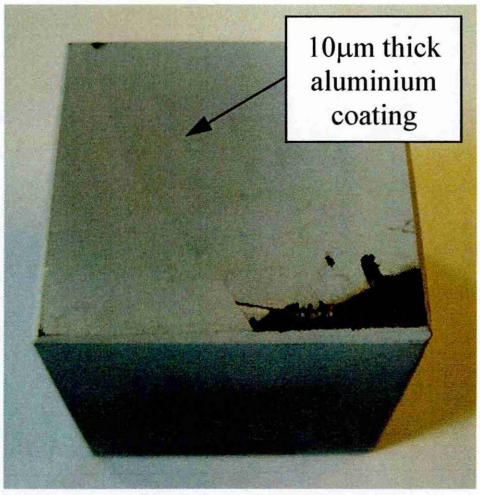

Figure. 3-23. Preparation of Zerodur® block

Heat was applied on the bottom surface of the lower plate using a hotplate, with the rest of the assembly exposed to ambient conditions. Thirty data points were recorded prior to applying heat. The hotplate was switched on and left running for about four hours. In the final stage the hotplate was switched off and left running for about an hour. Temperature and thermal distortion were monitored every five seconds using two data acquisition boards controlled by a computer see Figure 3-24 for measurement setup.

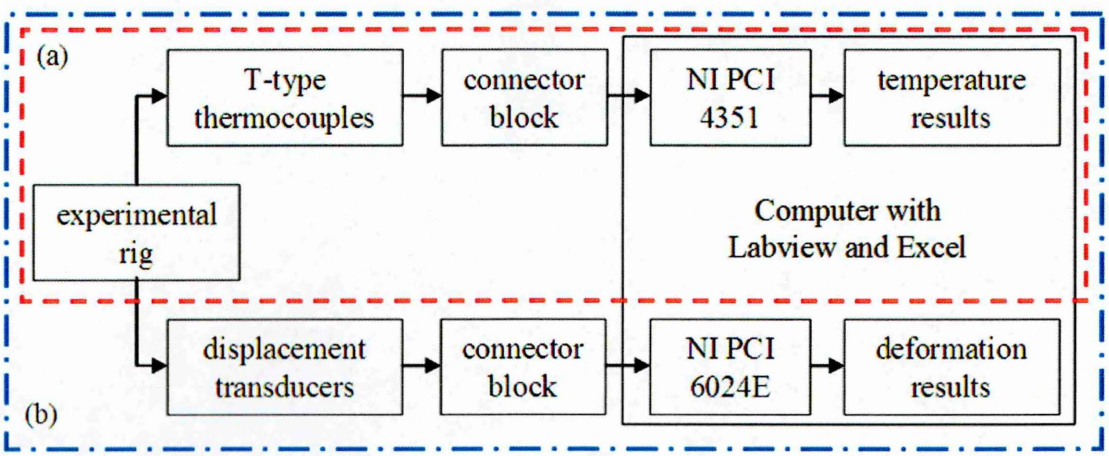

Figure 3-24. Measurement setup; (a) two block analysis, (b) three blocks analysis

All tests were prepared and setup the day before and left all night to thermally settle down. This meant that the assembly was at steady-state under ambient conditions before the tests were conducted the following day. Experiments were conducted in an environment free of human presence or other activities.

3.4.5 Calibration of Displacement Transducers

All three NCDT's were calibrated individually using a setup comprising of a Nanotech 350UPL diamond turning machine (manufacturer: Moore Nanotechnology Systems, 1 nm linear resolution, 25 nm position accuracy) and a magnetic base holder, see Figure 3-25. The machine's Z-axis was programmed to move 150 μm forward (towards) and backwards (away) from NCDT sensing surface, in steps of 5 μm with 5s pause between each step. The readings were captured and recorded after each step using a NCDT via a data acquisition card (NI PCI 6024E) connected to a computer.

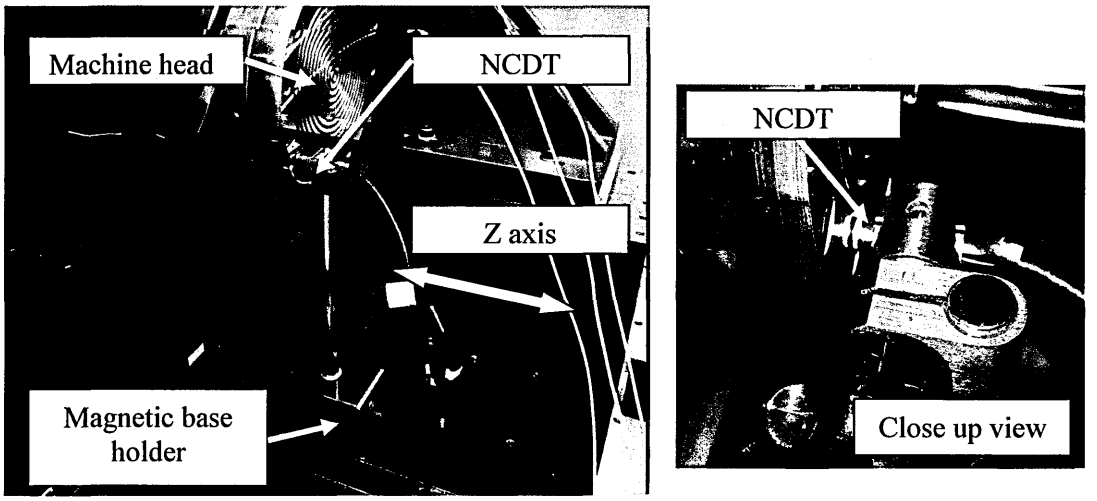

Figure 3-25. Experimental setup used for calibrating NCDT's

The original readings for each NCDT including the error between consecutive steps are plotted in three separate graphs Figure 3-26, Figure 3-27 and Figure 3-28, representing NCDT-1, NCDT-2 and NCDT-3 respectively.

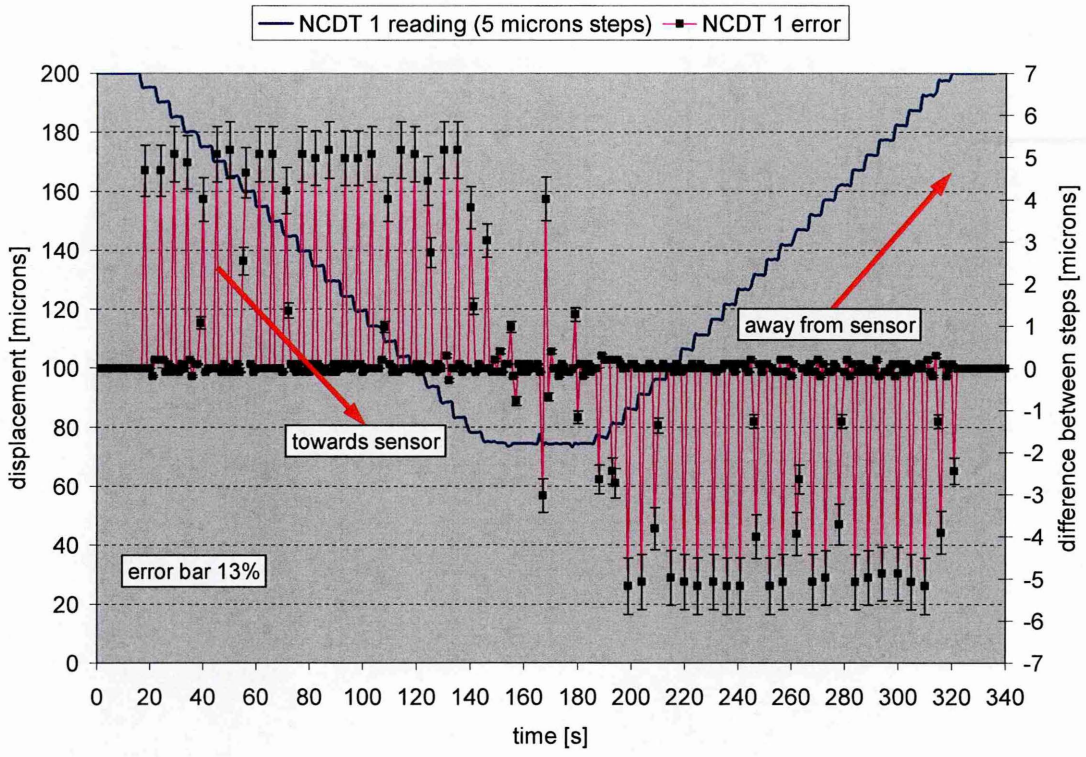

Figure 3-26. Calibration data for NCDT-1

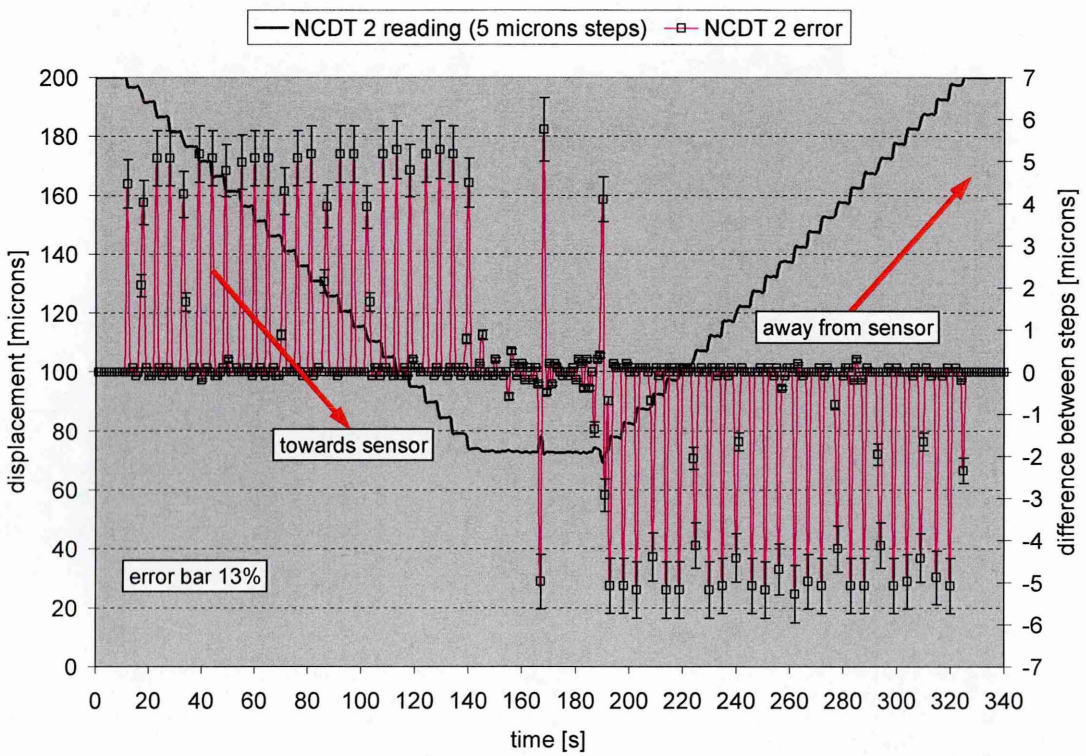

Figure 3-27. Calibration data for NCDT-2

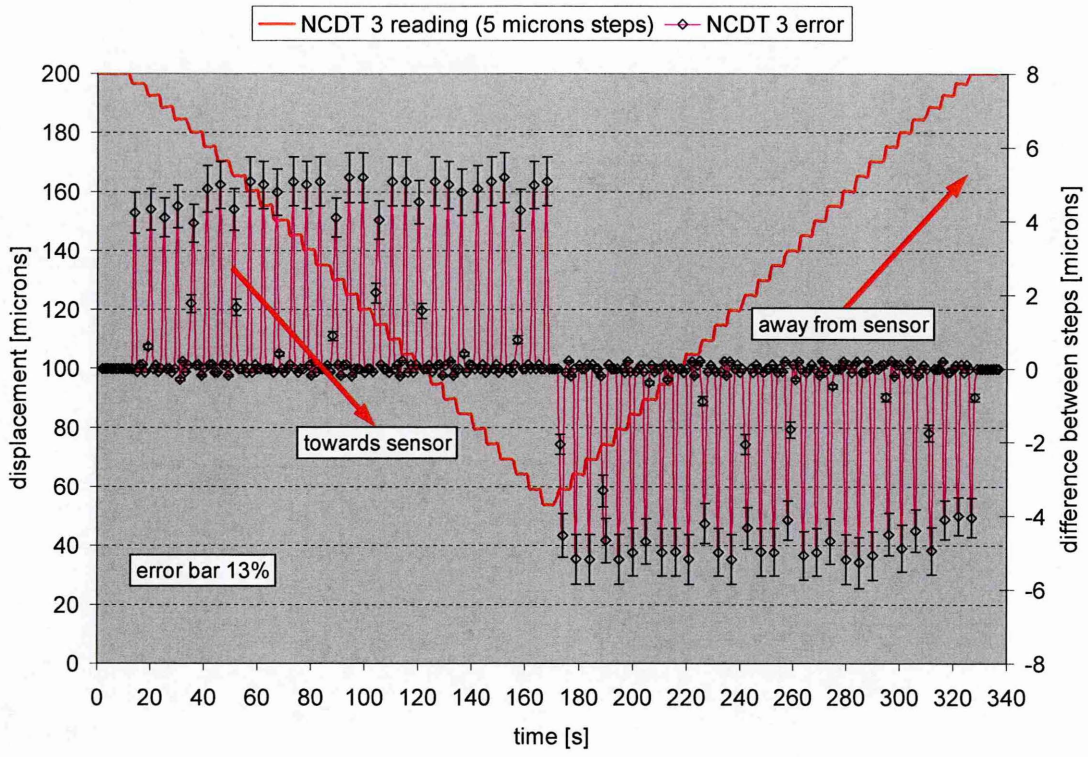

Figure 3-28. Calibration data for NCDT-3

The solid stepped lines represent the readings captured by NCDT's at each programmed machine step of 5 μm in the vertical direction. The lines with error bars represent the difference between each consecutive machine step of 5 μm. The maximum error is found to be around 13% for each NCDT.

3.5 Finite Element Analysis (FEA)

FEA is a numerical method used to model a wide range of physical phenomena. Numerical methods transform differential equations to a set of algebraic equations of a discrete model. Although some finite element features can be found in the work by Hrenikoff (1941) and Courant (1943) the recognition of the method is attributed to Turner, Clough, Martin and Toop (1956) and Argyris and Kesley (1960). Turner, et.al (1956) published a paper in which the stiffness and deflection of mechanical structures was presented. Since its origin the FEA has advanced tremendously. Initially the method was used in aerospace, automotive, defence and other specialist industries. Nowadays the method is used in most engineering industries including machine tools. With advancement in computer and software technology the FEA has become a benchmark in analysis of complex engineering problems [126].

This following section discusses the procedure undertaken for the thermal and deformation analysis of bolted metal bodies in contact, having different surface characteristics under varying contact pressures exposed to ambient conditions.

3.5.1 Finite Element Analysis Process

The geometric model is divided into a mesh of specified elements and nodes, allowing numerical iteration to solve the differential equations. The purpose of a FEA is to model the behaviour of a structure under a system of loads. In other words the analysis must be an accurate mathematical model of a physical prototype. The simulation model in general comprises of the nodes connected by vertices to form the elements, material properties, various constants (e.g., ambient temperature, acceleration due to gravity), boundary conditions, etc. In order to increase the accuracy of the results, all influencing factors were considered and determined whether their effects are considerable or negligible on the final result. In the simulations herein great care was taken to use appropriate heat transfer and structural elements, material properties, mesh generation boundary conditions and constrains.

In this research all modelling was carried out using a general multi-purpose finite element code called NX TMG thermal analysis, and model solution for thermal deformation analysis integrated in I-DEAS NX.

NX TMG thermal analysis software is a comprehensive heat transfer simulation package, which provides fast and accurate solutions to complex steady-state and transient thermal and structural problems. It uses advanced finite difference control volume technology that makes it easy to model nonlinear and transient heat transfer processes including conduction, convection and radiation. The software is capable of modelling the thermal and mechanical contact at the interface [127].

A combined pre and post-processing integrated into I-DEAS NX was used for formation of the models geometry and meshing. The software editor provides all the actions for the determination of analysis steps, output requests, and thermal and mechanical contacts surfaces, definition of elements and nodes, boundary conditions and thermal and mechanical loads. The detailed FEA scheme for two block analysis and three block analysis is depicted in Figure 3-29.

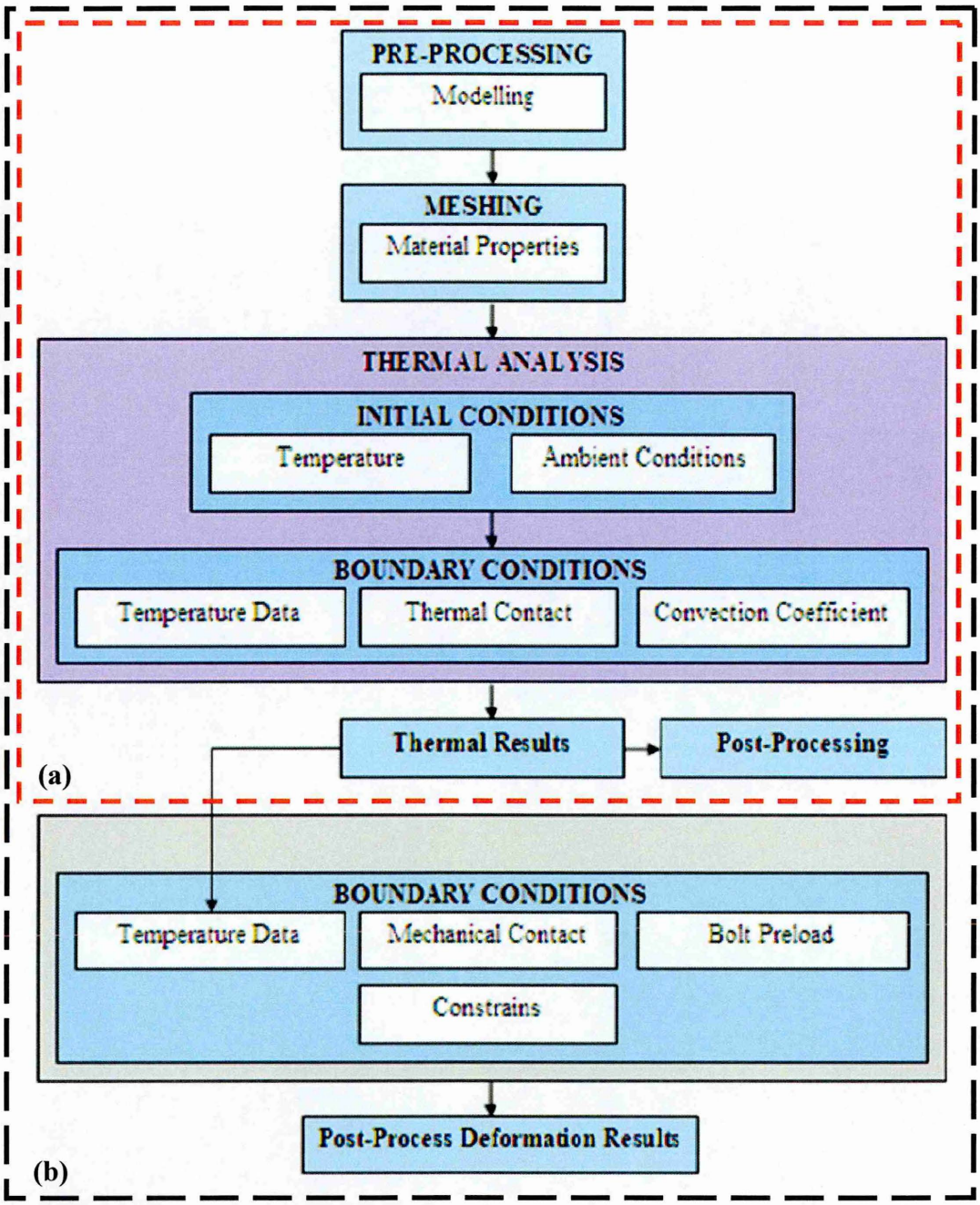

Figure 3-29. Detailed scheme of FEA procedure: (a) two block analysis, (b) three block analysis

Initially thermal analysis is conducted using NX TMG. The software calculates the nodal temperatures including thermal contact and convection heat transfer for two block analysis and three block analysis. Secondly the nodal temperature data from thermal solutions are used as boundary condition for thermal deformation in three block analysis. NX TMG uses a control volume formulation for the solution [127]. A calculation point is established at each element's centre of gravity, see Figure 3-30.

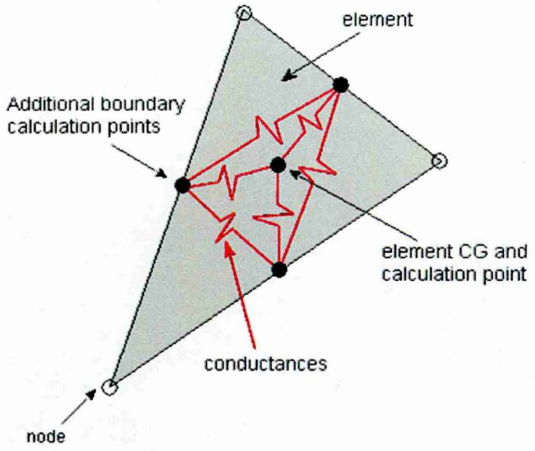

Figure 3-30. NX TMG solver uses the element centre of gravity as calculation point [127]

- For a three-dimensional element an additional calculation point is added at the midpoint of each two-dimensional face of the element.
- For a two-dimensional element an additional calculation point is added at the midpoint of each one-dimensional edge of the element.

a. 3D Modelling

The process of FEA begins with pre-processing, in other words modelling the geometry of individual steel blocks. After the blocks are modelled then an assembly is created. This way the boundary conditions or any interaction between the blocks such as thermal and mechanical contact can be defined [127].

b. Meshing

The meshing simulation task creates the thermal model's finite element mesh and defines associated material and physical properties. The element types supported by I-DEAS NX are shown in Figure 3-31. The topology of the elements is as follows [127]:

- *One-dimensional (1D beam)* – this type of element is significantly longer than its width or depth. The stiffness characteristics of beam element depend on the properties of its cross-section.
- *Two-dimensional (2D shell)* – this type of element is created on and associated with a surface. All elements on a surface are two-dimensional and each element shares two nodes with the neighbouring element. Heat is transferred in plane only and temperature is assumed constant across the thickness of the element.

- *Three-dimensional (3D solid)* – this type of element is created on and associated with a volume. All elements on a volume are three-dimensional and each element shares nodes with the neighbouring element. The number of shared nodes depends on the type of element used. Heat is transferred in plane only and temperature is assumed constant across the thickness of the element.

Type	Topology	Nodal DOF		Properties			
		Trans.	Rot.	Physical	Material	Cross Section	Assoc. Data
3D Solid	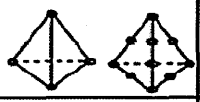	3	0	formulation (default)	-isotropic -orthotropic -anisotropic	N/A	material orientation
2D Shell	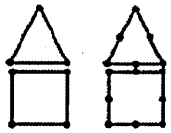	3	2 or 3	thickness	-isotropic -orthotropic -laminate	N/A	material orientation
1D Beam		3	3	nonstructural mass	isotropic	required	beam geometric data

Figure 3-31. Element types supported by I-DEAS [127]

The above elements can be used individually or in combination as and when appropriate. For the simulations conducted in this research, all three types of elements were used. Solid elements were used to mesh the three-dimensional components, shell elements were used to mesh the outside surfaces of the components to account for convection, and beam elements were used to model the bolts.

The mesh is made up of elements connected by nodes. I-DEAS NX supports three types of solid meshing:

- *Free-meshing* capabilities are unrestricted. The software automatically builds the mesh according to the complexity of component's geometry. The software uses an algorithm to read the geometry and it specifies and generates an appropriate number and shape of elements. However the number and shape of elements can be

overridden by the user if need be. This method of meshing is the most flexible and is recommended when dealing with complex and unstructured geometries.

- *Mapped meshing* is limited on its usage. If the component being meshed has complex geometry and features within, then a direct mapped meshing can not be used. Partitioning lets you define two or more volumes through a component. The partitioning volumes become constituents of the components topology. Each resulting volume can then be meshed independently, and the elements will be aligned at the boundaries of the volumes, see Figure 3-32.

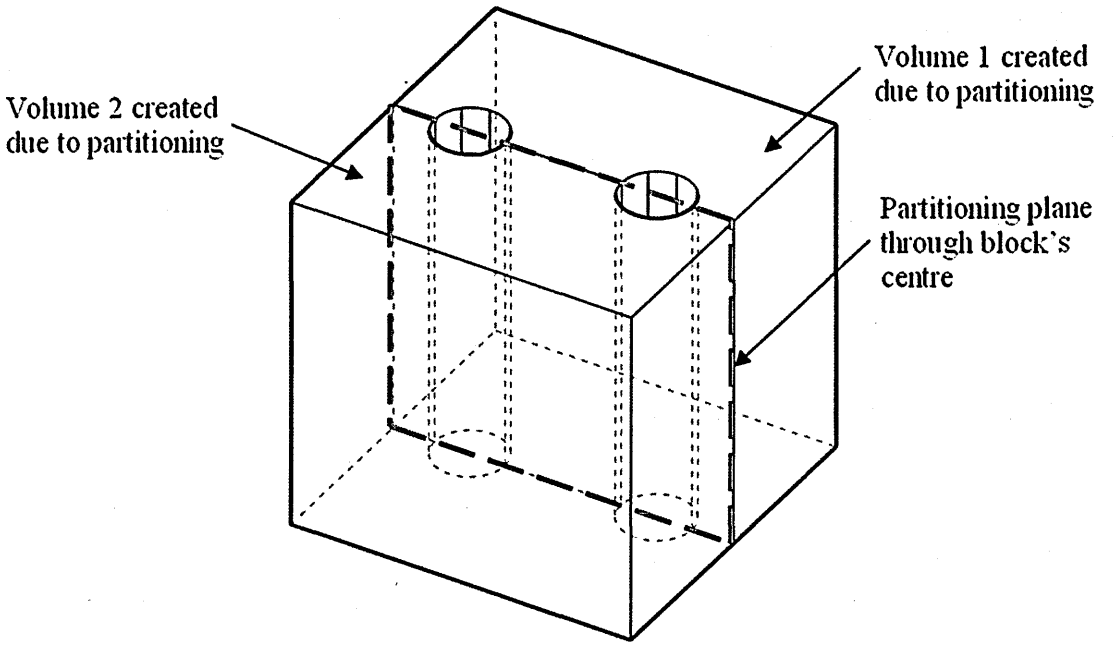

Figure 3-32. Component partitioning process for mapped meshing

The advantage of mapped meshing over free-meshing is that the element size and shape can be accurately defined and controlled by the user. This means that if mapped meshing is used the solution will be more accurate mainly due to the symmetry and alignment of elements.

- *Sweeping mapped meshing* works best when the geometry of the component is continuous with no interfering features over its entire length. A good example is the cylinder or the steel blocks used in this research. One of the surfaces of the block can be mapped meshed then the mesh can be swept along the entire length of the block allowing the user to define the number of elements, see Figure 3-33.

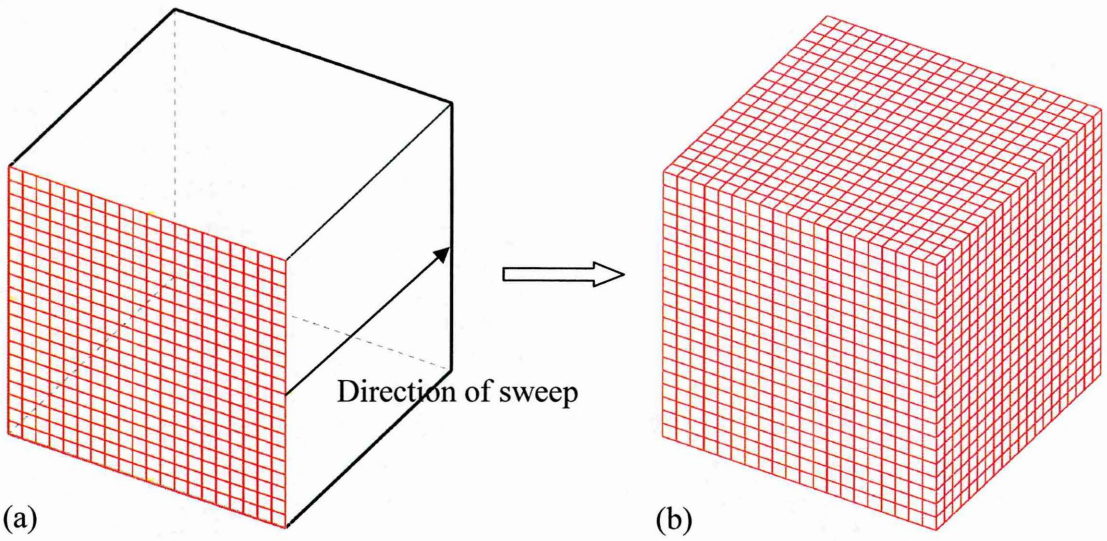

Figure 3-33. Sweeping mapped mesh; (a) mapped mesh is defined on a surface of the block, (b) final result after mesh is swiped

As mentioned above the size and shape of the element in FEA plays an important part on the accuracy of results. According to NAFEMS (National Agency for Finite Element Methods and Standards) [128] the ideal element shape is a square (1.0 x 1.0) and errors start to occur with any value below 1.0 as shown in Figure 3-34.

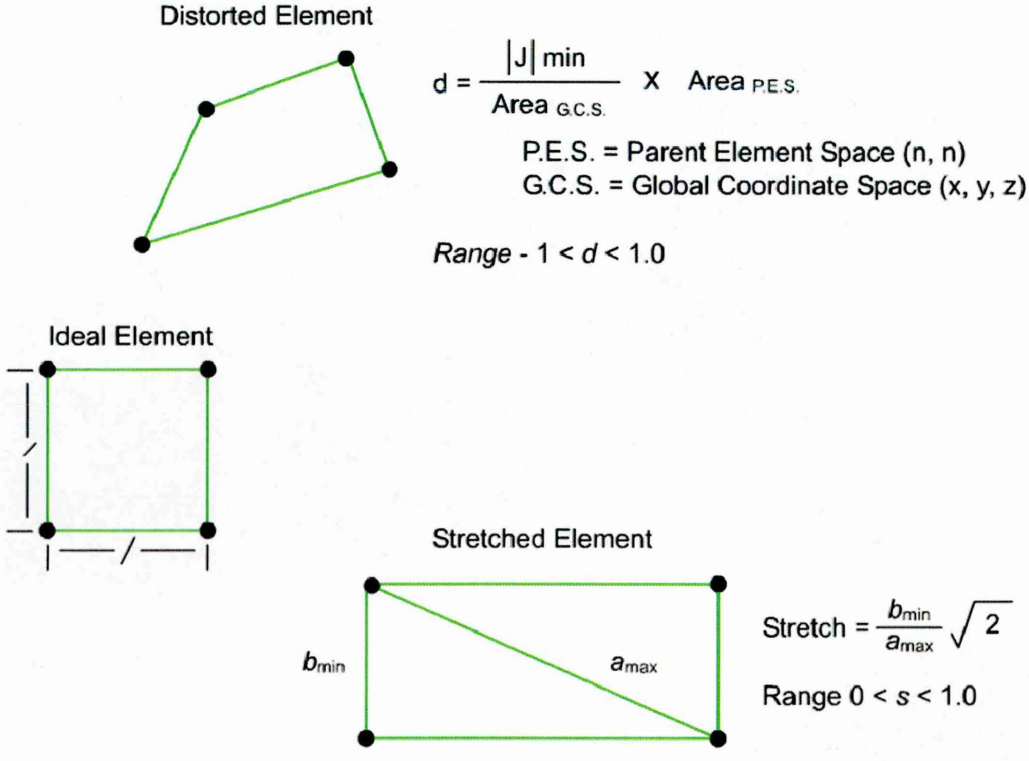

Figure 3-34. Ideal and distorted elements [127]

Guidelines for distortion and stretch criteria of 2D quadrilateral elements are as follows [128]:

- For critical regions distortion and stretch should be greater than or equal (≥) to 0.7.
- For general regions distortion and stretch should be greater than or equal (≥) to 0.3.
- Distortion less than or equal (≤) to 0 will generate an error.

The distortion and stretch of all elements generated in simulations have been checked for compliance with the above criteria and none have been found to disobedient, see Figure 3-35 and Figure 3-36. In the cumulative graph, the Y axis represents the total number of selected elements. The software uses this equation to calculate the cumulative function:

$$F(x_N) = \sum_{i=0}^{N} f(x_i)$$

Eq. 132

Where $f(x_i)$ is the number of element quality check values that fall in the bounds of the i^{th} interval. The explanation is as follows, see Figure 3-35:

- Line 1 indicates that 25% or 5671 elements of the total number of elements have qualities less than 0.97.
- Line 2 indicates that 50% or 11341 elements of the total number of elements have qualities less than 0.99, and
- Line 3 indicates that 75% or 17012 elements of the total number of elements have qualities less than 1.0.

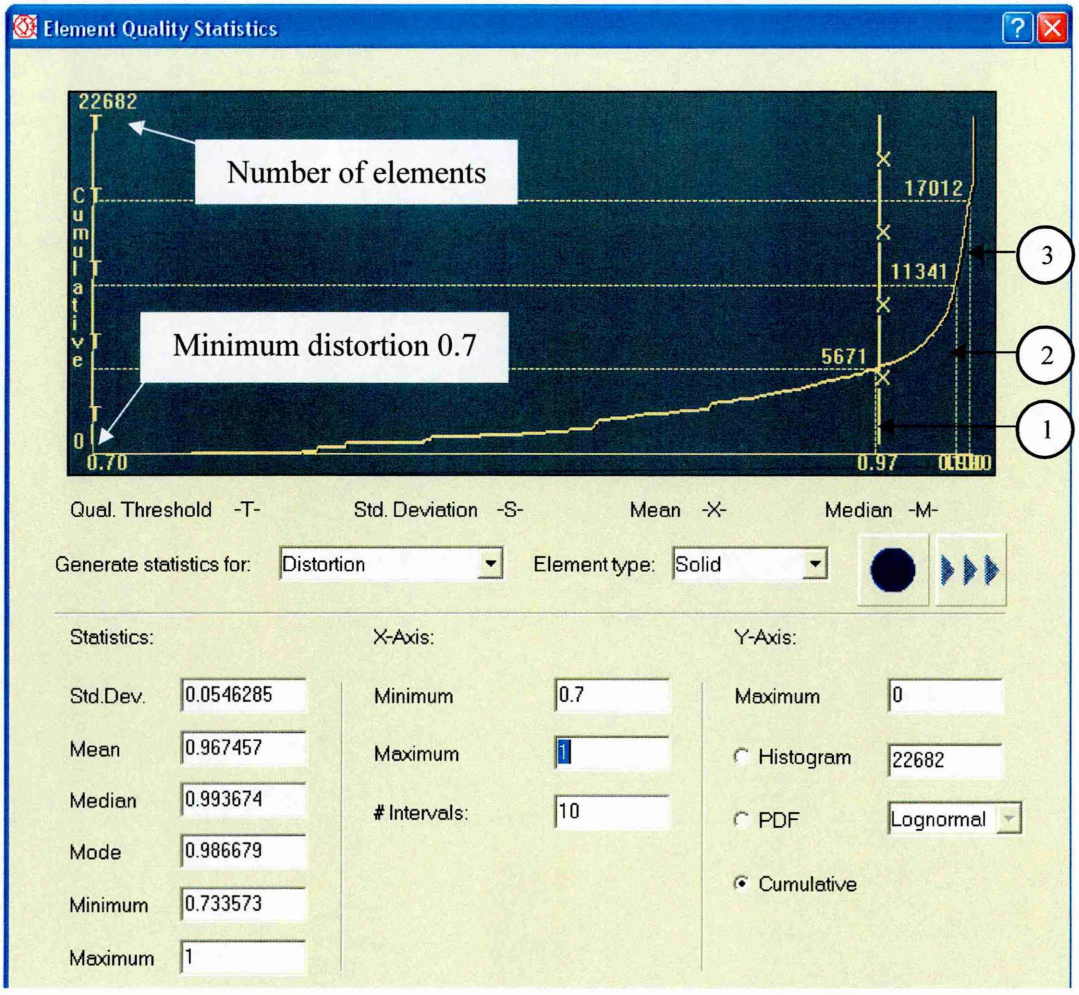

Figure 3-35. Element quality statistics, distortion analysis [127]

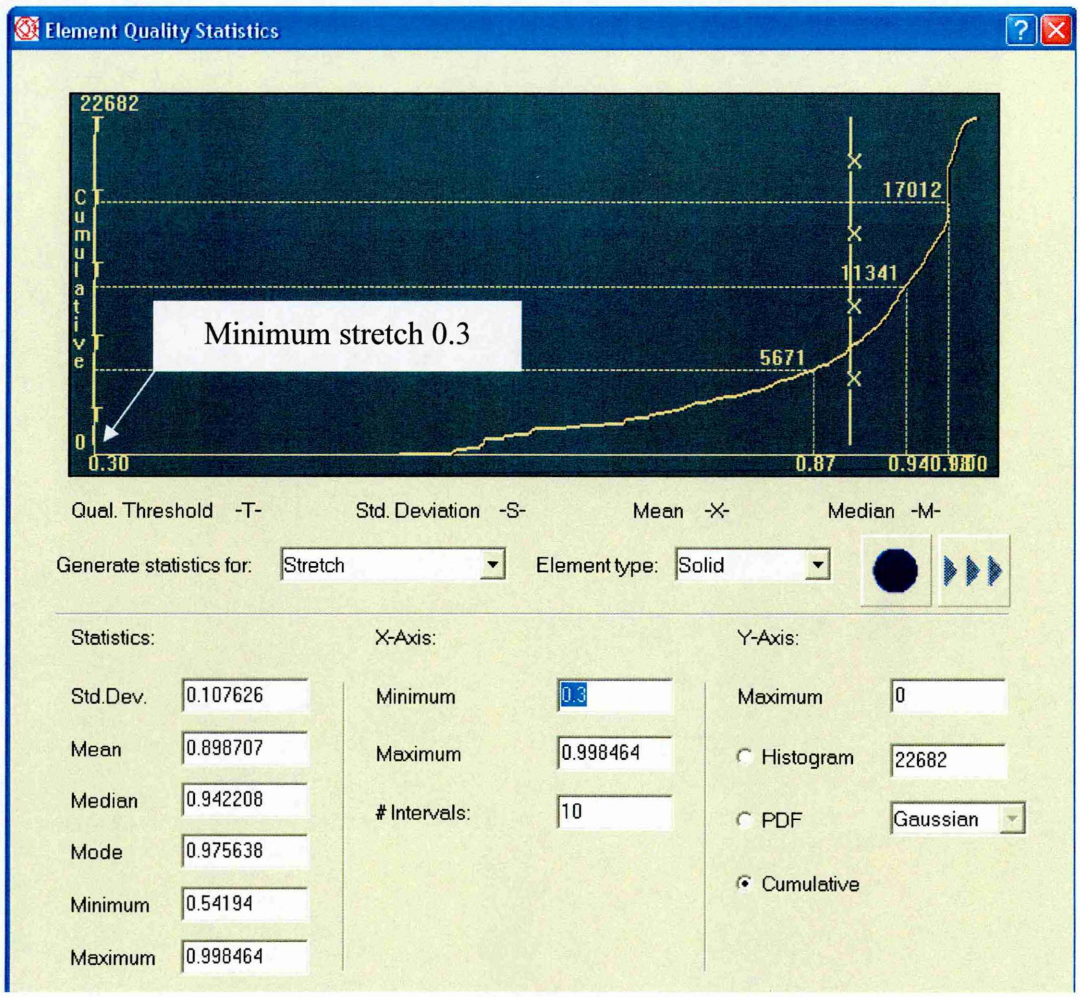

Figure 3-36. Element quality statistics, stretch analysis [127]

The accurate determination of local temperatures, for examined thermal contact necessitates careful attention in the choice of the mesh size. For this purpose a study consisting of choosing the appropriate mesh size is undertaken. An iteration approach is used to determine the minimum mesh size near the interface in order to achieve convergence. Four iterations were carried out until the convergence was achieved. It was found that the minimum mesh of size three was required, see Appendix C for detail. Meshing of the two experimental setups is shown in Figure 3-37, Figure 3-38 and Figure 3-39.

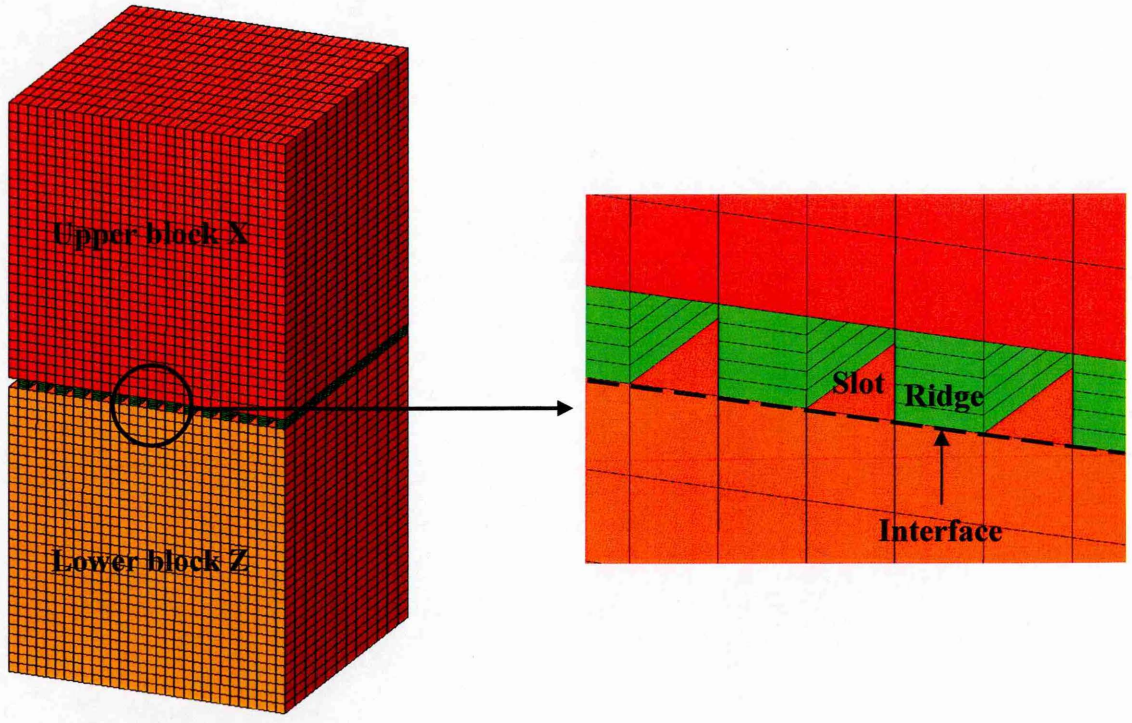

Figure 3-37. Meshed assembly block X (2 mm slots) in contact with block Z, representing tests A1 to A6 and C1 to C6 (22140 elements)

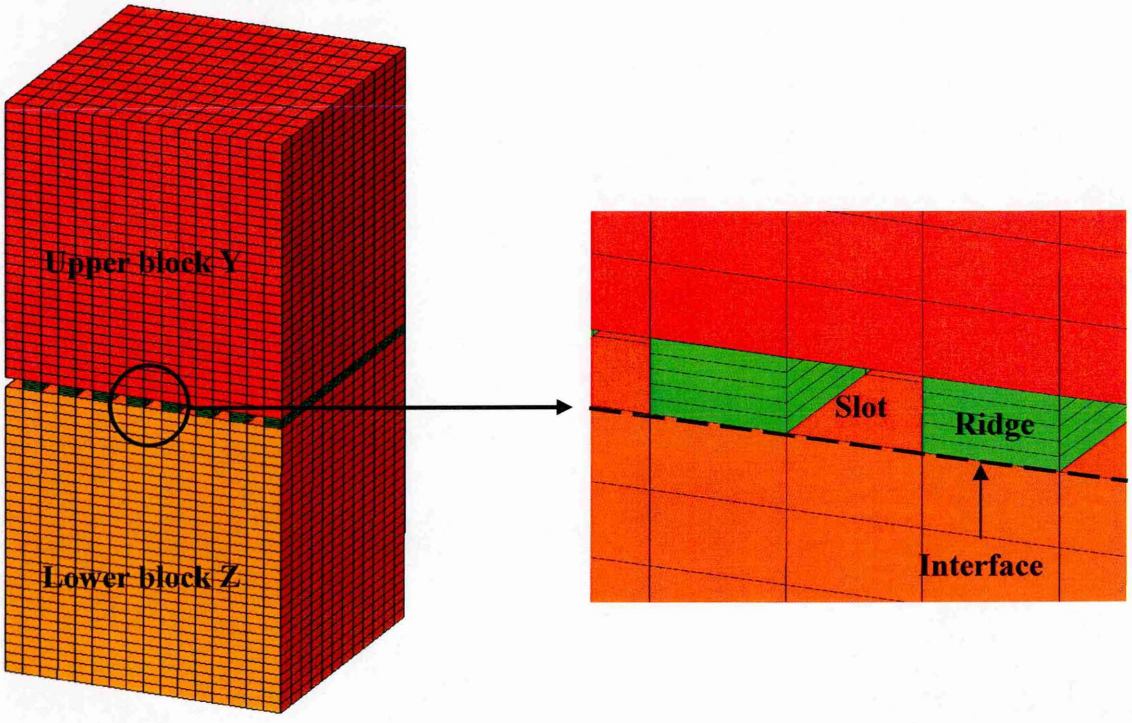

Figure 3-38. Meshed assembly block Y (3.75 mm slots) in contact to block Z, representing tests B1 to B6 and D1 to D6 (11808 elements)

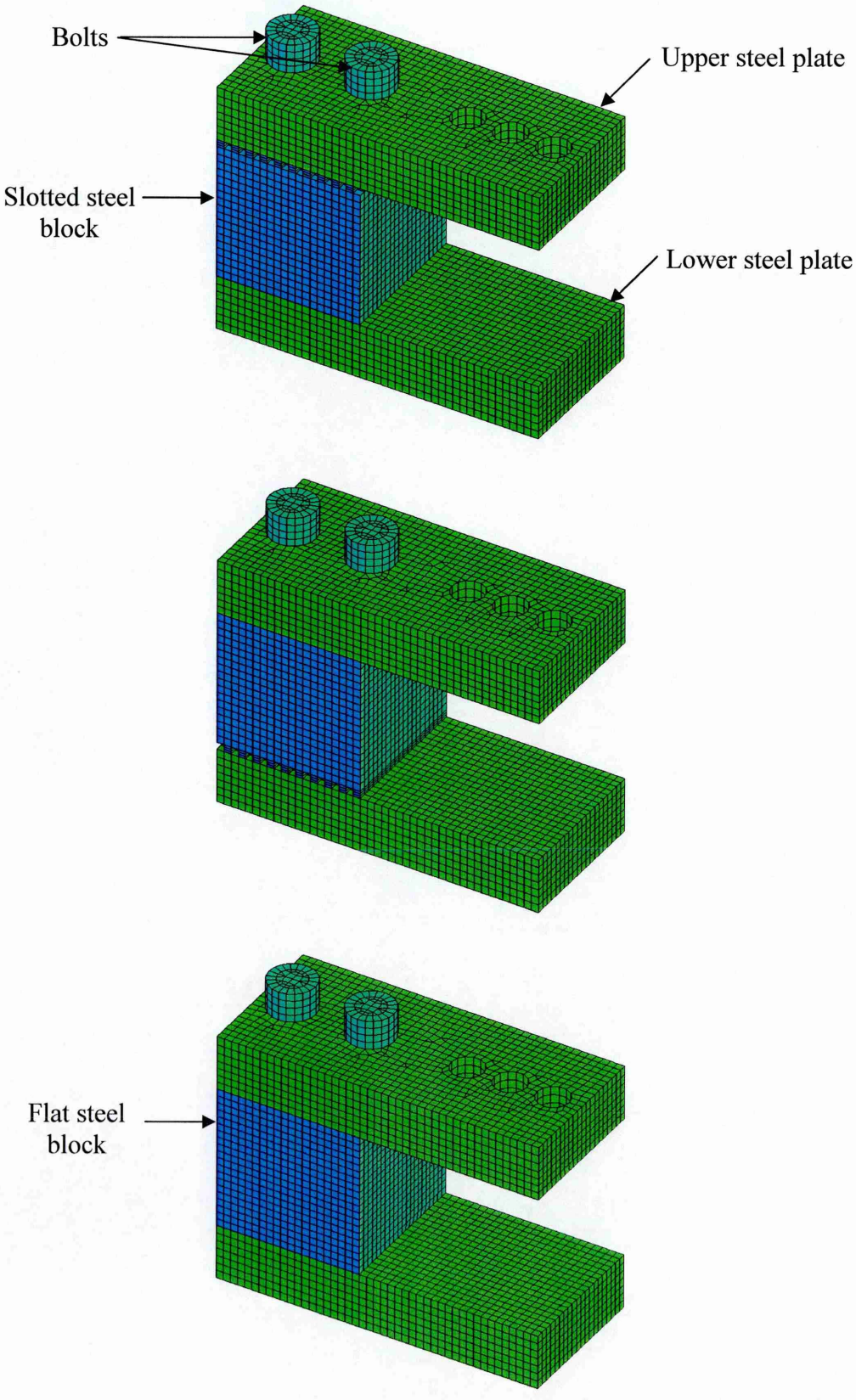

Figure 3-39. Mapped meshing of three blocks analysis

c. Material Properties

Material properties are very important parameter in FEA simulation. The magnitude and linearity of properties varies from material to material. The significance of temperature on the thermal conductivity of steel is small if the temperature is less than or equal to 100°C. Thermal conductivity of steel begins to drop if the temperature is greater than 100°C. Whereas, the heat capacity of steel increases dramatically from 13 J/kg°C to 216 J/kg°C for temperatures of 20°C and 100°C respectively, see Figure 3-40. In steady-state heat transfer simulations thermal conductivity is an important material property, and must be defined. In transient heat transfer simulations material's density, thermal conductivity and specific heat capacity must all be defined. This can be explained by the fact that thermal diffusivity is a function of material's density, thermal conductivity and specific heat capacity. So, if any of the above properties are not defined the results would produce errors or singularities. The maximum temperature reached in experimental tests conducted in this research was 78°C. Thermal conductivity and heat capacity values used in simulations were interpolated from published data, and a constant value was assumed throughout the simulations. For material's properties see Table 3-3.

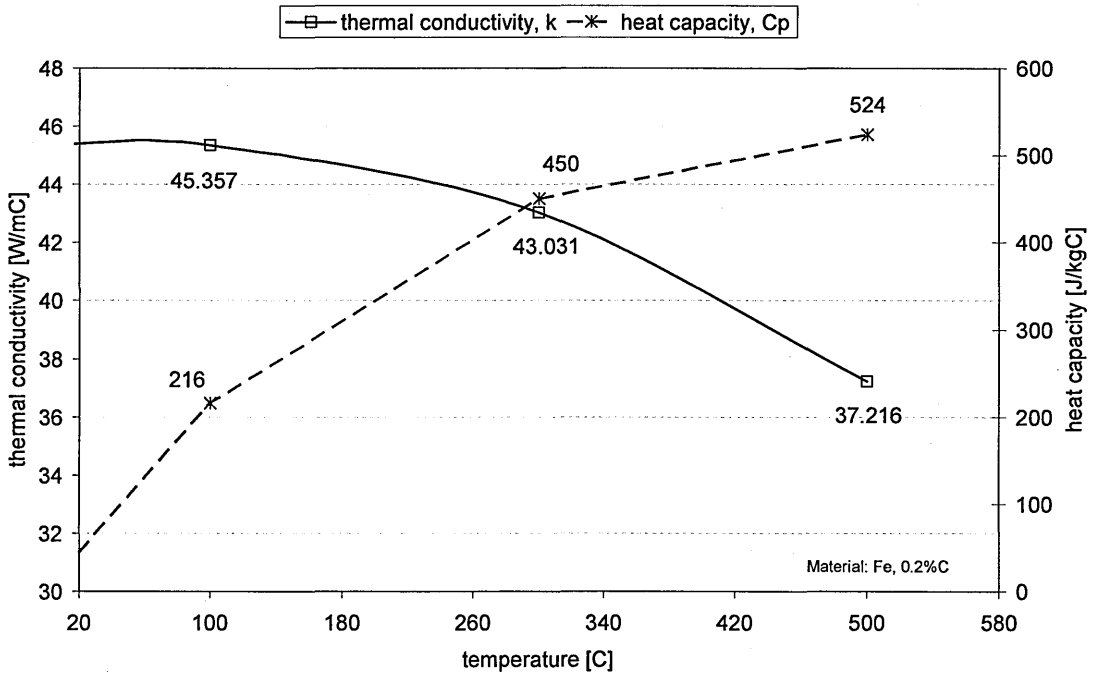

Figure 3-40. Thermal conductivity and specific heat as a function of temperature for Fe, 0.2%C steel [129]

d. Boundary Conditions

The determination of boundary conditions was varied from test to test to represent the experimental situation. Thermal boundary conditions define known thermal conditions in the model. It sets up the initial conditions (temperature, pressure), convection coefficients, transient temperatures, thermal and mechanical coupling, bolt preload and constraints.

Thermal boundary conditions are normally applied to the geometry that has been meshed with the corresponding order of elements. When thermal boundary conditions are applied to geometry, they are fully associative, that is if the geometry is altered, the shape of the boundary condition updates automatically. Each of the boundary conditions used in FEA are explained below [127].

i. Initial Temperature Condition

Initial temperature boundary condition defines the initial temperature of elements for thermal simulation. The initial temperatures will not affect the final results, but can greatly influence solution time. The initial temperature for each test was measured experimentally prior to running the tests and it was found to be between 23°C and 25°C.

ii. Ambient Conditions

All the tests in this research were conducted under ambient conditions in still air. Ambient conditions includes: ambient temperature, ambient pressure, and thermal properties of the surrounding fluid. Ambient conditions such as temperatures (24.5°C to 25.6°C depending on the test) and ambient pressure (101.325 kPa for all tests) were assumed to be constant, and so was acceleration due to gravity (9.81 m/s^2 for all tests).

Experimental measurements showed that the variation of ambient temperature during the tests was not more than ±1°C, see Figure 3-41. For this reason ambient conditions were assumed constant in all simulations.

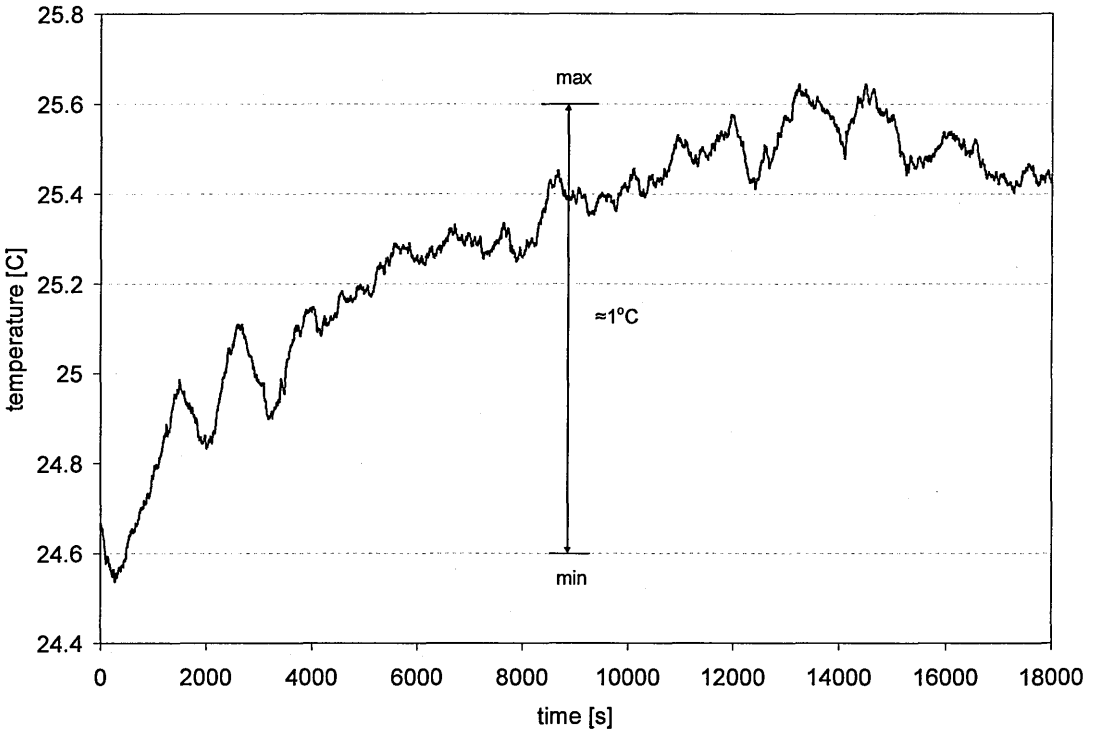

Figure 3-41. Variation of ambient temperature in a typical test

iii. Temperature Boundary Condition

Transient temperature boundary conditions used in simulation were those measured experimentally. The arrays of temperature data representing the "hot surface" (the surface where hotplate was placed) and the "cold surface" at the opposite end were loaded into the model, and solution time step of 20 was specified, see Figure 3-42. This meant that for a total typical time of 14000 s, temperatures were calculated every 700 s. This approach was used in both two block analysis and three block analysis.

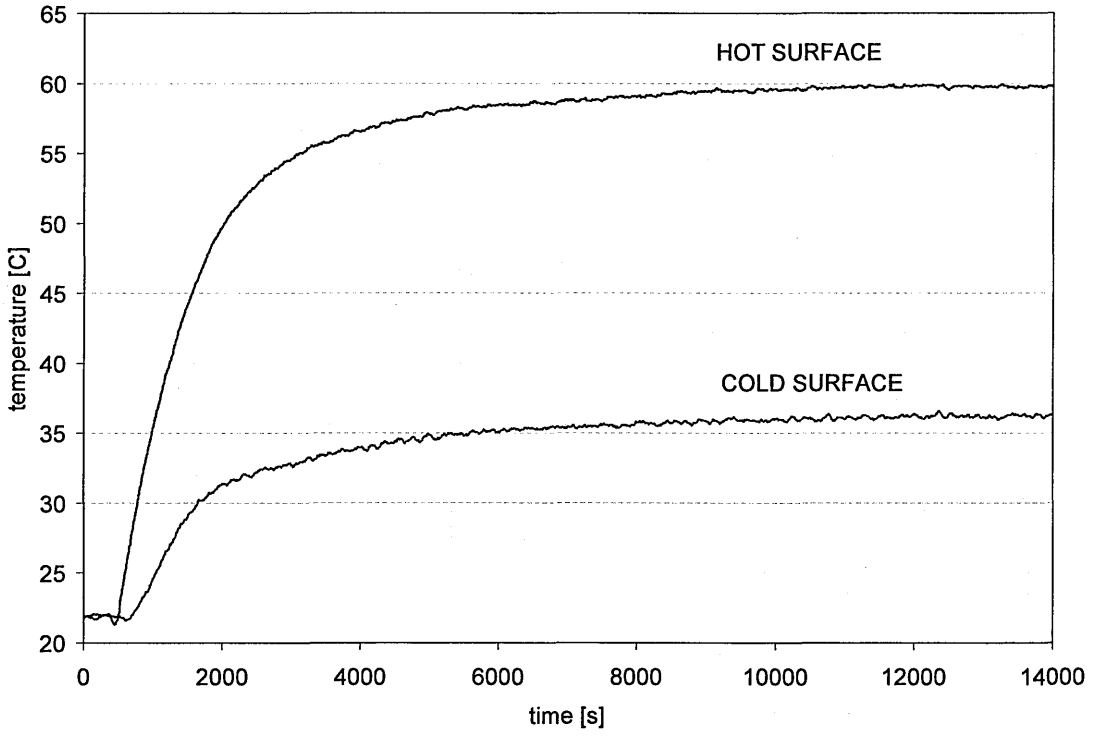

Figure 3-42. Typical temperature history measured. Hot and cold surfaces represent the surface in contact with hotplate and surface in the opposite end respectively

iv. Convection Coefficient

Convection boundary condition defines a heat transfer coefficient from outside surfaces and environmental temperature. A steady-state coefficient was calculated individually for each block and used in analysis, see Table 3-11. The separate calculation for individual block was necessary because convection coefficient depends on the surface temperature and the orientation of the surface relative to gravity. Convection cooling and detailed calculation process are shown in Appendix A.

Surface	Convection Coefficient, h [W/m^2°C]				
	Two block analysis		Three block analysis		
	Top block	Bottom block	Middle block	Top block	Bottom block
Top surface	-	-	-	5.22	5.59
Side surface	6	6	8.13	10.31	10.6
Bottom surface	-	-	-	2.86	-

Table 3-11. Calculated convection coefficient values used in numerical modelling

v. Thermal Contact

To model contact problems, the parts in contact must be identified for possible interaction. If the contact is at a surface then the surface-to-surface contact must be defined. Other contact types are possible, such as node-to-surface and node-to-node. If the contact is mechanical then the simulation software (Section 3.5.1) recognises the contact interaction, whereas for thermal problems the contact must be specified by the user. Thermal and mechanical contacts defined in the simulations are explained in sections following [127].

Thermal coupling works by allowing geometrically separate components that are in mechanical contact to be thermally connected. Resistances are created between elements coated on the corresponding contact surfaces, see Figure 3-43. Other thermal coupling such as conductance, joint, interface, are available. The couplings are established based on element proximity, and are distributed to account for overlap and mismatch between disjoint or dissimilar meshes [127].

In order to assure best possible thermal couplings and high accuracy with no mismatch between elements at the interface, the mesh generated was 6-noded quadrilateral type of shape 1.0 x 1.0 (see section above for explanation on element shape) [127]. Each element of surface 1 was coupled to a corresponding element of surface 2. Thermal contact resistance used in the simulation is based on the measurements found experimentally for each test. For all the simulations conducted herein, the contact was assumed to be perfect, that is when waviness and out-of-flatness deviation of surfaces in contact is small in comparison to the surface roughness.

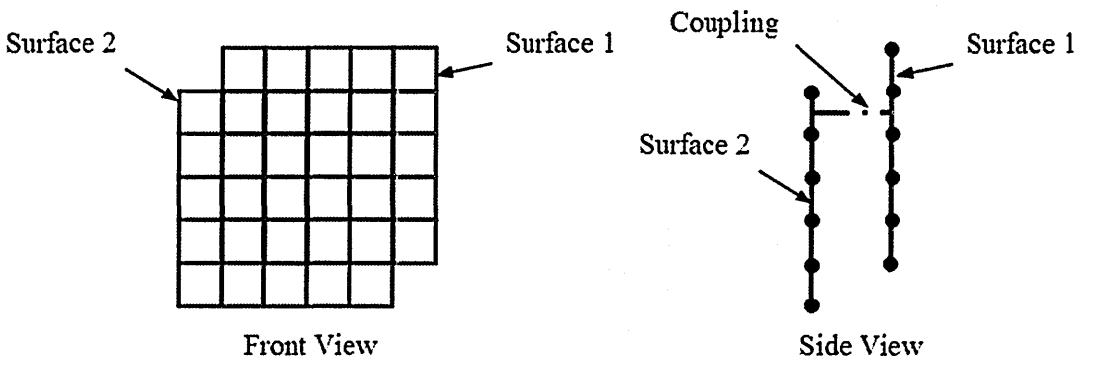

Figure 3-43. Thermal coupling scheme [127]

To take into account the resistance at contact between contacts and target surfaces, the thermal contact resistance coefficient was specified as a constant. From theory the thermal contact resistance between two contacting surfaces is defined as:

$$TCR = \frac{\Delta T}{Q} \qquad \text{Eq. 133}$$

Where Q is the heat transfer across interface, ΔT is the temperature drop across interface. The TCR value is defined as a constant which can be made a function of temperature, contact pressure and location.

vi. Mechanical Contact

Contact problems are highly nonlinear and present two significant difficulties:

- First the contact regions are usually not unknown until the simulation is run. The contact region is a function of many variables: the contact pressure, material properties, and boundary conditions.
- Secondly most contact problems including the problem dealt with in this thesis, need to account for mechanical friction. All the friction laws and models are nonlinear therefore accurate calculation of friction coefficient it's usually not straightforward. The static friction coefficient was calculated and assumed constant, 0.3.

The contact elements in I-DEAS NX use a "target surface" and a "contact surface" whereby forming a contact pair [127], as shown in Figure 3-44.

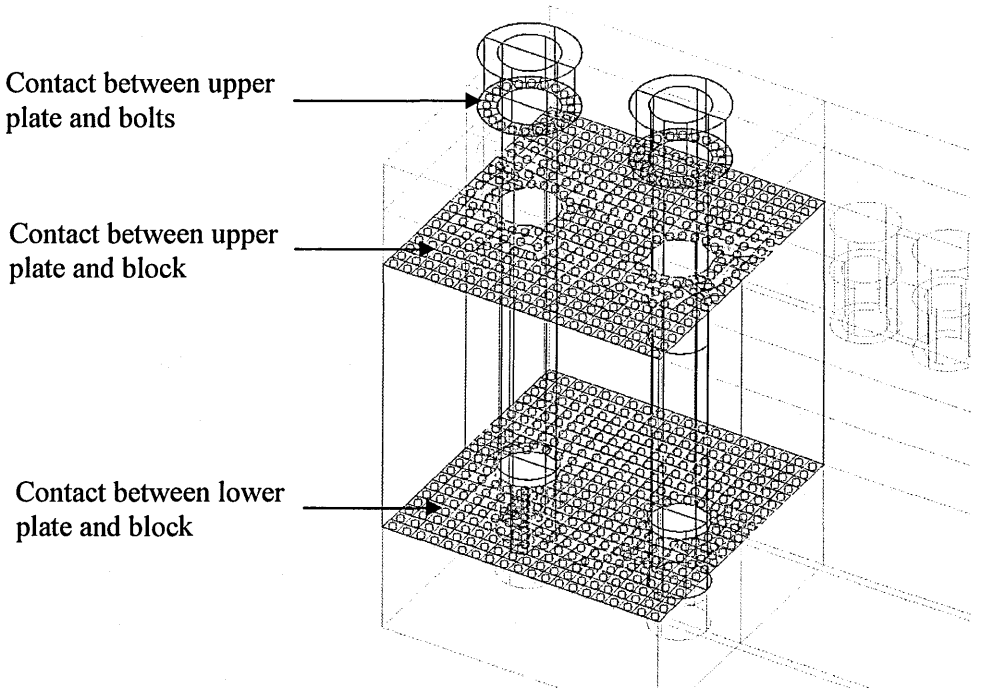

Figure 3-44. Contact regions identified by the software

vii. Bolt Preload

Bolts in connecting the blocks together were modelled using beam elements. Bolts were created using two 8 mm diameter, length 40 mm cylindrical cross-sections. The threaded end of the bolts was connected to the hole using additional beam elements constrained in all directions but free to move with the lower block, see Figure 3-45.

Bolt preload comes from the installation torque applied when the bolts are installed. The preload values corresponding to applied torques were incorporated into the beam elements, see Table 3-12.

Applied torque [Nm]	Bolt preload [kN]
25	15.63
50	31.25
75	46.88

Table 3-12. Applied torque and corresponding bolt preload

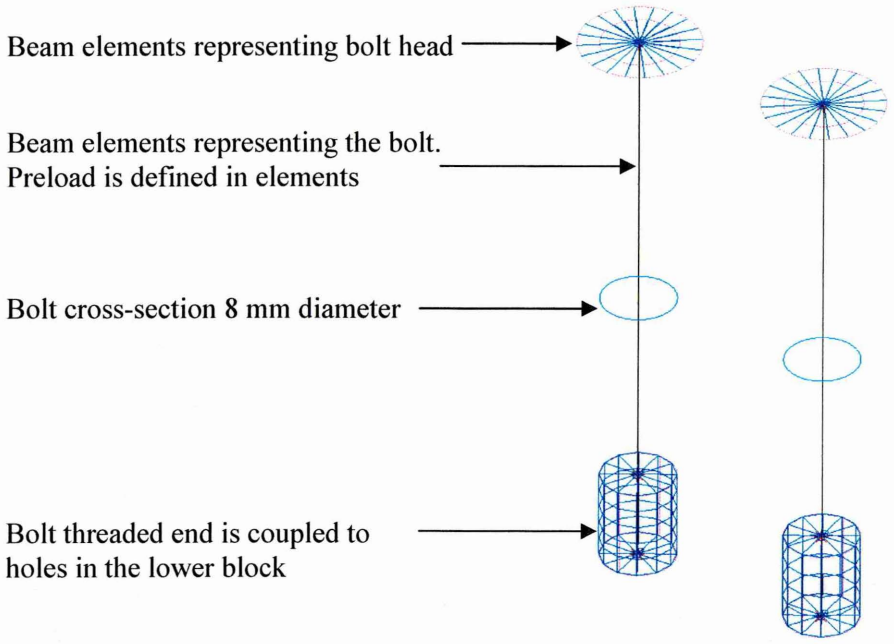

Figure 3-45. Modelling the bolts [127]

The complete assembly showing the meshing and the boundary conditions in the three blocks analysis is shown in Figure 3-46 and Table 3-13.

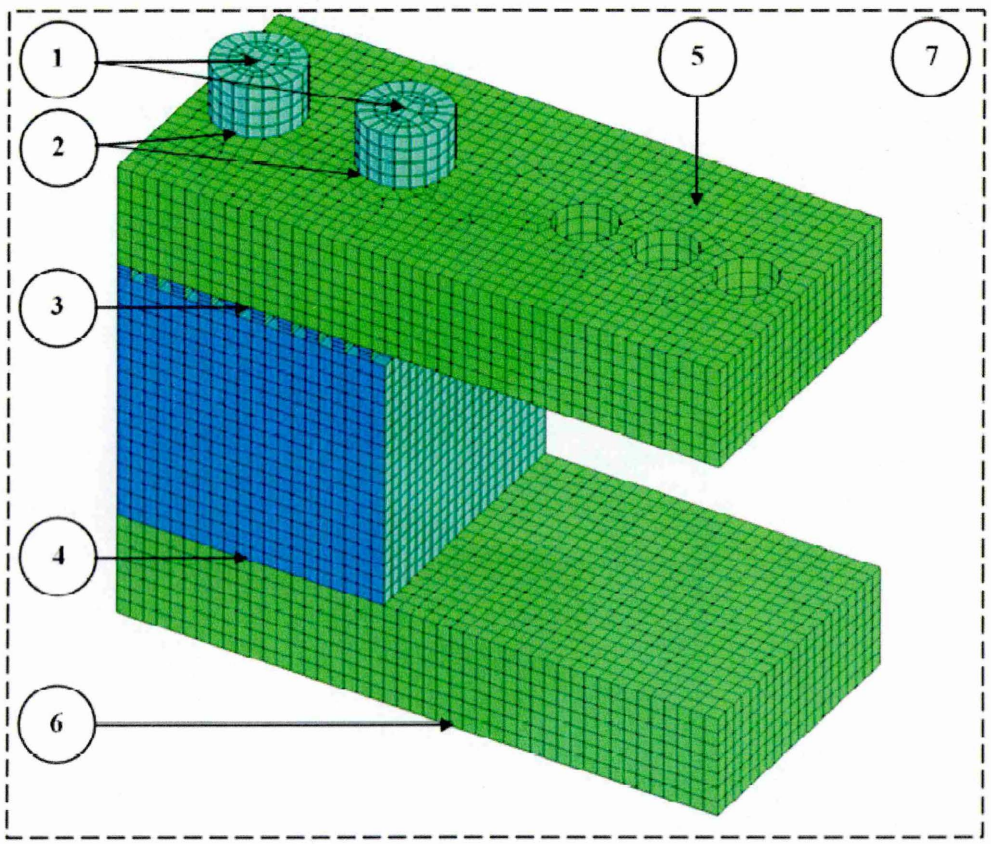

Figure 3-46. Applying boundary conditions (see Table 3-13 for explanation of points)

①	Bolt preload is theoretically calculated and the appropriate value was used in the simulation
②	Thermal and mechanical contact is found theoretically and experimentally between bolts and the upper plate.
③	Thermal and mechanical contact is found theoretically and experimentally between upper plate and block
④	Thermal and mechanical contact is found theoretically and experimentally between lower plate and block
⑤	Convection coefficient was theoretically calculated according to boundary conditions and the value used in simulation
⑥	Transient temperature data collected experimentally was applied on the bottom surface of the lower plate
⑦	Ambient conditions: temperature, ambient pressure and acceleration due to gravity were defined

Table 3-13. Boundary conditions explained, see Figure 3-46 for the location of numbers

e. Post-Processing

The post-processing simulation task displays the data in a graphical or tabular form. After the solution is obtained, results are loaded into the model. The nodal temperatures in FEA simulation corresponding to thermocouple locations TC25 to TC95 for two block analysis (see Figure 3-3), and TC1 to TC13 for three block analysis were read and written to a spreadsheet for analysis (see Figure 3-15 to Figure 3-17). The FEA temperature profile data is then plotted together with experimental temperature profile for comparison.

In three block analysis, the nodal temperature results are uploaded into the model. The simulation software (Section 3.5.1) calculates the corresponding deformation based on the temperature rise and the material properties.

4 Experimental and FEA Results

4.1 Two Block analysis

In this section experimental and FEA results for two block analysis, tests A1 to D6 are presented. All experimental tests were conducted under surrounding ambient conditions by varying the design factors: contact geometry, contact pressure, interface material and surface topography. For detailed explanation of experimental design see Chapter 3, Section 3.3.

Each experimental test was simulated individually using FEA. Transient temperatures collected experimentally were uploaded into the model in a tabular form and applied on the top surface of the upper block to simulate the experimental situation. Thermal coupling representing thermal contact resistances were calculated based on measured temperature drop across the interface and appropriate values used in all FEA models. After the simulation was complete, the temperature data representing thermocouple locations (TC25 to TC95) were extracted and written to a spreadsheet for analysis.

With the hotplate at the top, heat is conducted into the upper block, across the interface and into the lower block. For all tests heat flow along upper blocks X (2mm slots) or Y (3.75mm slots), and the lower block Z was calculated by substituting the thermal conductivity (k), temperature gradient in the upper block (ΔT_U), temperature gradient in the lower block (ΔT_L), the cross sectional area (A) and the length of the blocks (Δx) into the Fourier's heat conduction equation (Eq.13, section 2.11.1). Experimental and corresponding FEA temperature results for each test at steady-state conditions were plotted in the same graph for assessment and correlation (Appendix I). Each graph shows temperature profiles along the upper and lower block for the tests representing changing contact pressures with or without interface material.

4.1.1 Poor Contact Conformance

In total eleven tests were executed by varying the design factors (see Table 3-2 for experimental design). Five tests were executed by placing block Y with 3.75mm slots in contact with block Z and five tests by placing block X with 2mm slots in contact with block Z. In these tests peak to valley height R_t and surface form error P_t of contacting

surfaces were higher. Surface topography parameters of blocks and of contact representing tests A1 to B6 are shown in Table 4-1.

Block	Surface roughness R_a [μm]	Max. peak to valley height R_t [μm]	Surface form error P_t [μm]	Mean value of surfaces in contact		
				Surface roughness R_a [μm]	Max. peak to valley height R_t [μm]	Surface form error P_t [μm]
Y	0.12	6.81	13	0.115	6.64	13.49 ↓
Z	0.11	6.47	13.97			
X	0.12	9.22	26.68	0.115	7.845	20.32 ↑
Z	0.11	6.47	13.97			

Table 4-1. Contact surface topography parameters and the mean value of surfaces in contact for blocks X, Y and Z for tests A1 to B6 having poor conforming contact

a. Block Y (3.75mm slots) in Contact with Block Z

Tests A1 to A6

Test A1 represents the case when 5.64 MPa contact pressure was applied at the interface with air. Measured temperature drop across the interface was 2.07°C, and the FEA prediction of temperature drop across the interface was 1.55°C. The difference between measured and calculated results is 25%. Experimental and FEA temperature profiles at steady-state condition across the interface are shown in Figure 4-1.

With increased contact pressure to 14.2 MPa representing test A3, measured temperature drop across the interface was 1.19°C and the FEA prediction of temperature drop across the interface was 1.11°C. The difference between measured and calculated results is 7.5% which is better correlation than in test A1. The better agrement between experimental and FEA results in test A3 is due to increase in the contact area with increased contact pressure. Temperature profiles at steady-state conditions are shown in Figure 4-1.

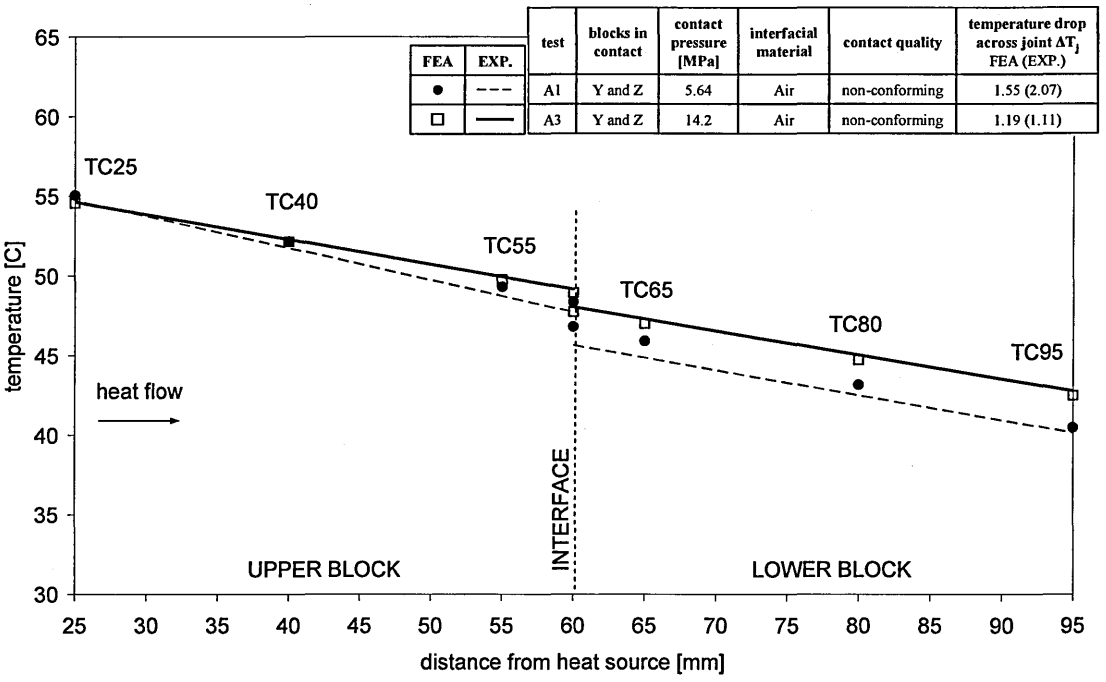

Figure 4-1. Temperature profile across the interface at steady-state showing tests A1 and A3

When a material with lower thermal conductivity is placed at the contact interface, thermal contact resistance would be higher. However, it was found that this is true only if the contact pressure is not taken into consideration.

The effect of thermal grease on the temperature drop across the interface was shown in tests A4 to A6. In these test decrease in thermal contact resistance was expected, due to the thermal conductivity of thermal grease being about 35 times higher than the thermal conductivity of air (see Table 3-3). However, temperature drop across the interface was higher when thermal grease was placed at the interface. This can be explained by the fact that if the thermal grease layer wetting the contacting surfaces is too thick or thicker than the surface roughness (Figure 4-2) and if the contact pressure is not high enough to squeeze out excess grease, then the number of surface asperities coming into contact would be less than when thermal grease is absent (Figure 4-3).

Moreover, when contact pressure was increased from 5.64 MPa (test A4) to 14.2 MPa (test A6), temperature drop across the interface was more pronounced in tests having thermal grease at the interface then in tests with air at the interface.

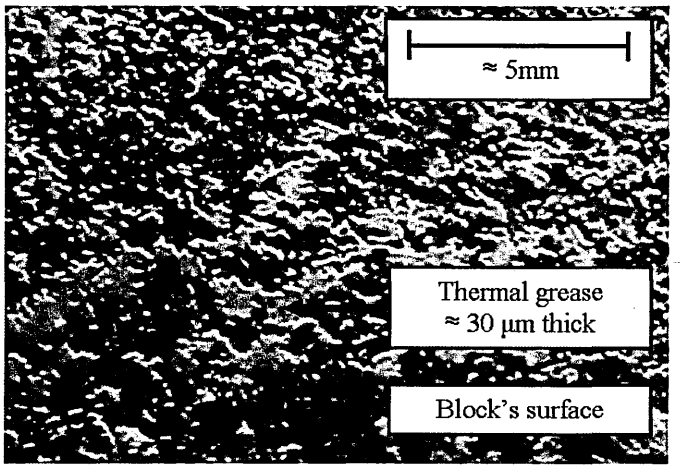

Figure 4-2. Thickness of thermal grease relative to surface roughness

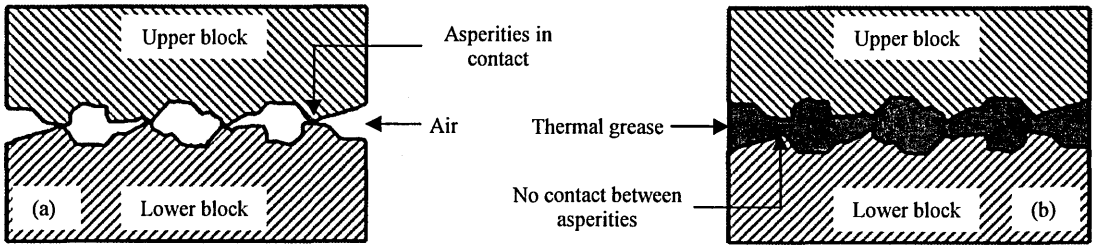

Figure 4-3. Schematic representation of a contact formed between two rough and conforming surfaces; (a) bare interface with air, (b) interface with thermal grease

b. Block X (2mm slots) in Contact with Block Z

Tests B1 to B6

Test B1 represents the case when 5.64 MPa contact pressure was applied at the interface with air. Measured temperature drop across the interface was 4.41°C, and the FEA temperature drop across the interface was calculated as 2.3°C. The percentage difference between measured and calculated results is 91% which is very poor correlation between measured and calculated results.

Increasing contact pressure should affect temperature drop across the interface. This is shown in test B2 and B3 with contact pressures of 10 MPa and 14.2 MPa respectively. In these tests, measured temperature drop across the interface were 2.95°C and 2.53°C respectively. The FEA prediction of temperature drop across the interface was 1.73°C and 1.53°C respectively. The percentage difference between measured and calculated results is 41% and 39% for tests B2 and B3 respectively, which is much better

correlation than in test B1 when the contact pressure was lower. Results in tests B2 to B3 showed that FEA prediction of temperature drop across interfaces is more accurate at higher contact pressures. Furthermore, it is interesting to note that temperature drop across the interface with thermal grease is lower in tests B4 and B6 (block X and Z), then in tests A4 and A6 (block Y and Z). This is because the surface form error of block X is 26.68 μm, and the surface form error of block Y is 13 μm (see Table 4-1).

When peak to valley height R_t and surface form error P_t of contacting surfaces are high, the macroscopic gaps at the interface are filled with air if the interface is bare. By filling the macroscopic gaps with a material with higher thermal conductivity such as thermal grease, the overall thermal contact resistance decreases and consequently the temperature drop across the interface becomes less pronounced. Increased contact pressure showed higher effect on tests having air at the interface, but less effect on tests having thermal grease at the interface. Another important finding is that when interface material was thick in comparison to contact surface roughness, and if contact pressure is low then thermal contact resistance does not decrease. Combined temperature drop across interfaces versus contact pressures are shown in Figure 4-4.

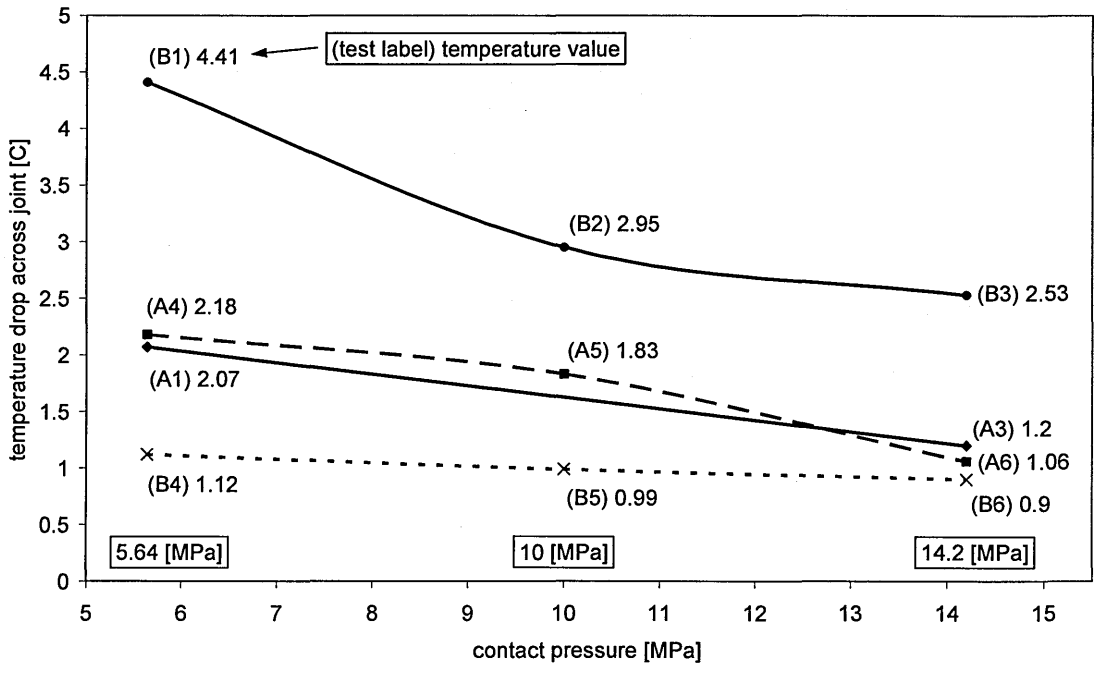

Figure 4-4. Temperature drop across interface versus contact pressure for tests A1 to B6

Measured and corresponding FEA results are plotted in the same graph for correlation assessment. Temperature drop across interfaces of adjacent tests were divided to each other representing x-axis and the inverse of contact pressures of adjacent tests were divided to each other representing y-axis, as shown in Figure 4-5. For clarity, the calculation of temperature drop across the interface for adjacent tests A1 and A3 is shown here and is as follows:

Experimental temperature drop across the interface: $\Delta T_J = \frac{A3}{A1} = \frac{1.2^\circ C}{2.07^\circ C} = 0.579$

FEA temperature drop across the interface: $\Delta T_j = \frac{A3}{A1} = \frac{1.2^\circ C}{1.55^\circ C} = 0.774$

The ratio of contact pressure between adjacent tests A1 and A3 is calculated as follows:

Contact pressure: $\frac{A1}{A3} = \frac{5.64MPa}{14.2MPa} = 0.397$

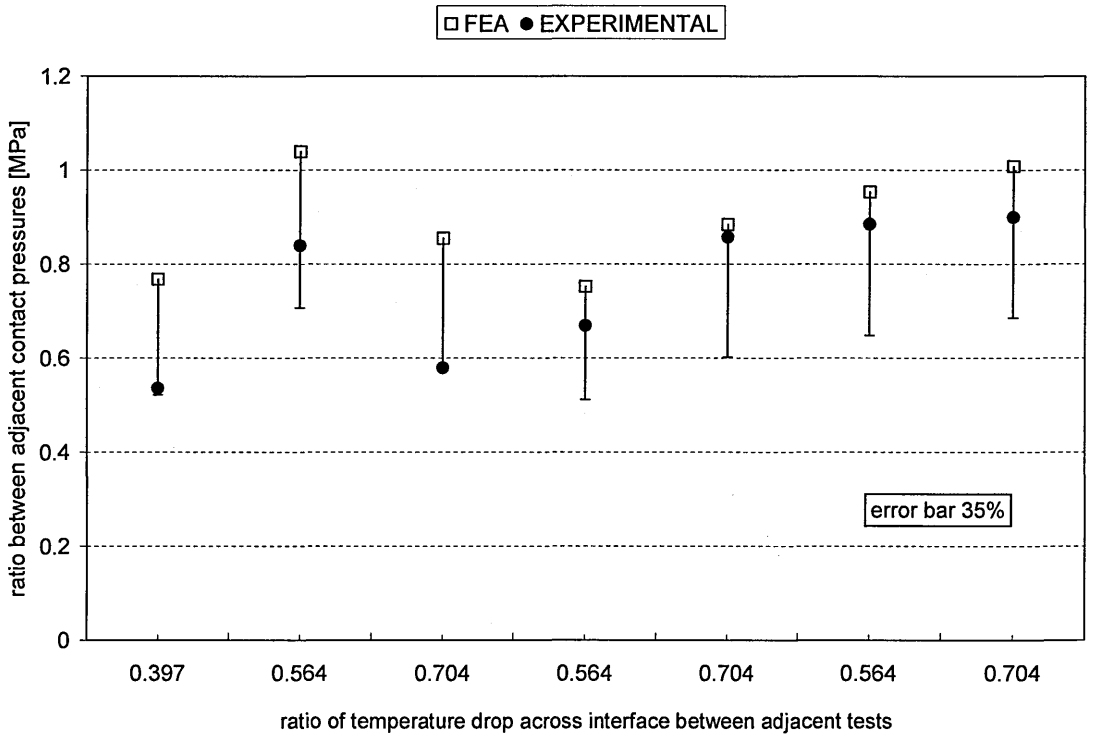

Figure 4-5. Correlation between experimental and FEA prediction for tests A1 to B6

FEA temperature contours at steady-state representing tests A1-A6 and C1-C6 are shown in Figure 4-6.

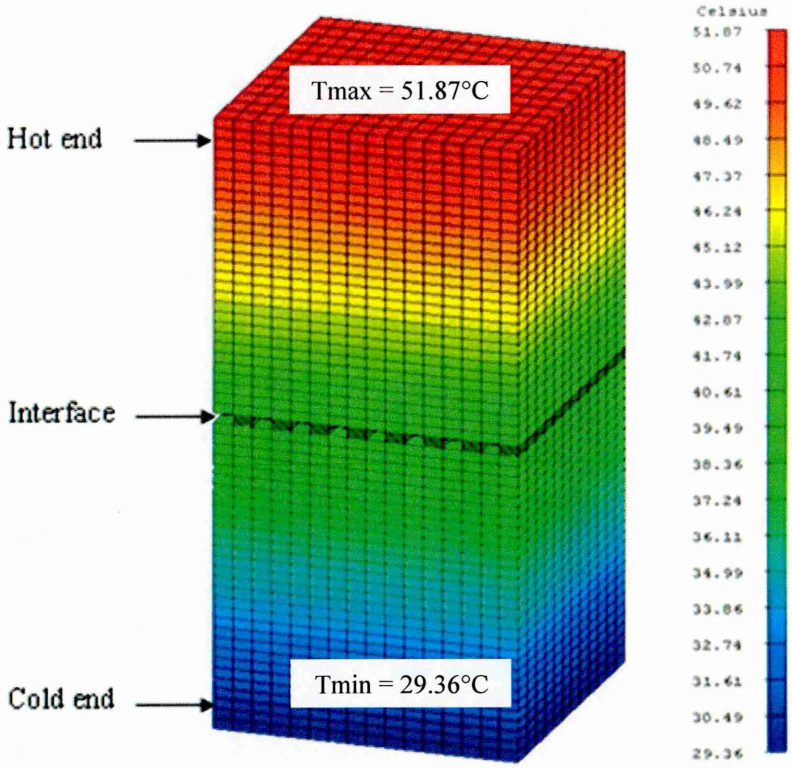

Figure 4-6. FEA steady-state temperature contour representing tests A1 to A6 and C1 to C6

4.1.2 Good Contact Conformance

In total twelve tests were executed by varying the design factors (see Table 3-2 for experimental design). Six tests were executed by placing block Y with 3.75mm slots in contact with block Z and six tests by placing block X with 2mm slots in contact with block Z. In these tests peak to valley height R_t and surface form error P_t of contacting surfaces were lower than in tests A1 to B6. Surface topography parameters for blocks representing tests C1 to D6 are shown in Table 4-2.

Block	Surface roughness R_a [μm]	Max. peak to valley height R_t [μm]	Surface form error P_t [μm]	Mean value of surfaces in contact		
				Surface roughness R_a [μm]	Max. peak to valley height R_t [μm]	Surface form error P_t [μm]
Y	0.03	3.82	7.52	0.07	5.145	10.745 ↑
Z	0.11	6.47	13.97			
X	0.14	3.19	5.8	0.13	5	9.4 ↓
Z	0.11	6.47	13.97			

Table 4-2. Contact surface topography parameters and the mean value of surfaces in contact for blocks X, Y and Z for tests C1 to D6 having good conforming contact

a. Block Y (3.75mm slots) in Contact with Block Z

Tests C1 to C6

Tests C1, C2 and C3 represent the case when block Y is placed in contact with block Z, having air at the interfaces and contact pressures of 5.64 MPa, 10 MPa and 14.2 MPa respectively. In these tests the correlation between measured and FEA prediction of temperature drop across the interfaces are better than in previous tests having poorer contact conformance. This is because the contact has better conformance with mean maximum peak to valley height R_t of 5.145 μm and mean surface form error P_t of 10.745 μm (see Table 4-2). The maximum discrepancy between measured and FEA prediction is 15%.

Tests C4, C5 and C6 have same arrangement as tests C1, C2 and C3 but with thermal grease at the interface. Again thermal grease has increased thermal contact resistance.

The effect of thermal grease at temperature drop across the interface was also shown in tests A4, A5 and A6. This explains the fact that thermal grease was thicker than the surface roughness, and the contact pressures were not high enough to squeeze out excess grease and bring surface asperities into contact, which otherwise would be if the interface was bare with air. The correlation between measured and FEA prediction is good with maximum discrepancy of 24%.

b. Block X (2mm slots) in Contact with Block Z

Tests D1 to D6

Tests D1, D2 and D3 represent the case when block X was placed in contact with block Z, having air at the interface and contact pressures of 5.64 MPa, 10 MPa and 14.2 MPa respectively. Under these conditions it was found that measured temperature drop across interfaces were 0.86°C, 0.64°C and 0.5°C respectively. For the same contact conditions the FEA temperature drops were 1.1°C, 0.81°C and 0.6°C respectively (see Appendix I). The maximum difference between measured and FEA prediction is 21%.

Tests D4, D5 and D6 have same arrangement as tests D1, D2 and D3 but with thermal grease at the interfaces. Again thermal grease has increased thermal contact resistance. This was also shown in most previous tests having thermal grease at the interface. The correlation between measured and FEA prediction is very good with maximum discrepancy of 20%.

Measured and corresponding FEA results are plotted in the same graph for correlation assessment. Temperature drop across interfaces of adjacent tests were divided to each other representing x-axis and the inverse of contact pressures of adjacent tests were divided to each other representing y-axis, as shown in Figure 4-7. FEA temperature contours at steady-state representing tests B1-B6 and D1-D6 is shown in Figure 4-8. Combined temperature drop across interfaces versus contact pressures are shown in Figure 4-9.

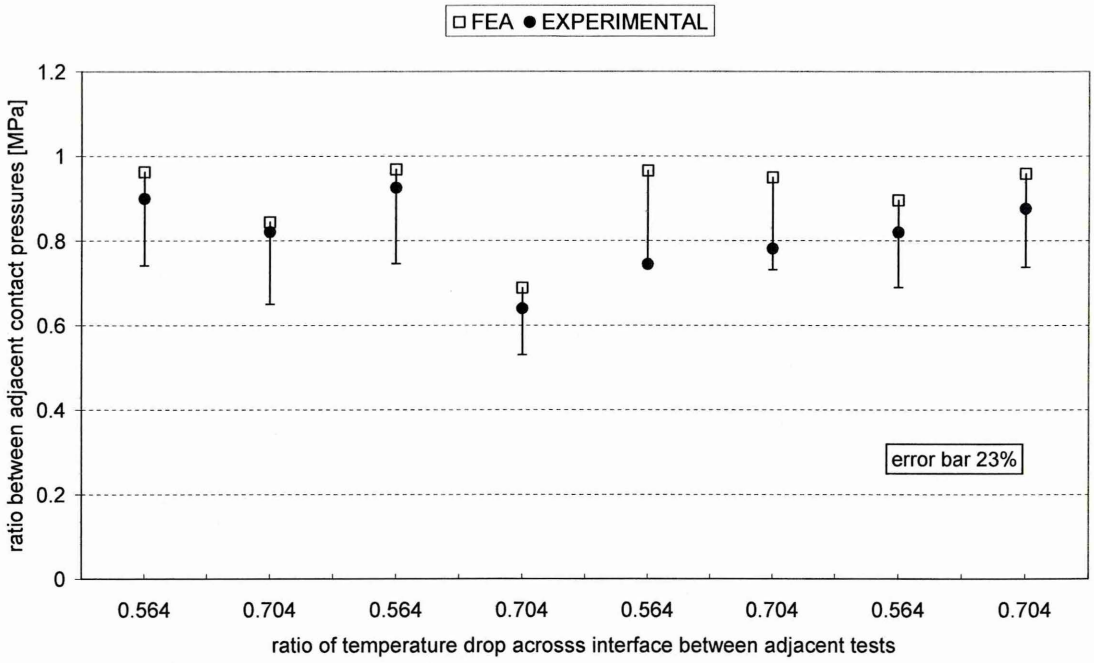

Figure 4-7. Correlation between experimental and FEA prediction for tests C1 to D6

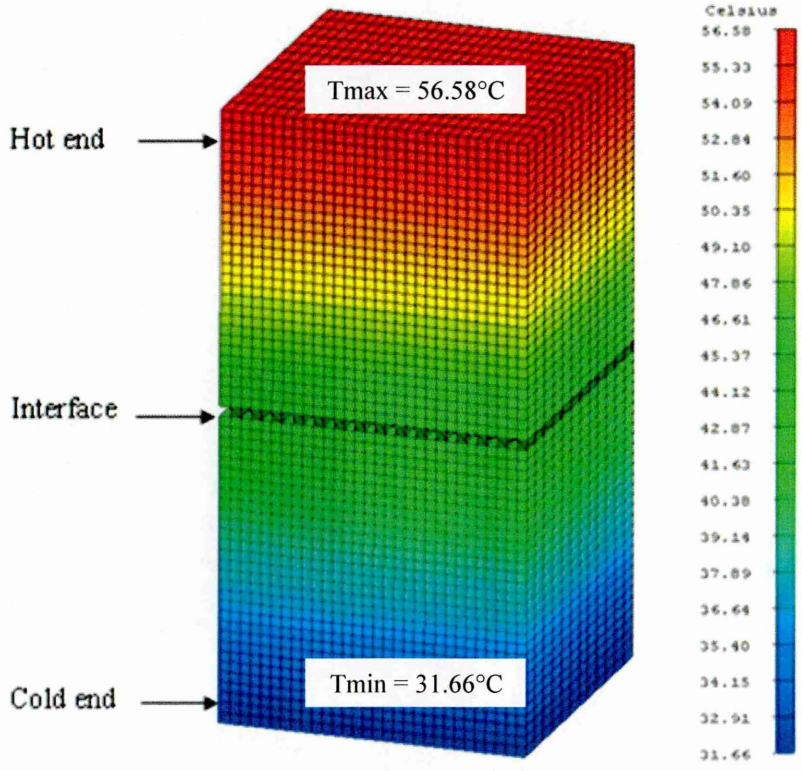

Figure 4-8. FEA steady-state temperature contours representing tests A1 to A6 and C1 to C6

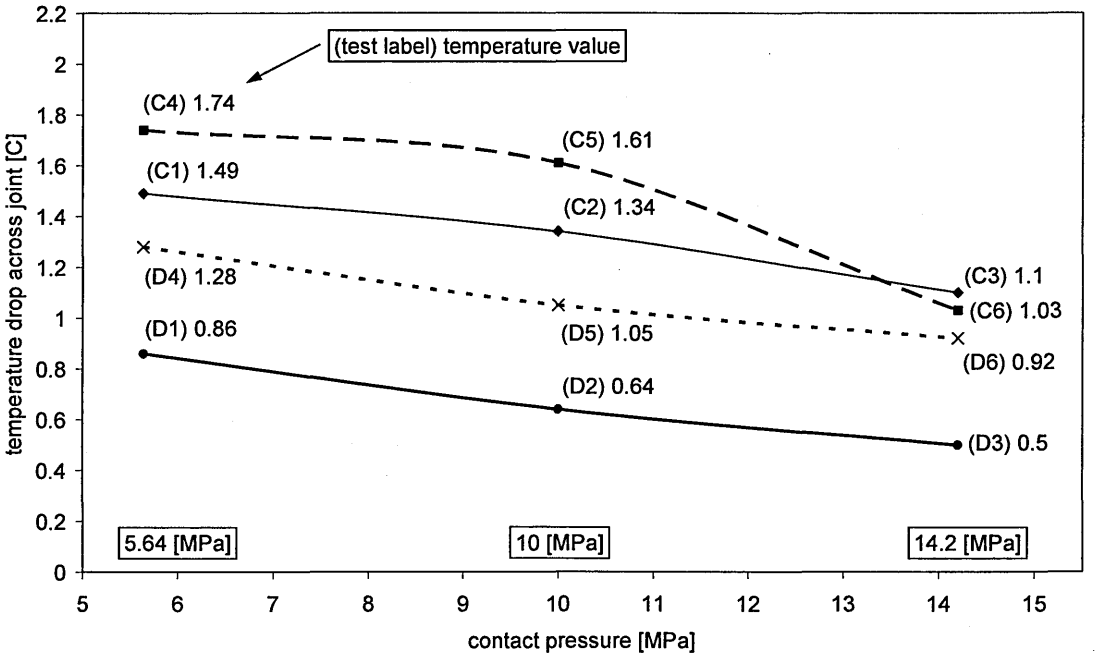

Figure 4-9. Temperature drop across interface versus contact pressure for tests C1 to D6

The objective of conducting tests having different contact geometry arrangement was to investigate the importance of the spread of contact regions in the heat transfer across interfaces. Both contact arrangements were modelled using FEA and the numerical results indicated that the difference in temperature results is insignificant on overall heat transfer across interface (see Appendices G for details).

4.2 Three Block Analysis

In this section heat transfer and associated dimensional distortion results of three steel blocks in contact is presented. Experimental tests were simulated individually using FEA. Transient temperatures collected experimentally were uploaded into the model in a tabular form and applied on the bottom surface of the lower block to simulate the experimental situation. Thermal coupling representing thermal contact resistances were calculated using mathematical models as explained in Chapter 2 and calculated contact resistance values were used in FEA modelling, see Table 4-3. The code written in Matlab® is used to calculate thermal contact resistances formed by two conforming metal bodies in contact. The code is based on theory of heat transfer across interfaces as explained in Chapter 2. The code works for both, plastic and elastic contact deformation (see Appendix F).

	Upper block				Lower block			
	5.64 MPa		10 MPa		5.64 MPa		10 MPa	
	Air	Grease	Air	Grease	Air	Grease	Air	Grease
Flat block	0.0079	0.0078	0.0046	0.0045	0.0077	0.0075	0.0043	0.0041
Slotted block	0.0015	0.0013	0.00092	0.00089	0.0069	0.0073	0.004	0.0037

Table 4-3. Thermal contact resistance values used in FEA

Convection coefficients were mathematically calculated and steady-state values were used in all FEA models. After the FEA simulations were complete, the temperature data representing thermocouple locations (TC1 to TC13) and the deformation data representing NCDT locations (NCDT-1 to NCDT-3) were extracted and written to a spreadsheet for analysis.

Three different contact arrangements were considered; slotted block in contact with upper block, slotted block in contact with lower block and, flat block sandwiched between the lower and the upper block. Each of the three different contact arrangement is explained separately in the following sections.

4.2.1 Slotted Block in Contact with Upper Block

Three steel blocks were bolted together using two M8 high tensile steel bolts with slotted surface of the middle block placed in contact with the upper block. The apparent contact areas at upper interface (further away from the heat source) was 0.0008 m^2 and

at lower interface (closer to the heat source) was 0.0016 m^2. As heat flows into the assembly each steel block and consequently the whole assembly expands with increase in temperature. The amount of expansion depends on material's coefficient of thermal expansion, whereas the direction of deformation depends on location and magnitude of constraints applied by the bolts.

The lower block expanded the most because it is nearest to heat source where the temperature is highest. As the lower block expands it pushes the middle block, the Zerodur® block and consequently the upper block vertically upwards. The bolts hold the blocks together under pressure and partly constrain them from expanding upwards. As the assembly expand and deforms, displacement transducers measure the deformation relative to the top surface of Zerodur® block which is placed on top of the lower block, see Figure 3-15 in Chapter 3.

Four different tests were carried out by varying the design factors (see section 3.4.1 for experimental design). First test E1 represent the case when contact pressure of 5.64 MPa was exerted at the interface with air. At the early stages of heat flow the difference in temperature between adjacent thermocouples was small. As heat flowed with time, the temperature difference between adjacent thermocouples became more pronounced, and it continued to be so until the system reached the thermal steady-state.

At steady-state condition the maximum and minimum temperature recorded by TC1 and TC13 were 71.85°C and 62.8°C respectively that is a difference of 9.06°C. These values compare with the maximum and the minimum FEA temperatures of 71.87°C and 65.2°C. Experimental transient temperature results are shown in Figure 4-10 and FEA transient temperature results and temperature contours are shown in Figure 4-11 and Figure 4-12 respectively.

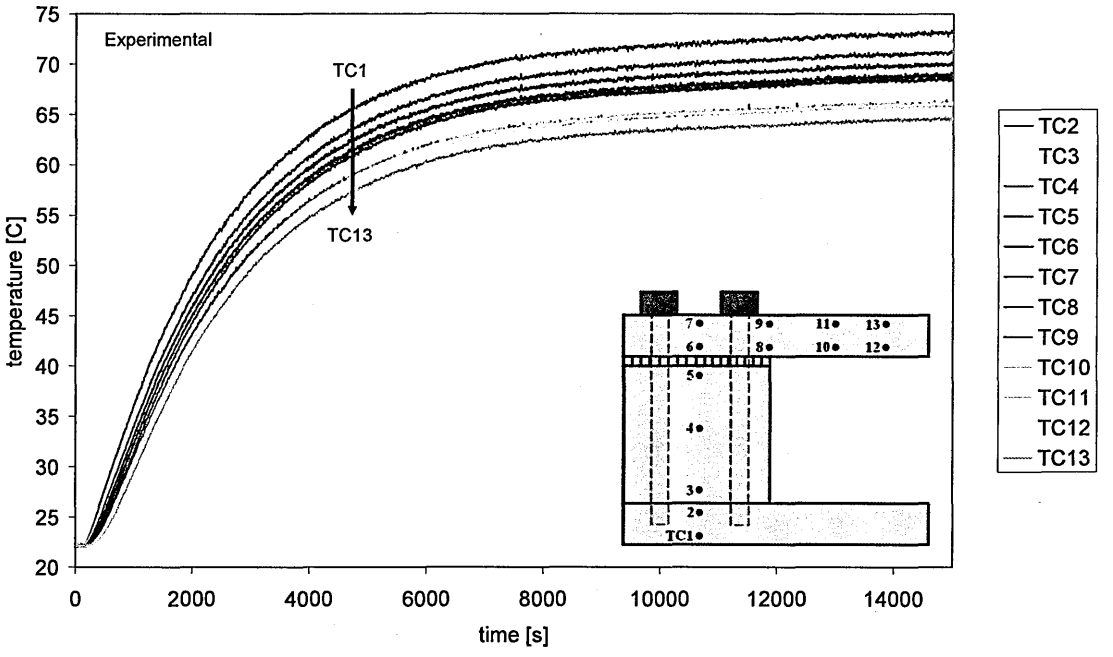

Figure 4-10. Experimental transient temperature histories, showing test E1

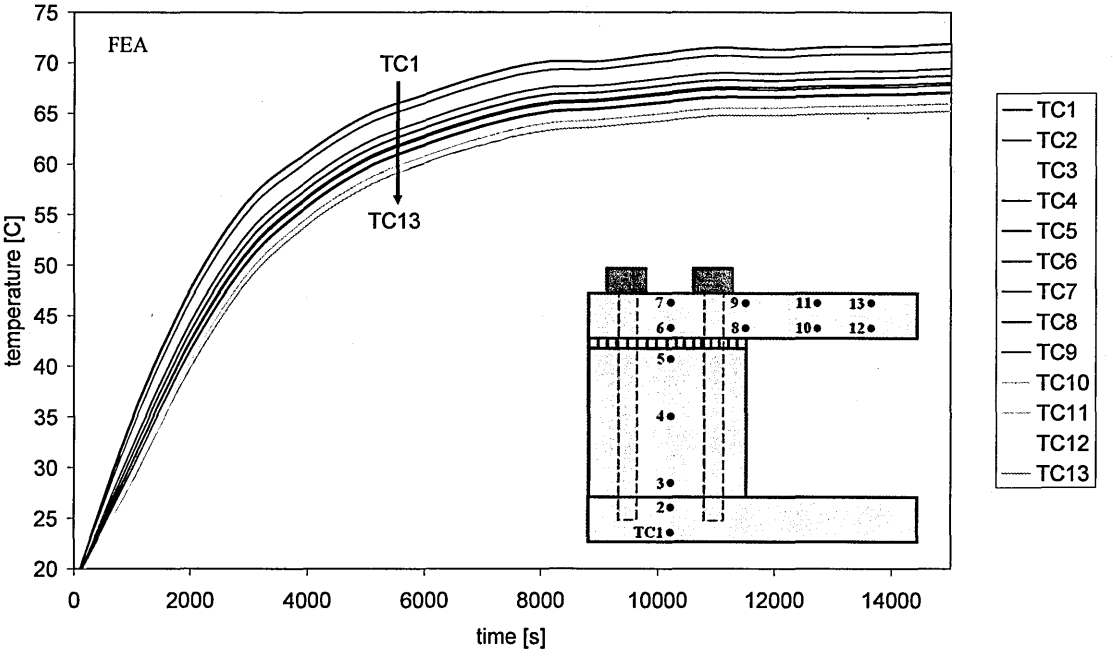

Figure 4-11. FEA transient temperature histories, showing test E1

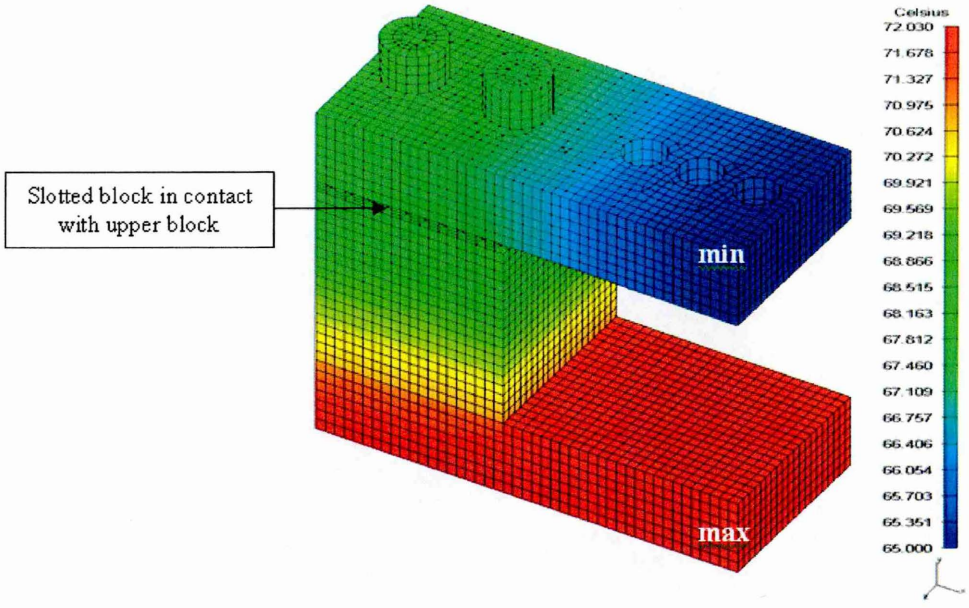

Figure 4-12. Temperature contours at steady-state showing test E1

Experimental and FEA transient deformation results were plotted in the same graph for correlation assessment as shown in Figure 4-13 and the FEA deformation contours are shown in Figure 4-15. The numerical prediction of transient thermal deformation is comparable to experimental results in terms of magnitude and direction.

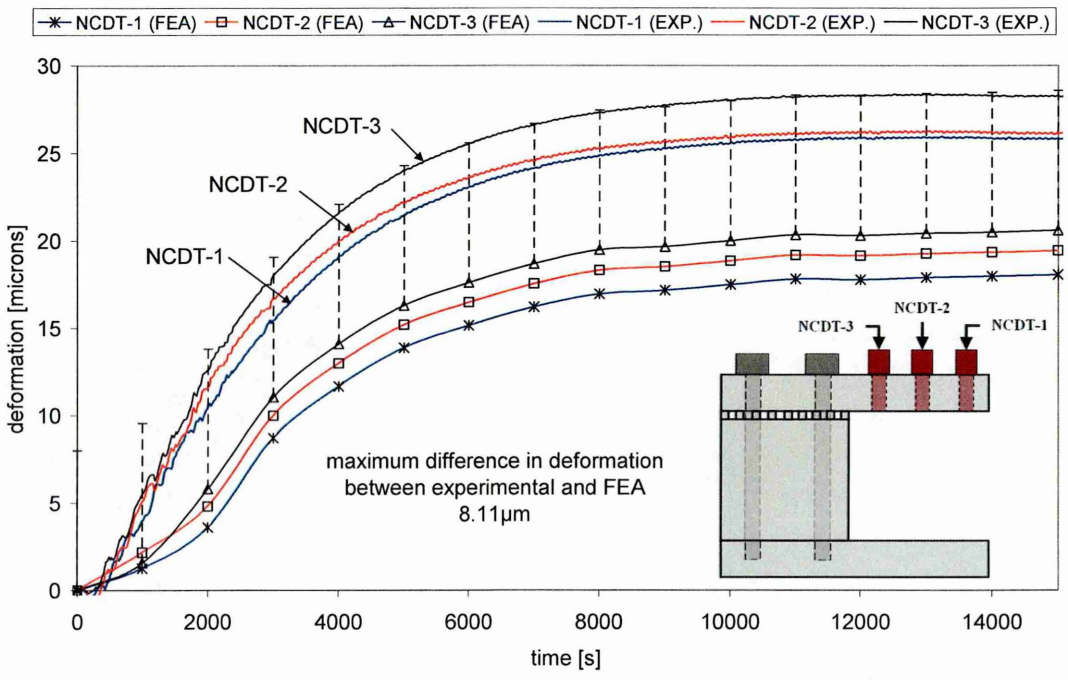

Figure 4-13. Transient deformation histories for test E1

The side of the assembly nearest to the bolts expanded the most as measured by NCDT-3. Moving away to the right from the bolted end, the upper block bends downwards as measured by NCDT-2 and NCDT-1, see Figure 4-14. This is known as the tilt error associated with the bending of the lower block. It is clear that because of the constraints placed by the bolts, the edges of the upper block in the near region surrounding the bolts are free to move upwards, which in turn makes the far end of the upper block move downwards as shown in Figure 4-14 and Figure 4-15.

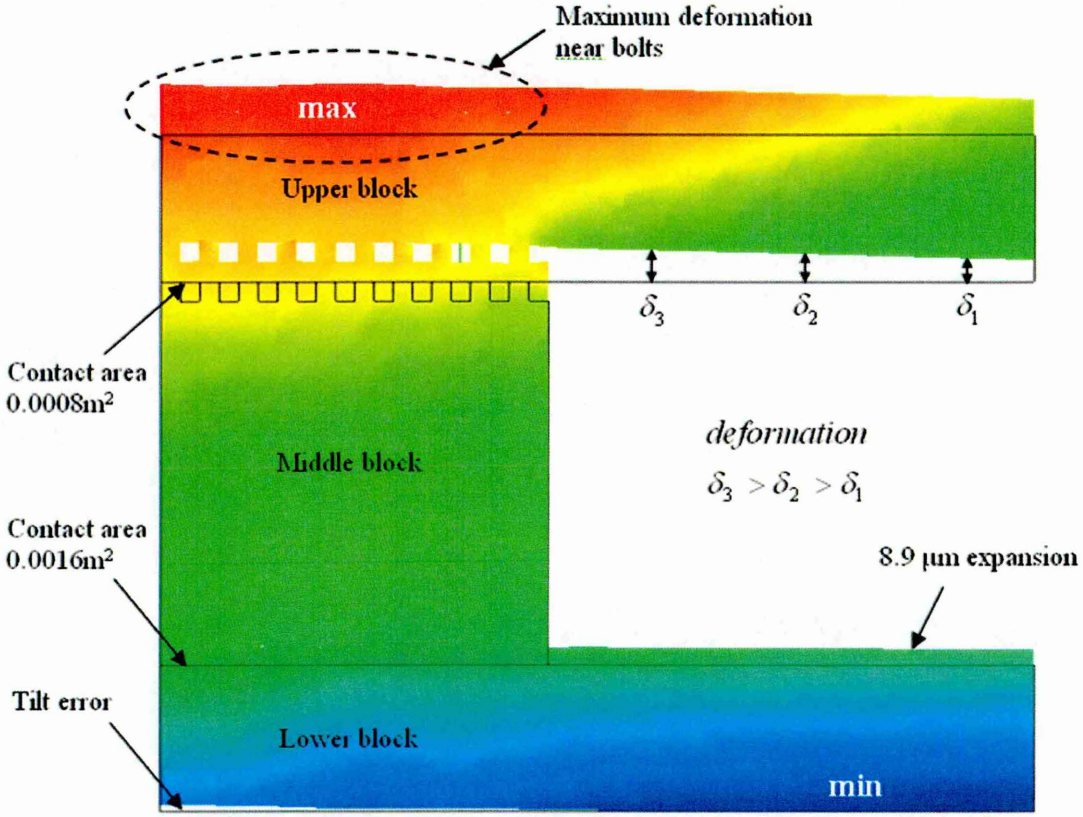

Figure 4-14. FEA deformation contour showing the deformation of the assembly for test E1

The maximum discrepancy between experimental and FEA deformation results is 8.11 μm. The discrepancy can be explained by the fact that if we assume that Zerodur® block does not expand, then any vertical upwards movement of the Zerodur® block is due to the expansion of the lower block. Based on FEA results it was found that lower block expands 8.9 μm vertically upwards as shown in Figure 4-14 and Figure 4-15. This fact explains the discrepancy of 8.11 μm between experimental and FEA results.

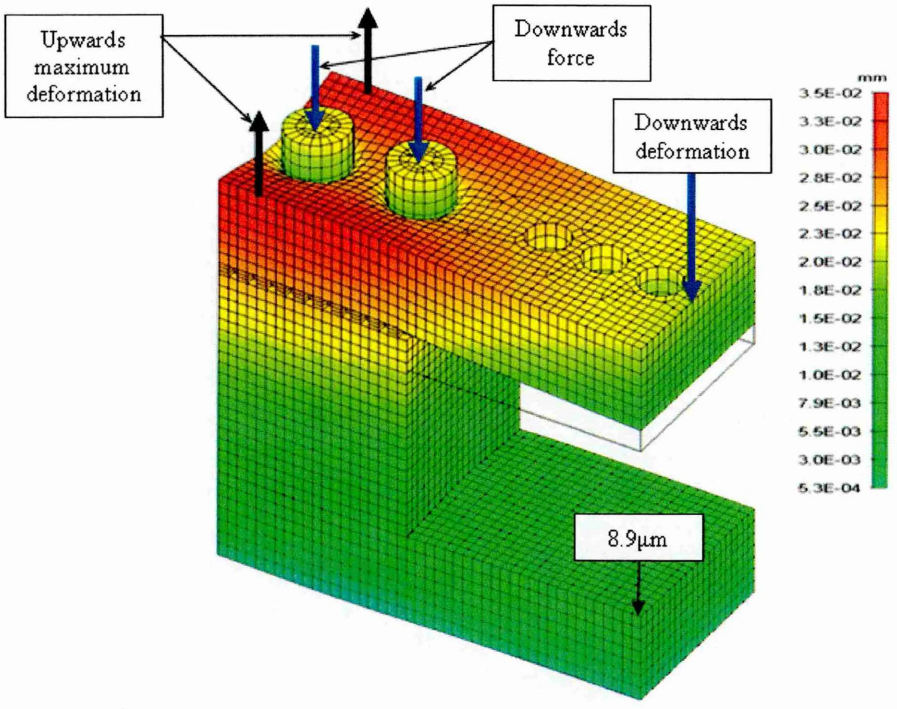

Figure 4-15. FEA deformation contours at steady-state showing test E1

Test E2 had the same arrangement as test E1, but with contact pressure of 10 MPa. Contact pressure has a significant effect on heat transfer across contact interfaces, therefore increasing contact pressure from 5.64 MPa to 10 MPa reduces thermal contact resistance and consequently encourages heat transfer across interfaces.

Increasing contact pressure from 5.64 MPa to 10 MPa reduced maximum deformation to 26 µm and 17 µm for experimental and FEA respectively. This effect of contact pressure on deformation can be explained by the fact that the relative deformation of the upper block to the lower block is constrained by the opposite counter-acting force applied by the bolts. Increased contact pressure is the consequence of increased bolt preload. Combined experimental and FEA deformation results are shown in Figure J-1.

4.2.2 Slotted Block in Contact with Lower Block

Same slotted block used in Section 4.2.1 was used in the following tests F1 to F4. Slotted block was turned upside down so that the slotted surface is in contact with the lower block as opposed to the upper block. The apparent contact areas at upper interface (further away from the heat source) was6 0.0016 m^2 and at lower interface (closer to the heat source) was 0.0008 m^2.

Test F1 represents the case when contact pressure of 5.64 MPa was exereted at the interface with air. Heat was applied on the bottom surface of the lower block, conducted through two interfaces and through the upper block. Transient thermal deformation results and the FEA temperature contours for test F1 are shown in Figure 4-16 and Figure 4-17 respectively.

Maximum deformation nearest to the bolted end (NCDT-3) is 28 μm, and minimum deformation furthest away from the bolted end (NCDT-1) is 25.6 μm. For the same arrangement but with slotted block in contact with upper block (test E1) maximum and minimum deformations were measured as 28.5 μm and 26.2 μm respectively, and the FEA maximum and minimum deformations were 26.6 μm and 25 μm respectively. The FEA prediction of deformation results is very good with the maximum deviation of 4.6%. The close correlation on results between tests F1 and E1 indicates that regardless of the orientation of the slotted block, the magnitude of deformation remains approximately the same.

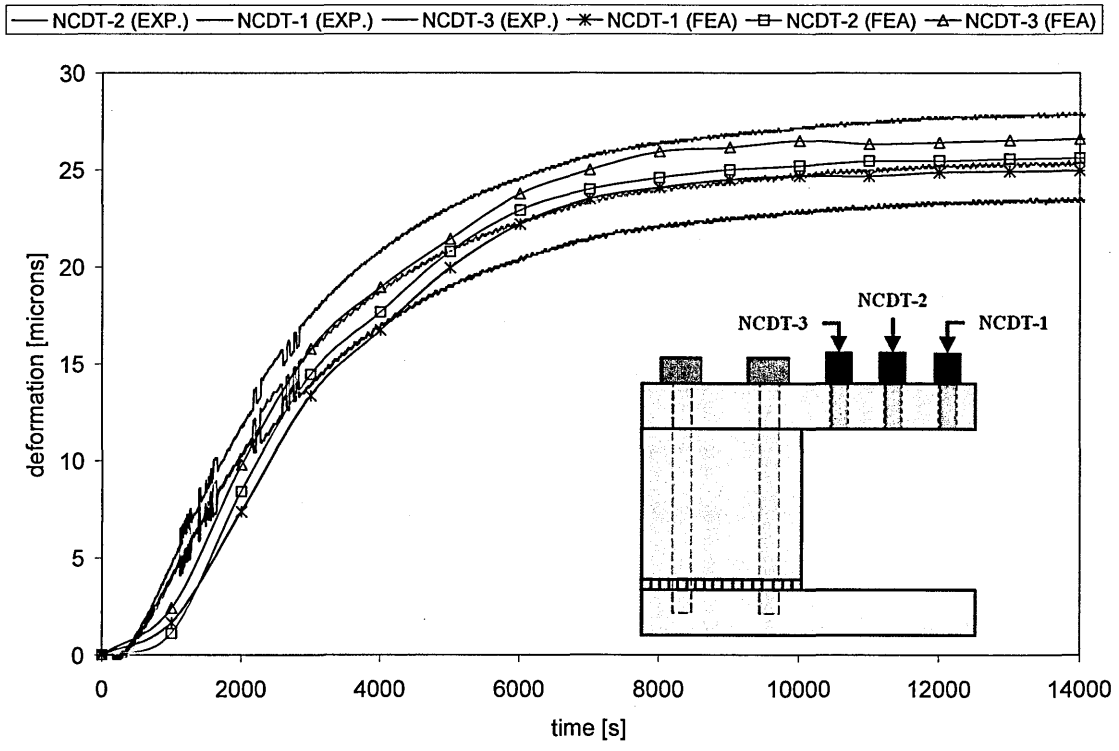

Figure 4-16. Transient deformation results, showing test F1

To investigate the effect of contact pressure on deformation results, the pressure was increased to 10 MPa (test F2), see Appendix J, Figure J-4. Again maximum deformation

takes place nearest to the bolted end (NCDT-3) and it is 28.9 μm and the minimum deformation furthest away from the bolted end (NCDT-1) is 26.4 μm. In comparison to test E2 that is slotted block in contact with upper block the maximum and minimum deformation were 26.95 μm and 25.6 μm respectively. The difference in deformation results between tests F2 and E2 is very small 1.95 μm and 0.8 μm for the maximum and minimum deformation respectively. The close correlation between test F2 and E2 indicate that the orientation of the slotted block relative to the heat source is insignificant on the deformation results.

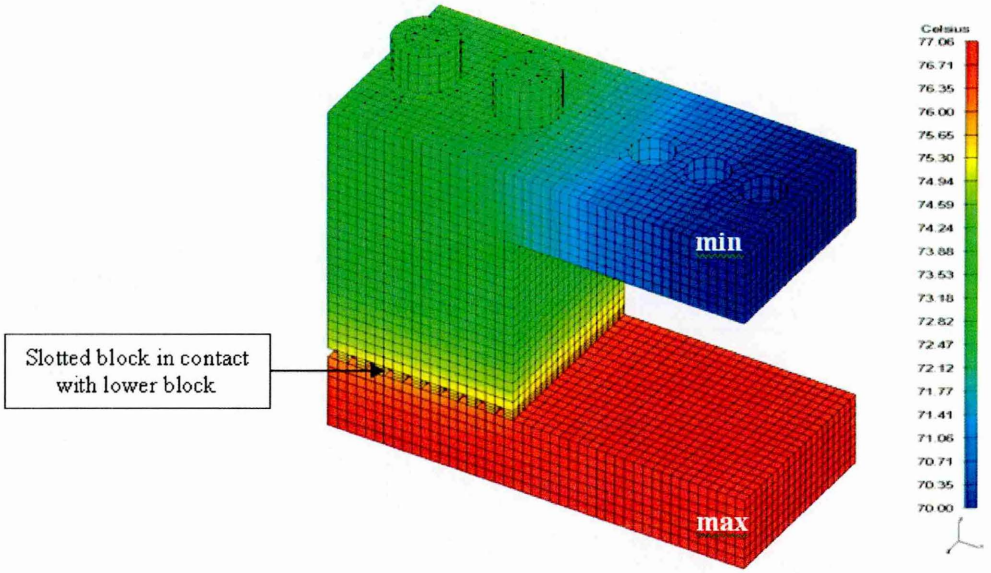

Figure 4-17. Temperature contours at steady-state showing test F1

4.2.3 Flat Block

In these set of tests a nominally flat block without slots was sandwiched between the same lower and upper blocks used in the previous arrangements. In this arrangement the apparent contact area formed at upper and lower interfaces is the same 0.0016 m^2. The resistance at the lower and upper interface is due to the contact surface topography alone. In the previous tests the resistance to heat flow across slotted interface was higher due to introduction of slots.

Test G1 represents the case when contact pressure of 5.64 MPa was exerted at the interface with air. FEA temperature and deformation contours at steady-state are shown in Figure 4-18 and Figure 4-19 respectively.

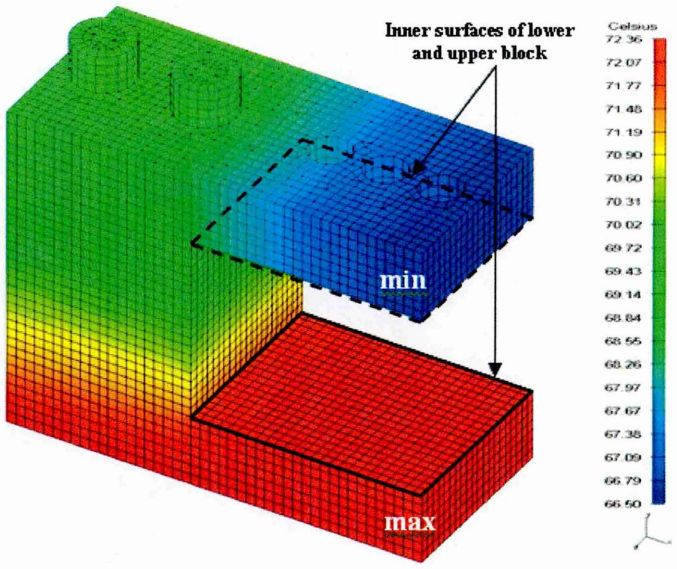

Figure 4-18. Temperature contours at steady-state showing test G1

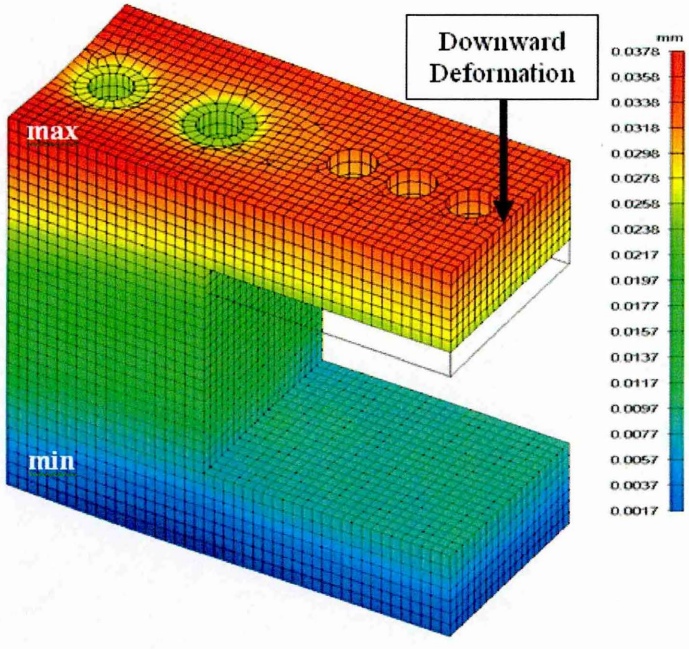

Figure 4-19. FEA deformation contours at steady-state showing test G1

Transient experimental and FEA deformation results are shown in Figure 4-20. Maximum deformation nearest to the bolted end (NCDT-3) is 30.11 μm, and minimum deformation furthest away from the bolted end (NCDT-1) is 27.78 μm. The FEA prediction of deformation results is good with the maximum of 26 μm and the minimum of 25.4 μm with the maximum deviation of 13.6% between experimental and FEA.

The contact pressure was increased to 10 MPa (tests G2). Again maximum deformation takes place nearest to the bolted end (NCDT-3) and it is 29.8 μm and the minimum deformation furthest away from bolted end (NCDT-1) is 27.3 μm, see Figure J-7. The maximum FEA deformation results were calculated as 22.5 μm and 21.8 μm respectively. In this test the discrepancy between experimental and FEA deformation results is 24.5%.

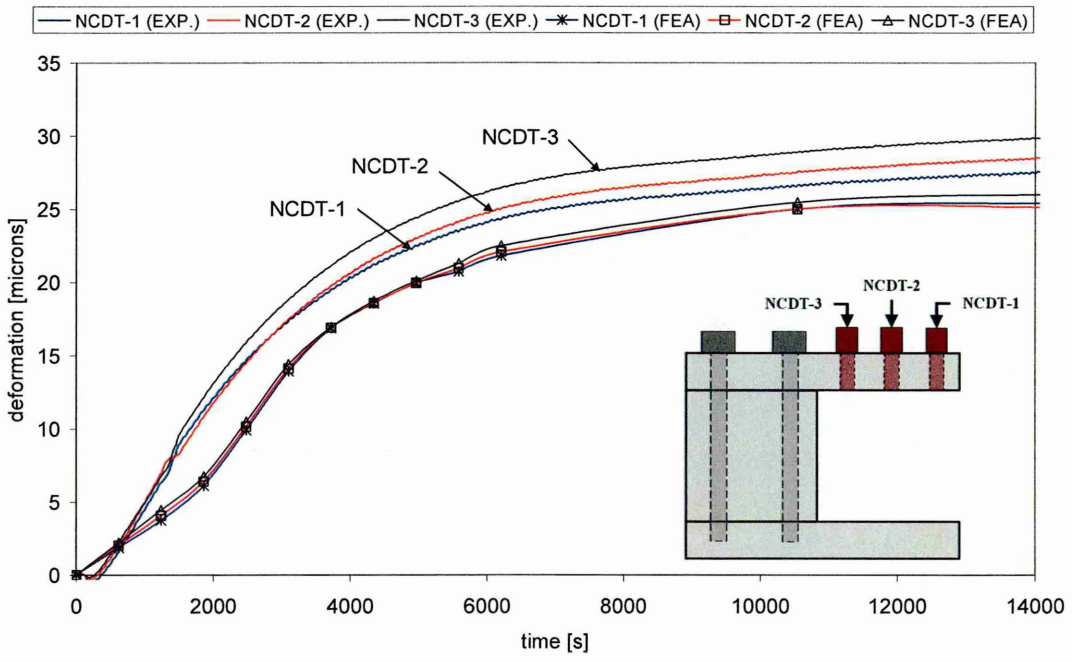

Figure 4-20. Transient deformation results, showing test G1

In all tests conducted herein, the maximum deformation is found to take place nearest to the bolted end, and the minimum deformation at the furthest end away from the bolted end. The results indicate that the assembly expands vertically upwards due to temperature rise in the blocks and it tilts clockwise. The tilt effect is shown in Figure 4-14.

4.3 Effect of Convection Coefficient on Heat Transfer Across Interface

Convection coefficient dictates heat loss from outside surfaces. In order to investigate the effect of convection coefficient on heat transfer across interfaces, test G1 that is flat block in contact with lower and upper blocks was simulated using FEA with five different convection coefficient values; 1 W/m^{2}°C, 5 W/m^{2}°C, 6 W/m^{2}°C, 7 W/m^{2}°C and 10 W/m^{2}°C.

Initially at steady-state under ambient temperature conditions the temperature difference between locations 2 and 3 is zero, see Figure 4-21.

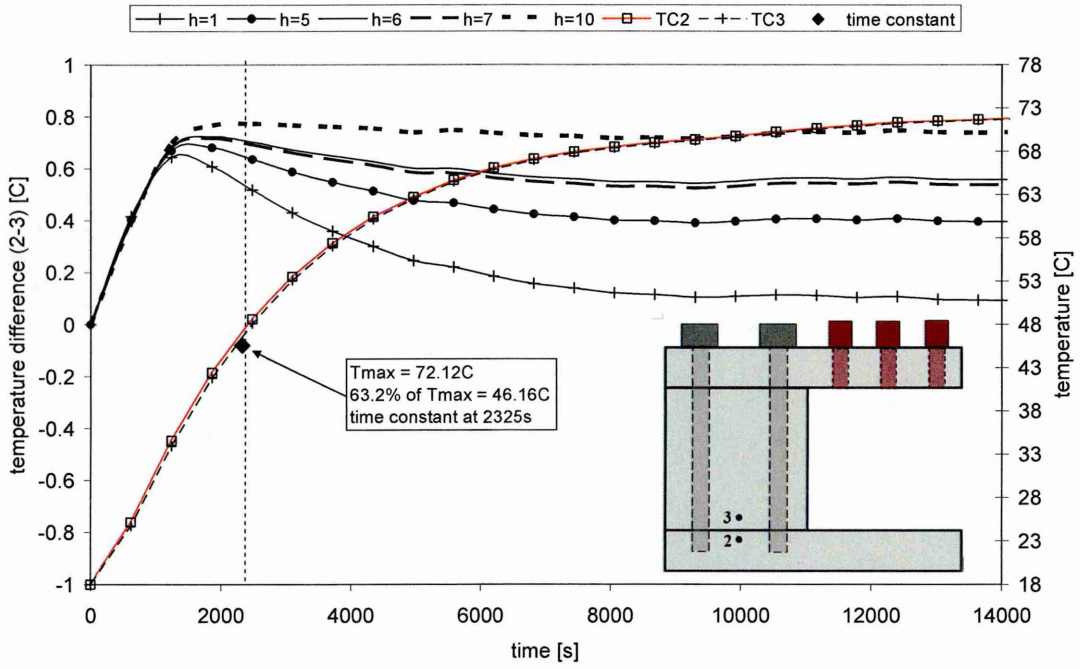

Figure 4-21. FEA results showing the effect of convection coefficient on heat transfer across interface

As heat flows into the lower block and across the interface and into the middle block, the difference in temperature between adjacent locations 2 and 3 changes from 0°C to around 0.7°C in around 1500s. During heating, the difference in temperature between locations 2 and 3 follows the same trend for differing convection coefficients. After around 1500s the temperature difference becomes less apparent and it continues to do so until the system reaches thermal steady-state conditions at around 9300s.

When convection coefficient is high, 10 W/m^{2}°C, the difference in temperature across interface (locations 2 and 3) after 1500s is very small, around 0.057°C and it remains

constant all the way until the system reaches thermal steady-state condition. Whereas when convection coefficient is an order of magnitude smaller, 1 $W/m^{2o}C$, the temperature across interface drops from 0.61°C at 1500s to 0.54°C at 9300s. Up to 2325s (the system's time constant) the difference is not as significant, as the system heats-up the effect of convection coefficient becomes more pronounced.

This finding indicates that convection coefficient is an important factor on heat transfer across interface. It's also important to note that the difference in temperature between results having convection coefficient of 6 $W/m^{2o}C$ and 7 $W/m^{2o}C$ is very small. This close correlation indicates that the actual average natural convection is in the region of 6 $W/m^{2o}C$ and 7 $W/m^{2o}C$.

5 Discussion

It has been demonstrated that the process of heat transfer across joint interfaces is complex because the thermal contact resistance is a function of surface topography, interface material, mechanical properties, geometrical configuration and thermal contact parameters.

Prediction and modelling of heat transfer across machine tool interfaces is important. This is because machine tools are built from many individual members jointed together. Heat generated at some point in a machine tool will be conducted along a member and across joint interface into another member. Due to the heat conducted across machine members the members will expand or deform and as the consequence the relative position between the tool and the workpiece will be affected.

5.1 Mathematical Models

Mathematical models for predicting heat transfer across conforming contacts are developed and advanced enough if factors such as changing ambient temperature, magnitude of convection coefficient, contaminant films at the interface, and changes in the contact parameters due to transient effect are assumed negligible. These models allow designers and researchers to predict thermal and mechanical behaviour of joint interfaces under different contact conditions. The accurate prediction can only be achieved if the heat input, convection coefficient, contact pressure, contact configuration, material properties and surface topography parameters are accurately known. In many situations the accurate determination of each factor is difficult, especially if heat transfer is transient.

If the contact is non-conforming the accurate determination of each interface parameter is often difficult and in many situations impossible. Due to the difficulties in accurately measuring the contact non-conformance, prediction of heat transfer across contact interface is more challenging as explained in Chapter 2. In such case only an approximate prediction can be achieved.

5.2 Two Block Analysis

5.2.1 Initial Setup

Initially a number of tests in the two block analysis were conducted with the hotplate placed at the bottom of the assembly, under ambient conditions as shown in Figure 5-1.

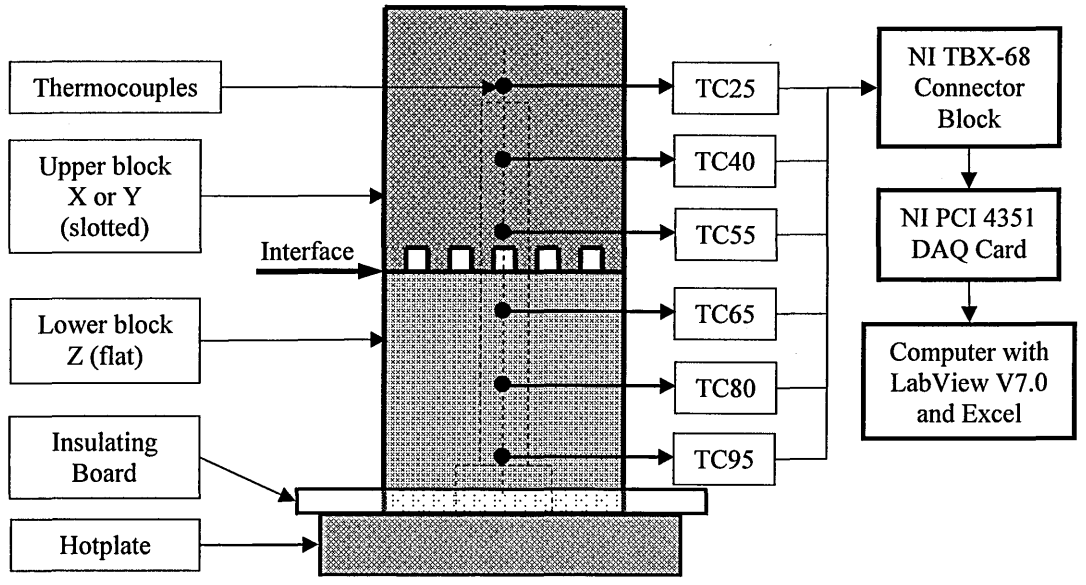

Figure 5-1. Initial experimental setup in two block analysis with the hotplate at the bottom of assembly

This experimental approach was much easier to setup and control than the experimental setup used throughout this research as shown in Figure 3-3. However, this approach with the hotplate at the bottom did not produce good results and the temperature drop across the interface was not so evident. At the early stages, heat flows faster into the lower block, across the interface and into the upper block. As heat builds up in the blocks, it starts to flow slower until the system reaches the steady-state at which point the blocks would have reached the maximum temperature. The top and the side surfaces of the blocks are exposed to the ambient, so a small amount of heat is lost by convection. Since the amount of heat loss by convection is small in comparison to the heat conducted, most of the heat is stored in the blocks and this creates the so called heat-sink effect.

5.2.2 *Factors Influencing Heat Transfer across Joint Interface*

In this research heat transfer and associated dimensional distortion of interfaces was investigated. The effect and the significance of surface topography, contact geometry, interface material and contact pressure were considered. The influence of each parameter on heat transfer across interfaces considered is discussed below.

a. Influence of Contact Geometry on Heat Transfer across Interface

The objective of carried out tests having different contact geometry arrangement was to investigate the importance of the spread of contact regions on heat transfer across interfaces. Two different contact geometry arrangements were considered. Both contact arrangements were investigated experimentally and numerically using FEA, see Figure 3-5, section 3.3.3 for configuration.

Numerical results indicated that the difference on overall heat transfer and temperature drop across the interface between the two contact geometry studied is extremely small and can be regarded as insignificant. Figure 5-2 shows the temperature profile across and near the interface for the two contact geometry arrangements. As it can be seen in the Figure 5-2 the two lines follow the same trend and are extremely close to each other with calculated maximum deviation of 0.15%.

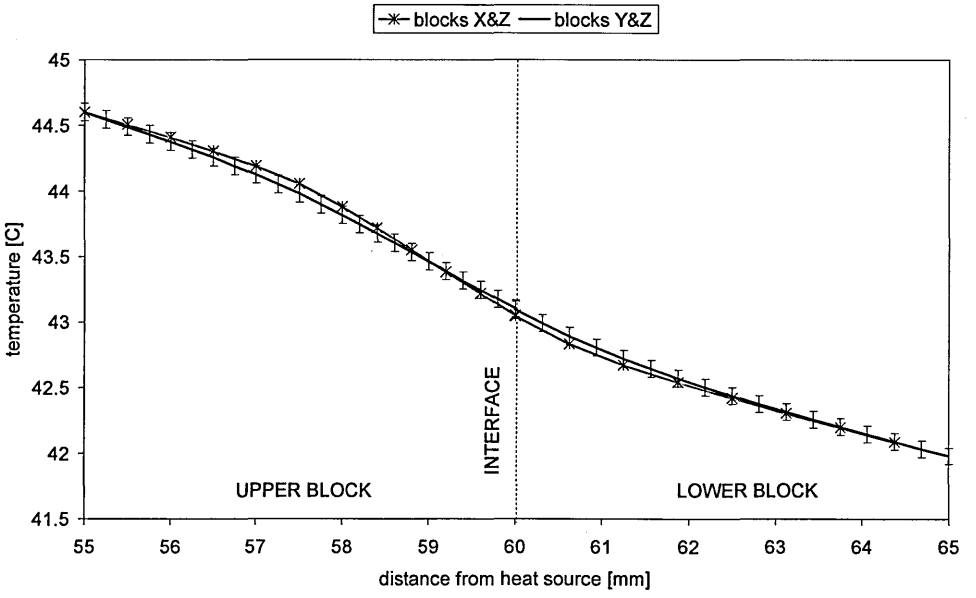

Figure 5-2. FEA temperature profile near the interface for both contact geometry arrangements used in two block analysis

This is due to the fact that the width of the ridges being perpendicular to heat flow lines, so the overall heat loss due to convection from the outer surfaces of the ridges is the same in both contact arrangements. Another explanation is that the ratio of the volume removed (3.6E-06 m^3) due to introduction of slots to the volume of the conducting ridges (3.6E-06 m^3) is the same in both arrangements.

b. Influence of Contact Conformance on Heat Transfer across Interface

Increase in contact pressure showed a bigger effect in a situation where the interface was bare with air, but less effect when grease was used at the interface. This can be explained by the fact that when the interface is clean there are more surface asperities in contact. As a result, more heat flows across the interface because the thermal conductivity of parent material steel is higher than that for thermal grease.

It has been shown that if the interface material has a smaller thermal conductivity then the parent material, and if the interface material is thicker than the surface roughness, then the thermal contact resistance increases. Whereas when contact has poorer conformance, then the introduction of interface material is beneficial if heat flow across the interface is to be encouraged. This is because the bulk gaps present at the interface due to contact non-conformance are filled with a material with a higher thermal conductivity than air.

It was also found that surface roughness alone has a very small influence on heat transfer across the interface, for the minimum and maximum contact pressures of 5.64 MPa and 14.2 MPa respectively. The most significant surface topography parameter is found to be the surface form error.

When the mean surface form error of the interface is 13.49 μm the insertion of thermal grease at the interface does not significantly change the heat transfer. Whereas when the mean surface form error of the interface is 20.32 μm the insertion of thermal grease at the interface creates a significant change for the same contact pressures. Therefore in a situation where heat flow across the interface is to be encouraged, special attention should be paid in achieving low levels of waviness and flatness deviations.

If the waviness and the flatness deviations are higher than the surface roughness then another approach to encourage heat transfer is to use fluids with higher thermal conductivities than air such as thermal greases. However, special care must be taken

when using thermal greases as interface material, as shown in Section 4.1. It was found that thermal grease does not always improve heat transfer across the interface. If the thermal grease layer wetting the contacting surfaces is too thick or thicker than the surface roughness and the contact pressure is not too high, then the number of surface asperities coming into contact would be smaller than when thermal grease is absent. This is because the thermal grease covers the whole contacting surface hence preventing the contact between the asperities. This way thermal contact resistance increases because thermal conductivity of thermal grease is lower than parent material steel.

c. Influence of Convection Coefficient on Heat Transfer across Interface

It was found using FEA that when the convection coefficient is high (10 $W/m^{2o}C$) the temperature drop across the interface is insignificant after the thermal steady-state condition. When convection coefficient is an order of magnitude smaller (1 $W/m^{2o}C$) the temperature drops from 0.61°C at 1500s to 0.54°C at 9300s. Up to the assembly's time constant at 2325s the difference was not as pronounced. As heat flows across the interface up to the steady-state conditions, the effect of the convection coefficient became more pronounced.

The assembly was further simulated using three other convection coefficients; 5 $W/m^{2o}C$, 6 $W/m^{2o}C$ and 7 $W/m^{2o}C$. It was found that although the difference between the three coefficients is one unit, the temperature drop across the interface when the convection coefficient was 5 $W/m^{2o}C$ was further away from 6 $W/m^{2o}C$ and 7 $W/m^{2o}C$, see Figure 4-21.

This finding indicates that the convection coefficient is an important factor on heat transfer across the interface. This close correlation between results having different convection coefficient indicates that the actual average natural convection is in the region of 6 $W/m^{2o}C$ to 7 $W/m^{2o}C$, see Appendix A for details. This approach to optimization could be used in systems under thermal investigation in order to calculate the actual convection coefficient.

5.2.3 FEA Thermal Coupling

a. Conforming Contact

It was found that if the contact at the interface is conforming, the FEA modelling can be an accurate representation of the real situation if transient effects are ignored. In order for the FEA modelling to work the surface roughness, the contact pressure, the interface material and material properties must be accurately known. Once the above parameters are known, the thermal contact resistance can be calculated using the appropriate mathematical models for conforming contact, see Section 2.13.1. Calculated thermal contact resistance can then be directly used in the FEA modelling.

b. Non-conforming Contact

If the contact at the interface is non-conforming an accurate definition of the contact parameters is impossible. In such cases only an approximate thermal coupling can be defined. An approximation can be done by calculating thermal contact resistance using appropriate mathematical models and using the values to couple the interfaces, see Section 2.13.2. This way the calculated thermal contact values would be assumed constant across the whole contact region. Coupling the contact non-conformance using approximate values would therefore over or underestimate the thermal contact resistance, producing inaccurate results. This was shown in Section 4.1.1(b) where the temperature drop across the interface was 4.41°C and 2.3°C for experimental and FEA prediction respectively. The discrepancy between experimental and FEA results is 91%.

Other aspects that complicate thermal contact are the transient effects. In the experiments carried out here, steel blocks were held together using high tensile steel bolts. Since the thermal conductivity and the coefficient of thermal expansion of the bolts were lower than blocks then as heat flows across the interface the blocks expand more than the bolts. Due to the difference in coefficient of thermal expansion the contact pressure increased with increased temperature at the interface. As the contact pressure increases, the real area of contact increases forcing thermal contact resistance to drop. This shows that the contact resistance is transient as a function of heat transfer across the interface.

5.3 Three Block Analysis

5.3.1 Thermal Deformation

It has been shown that FEA prediction of thermal deformation is achievable and comparable to the experimental results in terms of magnitude and direction. Each steel block and consequently the whole assembly expands with an increase in the temperature, see Section 4.2. The amount of expansion depends on material's coefficient of thermal expansion and the difference in the temperature from the steady-state condition. The direction of deformation depends on factors such as location and the magnitude of constraints applied by the bolts.

The lower block expanded the most because it was the closest to the heat source where the temperature was the highest. As the lower block expanded it pushed the middle block, the Zerodur® block and consequently the upper block vertically upwards. The bolts held the blocks together and partly constrained them from expanding upwards relative to each other.

When a contact pressure of 5.64 MPa was exerted at the interface, the maximum thermal deformation was recorded by the sensor nearest to the bolted end and was found to be 28.3 μm and 20.3 μm for experimental and FEA respectively. Increased contact pressure to 10 MPa reduced maximum deformation to 26 μm (8.1%) and 17 μm (16.2%) for experimental and FEA respectively, see Section 4.2.1.

Above results indicate that the contact pressure exerted by the applied torque to the bolts, influences thermal deformation of the structure. It was found that FEA simulation underestimates the magnitude of deformation compared to experimental results. It was also found that the FEA simulation overestimate the reduction in the deformation results with increase in contact pressure. The discrepancy between experimental and FEA prediction are due mainly to uncertainties within the boundary conditions in the modelling

Three contact geometry arrangements were considered; see Figure 3-15 to Figure 3-17 . When the slotted block was placed in contact with the upper block the maximum deformation recorded by the NCDT-3 closest to the bolted end was 28.5 μm. When the slotted block was placed in contact with the lower block the maximum deformation was

measured to be 28 μm. When the flat block was used the maximum deformation was 30.11 μm.

The maximum discrepancy between results is 2.11 μm or 7%. This discrepancy between results is due to the uncertainties within the NCDT's which were found to be 1.5 μm, see Section 4.2.3. The 0.61 μm is related to the uncertainties with the instrumentation see Appendix H.

a. Influence of Contact Pressure on Deformation Results

It was found that the contact pressure has a significant effect on deformation results. When contact pressure of 5.64 MPa is exerted at the interface, the maximum thermal deformation of 28.3 μm and 20.3 μm for experimental and FEA respectively (tests E1), as shown in Figure 4-13.

Increasing interface contact pressure to 10 MPa reduced maximum deformation by 2.3 μm to 26 μm and by 3.3 μm to 17 μm for experimental and FEA respectively (test E2). This is an 8.12% and 16% reduction in deformation results for experimental and FEA respectively. FEA prediction overestimates the reduction in deformation by about 8% compared to experimental results.

This effect of contact pressure on deformation can be explained by the fact that the relative deformation of the upper block to the lower block is constrained by the opposite counter-acting force applied by the bolts. Therefore increased contact pressure is the consequence of increased bolt preload.

Initially under ambient temperature conditions the contact pressures of 5.64 MPa in test E1 and 10 MPa in E2 are exerted by applied torque to the bolts. As temperature increased, the expansion of assembly including bolts and consequently the contact pressure increased until the thermal steady-state condition was reached. At thermal steady-state condition the maximum interface contact pressures of 40 MPa and 70 MPa representing tests E1 and E2 respectively, see Figure 5-3.

The contact pressure increases linearly from initial pressure to the final pressure at thermal steady-state condition, that is the mean ratios between the final and initial contact pressures is 7 MPa.

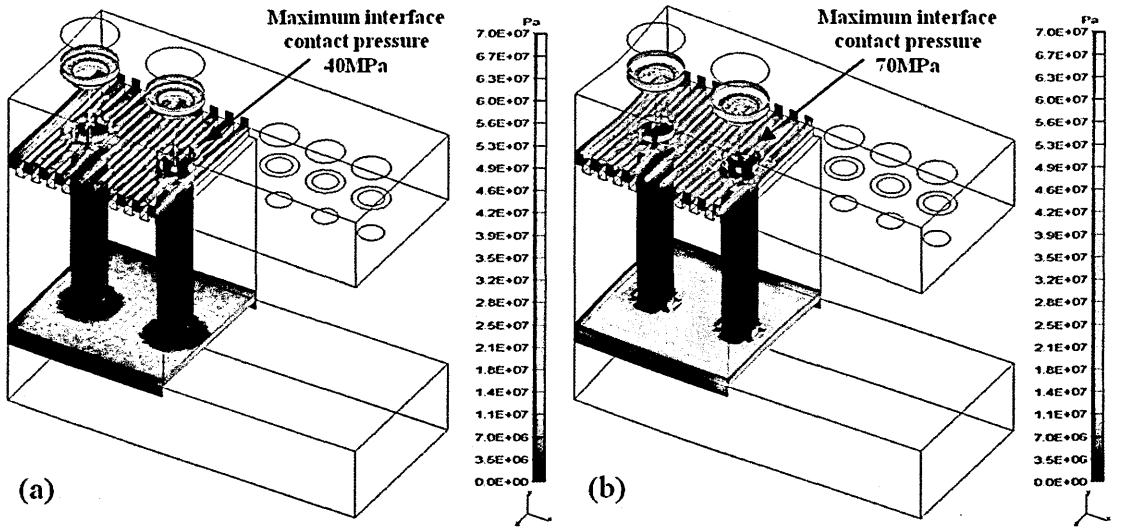

Figure 5-3. Magnitude of contact pressure under thermal steady-state conditions; (a) tests E1 with initial contact pressure of 5.64 MPa; (b) test E2 with initial contact pressure of 10 MPa

b. Influence of Thermal Grease on Deformation Results

Interface material plays a significant part in heat transfer across the contact interface. This fact was studied and presented in Section 4.1. The level of influence depends on the type and thickness of interface material. However, the thermal deformation has not been rigorously studied in the past. A number of tests were conducted in order to investigate the thermal deformation of bodies in contact having thermal grease at the interface.

First test E3 where the slotted block was placed in contact with the upper block, contact pressure 5.64 MPa with thermal grease at the interface. Transient thermal deformation results for tests E3 are shown in Figure J-2. Maximum deformation nearest to the bolted end (NCDT-3) was 29.88 μm, and minimum deformation furthest away from the bolted end (NCDT-1) was 26.46 μm, which is 3.42 μm or 11.4% reduction in deformation.

For the same contact arrangement as test E3, in test E1 (no grease at the interface) the maximum deformation was found to be 28.5 μm and the minimum deformation of 26.2 μm. The difference between test E1 having bare interface and tests E3 having thermal grease at interface is very small, 1.38 μm and 0.26 μm for maximum and minimum deformation respectively. This small difference between results is only 4.6% and 0.98% respectively with standard deviation of 0.97 and 0.18 respectively.

Second test E4 where the slotted block was placed in contact with the upper block, contact pressure 10 MPa with thermal grease at the interface. Transient thermal deformation results for tests E4 is shown in Figure J-3. Maximum deformation was 32.42 μm, and minimum deformation was 25.97 μm.

In test E2 having bare interface with air the maximum deformation was found to be 26.95 μm and the minimum deformation of 25.68 μm. The difference between tests E4 and E2 is 5.47 μm and 0.29 μm for NCDT-3 and NCDT-1 respectively.

Results show that the insertion of grease at interface does not significantly influence thermal deformation. This is due to the fact that the hardness and the thermal conductivity of the thermal grease are many times lower than the parent material steel.

6 Conclusions

This research was concerned primarily with investigating experimentally and predicting numerically heat transfer and associated dimensional distortion of bolted steel blocks. Factors such as contact pressure, interface material, and contact geometry configuration under surrounding ambient conditions were considered. Bolted interface configuration, contact geometry configuration and the effect of convection coefficient were factors that have not been studied before.

In recent years mathematical models to predict heat transfer across conforming contacts have advanced tremendously. Some models to predict heat transfer across non-conforming contact exist, but can not be used in every situation, and appear to be accurate only under well defined and controlled surface form deviation.

The accuracy of FEA models were tested and validated using experimental measurements. It was shown that the FEA modelling of conforming joint interfaces is accurate if surface roughness, contact pressure and the interface material are accurately known. However, the FEA of non-conforming contact is not possible due to the difficulties in defining and modelling the actual contact regions and the deviations due to surface form error. Experimental methods are important because they are used in the development of mathematical and numerical models. Numerical models are only as accurate as the mathematical models that characterize them, and can not predict a situation where the algorithms representing them are not sufficiently advanced. There are several conclusions and contributions to knowledge that can be drawn from this research:

1. It was found using FEA that convection coefficient is an important factor on the heat transfer across the interface. When the convection coefficient was high (10 $W/m^{2o}C$), the temperature drop across the interface was found to be insignificant. Whereas, when the convection coefficient was an order of magnitude smaller (1 $W/m^{2o}C$) the temperature drop was more pronounced. Furthermore, the effect of convection coefficient on heat transfer across interface became more pronounced after the assembly's thermal time constant. In many thermal problems the accurate determination of convection coefficient is difficult. In such cases the convection

coefficient could be calculated by implementing the same optimization approach used in this research.

2. It has been shown that the spread of contact ridges does not influence heat transfer across the interface for the same overall contact area. This is due to the fact that the widths of the ridges were perpendicular to heat flow lines and the ratio of the volume removed due to introduction of slots to the volume of the conducting ridges was the same in both arrangements.

3. Surface roughness alone has a very small influence on heat transfer across the interface, for the minimum and maximum contact pressures of 5.64 MPa and 14.2 MPa respectively. The most significant surface topography parameter was found to be the surface form error. When the mean surface form error of the interface was 13.49 μm the insertion of thermal grease at the interface did not significantly change the heat transfer. Whereas, when the mean surface form error of the interface was 20.32 μm, the insertion of thermal grease at the interface created a significant change for the same contact pressures.

4. If the contact formed by metal bodies is conforming and rough, then the overall contact resistance can be calculated using mathematical models - calculated contact resistance can then be used in numerical modelling to couple the contact interface. Whereas if the contact is non-conforming the surface roughness alone does not accurately represent the contact. In such case, the overall contact resistance can be approximately calculated. Direct coupling in numerical modelling can be done but the coupling would be approximate, which would lead to inaccurate prediction of thermal contact and hence heat flow.

5. An increase in contact pressure showed a bigger effect in a situation where the interface was bare with air, but less effect when grease was used at the interface. This can be explained by the fact that when the interface is clean there are more surface asperities in contact. As a result, more heat flows across the interface because the thermal conductivity of the parent material is higher than that of thermal grease.

6. When the interface material has a smaller thermal conductivity then the parent material, and if the interface material is thicker than the surface roughness, then the

thermal contact resistance increases. Whereas when contact has poorer conformance, then the introduction of interface material is beneficial if heat flow across the interface is to be encouraged. This is because the bulk gaps present at the interface due to contact non-conformance are filled with a material with a higher thermal conductivity than air.

7. Numerical prediction of transient thermal deformation of bodies in contact underestimated the magnitude of deformation compared to experimental results. The maximum discrepancy between experimental and numerical results was found to be 13.6%. This is partly due to the uncertainties with the measuring system and mainly due to the uncertainties with the boundary conditions in the numerical modelling. It was found that the insertion of grease at interface does not significantly influence thermal deformation. Whereas contact pressure was found to have a significant effect on deformation results. For increased contact pressure from 40 MPa to 70 MPa at thermal steady-state the maximum deformation dropped from 20.3 μm to 17 μm, this is a 16% reduction in deformation results.

7 Recommendations for Future Work

This research has demonstrated the difficulties associated with predicting and modelling heat transfer across joint interfaces. The complications arise due to the number of factors that contribute to the heat transfer and thermal deformation of bolted interfaces. Therefore, the following recommendations can be drawn:

1. Contact conformance was found to be one of the most significant factors especially in situation where heat flow across interface is to be encouraged. Factors such as surface roughness, surface waviness and flatness were investigated. If the contact is conforming then waviness and flatness deviations are ignored in the analysis. Interfaces having different levels of waviness and flatness deviations should be further investigated.

2. The contact geometry considered in this research was designed to have contacting ridges along the whole contact interface. Two widths of contact ridges were investigated, and it was found that the width of contact ridges does not influence the overall heat transfer. This is due to the slots having the same depth in both arrangements. Theoretically speaking the depth of slots being parallel to heat flow lines should have more influence on heat transfer across the interface. This is because the volume of the conducting material would be reduced and hence more heat lost by convection. Experimental and numerical investigation should be conducted in order to validate the effect of the slots depth on heat transfer across interfaces. The concept indicated here could be helpful to give an insight to any future work on similar interface design. The introduction of slots at interface could be used to accommodate other materials having different thermal properties. For instance fluid coolants could be feed through slots to cool or control the heat flow across the interface. By monitoring and controlling the fluid flow rate and fluid temperature, heat flow could be reduced or controlled to suit a given application.

3. It was shown using FEA that heat transfer across interfaces is affected by the convection coefficient from outer surfaces. Five values of convection coefficients were simulated using FEA. The bigger the difference between the specimens's surface temperature and the surrounding ambient temperature the higher the

convection coefficient. Experimental investigation should thus be carried out under controlled surrounding temperature conditions in order to validate the effects.

4. In the two block analysis, three levels of contact pressure were considered. It has been shown that contact pressure plays a significant role on heat transfer across interfaces. This is especially evident when the contact conformance is poor. The contact pressure could be extended to include different levels of magnitude.

5. It has been shown that contact pressure has an influence on thermal deformation of bolted interfaces. This is especially evident if the assembly is made of different materials with different coefficient of thermal expansion. Whereas, thermal grease as interface material was found to have negligible effect on thermal deformation results. The contact pressure could be extended to include different levels of magnitude.

6. Modelling of interfaces using FEA is important for machine tool applications. It has been shown that the accuracy of prediction of heat transfer across interfaces is highly dependant on the interface contact conformance. The accurate modelling of non-conformance is impossible mainly due to the difficulties with predicting the contact regions. The other difficulty is related to the transient effects of heat transfer across interfaces. As heat flows across the interfaces held under some pressure, the contact regions and the contact pressure will either increase or decrease. This will force the TCR to either drop or increase and consequently affect the amount of heat transfer. If for a given application and situation the contact parameters, the heat flow, changes in contact pressure and the contact regions are accurately known, the modelling can be an accurate representation of the real situation. Therefore the modelling of non-conformance should be studied further taking into account the transient effects on heat transfer across interfaces.

7. In the two block analysis the heat was applied on the top surface of the upper block. The assembly was then placed on top of a steel block partially submerged in flowing water. Initial tests were conducted where heat was applied at the bottom of the assembly using the same hotplate. This approach did not produce good results and the temperature drop across the interface was not so evident. This approach should

be studied further in order to understand the effect of heat-sinks on heat transfer across interfaces.

Reference List

[1] Srivastava, A.K., Veldhuis, S.C. and Elbestawit, M.A. (1995), 'Modelling Geometric and Thermal Errors in a five-axis CNC Machine Tool'. *International Journal of Machine Tools & Manufacture,* Vol. 35/9, pp. 1321-1337.

[2] Ramesh, R., Mannan, M.A. and Poo, A.N. (2000), 'Error compensation in machine tools -- a review: Part II: thermal errors', *International Journal of Machine Tools and Manufacture,* Vol. 40, No. 9, pp. 1257-1284.

[3] Weck, M., McKeown, P., Bonse, R. and Herbst, U. (1995), 'Reduction and Compensation of Thermal Errors in Machine Tools', *Annals of the CIRP,* Vol. 44/2, pp. 589-598.

[4] Bryan, J.B. (1990), 'International Status of Thermal Error Research', *Annals of the CIRP,* Vol. 39/2, pp. 645-655.

[5] Corbett. J., Mckeown. P. A., Peggs. G. N. and Whatmore. R. 'Nanotechnology: International Developments and Emerging Products.' *Annals of the CIRP, Keynote Papers,* Vol. 49/2/2000, pp. 523-545.

[6] McKeown, P.A. (1988), 'The Development of High Precision CNC Machine Tools.' *Journal of Mechanical Working Technology,* Vol. 17, pp. 225-236.

[7] ANSI Standard B89.6.2 (1973), 'Temperature and Humidity Environment for Dimensional Measurement.' *ASME 345 E. 47th Street, New York.*

[8] Donaldson, R.R. (1972), 'A Simple Method for Separating Spindle Error from Test Ball Roundness Error.' *Annals of the CIRP,* Vol. 21, pp. 125-126.

[9] Loxham, J. (1970), '"The Commercial Value of Investigations into Repeatability", *Cranfield Unit for Precision Engineering, Bedford, England.,*

[10] Bryan, J. B. (1993), 'The Deterministic Approach in Metrology and Manufacturing'. The American Society of Mechanical Engineers, International Forum on Dimensional Tolerancing and Metrology. pp. 1-12.

[11] Taeweon, G. (1997), Modelling and Evaluation of Time-Varying Thermal Errors in Machine Tool Elements, PhD thesis, Cranfield University, UK.

[12] Bryan, J. B., Loewen, E. G. (1974), 'The Limit of Accuracy of Machine Tools', International Conference on Production Engineering, Tokyo, pp.1-9.

[13] Weck, M. (1984), Handbook of Machine Tools: Metrological Analysis and Performance Tests. John Wiley & Sons, New York, ISBN: 0471262269.

[14] Cornell University Ergonomics Web (2006), *Ambient Environment: Thermal Conditions,* available at: http://ergo.human.cornell.edu/studentdownloads/DEA350notes/Thermal/thcondnotes.html (accessed 2006).

[15] Chen, J.S. (1995), 'Computer-aided accuracy enhancement for multi-axis CNC machine tool.' *International Journal of Machine Tools and Manufacture,* Vol. 35, pp. 593-605.

[16] Vanherck, P. Dehaes, J. and Nuttin, M. (1997), 'Compensation of thermal deformations on machine tools with neural networks.' *Computers in Industry,* vol. 33/1, pp. 119-125.

[17] Ramesh, R., Mannan, M.A. and Poo, A.N. (2000), 'Error compensation in machine tools -- a review: Part I: geometric, cutting-force induced and fixture-dependent errors', *International Journal of Machine Tools and Manufacture,* Vol. 40, No. 9, pp. 1235-1256.

[18] Shore, P. (2006), *Precision Engineering Short Course Lecture Notes*, Cranfield University, Bedford, UK.

[19] Kim, J.-J., Jeong, Y.H. and Cho, D.-W. (2004), 'Thermal behavior of a machine tool equipped with linear motors', *International Journal of Machine Tools and Manufacture,* Vol. 44, No. 7-8, pp. 749-758.

[20] Jang, C., Kim, J. and Kim, Y. (2002), 'Thermal resistance modeling of linear motor driven stages for chip mounter applications.', International *Society Conference on Thermal Phenomena.,* pp. 77-84.

[21] Yang, J., Yuan, J. and Ni, J. (1999), 'thermal error mode analysis and robust modelling for error compensation on a CNC turning centre. ', International *Journal of Machine Tools and Manufacture,* Vol. 39, pp. 1367-1381.

[22] Yun, W.S., Kim, S.K. and Cho, D.W. (1999), 'thermal error analysis for a CNC lathe feed drive system.' International *Journal of Machine Tools and Manufacture,* Vol. 39, pp. 1087-1101.

[23] Harris, T. A. (1991), Rolling Bearing Analysis, 3rd ed., John Wiley & Sons, Inc., New York, ISBN 0471513490.

[24] Min, X., Shuyun, J. and Ying, C. (2006), 'An improved thermal model for machine tool bearings', International Journal of Machine Tools and Manufacture, Vol. 47, Issue 1, pp. 53-62.

[25] Kim, S.M. and Lee, S.K. (2001), 'Prediction of thermo-elastic behaviour in a spindle-bearing system considering bearing surroundings', *International Journal of Machine Tools and Manufacture,* Vol. 41, pp. 809-831.

[26] Koch, A. (1995), *Steigerung der Hochstdrehzahl von Schragkugellagern bei Oliminimalmengenschmierung.* PhD thesis, University of RWTH Aachen., RWTH Aachen.

[27] Bossmanns, B. and Tu, J.F. (1999), 'A thermal model for high speed motorized spindles.', International *Journal of Machine Tools & Manufacture.,* Vol. 39, pp. 1345-1366.

[28] Bossmanns, B. and Tu, J.F. (2001), 'A power flow model for high speed motorized spindles--heat generation characterization.', Transactions *of the ASME, Journal of Manufacturing Science and Engineering.,* Vol. 123, pp. 494-505.

[29] Lin, C.-W., Tu, J.F. and Kamman, J. (2003), 'An integrated thermo-mechanical-dynamic model to characterize motorized machine tool spindles during very high speed rotation.', International *Journal of Machine Tools & Manufacture.,* Vol. 43, pp. 1035-1050.

[30] Choi, J.K. and Lee, D.G. (1998), 'Thermal characteristics of the spindle bearing system with a gear located on the bearing span', International *Journal of Machine Tools & Manufacturing.,* Vol. 38, pp. 1017-1030.

[31] Mladenov, D. (2002) 'Assessment and Compensation of Errors in CNC Turning'. University of Manchester, Institute of Science and Technology.

[32] Jedrzejewski, J. and Morzycki, W. (1992), 'A new approach to modelling thermal behaviour of a machine tool under service conditions.', Annals *of the CIRP,* Vol. 41(1), pp. 455-458.

[33] Jedrzejewski, J., Kaczmarek, J., Kowal, Z. and Winiarski, Z. (1990), 'Numerical optimisation of thermal behaviour of machine tools.' *Annals of the CIRP,* Vol. 39(1), pp. 379-282.

[34] Venugopal, R. and Barash, M. (1986), 'Thermal Effects on the Accuracy of Numerically Controlled Machine Tools.', Annals *of the CIRP.,* Vol. 35(1), pp. 255-258.

[35] K-D Kim, M-S Kim and S-C Chung. (2004), 'Real-time compensatory control of thermal errors for high-speed machine tools', *Proceedings of the Institution of Mechanical Engineers,* Vol. 218, No. 8, pp. 913.

[36] Vanherck, P., Dehaes, J. and Nuttin, M. (1997), 'Compensation of thermal deformations in machine tools with neural nets', *Computers in Industry,* Vol. 33, No. 1, pp. 119.

[37] Suh, J.D. and Lee, D.G. (2004), 'Thermal characteristics of composite sandwich structures for machine tool moving body applications', *Composite Structures.,* Vol. 66, pp. 429-438.

[38] McKeown, P.A., Weck, M. and Bonse, R. (1995),'Reduction and Compensation of Thermal Errors in Machine Tools', *Annals of the CIRP,* Vol. 44(2).

[39] Donmez, M.A. , Liu, C.R. and Barash, M.M. (1986), 'General Methodology for Machine Tool Accuracy Enhancement by Error Compensation.' *Precision Engineering,* Vol. 8(4), pp. 187-196.

[40] Ichimiya, R. (1980), "Compensation for Thermal Deformation of Milling Machine," Proc. Conf. Numerical Methods in Machine Tool Design, Wroclaw, Poland, pp. 39–49.

[41] Weck, M., Schuze, O., and Michels, F. (1994), ASME Symposium on Intelligent Machine Tool Systems.

[42] Moriwaki, T. and Zhao, C. (1992), Prediction of Thermal Deformation of

Machining Center by Applying Neural Network', Trans. Japn. Soc. Mech. Eng., Vol.58, No.550, pp.1932-1937.

[43] Moriwaki, T. (1988), 'Thermal Deformation and its On-Line Compensation of Hydrostatically Supported Precision Spindle. Annals of the CIRP, Vol. 37(1), pp. 393-396

[44] Takeuchi, Y., Okubo, N., and Sata, T. (1976) 'On-Line Control of Thermal Deformation of Machine Tool Structure by Measurement of Temperature Distribution., Japanese Society for Precision Engineering, Vol.42, No.11.

[45] Attia, M.H. and Fraser, S.A. (1999), 'Generalized modelling methodology for optimized real-time compensation of thermal deformation of machine tools and CMM structures.', International *Journal of Machine Tools & Manufacture,* Vol. 39, pp. 1001-1016.

[46] Attia, M.H., Fraser, S. and Osman, M.O.M. (1999), 'On-line estimation of time-variant thermal load applied to machine tool structures using a s-domain inverse solution', *International Journal of Machine Tools and Manufacture,* Vol. 39, No. 6, pp. 985-1000.

[47] Chen, J.S. and Chiou, G. (1995), 'Quick testing and modeling of thermally-induced errors of CNC machine tools', *International Journal of Machine Tools and Manufacture,* Vol. 35, No. 7, pp. 1063-1074.

[48] Chen, J.S., Yuan, J.X., Ni, J. and Wu, S.M. (1991), 'Sensors, controls and quality issues in manufacturing.' ASME, vol. 55, pp. 241-249.

[49] Srinivasa, N., Ziegert, J.C. and Smith, S. (1992), 'Sympozium of Flexible Automation', ASME, Vol. 1, pp. 203.

[50] Kang, Y., Chang, C.-W., Huang, Y., Hsu, C.-L. and Nieh, I.-F. (2007), 'Modification of a neural network utilizing hybrid filters for the compensation of thermal deformation in machine tools.', International *Journal of Machine Tools & Manufacture,* Vol 47/2, pp. 376-387.

[51] University of Texas (2006), *Quasi-Static processes,* available at: http://farside.ph.utexas.edu/teaching/sm1/lectures/node35.html (accessed 2006).

[52] Yang, H. and Ni, J. (2003), 'Dynamic Modelling for Machine Tool Thermal Error Compensation.', Journal *of Manufacturing Science and Engineering (ASME).*, Vol. 125, pp. 245-254.

[53] Yang, S., Yuan, J. and Ni, J. (1996), 'The improvement of Thermal Error Modeling and Compensation on Machine Tools by Neural Network.', International *Journal of Machine Tools & Manufacture.*, Vol. 36(4), pp. 527-537.

[54] Attia, M.H. and Kops, L. (1979), 'Computer Simulation of Nonlinear Thermoelastic Behavior of a Joint in Machine Tool Structure and its Effect on Thermal Deformation', Journal *of Engineering for Industry,* Vol. 101, pp. 355-361.

[55] Donmez, M. (1985), 'A General Methodology for Machine Tool Accuracy Enhancement: Theory, Application and Implementation', PhD dissertation, Purdue University, West Lafayette, IN, USA, 1985.

[56] Gashi, B. and Shore, P. (2006), 'Thermal Analysis of Joint Interfaces in Machine Tools'. Proceedings of 6th euspen International Conference, Vol. 1, pp. 269-272, Baden bei Wien, May 2006, Austria.

[57] Cooper, M.G., Mikic, B.B. and Yovanovich, M.M. (1969), 'Thermal contact conductance.', International *Journal of Heat and Mass Transfer.*, Vol. 12(3), pp. 279-300.

[58] Greenwood.J.A. (1966), 'Constriction resistance and the real area of contact', Brit.J.Appl.Phys. Vol. 17, pp. 1621-1632.

[59] Greenwood, J.A. and Tripp, J.H. (1967), 'The elastic contact of rough spheres', Transaction *of ASME,* Vol. 34, pp. 153-159.

[60] Greenwood, J.A. and Williamson, J.B.P. (1966), 'Contact of nominally flat surfaces.' *Proceedings of Royal Society London.* Vol. A-195., pp. 300-319.

[61] Mikic, B.B. (1974), 'Thermal contact conductance.' *International Journal of Heat and Mass Transfer.* Vol. 17, pp. 205-214.

[62] Sridhar, M.R. and Yovanovich, M.M. (1996), 'Elastoplastic Contact Model for

Isotropic Conforming Rough Surfaces and Comparison with Experiments.', Journal *of Heat Transfer.,* Vol. 118(1), pp. 3-9.

[63] Sridhar, M.R. and Yovanovich, M.M. (1996), 'Elastoplastic Constriction Resistance Model for Sphere-Flat Contacts.', Journal *of Heat Transfer.,* Vol. 118(1), pp. 202-205.

[64] Bahrami, M. (2004), "Modelling of Thermal Joint Resistance for Sphere-Flat Contacts in a Vacuum", Waterloo, Ontario, Canada, University of Waterloo, Mechanical Engineering.

[65] Bahrami, M., Culham, J.R. and Yovanovich, M.M. (2004), 'Modeling Thermal Contact Resistance: A Scale Analysis Approach', Transactions *of the ASME,* Vol. 126, pp. 896-905.

[66] Bahrami, M., Culham, J. R., and Yovanovich, M. M. (2004), 'Thermal Resistance of Gaseous Gap for Conforming Rough Contacts'. 42nd AIAA Aerospace Meeting and Exhibit.

[67] Bahrami, M., Culham, J. R., Yovanovich, M. M., and Schneider, G. E. (2003), 'Thermal Contact Resistance of Non-Conforming Rough Surfaces', Part 1: Contact Mechanics Model. 36th AIAA Thermophysics Conference Meeting and Exhibit.

[68] Bahrami, M., Culham, J. R., Yovanovich, M. M., and Schneider, G. E. (2003), 'Thermal Contact Resistance of Non-Conforming Rough Surfaces', Part 2: Thermal Model. 36th AIAA Thermophysics Conference, pp.1-11.

[69] Song, S. and Yovanovich, M.M. (1989), 'Contact Interface Gas Heat Transfer, A Method of Measuring Thermal Accommodation Coefficient.', *Proccedings of 9th Annual Internatinal Electronics Packaging Conference.,* San Diego, CA., pp.925-936,

[70] Al-Astrabadi, F.R. (1978), *Thermal Resistance of Presses Contact*, PhD thesis, Cranfield, Cranfield Institute of Technology.

[71] Lawton, B. and Klingenberg, G. (1996), Transient Temperature in Engineering and Science, Oxford University Press, Oxford. ISBN 0-19-856260-8.

[72] Savija, I., Culham, J. R., Yovanovich, M. M., and Marotta, E. E. (2002). '*Review of Thermal Conductance Models for Joints Incorporating Enhancement Materials*'. 40th AIAA Aerospace Sciences Meeting & Exhibit, Reno, NV

[73] O'Callaghan, P. W., Jones, A. M., and Probert, S. D. (1975), "Research Note: The Thermal Behaviour of Gauzes as Interfacial Inserts Between Solids,"Journal of Mechanical Engineering Science, Vol. 17/4, pp. 233–236.

[74] Barzelay, M.E. (1960), Range of Interface Thermal Conductance for Aircraft Joints, NASA Report No. TN D-426.

[75] Barzelay, M.E., Tong, K.N., and Holloway, G.F. (1955), Thermal conductance of filled aluminium and magnesium joints in a vacuum environment, NASA Report No. TN-3295.

[76] Ruiping, Xu and Lie, Xu (2005), 'An experimental investigation of thermal contact conductance of stainless steel at low temperatures', *Cryogenics,* Vol. 45, pp. 694-704.

[77] Mann D. LNG materials and fluids. First ed. Boulder, CO: National Bureau of Standards; 1977. US Advanced Research Projects.

[78] Al-Astrabadi, F. R. (1978), "Thermal Resistances of Pressed Contact," Ph.D. Thesis, Cranfield Institute of Technology.

[79] Yip, F. C. (1974), 'Effect of oxide films on thermal contact resistance', AIAA/ASME Thermophysics and Heat Transfer Conference., Boston MA, paper 74-693.

[80] Brunot, A.W. and Buckland, F.F. (1949), 'Thermal Contact Resistance of Laminated and Machined Joints', Trans. *ASME.,* Vol. 71, pp. 253-257.

[81] Antonetti, V.W. and Yovanovich, M.M. (1985), 'Enhancement ofThermal Contact Conductance by Metallic Coatings: Theory and Experiments.', Journal *of Heat Transfer,* Vol. 107, pp. 513-519.

[82] Li, Y.Z., Madhusudana, C.V. and Leonardi, E. (2000), 'On the Enhancement of the Thermal Contact Conductance Effect of Loading History.', Transaction *of the ASME.,* Vol. 122, pp. 46-49.

[83] Jeng, Y.R., Chen, J.T. and Cheng, C.Y. (2006), 'Thermal contact conductance of coated surfaces.', Wear, Vol. 260, pp. 159-167.

[84] Song, S. (1988), 'Analytical and Experimental Study of Heat Transfer through Gas Layers of Contact Interfaces', Waterloo, Ontario, Canada, University of Waterloo.

[85] Kumar, S.S. and Ramamurthi, K. (2003), 'Influence of Flatness and Waviness of Rough Surfaces on Surface Contact Conductance', Transactions *of the ASME,* Vol. 125, pp. 394-402.

[86] Madhusudana, C.V. (2000), 'Accuracy in Thermal contact conductance experiments - the effect of heat losses to the surroundings', *Int. Comm. Heat Mass Transfer,* Vol. 27/6, pp. 877-891.

[87] Attia, M.H. and Kops, L. (1980), 'Importance of Contact Pressure Distribution on Heat Transfer in Structural Joints of Machine Tools', *Journal of Engineering for Industry,* Vol. 102, pp. 159-167.

[88] Attia, M.H. and Kops, L. (1979), 'Nonlinear Thermoelastic Behaviour of Structural Joints - Solution to a Missing Link for Prediction of Thermal Deformation of Machine Tools ', *Transactions of the ASME,* Vol. 101, pp. 348-354.

[89] Lee, S., Song, S., Moran, K.P., and Yovanovich, M.M. (1993), *Analytical Modeling of Thermal Resistance in Bolted Joints*, ASME, HTD-Vol 236.

[90] Sridhar, M.R. and Yovanovich, M.M. (1996), 'contact conductance correlations based on Greenwood and Williamson surface model', International *Journal of Heat Transfer.,* Vol. 118, pp. 3-9.

[91] Antonetti, V.W., Whittle, T.D. and Simons, R.E. (1991), 'An Approximate Thermal Contact Conductance Correlation.', Experimental/*Numerical Heat Transfer in Combustion and Phase Change.,* Vol. 170, pp. 35-42.

[92] Attia, M.H. and Kops, L. (1978), 'On the Role of Fixed Joints in Thermal Deformation of Machine Tool Structures.', Annals *of the CIRP,* Vol. 27/1, pp. 305-310.

[93] Attia, M.H. and Kops, L. (1981), 'System Approach to the Thermal Behaviour and Deformation of Machine Tool Structures in Response to the Effect of Fixed Joints', *Journal of Engineering for Industry,* Vol. 103, pp. 67-72.

[94] Attia, M.H. and Kops, L. (1981), 'A New Method for Determining the Thermal Contact Resistance at Machine Tool Joints', Annals *of the CIRP,* Vol. 30/1/1981, pp. 259-264.

[95] Attia, M.H. and Kops, L. (1993), 'Thermometric design considerations for temperature monitoring in machine tools and CMM structures.', The *International Journal of Advanced Manufacturing Technology.,* Vol. 8, pp. 311-319.

[96] Whitehouse, D.J. (1994), Handbook of Surface Metrology, Institute of Physics Publishing, Bristol and Philadelphia, ISBN 0750300396.

[97] Taylor Hobson Limited (2003), Exploring *Surface Texture. A Fundamental guide to the measurement of surface finish,* Cambridge University Press, Great Britian.

[98] Lambert, M.A. and Fletcher, L.S. (1997), 'Review of models for thermal contact conductance of metals.', Journal *of Thermophysics and Heat Transfer,* Vol. 11(2), pp. 129-140.

[99] Holman, J.P. (1997), Heat Transfer, 8th edition, McGraw-Hill, Inc., New York, ISBN: 0070495475.

[100] Lienhard IV, J.H. and Lienhard V, J.H. (2003), A Heat Transfer Texbook, 3rd ed., Phlogiston Press, Cambridge Massachusetts, ISBN-10: 0971383537.

[101] Singal, V., Litke, P.J., Black, A.F. and Garimella, S.V. (2005), 'An experimentally validated thermo-mechanical model for the prediction of thermal contact conductance.', International Journal of Heat and Mass Transfer., Vol. 48, pp. 5446-5459.

[102] Tien, C. L. (1968), 'A correlation for thermal contact conductance of nominally flat surfaces in vacuum.' in *7th conference on thermal conductivity.* Vol. 126 at Gaithersburg, MD.; pp. 755-759.

[103] Zhao, J.F. (2005), 'Prediction of thermal contact conductance based on the statistics of the roughness profile characteristics.', International *Journal of Heat and Mass Transfer.,* Vol. 48, pp. 974-978.

[104] Yovanovich, M.M. (1982), 'New Contact and Conductance Correlations for Conforming Rough Surfaces.', in Dr. T.E.Horton *AIAA 16th Thermophysics Conference. Published in AIAA Progress in Aestronautics and Aeronautics, Spacecraft Radiative Transfer and Temperature Control.,* Palo Alto, California,

[105] Madhusudana, C.V. (1996), Thermal *contact conductance.* Springer-Verlag, New York.

[106] Yovanovich, M.M. (1982), 'Thermal Contact Correlations. in Progress in Astronautics and Aeronautics: Spacecraft Radiative Transfer and Temperature Control.', *AIAA,* Vol. 83, T.E. Horton, pp. 83-95.

[107] Abramowitz, M. and Stegun, I.A. (1995), Handbook of Mathematical Functions, Dover Publications, New York, ISBN-10: 0486612724.

[108] Song, S. and Yovanovich, M.M., (1988), 'Relative Contact Pressure: Dependence on Surface Roughness and Vickers Microhardness.', AIAA *Journal of Thermophysics and Heat Transfer.,* Vol. 2(1), pp. 43-47.

[109] Yovanovich, M.M., Hegazy, A.A., and DeVaal, J. (1982), 'Surface Hardness Distribution Effects upon Contact, Gap and Joint Conductances, AIAA-82-0887', *AIAA/ASME 3rd Joint Thermophysics, Fluids, Plasma and Heat Transfer Conference,* St. Louis, MO,

[110] Hegazy, A.A. (1985), *Thermal Joint Conductance of Conforming Rough Surfaces: Effect of Surface Microhardness Variation*, PhD thesis, University of Waterloo, Waterloo, Ontario, Canada.

[111] Kimura, Y. (1970), 'Estimation of the Number and the Mean Area of Real Contact Points on the Basis of Surface Profiles.', *Wear,* Vol. 15, pp. 47-55.

[112] Williamson, J.B., Pullen, J., Hunt, R.T. and Leonard, D. (1969), 'The Shape of Solid Surfaces, Surface Mechanics.', *ASME,* pp. 24-35.

[113] Sridhar, M.R. and Yovanovich, M.M. (1996), 'Thermal Contact Conductance of

Tool Steel and Comparison with Model.', *International Journal of Heat and Mass Transfer.,* Vol. 39(4), pp. 831-839.

[114] Sridhar, M.R. and Yovanovich, M.M. (1996), 'Empirical Methods to Predict Vickers Microhardness.', *Wear.,* Vol. 193, pp. 91-98.

[115] Grujicic, M., Zhao, C.L. and Dusel, E.C. (2004), 'The effect of thermal contact resistance on heat management in the electronic packaging.', *Journal of Applied Surface Science.,* Vol. 246, pp. 290-302.

[116] Kennard, E.H. (1938), *Kinetic Theory of Gases.*, McGraw-Hill., New York.

[117] Yovanovich, M.M., Hegazy, A.A., and DeVaal, J. (1982), 'A Statistical model to predict thermal gap conductance between conforming rough surfaces.', *AIAA/ASME 3rd Joint Thermophysics, Fluids, Plasma and Heat Transfer Conference,* St. Louis, Missouri.

[118] Savija, I., Yovanovich, M. M., and Culham, J. R. (2002), "Thermal Joint Resistance Models for Conforming Rough Surfaces with Grease Filled Interstitial Gaps". AIAA Aerospace Sciences Meeting and Exhibit, 40th, Reno, NV, Jan. 14-17.

[119] Yovanovich, M.M. (1969), 'Overall Constriction Resistance Between Contacting Rough, Wavy Walls.', *International Journal of Heat and Mass Transfer.,* Vol. 12, pp. 1517-1520.

[120] Thomas, T.R. and Sayles, R.S. (1975), 'random process analysis of the effect of waviness on thermal contact resistance.', *AIAA Prog. Astronaut. Aeronaut.,* Vol. 39, pp. 3-20.

[121] Lambert, M.A. and Fletcher, L.S. (2002), 'Thermal Contact Conductance of Non-Flat, Rough, Metallic Coated Metals.', *ASME Journal of Heat Transfer.,* Vol. 124, pp. 405-412.

[122] Marotta, E.E. and Fletcher, L.S. (2001), 'Thermal Contact Resistance Models of Non-Flat, Roughened Surfaces with Non-Metallic Coatings.', *ASME Journal of Heat Transfer.,* Vol. 123, pp. 11-23.

[123] Montgomery, D.J. (2001), *Design and Analysis of Experiments, 5th edition.*,

John Wiley & Sons, Inc., New York.

[124] Buczkowski.R and Kleiber.M. (2000), 'Statistical model of strongly anisotropic rough surface for finite element contact analysis', *International Journal for Numerical Methods in Engineering,* Vol. 49, pp. 1169-1189.

[125] Schott (2007), *Zerodur Glass Ceramic,* available at: http://www.schott.com/optics_devices/english/download/Zerodur®_catalog_2004.pdf (accessed 2007).

[126] Reddy, J.N. (2006), An Introduction to Finite Element Method, 3rd ed., McGraw-Hill International Edition, Boston, ISBN-10: 0070607419.

[127] UGS PLM Solutions (2006), *I-DEAS Help Library,* available at: C:\\UGSPLM\I-DEAS11\SDRCHelp\LANG\English\bookshelf\bookshelf.htm (accessed 2006).

[128] National Agency for Finite Element Methods and Standards (2007), available at: http://www.nafems.org (accessed 2007).

[129] Rohsenow, W.M., Hartnett, J.P. and Cho, Y.I. (1998), Handbook of Heat Transfer, Mc Graw Hill, New York, ISBN-10: 0070535558.

[130] Holman, J.P. (1978), *Experimental Methods for Engineers*, McGraw-Hill, Inc., New York.

[131] Omega (2006), *Thermocouple Tolerances,* available at: http://www.omega.com/toc_asp/frameset.html?book=Temperature&file=TC_GEN_SPECS_REF (accessed 2006).

[132] National Instruments (2006), *High Precision Data Acquisition (NI 435x),* available at: http://www.ni.com/pdf/products/us/2mhw296-297e.pdf (accessed 2006).

[133] National Institute of Standards and Technology (2006), *Cryogenic Technologies Group,* available at: http://cryogenics.nist.gov/NewFiles/304SS.html (accessed 2006).

[134] Postlethwaite. S.R., Allen. J.P., Ford. D.G., (1999), 'Machine tool thermal error reduction – an appraisal', Proc Instn Mech Engrs, Vol. 213, Part B, pp. 1-9.

Appendix A - Calculating Convection Coefficient

All experimental tests in this research were carried out in an open environment under ambient temperature conditions. Applied heat is conducted into the steel blocks and partially lost due to convection to the sourrounding ambient. Heat lost by convection is only a very small proportion of the total heat input. Convection coefficient is an important boundary condition therfore it must be calculated and defined in FEA.

In order to determine the convective heat transfer coefficient h, the two dimensionless parameters, the Nusselt number N_u and the Rayleigh number R must be calculated. The Nusselt number defines the relationship between convective and conductive heat transfer and is the ratio of convection heat transfer to conduction heat transfer. The Rayleigh number is associated with the heat transfer within the surrounding fluid and is defined as [99]:

$$R = \frac{g\beta(T_s - T_\infty)L_c^3}{\upsilon\alpha} \qquad \text{Eq. 134}$$

Where β is the thermal coefficient of expansion, υ is kinematic viscosity, α is thermal diffusivity, g is acceleration due to gravity, T_s is surface temperature, T_∞ is surrounding fluid temperature and L_c is the characteristic length. Properties of air are listed in Table A-1.

Property	Magnitude
Thermal Diffusivity, α	$0.2216x10^{-4}\ m^2/s$
Thermal Expansion, β	$3.2x10^{-3}C^{-1}$
Thermal Conductivity, k	$0.026W/mC$
Density, ρ	$1.1774\,kg/m^3$
Specific Heat Capacity, C_p	$1.0057\,kJ/kg\cdot C$
Kinematic Viscosity, υ	$15.69x10^{-6}\ m^2/s$
Prandtl Number, Pr	0.708

Table A - 1. Properties of air

The R for different orientations differs from their characteristic length, L_c. For vertical surfaces L_c is the height of blocks whereas for top side the L_c is the ratio of the area of the block's outer surface to its perimeter. After calculating the Rayleigh number, the Nusselt number was calculated. The Nusselt number for the vertical surfaces of the blocks takes the form:

$$Nu = 0.68 + \frac{0.67R^{1/4}}{[1+(0.492/\mathrm{Pr})^{9/16}]^{4/9}}, \text{ for } R<10^9 \qquad \text{Eq. 135}$$

Where Pr is the Prandtl number of the surrounding fluid air. The Nusselt number N_u for the upper surfaces of the blocks takes the form:

$$Nu = 0.27R^{1/4}, \text{ for } 105<R<1010 \qquad \text{Eq. 136}$$

With the known Nusselt number for different surfaces, the convective heat transfer coefficient for each surface was calculated using the following expression:

$$h = \frac{kN_u}{L_c} \qquad \text{Eq. 137}$$

Consider the steel block used in the two block analysis of dimensions 60x60x60 mm, as shown in Figure A-1.

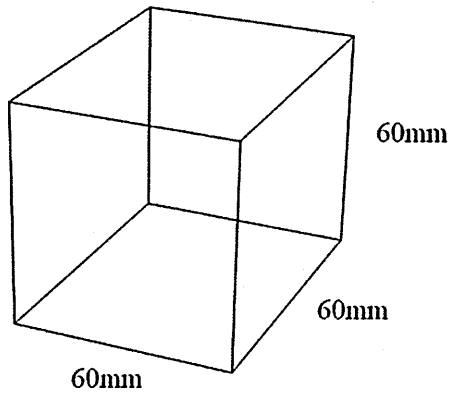

Figure A - 1. Schematic representation of a steel block used in two block analysis

If we assume that the bottom surface is insulated, that is convection heat transfer takes place from vertical surfaces and top surface only, the calculation is as follows:

1. Rayleigh number

For vertical surfaces the characteristic length is the height of a vertical side L_c=0.06m and the Rayleigh number is found by substituting the properties of air and the characteristic length into Eq. 134:

$$R = \frac{9.81\times 3.2x10^{-3}\times 22.46\times 0.06^3}{15.69x10^{-6}\times 0.2216x10^{-4}} \qquad \text{Eq. 138}$$

$$R = 4.38\times 10^5$$

For the top surface the characteristic length is the ratio of surface area to its perimeter:

$$L_c = \frac{Area(A)}{Perimeter(P)} = \frac{0.0036}{0.24} = 0.015m \qquad \text{Eq. 139}$$

So the Rayleigh number can now be found as follows:

$$R = \frac{9.81 \times 3.2x10^{-3} \times 22.46 \times 0.015^3}{15.69x10^{-6} \times 0.2216x10^{-4}} \qquad \text{Eq. 140}$$

$$R = 6.84 \times 10^3$$

2. *Nusselt number*

With known Rayleigh numbers, the Nusselt numbers can be calculated using Eq. 135. For vertical surfaces the Nusselt numbers following $R_a<10^9$ are:

$$Nu = 0.68 + \frac{0.67(4.38x10^5)^{1/4}}{[1+(0.492/0.708)^{9/16}]^{4/9}}$$

$$Nu = 13.9 \qquad \text{Eq. 141}$$

For top surfaces the Nusselt numbers can be calculated using Eq. 136 as follows:

$$Nu = 0.27R^{1/4} = 0.27(6.84 \times 10^3)^{1/4} = 2.45 \qquad \text{Eq. 142}$$

Now that the Nusselt numbers are found, the convection coefficient for vertical and top surfaces can be calculated using Eq. 137:

$$h_{vertical} = \frac{Nu_{vertical} \times k}{L_{c_{vertical}}} = \frac{13.9 \times 0.026}{0.06} = 6W/m^2 \cdot C \qquad \text{Eq. 143}$$

$$h_{top} = \frac{Nu_{top} \times k}{L_{c_{top}}} = \frac{13.9 \times 0.026}{0.015} = 4.3W/m^2 \cdot C \qquad \text{Eq. 144}$$

Convection coefficients for other blocks used in this research were found using the above procedure. Calculated values are shown in Table A-2.

Surface	Convection Coefficient, h [W/m^2°C]				
	Two blocks analysis		Three blocks analysis		
	Top block	Bottom block	Middle block	Top block	Bottom block
Top surface	-	-	-	5.22	5.59
Side surface	6	6	8.13	10.31	10.6
Bottom surface	-	-	-	2.86	-

Table A - 2. Calculated convection coefficient values used in numerical modelling

Appendix B - Applied Torque versus Contact Pressure

When a measured torque is applied to a bolt connecting two steel blocks a contact pressure with a certain magnitude is exerted at interface as shown in Figure B-1. The relationship between the applied torque and contact pressure was found experimentally as explained in the following section.

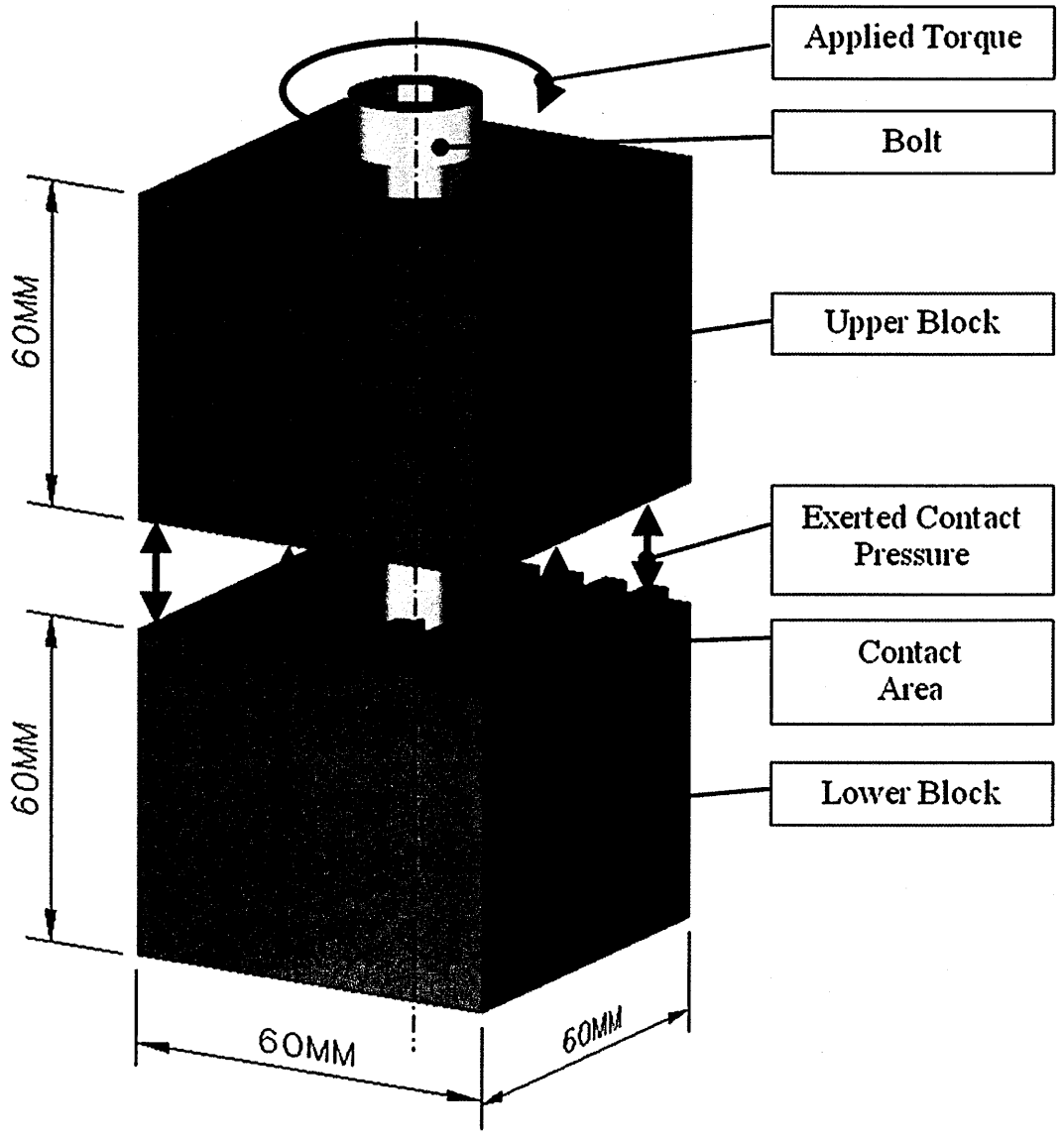

Figure B - 1. Bolted steel blocks

1. Torque versus Voltage Output from Pressure Transducer

First part of this experiment relates the torque applied to the bolt to the voltage output from pressure transducer. The pressure transducer used was a quartz sensor with extremely flat design for measuring of dynamic and quasi-static forces up to 50 kN. When the transducer is loaded it yields an electrical charge proportional to the pressure. The setup shown in Figure B-2 comprises of:

- A transducer sandwiched between two steel plates
- An amplifier which converts the charge produced by the quartz sensor into a proportional voltage
- An regulated DC power supply
- A oscilloscope to display the voltage output
- A torque wrench to measure the torque applied to the bolt, and
- A vice to hold the bottom steel plate on place while applying torque

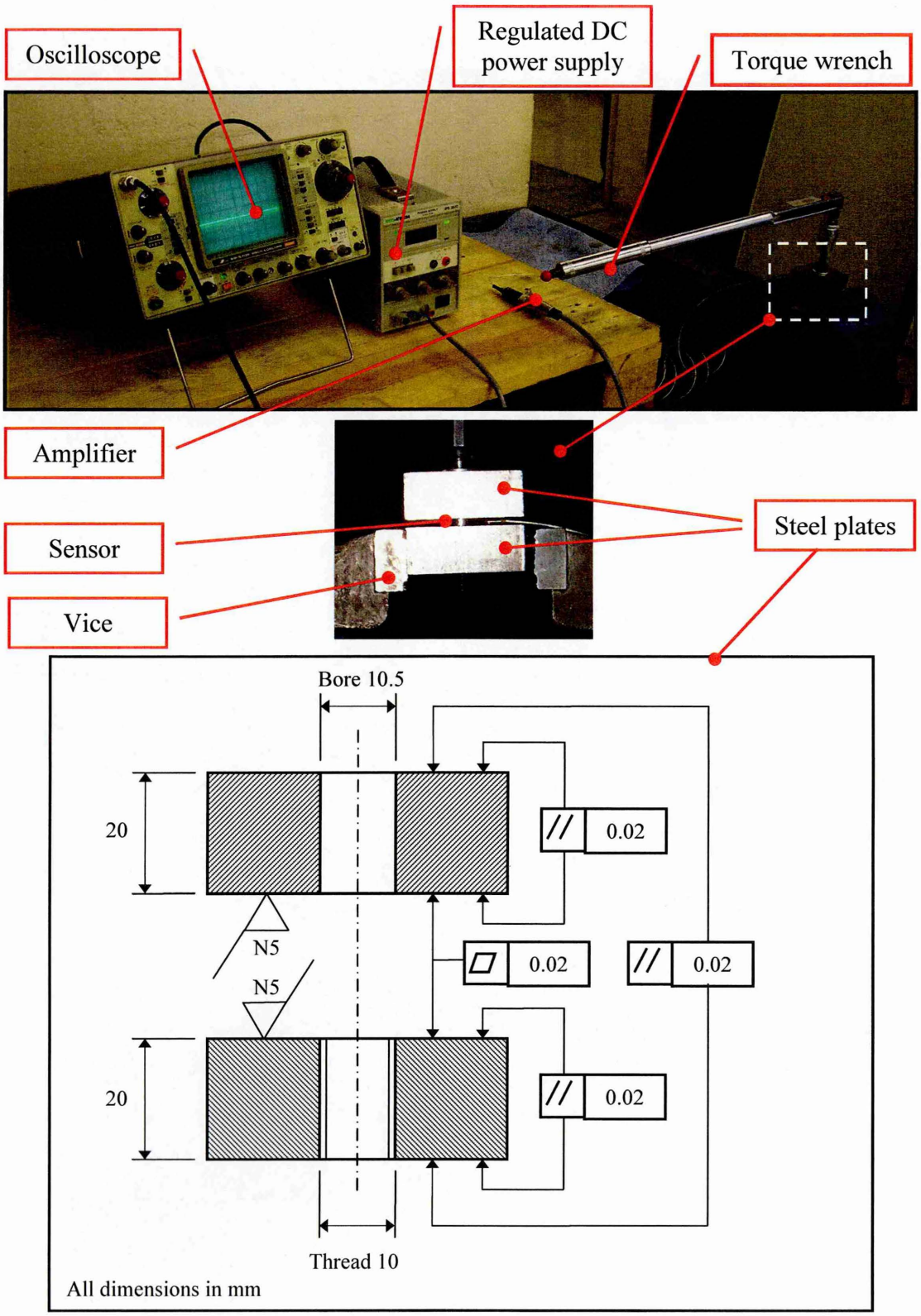

Figure B - 2. Calibrating pressure transducer

2. *Contact Pressure versus Voltage Output from Pressure Transducer*

Second part of this experiment relates the load applied to the pressure transducer to the voltage output from transducer. The setup shown in Figure B-3 comprises of:

- A transducer sandwiched between two steel plates
- An amplifier which converts the charge produced by the quartz sensor into a proportional voltage
- A regulated DC power supply and
- An oscilloscope to display the voltage output

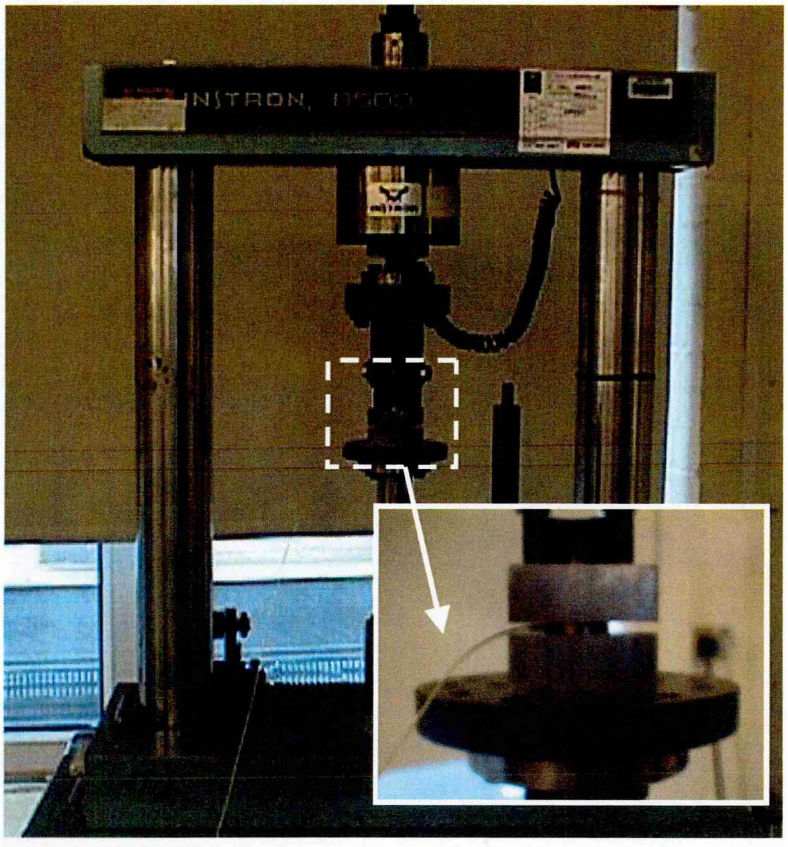

Figure B - 3. A universal compression testing machine

From experimental data the relationship between the contact pressure P, and applied torque τ was found to be (see Figure B-4):

$$P = 0.3827(\tau)^{0.8358} \qquad \text{Eq. 145}$$

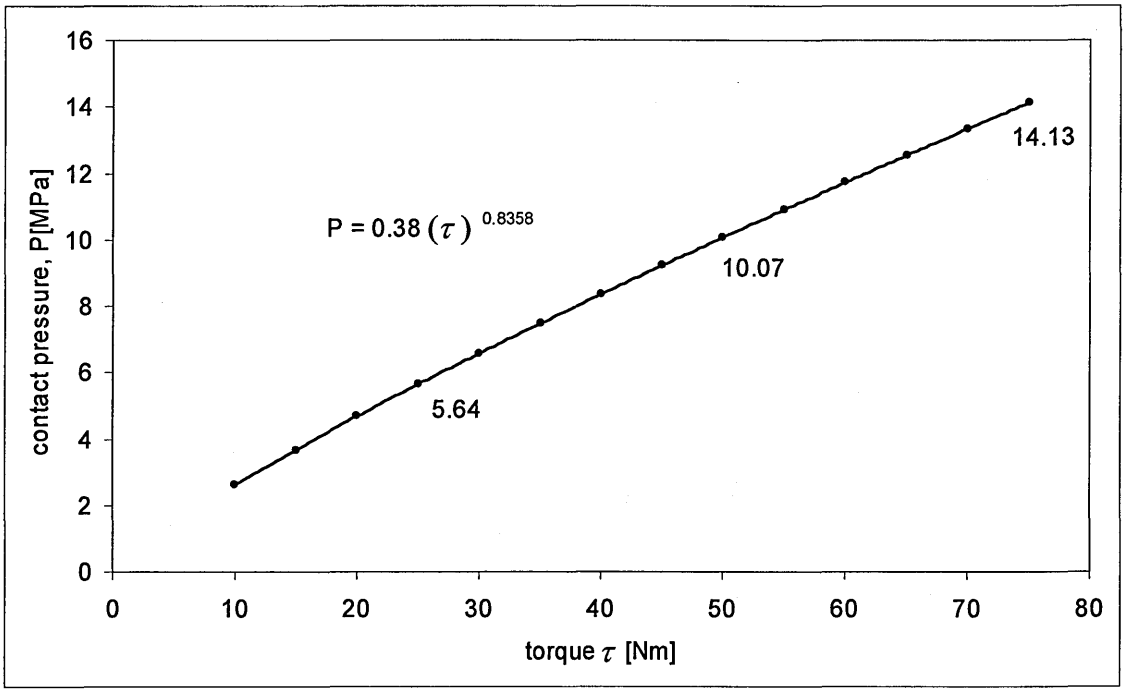

Figure B - 4. Relationship between torque and contact pressure

Appendix C - Influence of Mesh Size on Accuracy of FEA Results

The size of the mesh in finite element analysis plays an important role on the accuracy of results. The accurate determination of local temperatures, for examined thermal contact necessitates a careful attention in the choice of the mesh size. For this purpose a study consisting of choosing the appropriate mesh size is undertaken.

The original domain consists of two blocks in contact as shown in Figure C-1(a). Since the objective of this study is to find the appropriate mesh size near the interface the original domain was truncated, and the FEA analysis was carried out only on the near interface region, as shown in Figure C-2(b). This region was selected to include only two ridges in contact with the flat block. This arrangement should provide enough information in determining the appropriate mesh size.

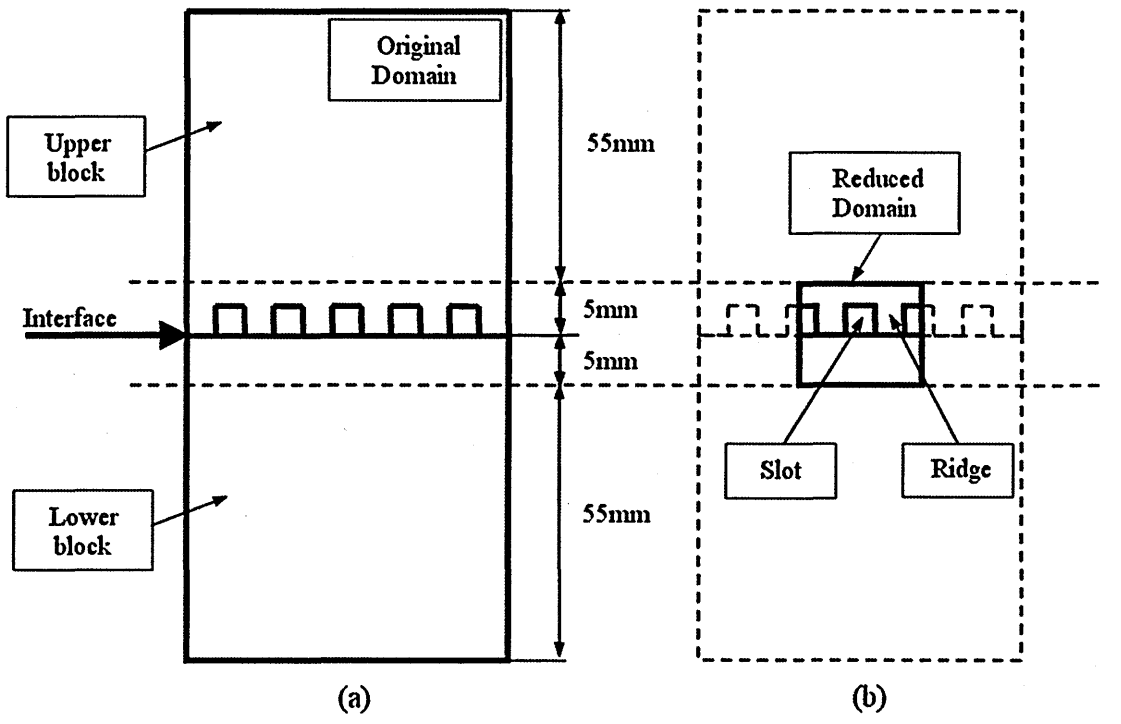

Figure C - 1. Reduction of the FEA domain, (a) original domain, (b) reduced domain

The mesh size shown in Figure C-2 was decreased until temperature results converged as shown in Figure C-3. Five different mesh sizes were generated and results were compared. It was found that for the interface comprising of smaller slots (2x2 mm) the convergence was achieved at the minimum of Mesh(3,3), whereas for the interface comprising of larger slots (3.75x2 mm) the convergence was achieved at the minimum

of Mesh(4,3), see Figure C-4. This investigation assures that the mesh size used in the FEA is correct.

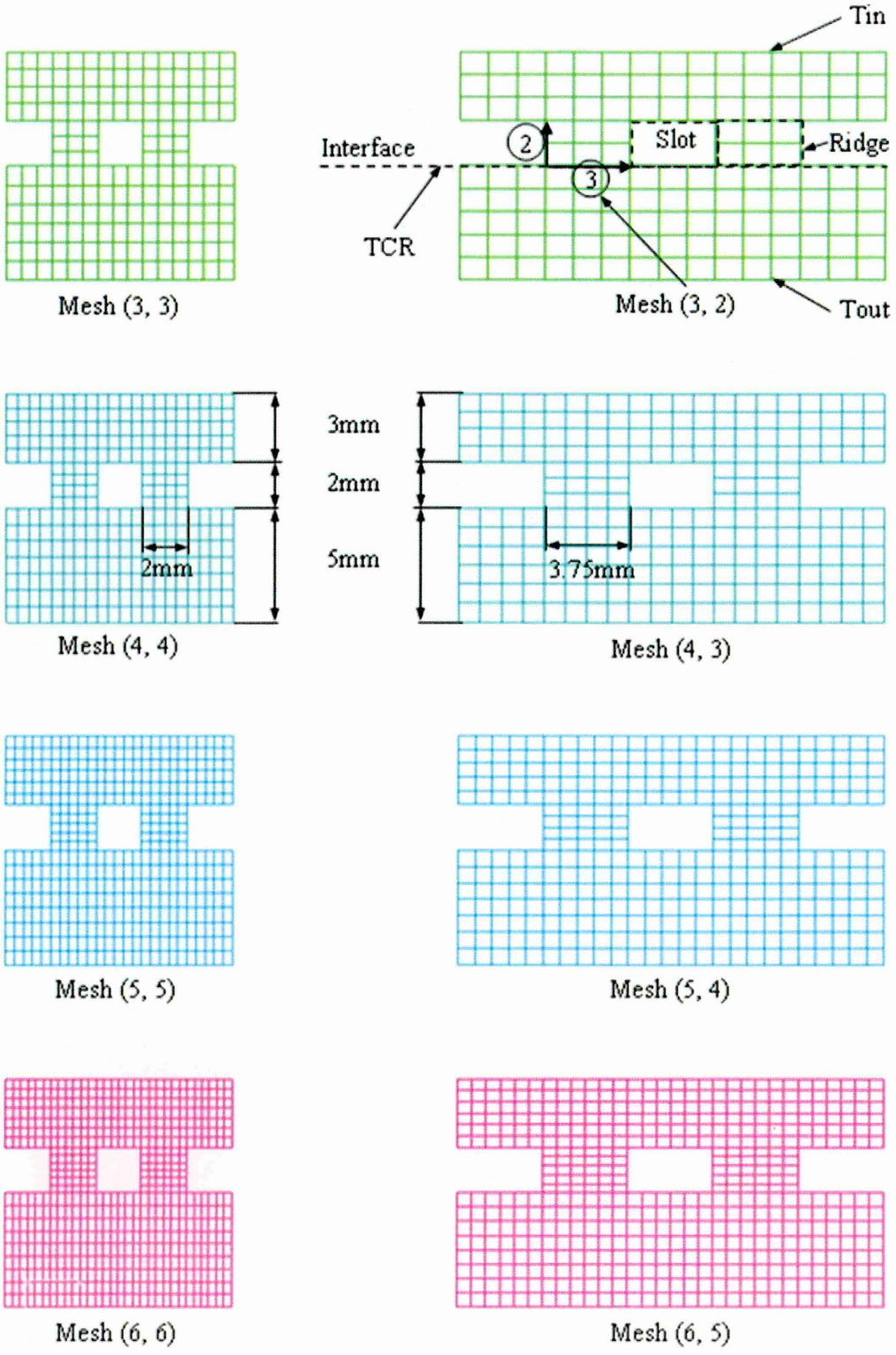

Figure C - 2. Mesh configuration

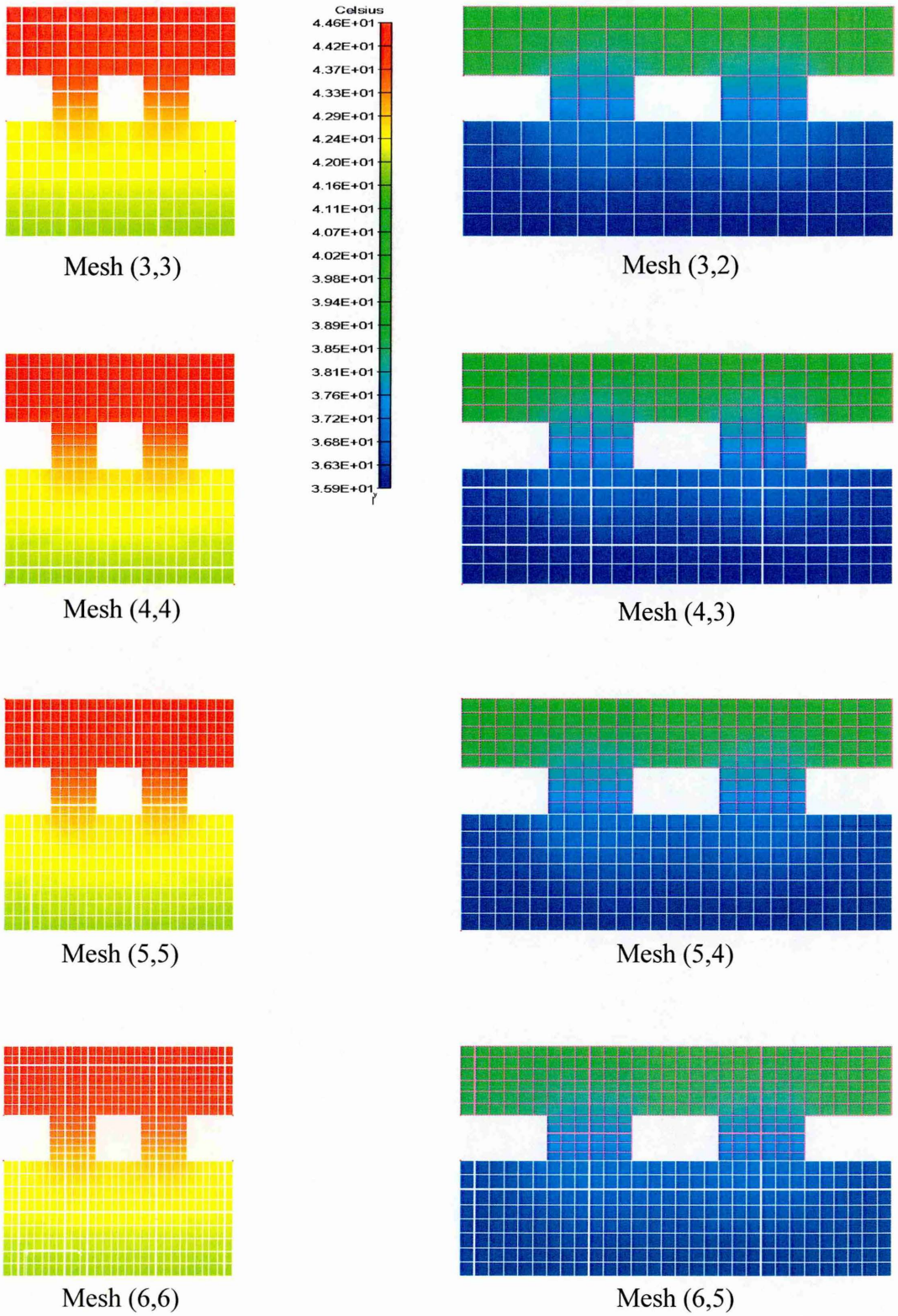

Figure C - 3. Influence of mesh on temperature results

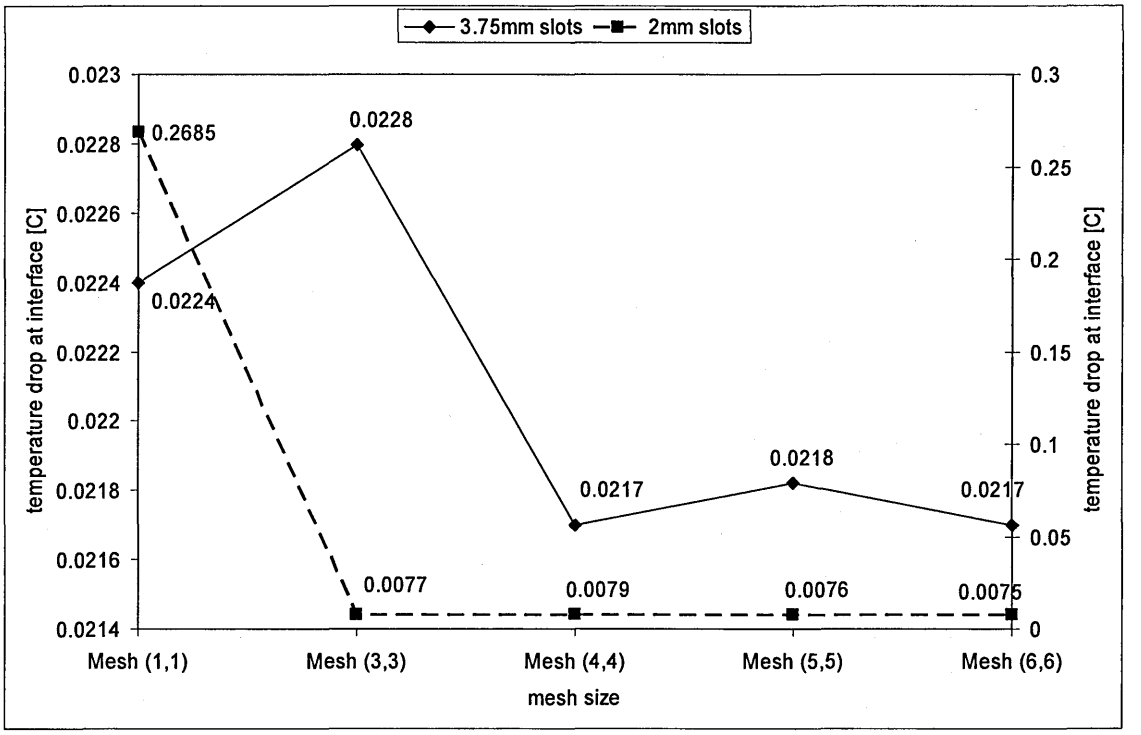

Figure C -4. Temperature drop across interface versus mesh size

Appendix D - Calculating Bolt Preload

Bolt preload comes from the installation torque τ applied when the bolts are installed. The inclined plane of the bolt thread helix converts torque to bolt preload. Bolt preload is computed as follows [43]:

$$F_{pl} = \frac{\tau}{Kd} \qquad \text{Eq. 146}$$

Where K is the torque coefficient, D is bolt nominal diameter. Torque coefficient K is a function of thread geometry, threads coefficient of friction μ_t and collar coefficient of friction μ_c, and is defined as:

$$K = \frac{(0.5d_p)(\tan\lambda + \mu_t \sec\beta')}{1 - \mu_t \tan\lambda \sec\beta'} + \frac{0.625\mu_c D}{D} \qquad \text{Eq. 147}$$

Where d_p is the bolt pitch diameter, β' is the thread profile half angle, $\tan(\lambda)$ is thread helix angle, and is given by:

$$\tan\lambda = \frac{p}{\pi d_p} \qquad \text{Eq. 148}$$

Where p is thread pitch. Bolt preloads were calculated analytically using the above formulas and used in FEA models. It was found that torques of 25 Nm, 50 Nm and 75 Nm correspond to 15.63 kN, 31.25 kN and 46.88 kN preload respectively, as shown in Figure D-1.

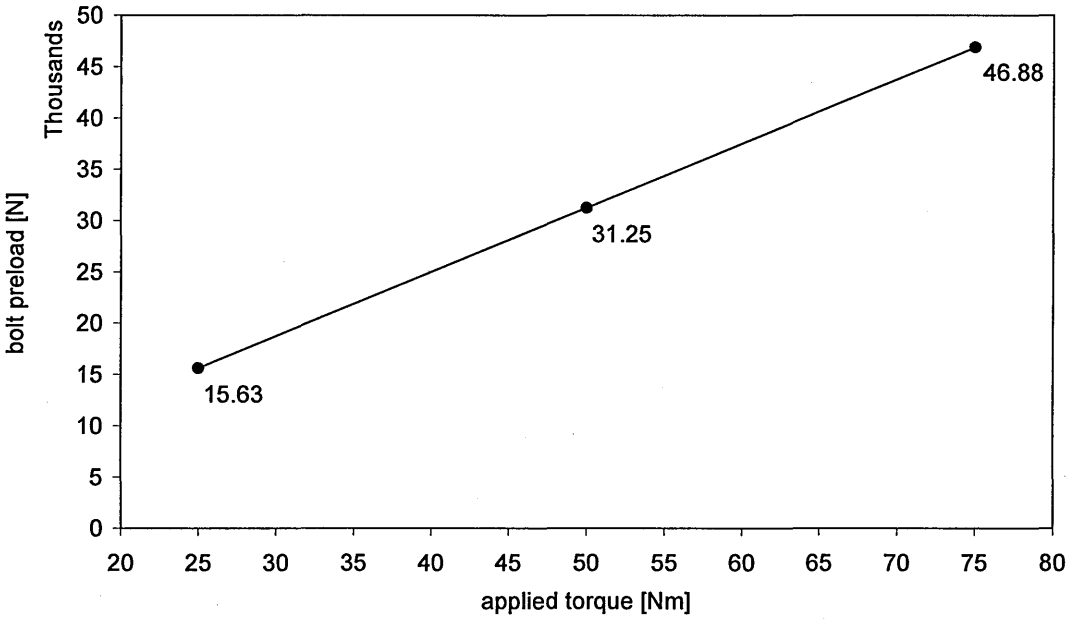

Figure D - 1. Calculated bolt preload with respect to applied torque

Appendix E - Calculating Thermal Contact Resistance

The TCR for an interface formed by two conforming rectangular, rough surfaces as a function of contact pressure where calculated. The calculation applies to interfaces filled with air and thermal grease. Thermal resistance of the contacting surfaces is assumed to be governed only by their roughness, the interface material and the contact pressure. The temperature drop across an interface is given by (see Chapter 2):

$$\Delta T = \frac{Q}{Ah_j}$$

Where Q is the heat transfer across interface, h_j is the thermal joint conductance, A is the area of contact. Thermal contact resistance R is the reciprocal of thermal contact conductance:

$$R = \frac{1}{Ah_j}$$

The thermal joint conductance h_j of the interface formed by two conforming, rough surfaces is given by the following simple model proposed by [24-27]:

$$h_j = h_c + h_g$$

Where h_c is the thermal contact conductance and h_g is the thermal gap conductance. The thermal contact conductance can be calculated using the following expression:

$$h_c = 1.25 k_s \frac{m}{\sigma}\left(\frac{P}{H_c}\right)^{0.95}$$

Where k_s is the effective thermal conductivity of the joint and is defined as:

$$k_s = \frac{2k_1 k_2}{(k_1 + k_2)}$$

Where k_1 and k_2 are the thermal conductivities of materials 1 and 2 respectively. The gap conductance, h_g, is given by the following:

$$h_g = \frac{k_g}{(\lambda + M)}$$

Where k_g is the thermal conductivity of the gap substance, λ is the mean plane separation and can be calculated by means of the following correlation [25]:

$$\lambda = \sqrt{2} erfc^{-1}\left(\frac{2P}{H_p}\right)$$

Where σ is the effective root mean squared surface roughness, ERFC is the complementary error function, P is the contact pressure, H_c is the micro-hardness of the softer material.

The gas parameter M accounts for rarefaction effects at high temperatures and low gas pressures. This gas-surface parameter depends on the thermal accommodation coefficients, the ratio of specific heats, the Prandtl number, and the molecular mean free-path of the gas. This complex gas-surface parameter depends on gas pressure and temperature according to the relationship [29]:

$$M = M_0 \frac{T}{T_0} \frac{P_{g,0}}{P_g}$$

Where M_0 denotes the gas parameter value at the reference values of gas temperature and pressure, T_0 and $P_{g,0}$, respectively.

Experimental investigation conducted by Williamson et al. [40] established that the surfaces produced by most of manufacturing processes have an isotopic Gaussian distribution of heights of the surface asperities. As a result the equivalent root-mean squared roughness σ and the mean absolute asperity slope m can be used and are defined as:

$$\sigma = \sqrt{\sigma_1^{\,2} + \sigma_2^{\,2}}$$

$$m = \sqrt{m_1^{\,2} + m_2^{\,2}}$$

The surface asperity slope is frequently not given. In this case the mean absolute asperity slope can be approximated by the correlation formula proposed by [28]:

$$m_{1,2} = 0.125\left(\sigma_{1,2} \times 10^6\right)^{0.402}$$

Three modes of deformation that can occur at the interface are: plastic deformation of the softer contacting asperities, elastic deformation of all contacting asperities, and elastic–plastic deformation of the softer contacting asperities. These modes of deformation give relationships for three important geometric parameters of the joint: the relative real contact area A_r/A_a, the contact spot density n, and the mean contact spot radius a in terms of the relative mean plane separation defined as $\lambda = Y/\sigma$. For the three deformation models there is one thermal contact conductance model given by [41, 42]:

$$h_c = \frac{2nak_s}{\psi(\varepsilon)}$$

Where $\Psi(\varepsilon)$ is the spreading/constriction parameter and its based on isothermal contact spots and it can be approximately calculated using the following formula:

$$\psi(\varepsilon) = (1-\varepsilon)^{1.5} \quad \text{for } 0 < \varepsilon < 0.3$$

The relative contact spot size is defined as:

$$\varepsilon = \sqrt{\frac{A_r}{A_a}}$$

$$na = \frac{1}{4\sqrt{2\pi}} \frac{m}{\sigma} \exp\left(-\frac{\lambda^2}{2}\right)$$

Calculated contact resistance values are shown in Table E - 1.

Contact pressure [MPa]	Thermal Contact Resistance [°C/W]					
	Middle block to top block		Middle block to bottom block		Bolts to top block	Bolts to holes
	Air	Grease	Air	Grease		
5.64	0.0083	0.0082	0.0085	0.0083	0.031	0.03
10	0.0048	0.0046	0.0049	0.0047	0.018	0.019

Table E - 1. Calculated thermal contact resistance values used in FEA

Appendix F - Matlab Code for Calculating Thermal Contact Resistance

This Matlab® code calculates thermal contact resistance formed by two conforming metal bodies in contact. The program is based on theory of heat transfer across interface as explained in Chapter 2. It works for both, plastic and elastic deformation.

Author: Bekim Gashi, PhD Student, 2007. Cranfield University, School of Applied Sciences, Precision Engineering Centre

% DEFINE VARIABLES:

% Rrms1,Rrms2 - Ra roughness of surfaces 1 and 2 [μm]

% Rrms - effective Ra surface roughness [μm]

% m1,m2 - slopes of surface 1 and 2 [rad]

% m - effective mean absolute slope of surface form error [rad]

% k1,k2 - thermal conductivity of material 1 and 2 [W/m°C]

% ks - harmonic mean thermal conductivity of material 1,2 [W/m°C]

% E1,E2 - elastic modulus of material 1 and 2 [GPa]

% E - reduced elastic modulus [GPa]

% p1,p2 - Poisson's ratio for material 1 and 2 [Pa]

% P - contact pressure [Pa]

% Hv - Vickers microharness [Pa]

% PI - plasticity index [dimensionless]

% Wp - plastic constriction alleviation factor [dimensionless]

% We - elastic constriction alleviation factor [dimensionless]

% hc - contact conductance [W/m^2C]

% hg - gap conductance [W/m^2C]

% hj - joint thermal conductance [W/m^2C]

```
% kg             - thermal conductivity of gap material [W/m°C]
% Y              - mean surface plane separation [μm]
% Aa             - apparent contact area [m^2]
% Ar             - real contact area [m^2]
% TJR            - thermal joint resistance [°C/W]
% Enter the Ra roughness in microns of contacting surfaces:
Rrms_1=input('Enter the Ra roughness in microns of contact surface 1: ');
Rrms_2=input('Enter the Ra roughness in microns of contact surface 2: ');
% Convert to microns:
Rrms1=Rrms_1*10^-6;
Rrms2=Rrms_1*10^-6;
% Calculate the effective surface roughness:
Rrms3=sqrt(Rrms1^2+Rrms2^2);
% Convert to microns:
Rrms=Rrms3*10^6;
% Write out the Rrms results:
fprintf('Rrms=%6.8f microns (is the effective surface roughness)\n',Rrms);
% Calculate the absolute surface slope m1, of surface 1:
m1=0.125*(Rrms1*10^6)^0.402;
% Calculate the absolute surface slope m2, of surface 2:
m2=0.125*(Rrms2*10^6)^0.402;
% Calculate the effective surface slope:
m=sqrt(m1^2+m2^2);
% Enter the thermal conductivity k1 and k2, of materials in contact:
k1=input('Enter the thermal conductivity of material 1 in W/mC: ');
```

```
k2=input('Enter the thermal conductivity of material 2 in W/mC: ');
% Calculate the effective thermal conductivity ks:
ks=2*(k1*k2)/(k1+k2);
% Enter modulus of elasticity E of materials in Pa:
E1=input('Enter elastic modulus of material 1 in Pa: ');
E2=input('Enter elastic modulus of material 2 in Pa: ');
% Enter Poisson's ration of materials:
p1=input('Enter Poisson's ration of material 1 in Pa: ');
p2=input('Enter Poisson's ration of material 2 in Pa: ');
% Calculate the reduced elastic modulus E of contact surfaces:
E=1/[((1-p1^2)/E1)+((1-p2^2)/E2)];
% Enter contact pressure P in Pa, and Vickers micro-hardness Hv in Pa:
P=input('Enter contact pressure P in Pa: ');
Hv=input('Enter Vickers micro-hardness Hv of material in Pa: ');
% Calculate the plasticity index PI (Mikic (1974)):
PI=Hv/(E*m);
% For plastic deformation the constriction alleviation factor is (Cooper (1969)):
Wp=(1-(P/(P+Hv))^0.5)^1.5;
% For elastic deformation the constriction alleviation factor is (Cooper (1969)):
We=[1-((P*sqrt(2))/(E*m))^0.5]^1.5;
if(PI)<0.33
   disp('The deformation is plastic because PI<0.33 ');
      hc=(ks/(2*pi*Wp))*(m/Rrms3)*exp(-[erfcinv((2*P)/(P+Hv))^2]);
elseif(PI)>0.33 & (PI)<3
   disp('This program can not be used because the plasticity index is 0.33<PI<3 ');
```

```
else(PI)>3
   disp('The deformation is elastic because PI>3 ');
      hc=(ks/(2*pi*We))*(m/Rrms3)*exp(-[erfcinv((2*sqrt(2)*P)/(E*m))^2]);
end
% Write out the hc results:
fprintf('hc=%6.8f C/W (is the thermal contact conductance)\n',hc);
if(PI)<0.33
   Y=sqrt(2)*Rrms3*(erfcinv((2*P)/Hv));
elseif(PI)>0.33 & (PI)<3
   disp('This program can not be used, because the plasticity index is 0.33<PI<3. ');
else(PI)>3
   Y=sqrt(2)*Rrms3*(erfcinv((4*P)/Hv));
end
% Enter apparent contact area Aa:
Aa=input('Enter apparent contact area Aa in m^2: ');
% Calculate the real contact area:
Ar=Aa*(0.5*erfc(L/sqrt(2)));
% Enter thermal conductivity of interface material:
kg=input('Enter thermal conductivity of interface material in W/m°C: ');
% Calculate mean surface plane separation:
Y=sqrt(2)*Rrms3*(erfcinv((2*P)/Hv));
% Calculate gap conductance:
hg=(kg/(Y+0.373));
% Calculate joint conductance:
hj=(hc+hg);
```

```
% Calculate thermal joint resistance:

TJR=(1/(hj*Aa));

% Write out TJR results:

fprintf('TJR=%6.8f C/W (is the thermal joint resistance)\n',TJR);
```

Appendix G - Influence of Slots Size on Heat Transfer across Interfaces

The original domain as shown in Figure G - 1(a) was truncated, and the FEA analysis was carried out on the near interface region in Figure G - 1(b). This region was selected to include only two ridges in contact with the flat block. This arrangement provides enough information in determining the influence of the slot size on the heat transfer.

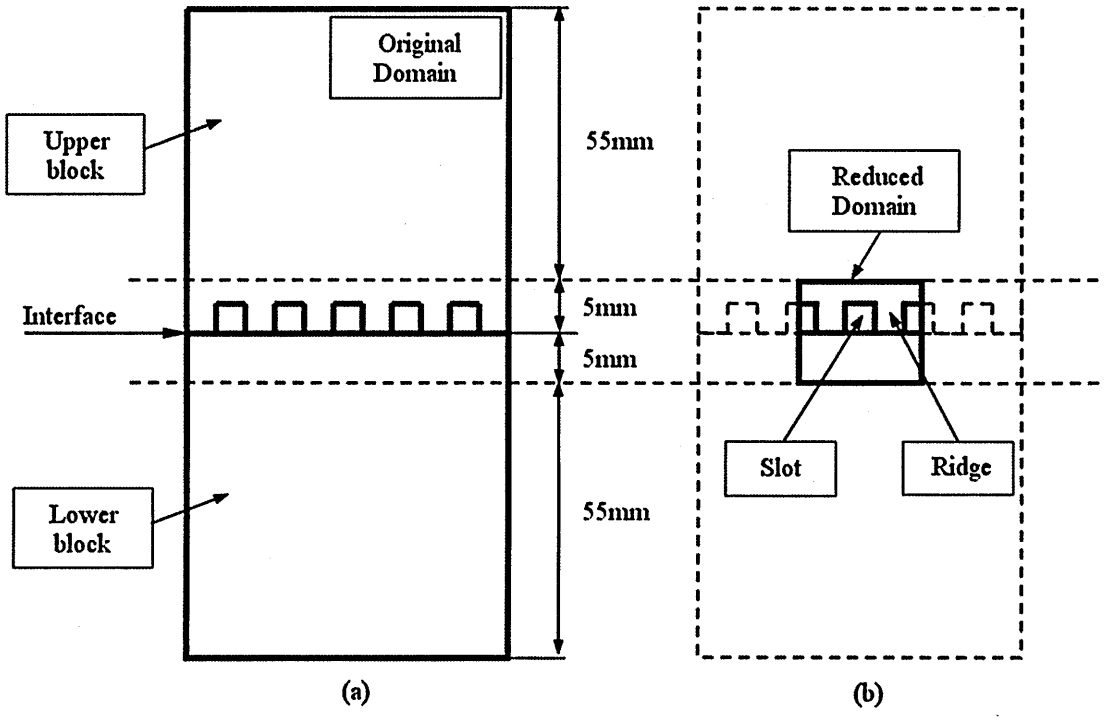

Figure G - 1. Reduction of the modelled domain; (a) original domain, (b) reduced domain

FEA temperature and heat flux contours at steady-state are shown in Figure G-2. Temperature and heat flux results at different locations along the interface are shown in Figure G-3 and Figure G-4.

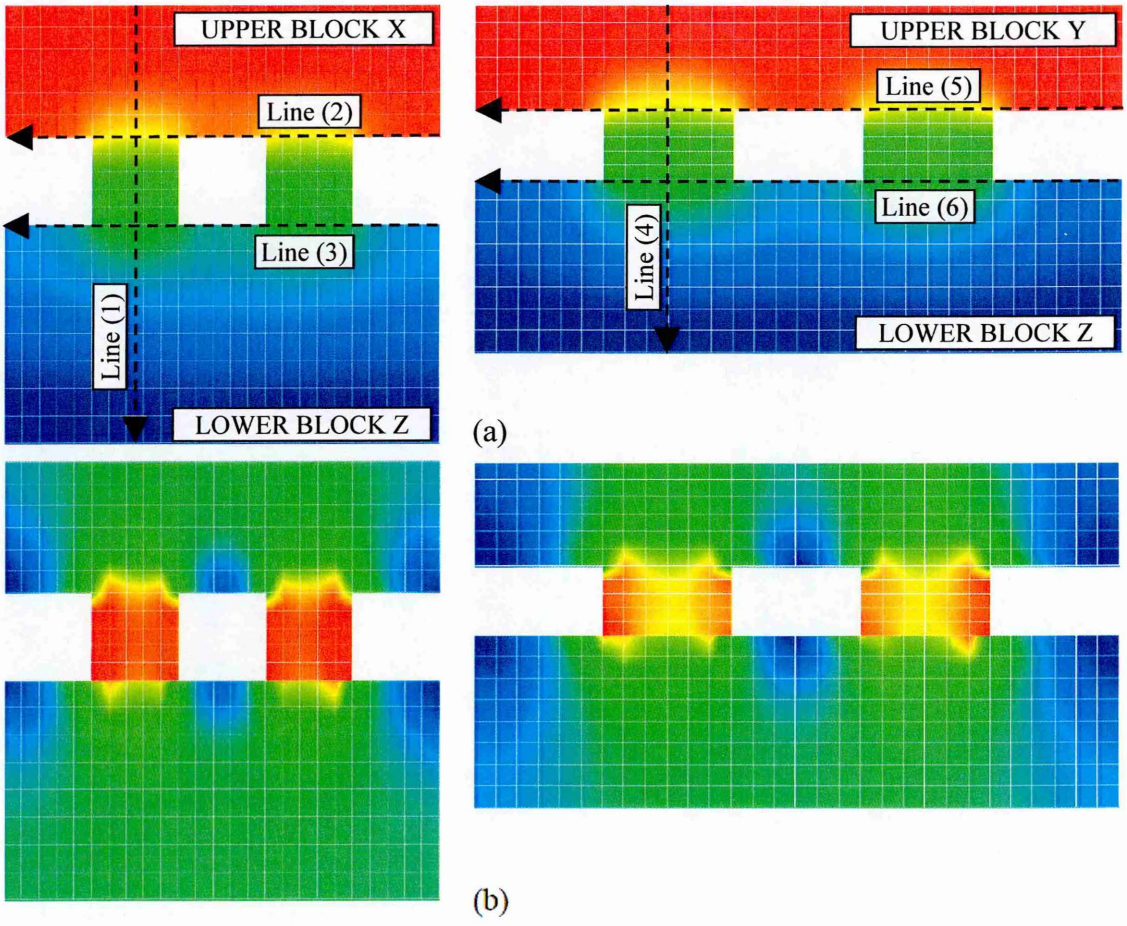

Figure G -2. (a) FEA temperature contours, (b) FEA heat flux contours

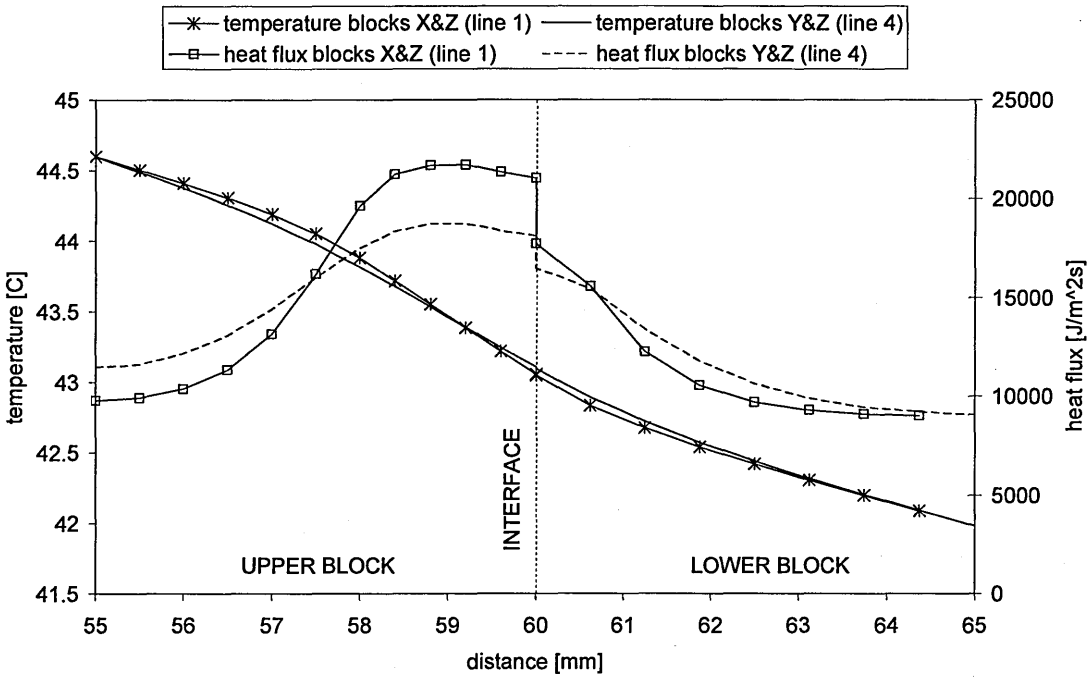

Figure G -3. FEA temperature and heat flux results across interface (line 1 and 4, see Figure G - 2)

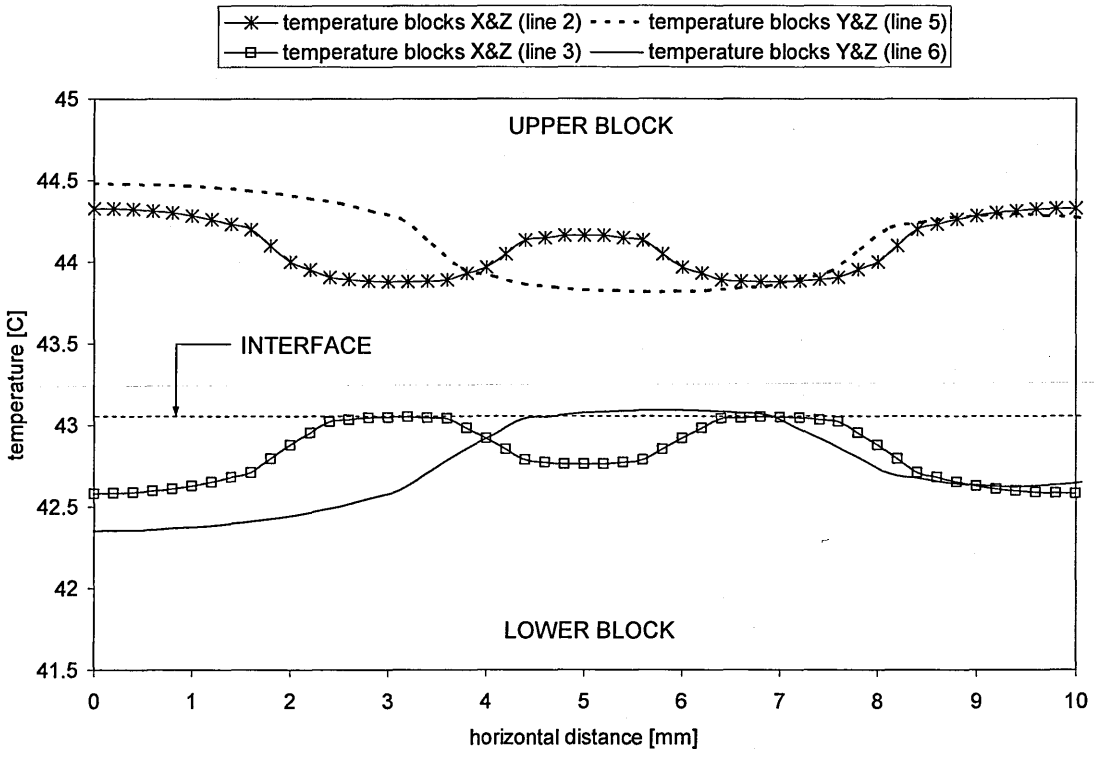

Figure G -4. FEA temperature results (lines 2, 3, 5, 6, see Figure G -2)

Appendix H - Uncertainty Analysis

The real errors in experimental data are those factors that are always unclear to some extent and carry some amount of uncertainty. The experimental uncertainty could be taken as the possible value the error may have. It is better to speak of experimental uncertainty as an alternative of experimental error, because the magnitude of an error is always uncertain [130].

First, there can always be errors within the apparatus or instrument construction. Secondly, there may be certain fixed errors (also known as systematic errors), which will cause repeated readings to be in error by roughly the same amount but for some unknown reason. Thirdly, there are the so called random errors which can be caused by random electronic fluctuation in the instrumentation, various influences of temperature, etc [130]. The most common procedure used to evaluate the uncertainty of the quantity calculated in this case is based on the Kline and McClintock (1953) method, as cited in [130]. When a certain quantity X is calculated from a number of n measured quantities Y, and each measured quantity has uncertainty ±U, the corresponding uncertainty of the calculated quantity U_X can be estimated from the following:

$$U_X{}^2 = \left(U_1 \frac{\partial X}{\partial Y_1}\right)^2 + \left(U_2 \frac{\partial X}{\partial Y_2}\right)^2 + \ldots\ldots + \left(U_n \frac{\partial X}{\partial Y_n}\right)^2 \qquad \text{Eq. 149}$$

In order to estimate the uncertainty in the system, the individual uncertainties must be calculated appropriately. The following sections explain in detail and attempt to estimate the uncertainty that exists within the system. Table H-1 shows the uncertainties in different parts of the system.

Measuring System	Uncertainty %
T-type thermocouples	±0.75%
DAQ board NI PCI 4351	±0.36%
DAQ board NI PCI 6024E	±0.36%
thermal conductivity of specimen	2%
vernier callipers	±0.4%
torque wrench	±5%
displacement transducers	±1%

Table H - 1. Magnitude of uncertainty associated with individual components

1. Temperature measurement

The temperature is measured using T-type thermocouples with uncertainty of ±0.75% [131]. The accuracy of the NI PCI 4351 measuring system is ±0.36% over its measuring range of ±5V [132]. The total uncertainty in measuring the temperature is the sum of the uncertainty of thermocouples and the uncertainty of measuring system. Assuming that the maximum temperature measured is 78°C, gives:

$$U_T = (78)(0.0075) + (10)(0.0036) = 0.311^\circ C \qquad \text{Eq. 150}$$

2. Length measurement

The specimen length, x, is measured using vernier callipers and the uncertainty of the length measurement is ±0.4%. Assuming that specimen length is 60 mm, gives:

$$U_x = (60)(0.004) = 0.14mm \qquad \text{Eq. 151}$$

3. Thermal conductivity

According to NIST [133], the uncertainty of the thermal conductivity, k, used for calculation is around 2%. Assuming that thermal conductivity is 51.9 W/m°C, with an uncertainty of 2% or 0.02, gives:

$$U_k = (51.9)(0.02) = 1.038W/m^\circ C \qquad \text{Eq. 152}$$

4. Heat losses due to convection and radiation

In the experiment heat losses result from several aspects: heat loss due to convection from the outer surfaces of the specimens 0.4W, heat loss due to radiation of the specimens 0.001W. Heat loss through 0.1 mm copper leads and 0.12 mm constantan leads is 0.0023W [76]. Thus, the total heat losses are 0.4033W. So, the uncertainty due to heat losses is:

$$U_{q'} = (0.4033)(0.013) = 0.00524W \qquad \text{Eq. 153}$$

5. Temperature drop across interface

The uncertainties associated with the measurement of temperature drop across the interface are the sum of uncertainties associated with the thermocouples, ±0.75%, and the extrapolated temperatures near interface, approximately ±1.9%. Therefore, the total

uncertainty in the measurement of temperature drop across the interface is approximately ±2.66%.

6. Heat flow through specimen

The one dimensional steady-state heat flux is defined as [105]:

$$q = \frac{Q}{A} = \frac{k\Delta T}{\Delta x} \qquad \text{Eq. 154}$$

The uncertainty of calculating the heat flux through the specimen is the sum of the uncertainties of thermal conductivity of material ±2%, temperature measurement ±0.75% and length measurement of the specimen ±0.4%.

Using Eq.149 the uncertainties associated with the heat flux can be found as follows:

$$U_q{}^2 = \left(U_k \frac{\partial q}{\partial k}\right)^2 + \left(U_T \frac{\partial q}{\partial \Delta T}\right)^2 + \left(U_x \frac{\partial q}{\partial \Delta x}\right)^2 \qquad \text{Eq. 155}$$

Calculating the partial derivatives in Eq.149 we obtain:

$$\frac{\partial q}{\partial k} = \frac{\Delta T}{\Delta x}\,;\ \frac{\partial q}{\partial \Delta T} = \frac{k}{\Delta x}\,;\ \frac{\partial q}{\partial \Delta x} = -\frac{k\Delta T}{(\Delta x)^2} \qquad \text{Eq. 156}$$

Substituting Eq.156 and values found in point 1 to 6 above into Eq.155 we obtain:

$$U_q{}^2 = \left(U_k \frac{\Delta T}{\Delta x}\right)^2 + \left(U_{\Delta T} \frac{k}{\Delta x}\right)^2 + \left(-U_x \frac{k\Delta T}{\Delta x}\right)^2 \qquad \text{Eq. 157}$$

Hence, the total uncertainty with calculating heat flux is the sum of all the individual uncertainties, which yields: $U_q = 0.25W$ or 2.3%.

7. Torque

Torque was measured using a torque wrench with uncertainty of ±5%. The maximum torque measured was 75 Nm, so the maximum uncertainty is:

$$U_\tau = (75)(0.05) = \pm 3.75Nm \qquad \text{Eq. 158}$$

8. Displacement

Displacement was measured using three non-contact displacement transducers with uncertainty of ±1%. The maximum displacement measured was 30 μm, so the maximum uncertainty is:

$$U_\tau = (30)(0.01) = \pm 0.3 \mu m \qquad \text{Eq. 159}$$

Appendix I - Results for Two Block Analysis

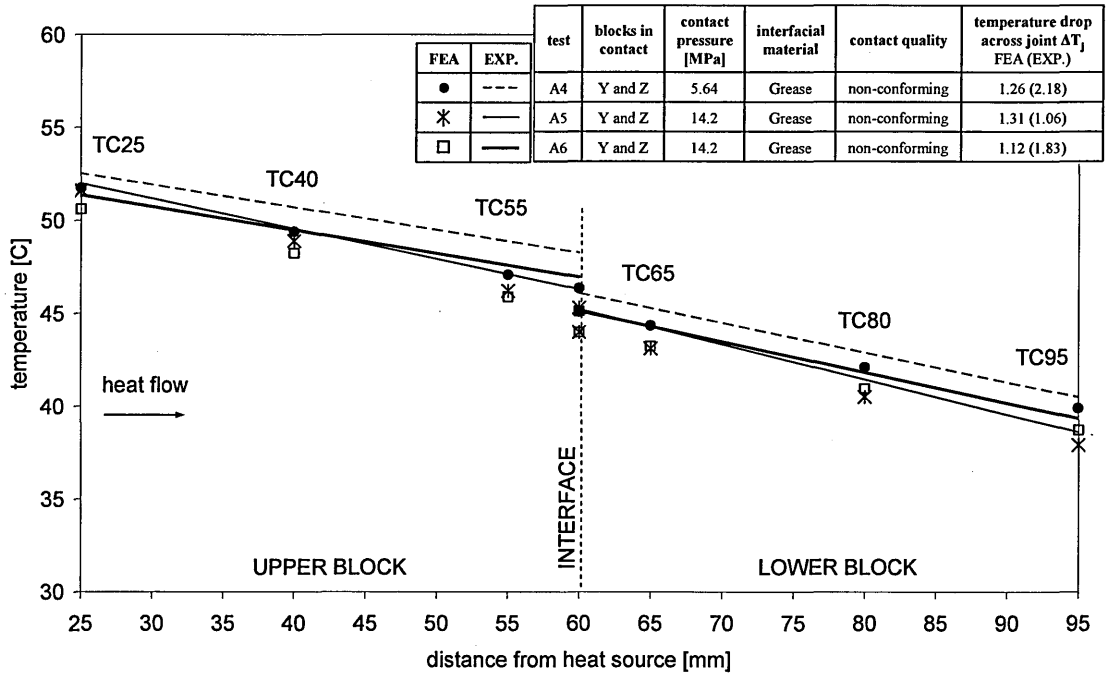

Figure I - 1. Temperature profile across interface at steady-state for tests A4, A5 and A6

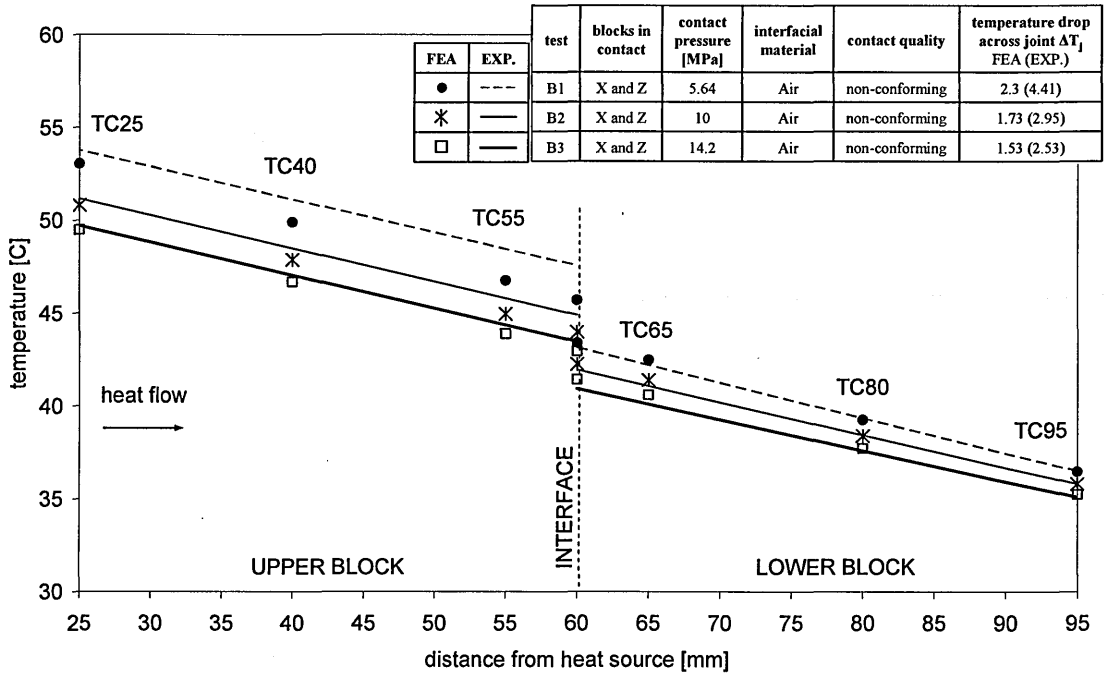

Figure I -2. Temperature profile across interface at steady-state for tests B1, B2 and B3

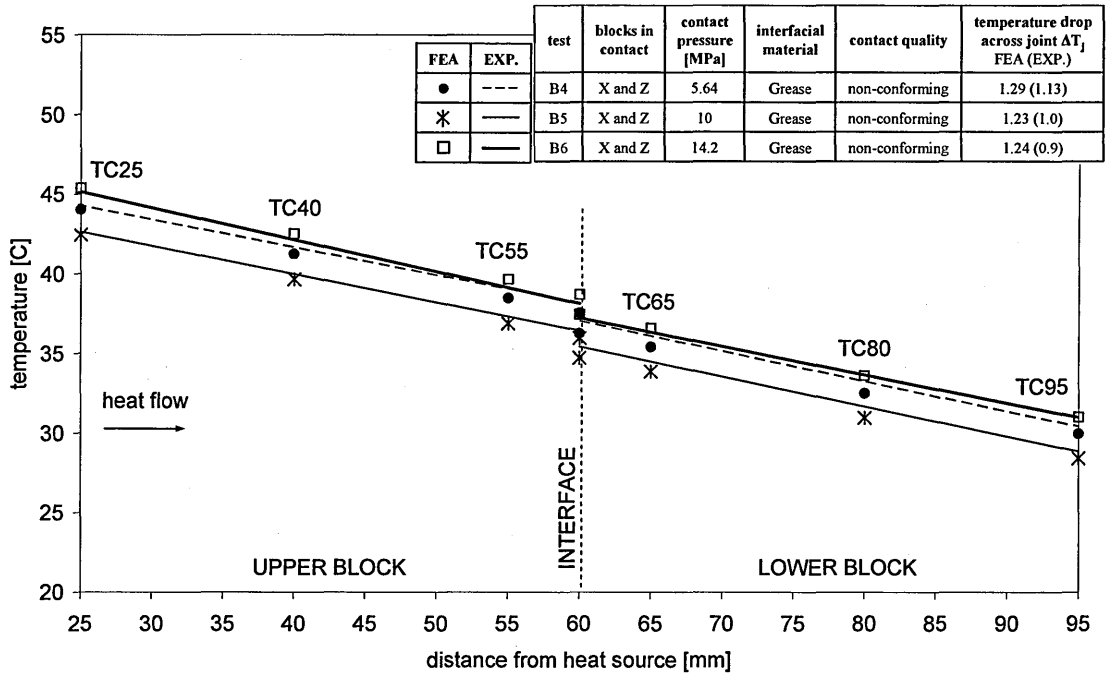

Figure I - 3. Temperature profile across interface at steady-state for tests B4, B5 and B6

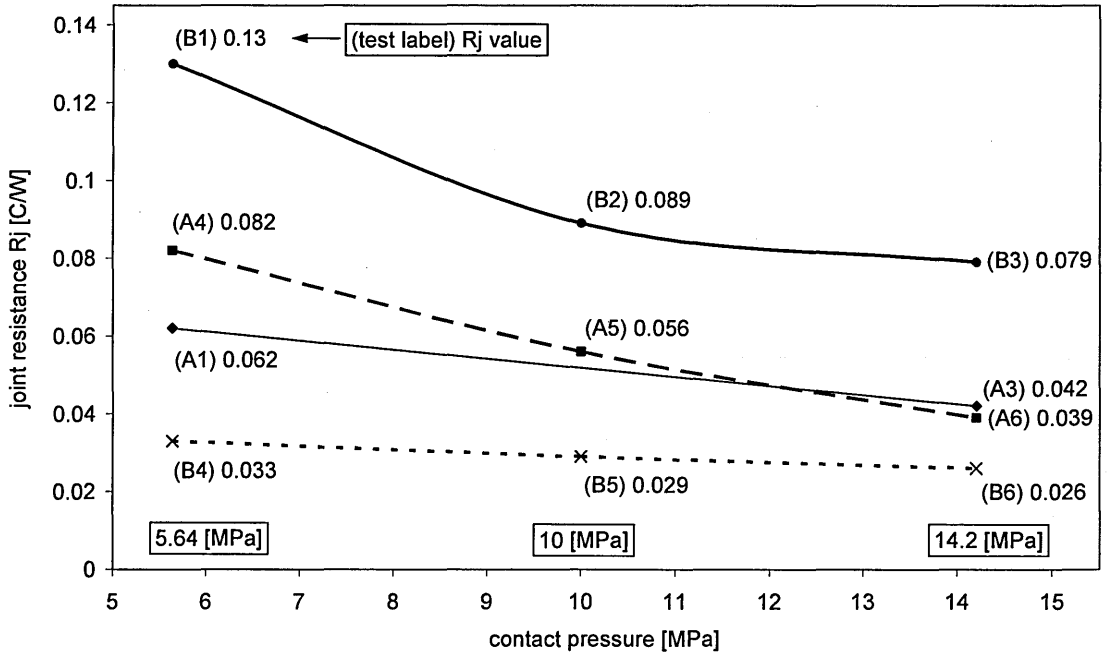

Figure I - 4. Joint resistance versus contact pressure for tests A1 to B6

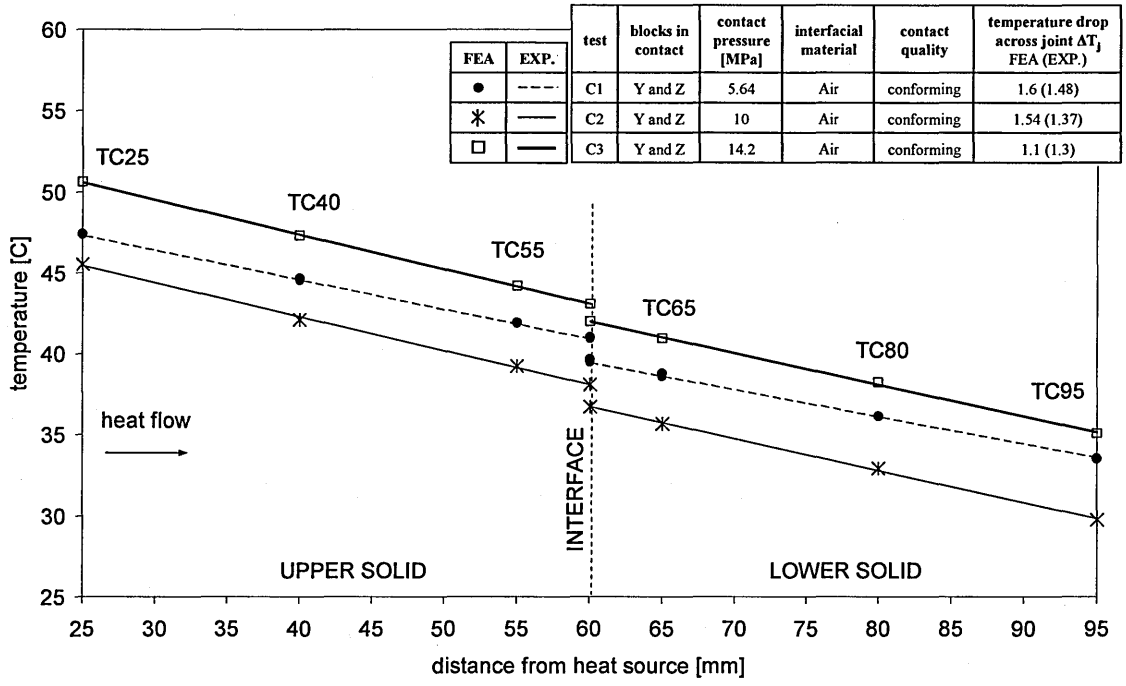

Figure I - 5. Temperature profile across interface at steady-state for tests C1, C2 and C3

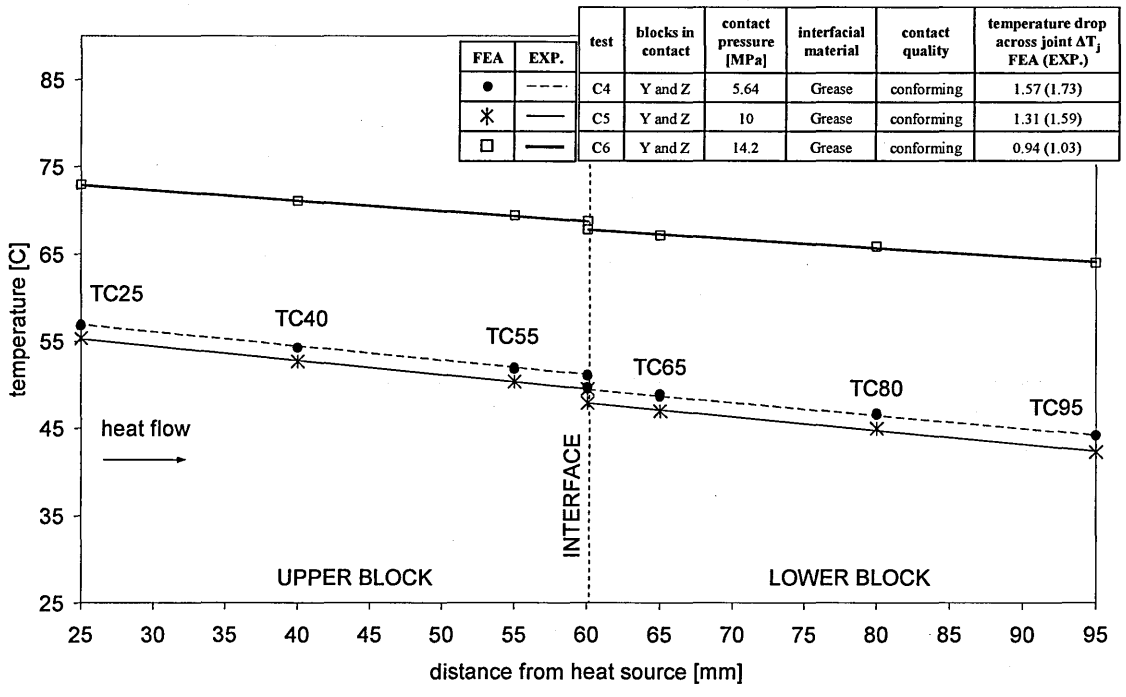

Figure I - 6. Temperature profile across interface at steady-state for tests C4, C5 and C6

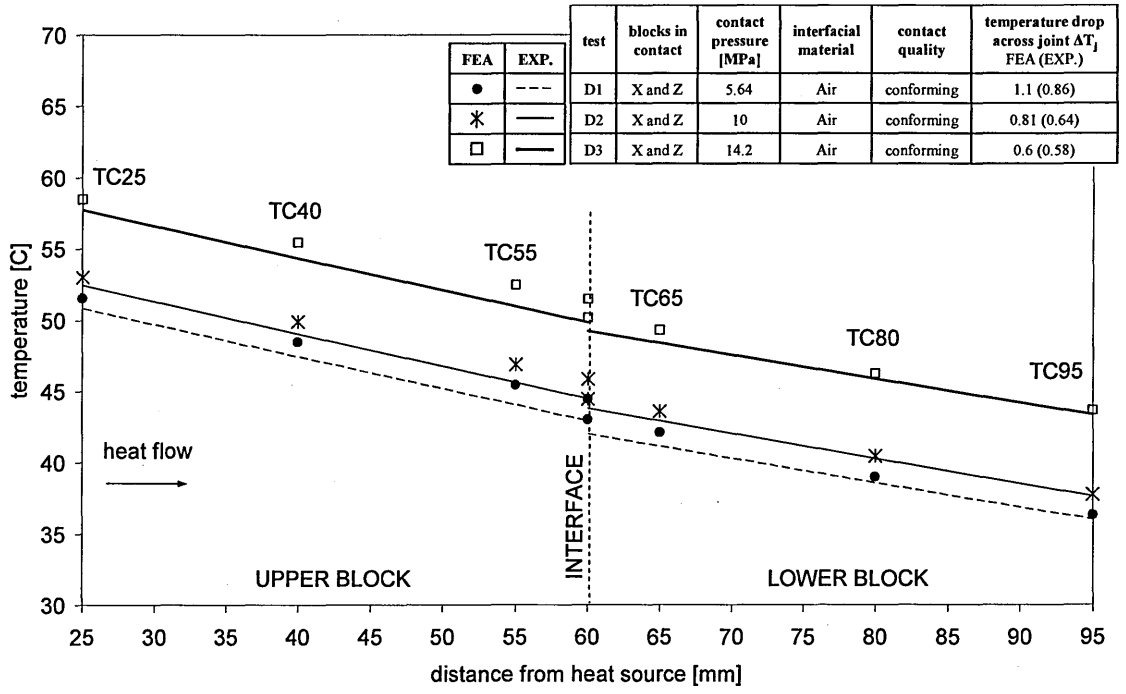

Figure I -7. Temperature profile across interface at steady-state for tests D1, D2 and D3

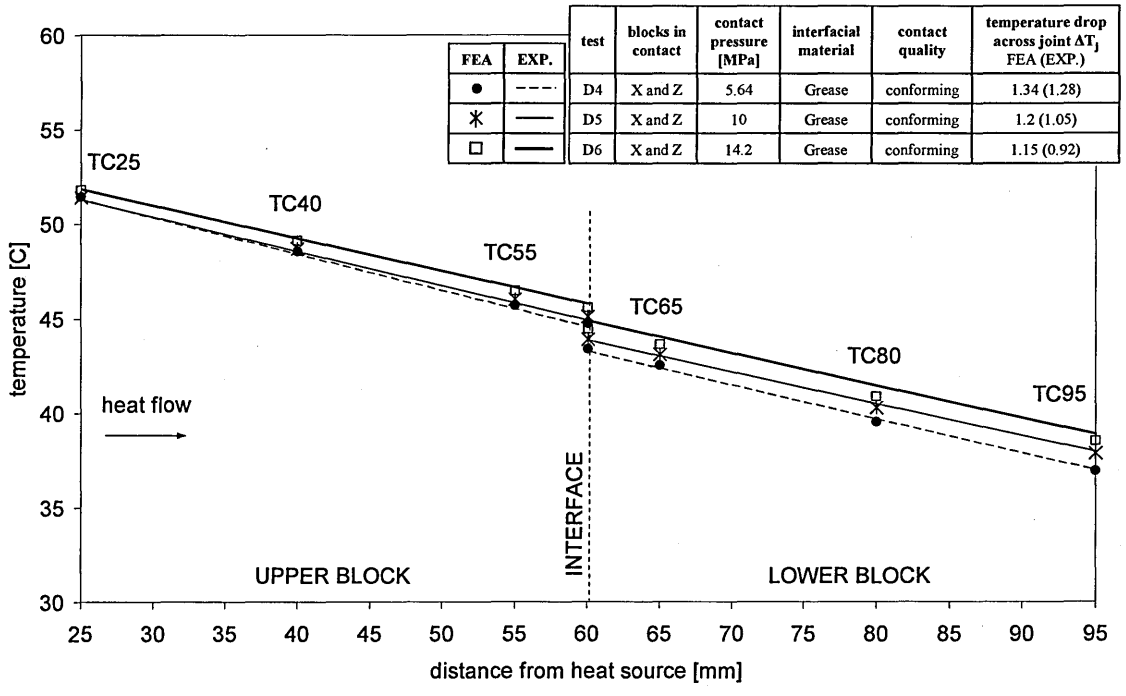

Figure I - 8. Temperature profile across interface at steady-state for tests D4, D5 and D6

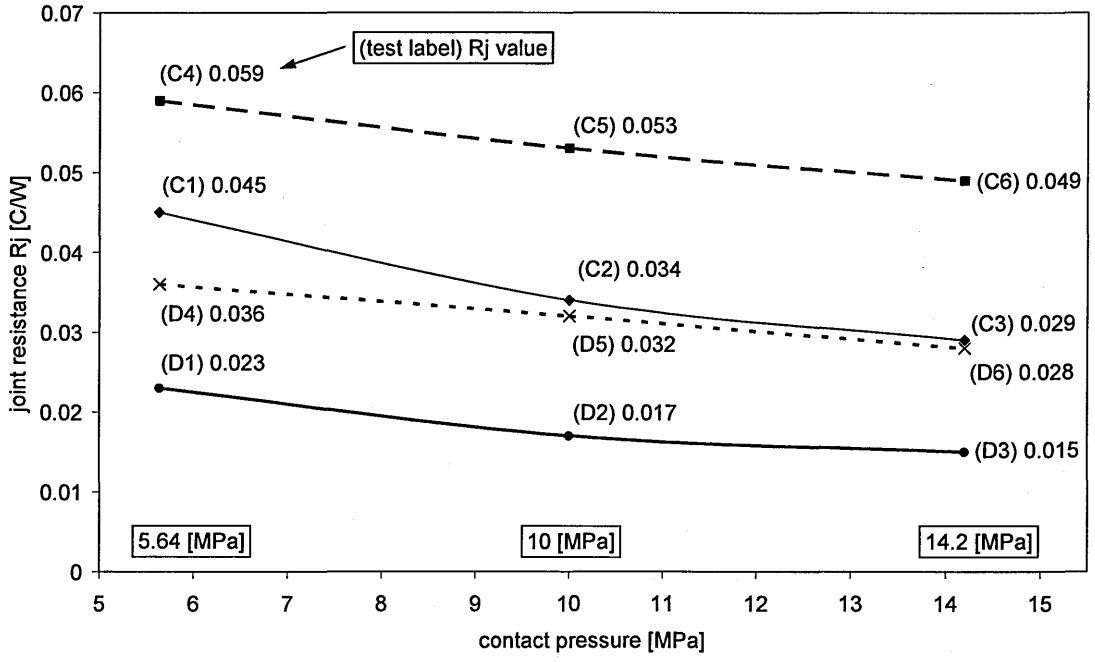

Figure I - 9. Joint resistance versus contact pressure for tests C1 to D6

Appendix J - Results for Three Block Analysis

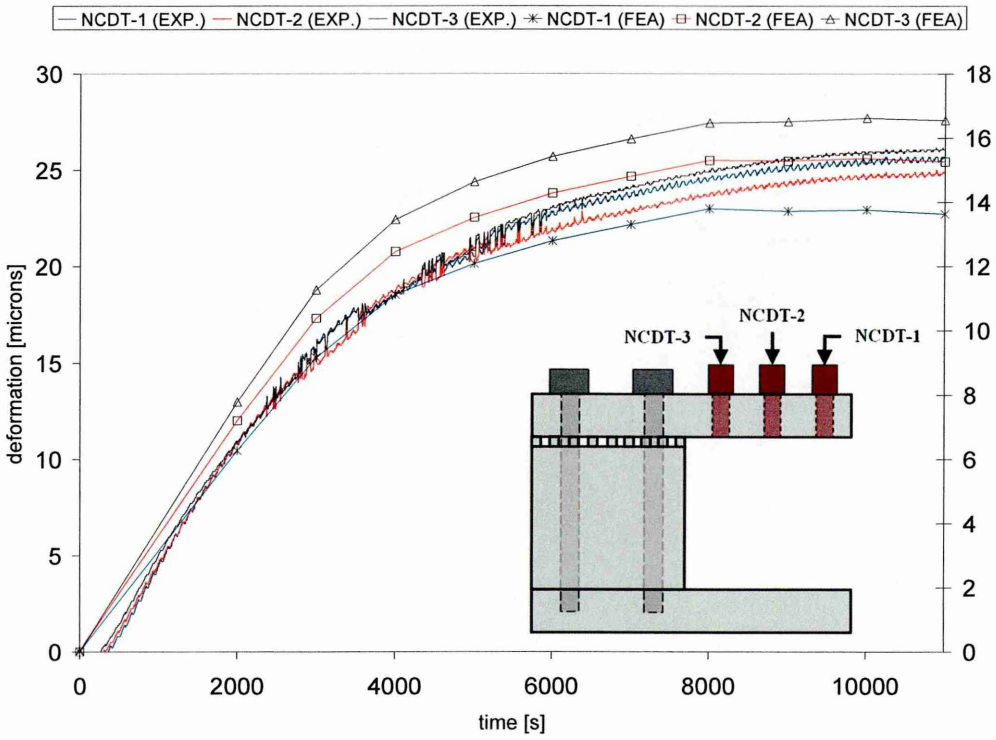

Figure J - 1. Transient deformation results, showing test E2

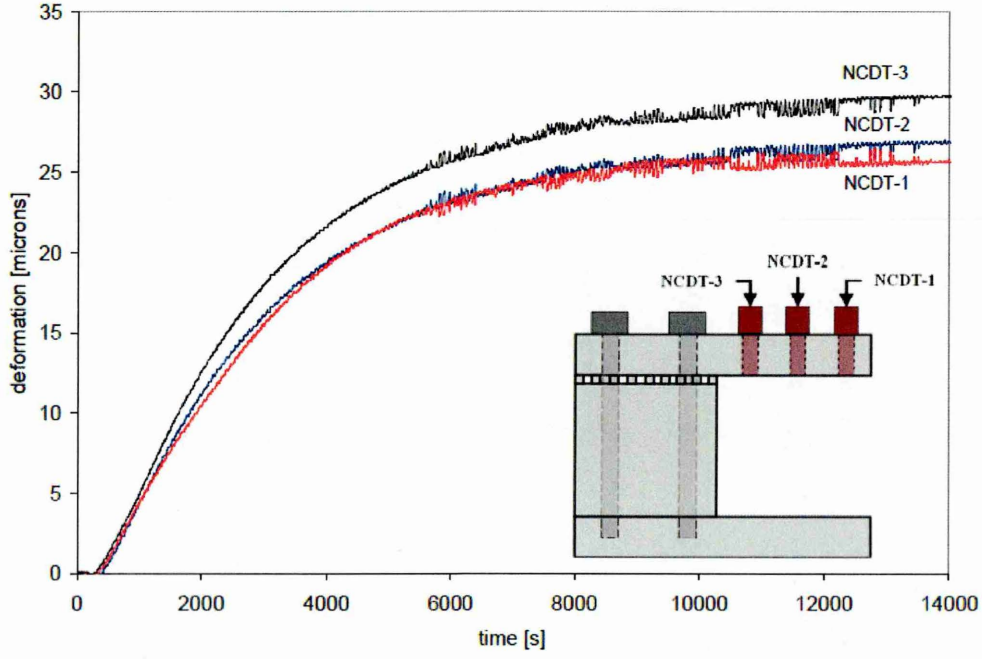

Figure J - 2. Transient deformation results, showing test E3

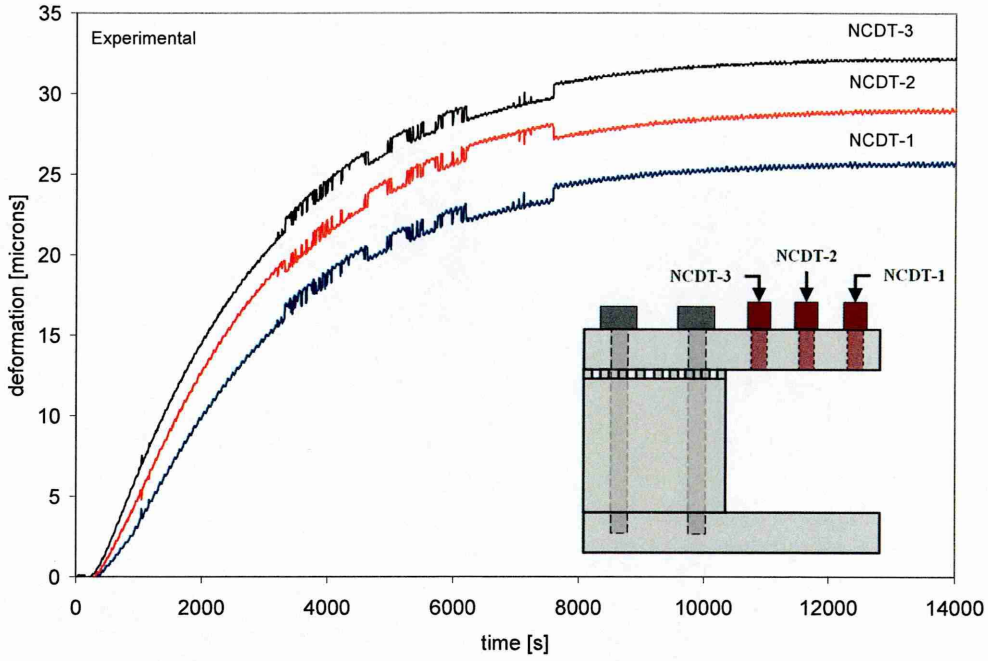

Figure J - 3. Transient deformation results, showing test E4

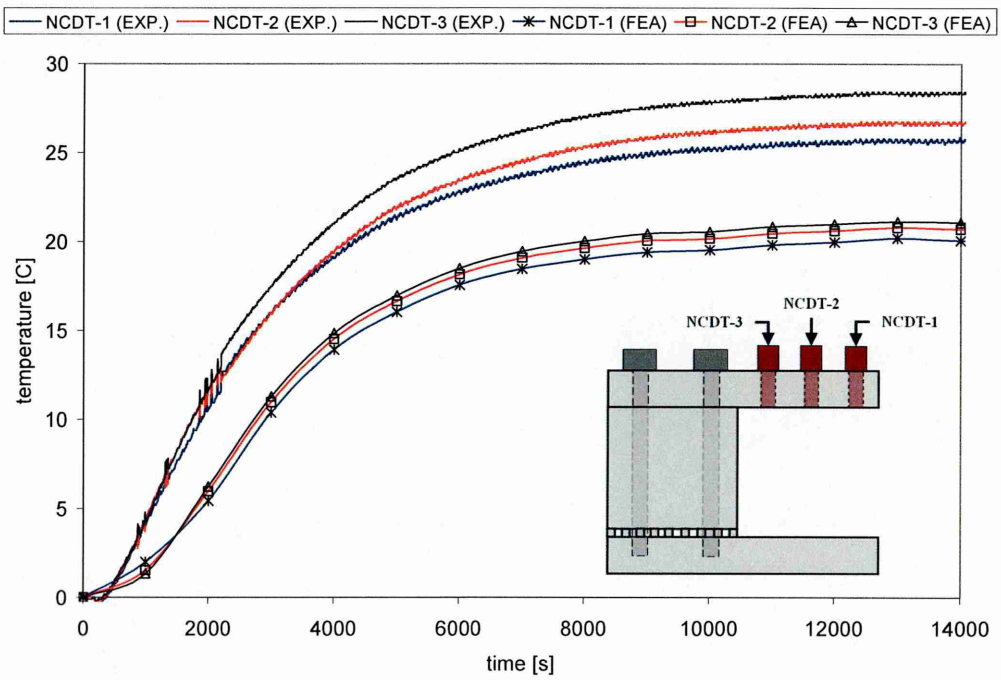

Figure J - 4. Transient deformation results, showing test F2

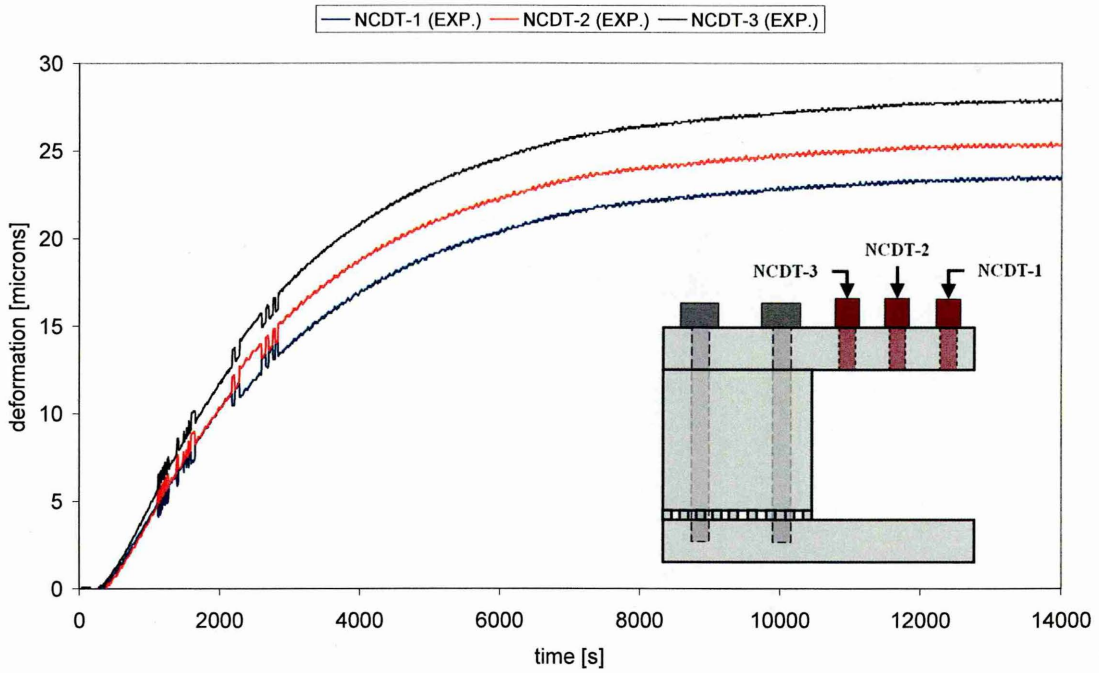

Figure J - 5. Transient deformation results, showing test F3

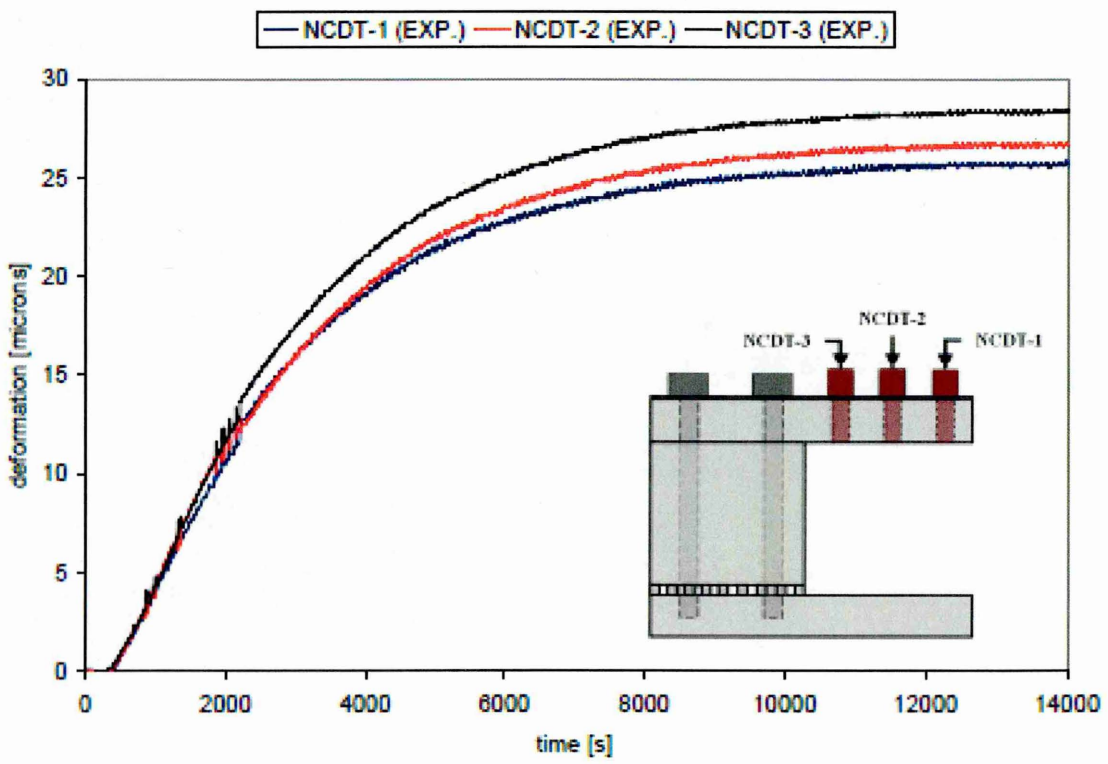

Figure J - 6. Transient deformation results, showing test F4

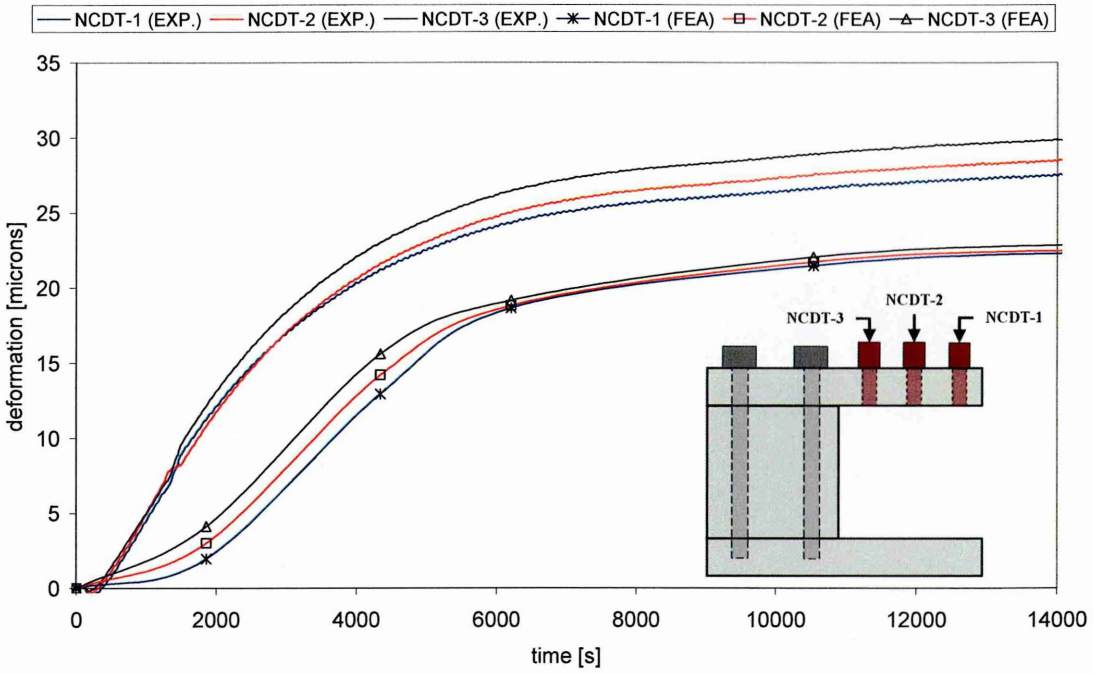

Figure J - 7. Transient deformation results, showing test G2

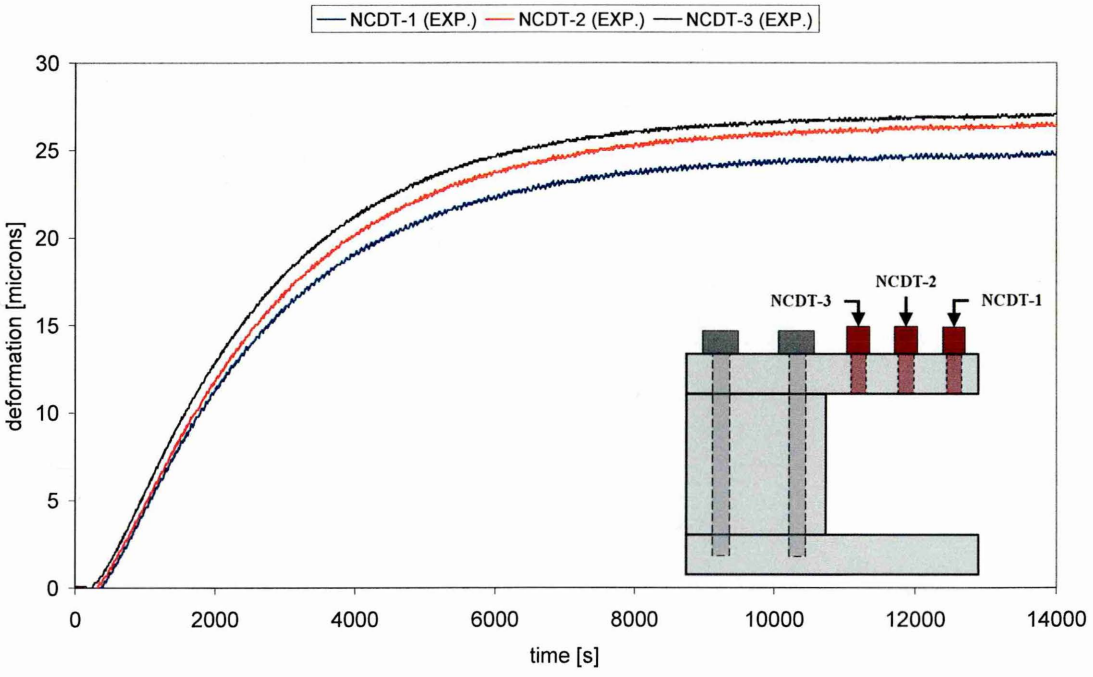

Figure J - 8. Transient deformation results, showing test G3

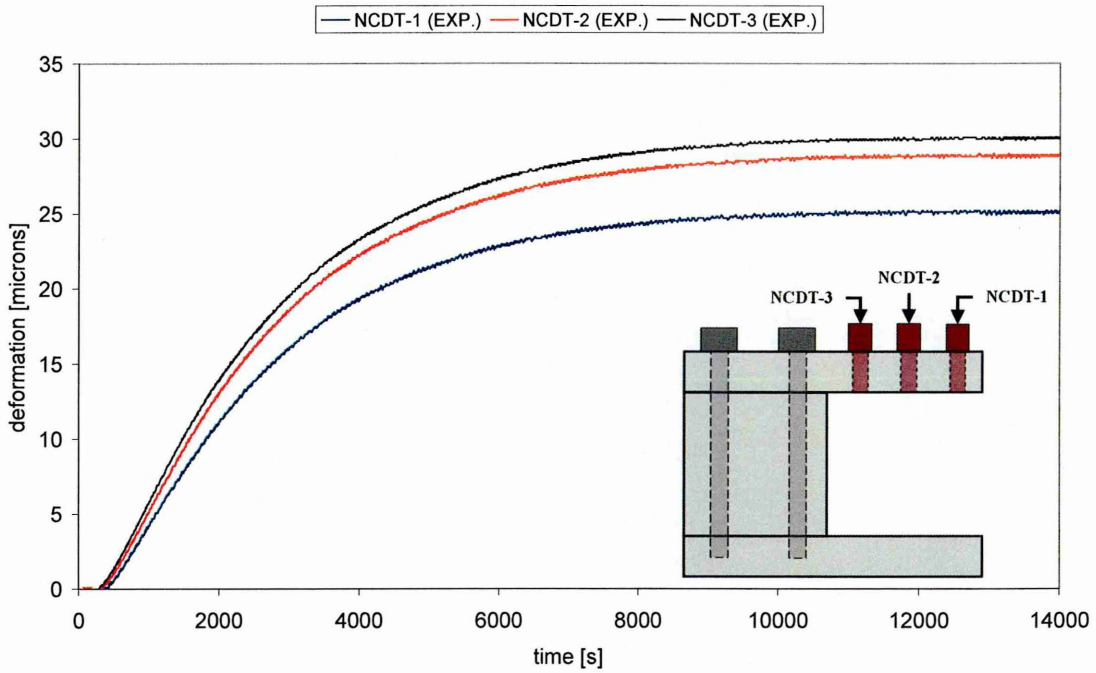

Figure J - 9. Transient deformation results, showing test G4

Appendix K - Publications

Peer reviewed conference papers:

1. Gashi. B, Shore. P., 'Thermal Analysis of Joint Interfaces in Machine Tools', Proceedings of 6th euspen International Conference, Vol. 1, pp. 269-272, Baden bei Wien, May 2006, Austria.
2. Gashi. B., Shore. P., Stephenson. J. D., (2005). '7th International Conference and Exhibition on Laser Metrology, Machine Tool, CMM & Robotic Performance, June 2005, Cranfield Management Development Centre, Cranfield, Bedfordshire, UK.

Special interest group:

3. Gashi. B., (2006). 'Special Interest Group Meeting: Thermal Issues in Precision Engineering', Dec 2006, Eindoven, Netherlands.